Accelerating Halide Perovskites for Photovoltaics through Atomistic Simulations

Yuhang Liang

Supervisor: Prof. Jun Huang
Co-supervisor: Prof. Rongkun Zheng

A Thesis Submitted in Fulfillment of the Requirement for the Degree of Doctor of Philosophy

School of Chemical and Biomolecular Engineering
Faculty of Engineering
The University of Sydney
2024

Declaration of Originality

This declaration affirms that the content of this thesis is my original work, and to the best of my knowledge, it does not include any material previously published or written by another individual, nor has it been submitted for any degree or diploma at the University of Sydney or or any other institution of higher learning, except where proper acknowledgment is made in the text.

Yuhang Liang

28 August 2024

Acknowledgements

This dissertation comprises the academic research I conducted during my PhD and serves as an expression of my gratitude to all those who supported me throughout the PhD candidate journey.

First and foremost, I extend my heartfelt gratitude to my supervisors, Professor Jun Huang and Professor Rongkun Zheng, for their steadfast help and support throughout my time as a PhD student. Professor Jun Huang welcomed me into his group at the University of Sydney and offered invaluable support in both academics and life over the past three years of my PhD candidacy, particularly arranging funding for my PhD scholarship and assisting with my application for various supporting funding such as Postgraduate Research Support Scheme. I would like to thank my co-supervisor, Professor Rongkun Zheng, who consistently found time for regular meetings, offering invaluable insights and information that helped me navigate a challenging period when my student visa application was inexplicably delayed by the Department of Immigration and Border Protection for nearly two years. As a result, my PhD studies are progressing very well. I often feel deeply grateful to have two such kind and supportive supervisors guiding me in both my research and personal life throughout my PhD journey.

Also, I would like to thank Dr. Carl Cui for his continued support, guidance, and technical expertise in scientific research and first-principles calculations. Despite his busy schedule, he gave me much valuable advice for going ahead and made himself available for numerous insightful discussions about my work, from which I gained a great deal. These engaging and thought-provoking conversations significantly contributed to my growth and understanding of computational materials science. Additionally, I would like to express my gratitude to the other members and collaborators with whom I interacted during my PhD studies: Dr. Feng Li, a senior experimental researcher in organic and halide perovskite devices; Prof. Catherine

Stampfl, an expert in DFT calculations; and Prof. Simon P. Ringer, a renowned expert in materials science. Their extensive support in data analysis and academic writing for my manuscripts greatly contributed to the success of my research endeavours. Moreover, I thank all my friends in the University of Sydney, including Dr. Hansheng Chen, Dr. Jiangtao Qu, Dr. Qi Wang, Dr. Hao Wang, Dr. Ranming Niu, Dr. Mengwei He, Dr. Lizhuo Wang, Dr. Weibin Liang, Dr. Rui Tang, Dr. Jiaquan Li, Dr. Zijian Yu, Miss. Xingmo Zhang, Miss. Fang Zeng, Mr. Taoyuze Lv, Mr. Runkai Liu, Mr. Joshua Nathan Maggiora, Miss Sibei Zou, Miss Haoyue Sun, Miss Xingxu Liu, Miss Ying Shu, Mr. Chunjing Su, Mr. Chao Huang, Mr. Kirk Chen, Miss. Haoruo Zhou, Mr. Qi Chen, Mr. Kaijuan Chen Mr. ZhiSheng Lin, Mr. Na MuRasaihan, etc.

Finally, I would like to express my heartfelt gratitude to my family. To my dear parents - Mr. Bizhong Liang and Mrs. Lianchao Chen, for not only bringing me into this world and raising me but also for their constant support in all my pursuits. Your belief in me has been a continuous source of strength. To my lovely wife - Mrs. Siyi Chen, a beautiful and considerate girl, who fills my life with care and happiness and has blessed me with a daughter and a son. Your love and companionship have made every challenge easier and every success sweeter. To my adorable children – Miss YueXuan Liang and Mr. Chengjun Liang, for bringing joy and completeness to my life. Your laughter and curiosity inspire me every day. Last to my grandmothers and all other my families, whose presence has made my life happy from birth to the present day. Your support and encouragement have been invaluable. Thank you all for your love and support.

The research reported in this thesis was supported by the award of the Faculty of Engineering Research Scholarship to the PhD Candidate.

Thesis Authorship Attribution Statement

Chapter 3 of this thesis is published as

Yuhang Liang,[1,2,*] *Xiangyuan Cui,[3,*] Feng Li,[2] Catherine Stampfl,[2] Simon P. Ringer,[3] Jun Huang,[1,*] Rongkun Zheng[2,*]*

Minimizing and controlling hydrogen for highly efficient formamidinium lead triiodide solar cells

J. Am. Chem. Soc. 2022, 144 (15), 6770–6778

DOI: 10.1021/jacs.2c00038

Chapter 4 of this thesis is published as

Yuhang Liang,[1,2] *Xiangyuan Cui,[3,*] Feng Li,[2] Catherine Stampfl,[2] Simon P. Ringer,[3] Jun Huang,[1,*] Rongkun Zheng[2,*]*

Trapped-hydrogen-induced energy loss in tin-based hybrid perovskite solar cells

Phys. Rev. Applied 2022, 18 (3), 034084.

DOI: 10.1103/PhysRevApplied.18.034084

Chapter 5 of this thesis is published as

Yuhang Liang,[1,2] *Xiangyuan Cui,[3,*] Feng Li,[2] Catherine Stampfl,[2] Simon P. Ringer,[3] Jun Huang,[1,*] Rongkun Zheng[2,*]*

Origin of enhanced nonradiative carrier recombination induced by oxygen in hybrid Sn perovskite

J. Phys. Chem. Lett. 2023, 14 (12), 2950–2957

DOI: 10.1021/acs.jpclett.3c00423

Chapter 6 of this thesis is published as

Yuhang Liang,[1,2,*] *Feng Li,*[2,*], *Xiangyuan Cui,*[3,*] *Taoyuze Lv,*[2] *Catherine Stampfl,*[2] *Simon P. Ringer,*[3] *Xudong Yang,*[4,5,6] *Jun Huang,*[1,*] *Rongkun Zheng*[2,*]

Toward stabilization of formamidinium lead iodide perovskites by defect control and composition engineering

Nat Commun 2024, 15 (1), 1707

DOI: 10.1021/acs.jpclett.3c00423

Chapter 7 of this thesis is published as

Yuhang Liang,[1,2,] *Feng Li,*[2,*], *Xiangyuan Cui,*[3,*] *Catherine Stampfl,*[2] *Simon P. Ringer,*[3] *Xudong Yang,*[4,5,6] *Jun Huang,*[1,*] *Rongkun Zheng*[2,*]

Multiple B-site doping suppresses ion migration in halide perovskites

Accepted by Science Advances

The following papers were published during the PhD candidacy but are not included in this thesis:

(1) **Liang, Y**.; Cui, X.*; Li, F.; Stampfl, C.; Huang, J.; Ringer, S. P.; Zheng, R.* Hydrogen-Anion-Induced Carrier Recombination in MAPbI3 Perovskite Solar Cells. ***J. Phys. Chem. Lett.*** 2021, 12 (43), 10677–10683.

(2) **Liang, Y**.; Cui, X.*; Li, F.; Stampfl, C.; Ringer, S. P.; Huang, J.*; Zheng, R.* Hydrogen-Induced Nonradiative Recombination in All-Inorganic CsPbI3 Perovskite Solar Cells. ***Solar RRL*** 2022, 6 (8), 2200211.

(3) **Liang, Y**.; Cui, X.*; Li, F.; Stampfl, C.; Ringer, S. P.; Huang, J.*; Zheng, R.* Interstitial Hydrogen Anions: A Cause of p-Type Conductivity in CsSnI3. ***J. Phys. Chem. C*** 2022, *126* (35), 14843–14849.

(4) **Liang, Y**.; Cui, X.*; Li, F.; Stampfl, C.; Ringer, S. P.; Zheng, R.* Atomic and Molecular Hydrogen Impurities in Hybrid Perovskite Solar Cells. ***J. Phys. Chem. C*** 2022, 126 (4), 1721–1728.

(5) Zeng, F.; Kong, W.; **Liang, Y**.; Li, F.; Lv, T.; Su, Z.; Wang, T.; Peng, B.; Ye, L.; Chen, Z.; Gao, X.; Huang, J.; Zheng, R.*; Yang, X.* Highly Stable and Efficient Formamidinium-Based 2D Ruddlesden–Popper Perovskite Solar Cells via Lattice Manipulation. ***Adv. Mater.*** 2023, *35* (42), 2306051.

(6) Lv, T.; **Liang, Y**.; Li, F.; Huang, J.; Zheng, R.* Kinetic Process with Anti-Frenkel Disorder in $CsPbI_3$ Perovskite. ***J. Phys. Chem. Lett.*** 2024, 2929–2935.

(7) Lv, T.; Zhong, Z.*; **Liang, Y**.; Li, F.; Huang, J.; Zheng, R.* Deep Charge: Deep Learning Model of Electron Density from a One-Shot Density Functional Theory Calculation. ***Phys. Rev. B*** 2023, *108* (23), 235159.

(8) Lv, T.; **Liang, Y**.; Li, F.; Yang, X.; Huang, J.; Zheng, R.* Two-Dimensional Halide Perovskites: A Review on Their Orientations. ***Sci. China Phys. Mech. Astron.*** 2022, *66* (1), 217306.

I independently carried out this work, including the literature review, project design, implementation of calculations, data acquisition and analysis, and manuscript drafting. Dr. Xiangyuan Cui, Prof. Jun Huang, and Prof. Rongkun Zheng provided project supervision, technical support, data analysis, and manuscript revisions. Dr. Feng Li, Prof. Catherine Stampfl, and Prof. Simon P. Ringer contributed to the data analysis and reviewed the manuscript.

In cases where I am not the corresponding author of a published item, permission to include the published material in this thesis has been granted by the corresponding author.

Yuhang Liang

28 August 2024

As supervisors for the candidature upon which this thesis is based, I can confirm that the authorship attribution statements above are correct.

Rongkun Zheng

28 August 2024

Jun Huang

28 August 2024

Table of Content

List of Figures

$(V_{Sn} - H_2)^0$ complex, where electrons are relocated from the yellow to the blue regions. The isosurfaces are taken at 0.01 $e/\text{Å}^3$. The notations of atoms are as those in **Figure 1** and the hydrogen interstitials are highlighted in red. 95

Figure 4.6. Formation energies of FA vacancy-hydrogen and I vacancy-hydrogen related defects under the Sn-rich and Sn-moderate growth conditions as a function of the Fermi level. The H-rich conditions are adopted as a reference. 96

Figure 4.7. (**a**) Configuration coordinate diagrams for the $(0/-)$ charge-state transition of the $VSn - H2$ complex. The generalized coordinate (Q) of each configuration is defined by its difference from the reference[142]: $Q = \sqrt{\sum_a m_a (R_a - R_{f,a})^2}$, where m_a and R_a are the mass and the Cartesian coordinate of atom a; subscript f stands for the final state of the charge transition. (**b**) Nonradiative capture coefficient of the $V_{Sn} - H_2$ complex as a function of temperature in $FASnI_3$. (**c**) The calculated and experimental PCE losses: the left-Y axis stands for the calculated nonradiative-induced PCE loss ($\Delta\eta_{nr}$) by the $V_{Sn} - H_2$ complexes as a function of the complex density at room temperature. The right-Y axis stands for the experimentally practical solar cell PCE losses relative to the S-Q efficiency limit of $FASnI_3$ (i.e., $\Delta\eta_{exp}$=33.09% – the reported PCE values). The measured deep-level trap densities and PCE values of α are taken from Ref.[164], β from Ref.[189], γ from Ref.[190], δ from Ref.[167], ε from Ref.[191], and θ from Ref.[166].....99

Figure 5.1. For the relative chemical potentials $\Delta\mu_i$ of host atoms (MA, Sn, I) in $MASnI_3$, they should be satisfied:

$$\Delta\mu_{MA} + \Delta\mu_{Sn} + 3\Delta\mu_I = \Delta H_f(MASnI_3)$$

To avoid the formation of the possible competing secondary compounds, including MAI, SnI_2, and SnI_4, and the pure elemental phases, there should be:

$$\Delta\mu_{MA} + \Delta\mu_I < \Delta H_f(MAI)$$

$$\Delta\mu_{Sn} + 2\Delta\mu_I < \Delta H_f(SnI_2)$$

$$\Delta\mu_{Sn} + 4\Delta\mu_I < \Delta H_f(SnI_4)$$

$$\Delta\mu_{FA} < 0;\ \Delta\mu_{Sn} < 0;\ \Delta\mu_{Br} < 0$$

where the $MASnI_3$ will be thermodynamically stable instead of its secondary phases or element phases of components. With all these conditions, the relative chemical potentials

$$\Delta\mu_{Pb} + 2\Delta\mu_{I} < \Delta H_f(PbI_2)$$

$$\Delta\mu_{FA} < 0;\ \Delta\mu_{Sn} < 0;\ \Delta\mu_{Br} < 0$$

where the $FAPbI_3$ will be thermodynamically stable instead of its secondary phases or element phases of components. With all these conditions, the relative chemical potentials $\Delta\mu_i$ are restricted in the red area. In this study, we chose the I-moderate growth conditions for further evaluating the defect formation energies.....128

Figure 6.2. Evolution of (**a**) the lattice parameters, (**b**) volume, (**c**) bandgap, and (**d**) the potential energy as a function of reaction coordinate of the α-δ phase transition in $FAPbI_3$, where the starting point (x=0) of the reaction coordinate is defined as the configuration of the initial α-phase state, and the endpoint (x=1) stands for the final δ-phase state configuration. (**e**) Side and (**f**) top views of the atomic displacements along the α-δ phase transition in $FAPbI_3$, where TS stands for the transition state.....133

Figure 6.3. Optimized structures of the (**a**) α-phase and (**b**) δ-phase of $FAPbI_3$. (**c**) Calculated band structure and (**d**) the density of state (DOS) of α-$FAPbI_3$. (**e**) The band structure and (**f**) the DOS of δ-$FAPbI_3$. The calculations of the electronic properties were based on density functional theory with the hybrid Heyd–Scuseria–Ernzerhof functional and spin–orbit coupling (HSE06-SOC). 134

Figure 6.4. Atomic structures of $FAPbI_3$ perovskite with FA-cationic disorder in various degrees extracted from *ab initio* molecular dynamic (AIMD) simulations at room temperature, namely, (**a**) Str.1, (**b**) Str.2, (**c**) Str.1, and (**d**) Str.4. Note that from Str.1 to Str.4, the orientational disorder of the FA cations is increasingly more significant compared with the pristine structure in **Figure 6.2a**. (**e**) Evolution of and the potential energy as a function of reaction coordinate of α-δ phase transition of pristine $FAPbI_3$ and those with FA-cationic disorder (Str.1-Str.4). 136

Figure 6.5. (**a**) The phase transition barriers (E_b) and (**b**) total energy differences between α- and δ-phase ($\Delta E_{\delta-\alpha}$) of pristine $FAPbI_3$ and systems with the presence of the low-energy intrinsic defects. The charge density plots for the transition states of α-δ phase transition of $FAPbI_3$ with (**c**) V_I^+ and (**d**) I_i^-, where the yellow iso-surfaces stand for the partial charge density for the states of the Pb dimer and I dimer. The iso-surfaces were taken at 0.01 $e/Å3$. 138

List of Tables

Abstract

Hybrid halide perovskites have drawn tremendous attention from the energy-related community owing to their low-cost solution-processed fabrication and outstanding optoelectronic properties. Particularly, perovskite-based solar cells (PSCs) have revolutionized the competition in photovoltaic performance with rapid progress in power conversion efficiency (PCE) currently exceeding 25%. This performance rivals, or even outperforms, that of commercial silicon or other organic and inorganic solar cells. Nevertheless, the commercialization of PSCs is still hindered by their poor long-term stability and toxicity of lead content. In this thesis, based on the rigorous first-principles calculations, we thoroughly studied the underlying mechanisms behind the nonradiative charge carrier recombination, perovskite phase degradation, and ion migration in the prototypical lead halide perovskites and tin halide perovskites. The theoretical insights provide rational engineering principles and scientific guidance for achieving high-efficiency and long-term stable halide perovskite-based solar cells and other optoelectronic devices in the near future. Specifically, this thesis is structured as follows:

In Chapter 1, we reviewed recent progress in the development of PSCs and highlighted current challenges in device commercialization, including nonradiative charge carrier recombination mechanism, phase transition, and ion diffusion. Thereafter, we discussed the existing compositional engineering strategies for improving the efficiency and stability of PSCs.

In Chapter 2, we introduced the first-principles approach based on density functional theory (DFT) together with Ab initio molecular dynamics (AIMD), which are the methodological foundation of the thesis. Specifically, the Generalized Gradient Approximation (GGA) functional in the Perdew-Burke-Ernzerhof (PBE) form has proven effective in accurately predicting atomic configurations and energies of systems, playing a crucial role in the current research on the defect physics and chemistry of halide perovskite materials. However, such a

theoretical scheme is known to have a bandgap error, which affects the accuracy of defect transition energy predictions. To address this limitation, the higher-level hybrid functional (HSE06) with spin-orbit coupling (SOC) was employed to ensure more reliable results.

In Chapter 3, we systematically studied the nonradiative recombination mechanism in the widely used formamidinium lead triiodide ($FAPbI_3$) perovskite active layers and demonstrated that the traditionally believed native point defects are not responsible for the nonradiative losses. Instead, hydrogen ions, which can be abundant under both iodine-rich and iodine-poor conditions in $FAPbI_3$, act as efficient nonradiative recombination centers, suppressing power conversion efficiency. Moreover, iodine-moderate synthesis conditions can favor the formation of electrically inactive molecular hydrogen, dramatically suppressing the detrimental hydrogen ions. This work identifies the dominant nonradiative recombination centers in the widely used $FAPbI_3$ layers and rationalizes how the prevailing iodine management reduces the nonradiative losses. Minimizing unintentional hydrogen incorporation in the perovskite is critical for achieving high device performance.

In Chapter 4, we reported an important but different nonradiative energy loss mechanism in the prototypical Sn-based $FASnI_3$ ($FA= HC(NH_2)_2$, formamidinium) perovskites as compared with the Pb-based counterparts. We discovered that high-density intrinsic tin vacancies (V_{Sn}) can effectively capture hydrogen to form $V_{Sn} - H_2$ complexes, which act as highly detrimental nonradiative recombination centers. We quantitatively showed that they can give rise to strong carrier recombination and thus energy loss due to a high nonradiative recombination rate constant. These key findings identify a hidden yet critical origin for the low performance of $FASnI_3$-based devices and highlight the significance of controlling the hydrogen environment in the development of broad high-efficiency non-toxic halide perovskite device applications.

In Chapter 5, we studied the underlying mechanism behind the commonly observed oxygen-ingression-induced carrier lifetime reduction in hybrid Sn-based perovskite $MASnI_3$ ($MA=CH_3NH_3$) and found that oxygen by itself is not a recombination center. Instead, it tends to form substitutional O_I by combining with native I vacancies (V_I), and remarkably increases the original recombination rate of V_I by two to three orders of magnitude. This rationalizes the experimentally observed sharp decline of carrier lifetime in perovskites exposed to air. The significantly enhanced carrier recombination is due to a smaller electron capture barrier of O_I, resulting from lattice strengthening and the suppressed structural relaxation upon electron capture. These insights offer a route to further improve device performance via anion engineering in broad Sn-based perovskite optoelectronics operating in ambient air. Moreover, our results highlight the important role of lattice relaxation in nonradiative carrier capture in materials.

In Chapter 6, we investigated the mechanism driving the undesired α-δ phase transition in $FAPbI_3$. Prevalent iodine vacancies and interstitials can significantly expedite the structural transition kinetics by inducing robust covalency during transition states. Extrinsically, the detrimental roles of atmospheric moisture and oxygen in degrading the $FAPbI_3$ perovskite phase are also rationalized. Significantly, we discover compositional design principles by categorizing that A-site engineering primarily governs thermodynamics, whereas B-site doping can effectively manipulate the kinetics of the phase transition in $FAPbI_3$, highlighting lanthanide ions as promising B-site substitutes. A-B mixed doping emerges as an efficient strategy to synergistically stabilize α-$FAPbI_3$, as experimentally demonstrated by substantially higher initial optoelectronic characteristics and significantly enhanced phase stability in Cs-Eu doped $FAPbI_3$ as compared to its Cs-doped counterpart. This study provides scientific guidance for the design and optimization of long-term stable $FAPbI_3$-based solar cells and other optoelectronic devices through defect control and synergetic composition engineering.

In Chapter 7, we unravel the interplay between the dynamics of perovskite octahedral lattice and the diffusion energy barrier associated with ion migration. Our results show that B-site substitution, particularly with alkaline earth and lanthanide elements, significantly strengthens lattice interactions, restrains octahedral oscillation, and increases iodine migration barriers, outperforming the commonly used A-site and X-site substitutions and interstitial doping. Moreover, the enhanced barrier correlates with the geometric factor of $\mu\tau$ (where τ and μ are the tolerance factor and octahedral factor, respectively), underlining the superior effectiveness of co- and multiple-element B-site doping in stabilizing the perovskite lattice and reducing ion migration. This is experimentally validated with the exemplary hysteresis-free Eu-Ca doped perovskite single crystals, which exhibit remarkable improvements in ambient stability and transport properties. These insights underline the potential of B-site compositional engineering in alleviating ion migration and improving the intrinsic stability of halide perovskites, with significant implications for achieving long-term operational stability and lead reduction in perovskite-based devices.

In Chapter 8, we summarize the main discoveries made in this thesis, highlight its academic contributions to the related research area, and provide an outlook on current and future research endeavours.

Table of Abbreviation

MHPs	Metal halide perovskites
LEDs	Light-emitting diodes
PSCs	Perovskite solar cells
PDs	Photodetectors
FETs	Field-effect transistors
QWS	Quantum well structures
PCE	Power conversion efficiency
ASE	Amplified spontaneous emission
EQE	External quantum efficiency
FA	Formamidinium
SQ	Shockley-Queisser
V_{oc}	Open-circuit voltage
GBs	Grain boundaries
DFT	Density functional theory
HF	Hartree-Fock
XC	Exchange and Correlation energy
LDA	Local density approximation
GGA	Generalized Gradient approximation
BLYP	Beche-Lee-Yang-Parr
PW91	Perdew-Wang functional
PBE	Perdew-Burke-Ernzerhof
HTCH	Hamperecht-Tozer-Cohen-Handy
HSE	Heyd, Scuseria and Ernzerhof
PAW	Projector-augmented wave pseudopotential

VASP	Vienna Ab-initio Simulation Package
MP	Monkhorst-Pack
TS	Tkatchenko-Scheffler
SOC	Spin-orbit coupling
VBM	Valence band maximum
CBM	Conduction band minimum
CI-NEB	Climbing image nudged elastic band
VTST	VASP Transition State Tool
E_f	Fermi level
HTL	Hole transport layer
ETL	Electron transport layer
TEM	Transmission electron microscopy
SRH	Shockley-Read-Hall
CCD	Configuration coordinate diagram
AIMD	*ab initio* molecular dynamics
VCNEB	Variable-cell nudged elastic band
USPEX	Universal Structure Predictor: Evolutionary Xtallography
MLMD	Machine Learning Molecular Dynamics
MLFF	Machine Learning Force Field
ITC	Inverse temperature crystallization
EDX	Energy-dispersive X-ray spectroscopy
SCLC	Space-charge-limited-current
TFL	Trap-filled limit
XRD	X-ray diffraction
PL	Photoluminescence

PLQE	Photoluminescence quantum efficiency

Chapter 1: Background and Introduction

1.1 Emerging Halide Perovskite Semiconductors

Metal halide perovskites (MHPs) have garnered significant attention over the past few decades within the material research community due to their outstanding optoelectronic characteristics as well as easy, cost-effective manufacturing process[1,2]. These exceptional materials have demonstrated unprecedented development across a wide variety of optoelectronic applications, such as perovskite solar cells (PSCs)[3–5], field-effect transistors (FETs)[6,7], photodetectors (PDs)[8,9], light-emitting diodes (LEDs)[10,11], and lasers[12,13]. MHPs typically feature with a chemical formula of ABX_3, where A stands for monovalent cations (such as organic $HC(NH_2)_2^+$ (FA), $CH_3NH_3^+$ (MA), and inorganic Cs^+), B denotes divalent metal (such as Pb^{2+} and Sn^{2+}), and X for halide anions (such as I^-, Br^-, and Cl^-). For an ideal cubic perovskite structure, as shown in **Figure 1.1a**, the B-site coordinates with six X-site anions forming an inorganic network of corner-sharing BX_6 octahedra, and the larger A-site cations occupy the octahedral void. Therefore, the ionic radii of A-site cation play a critical role in forming a close-packed perovskite structure.

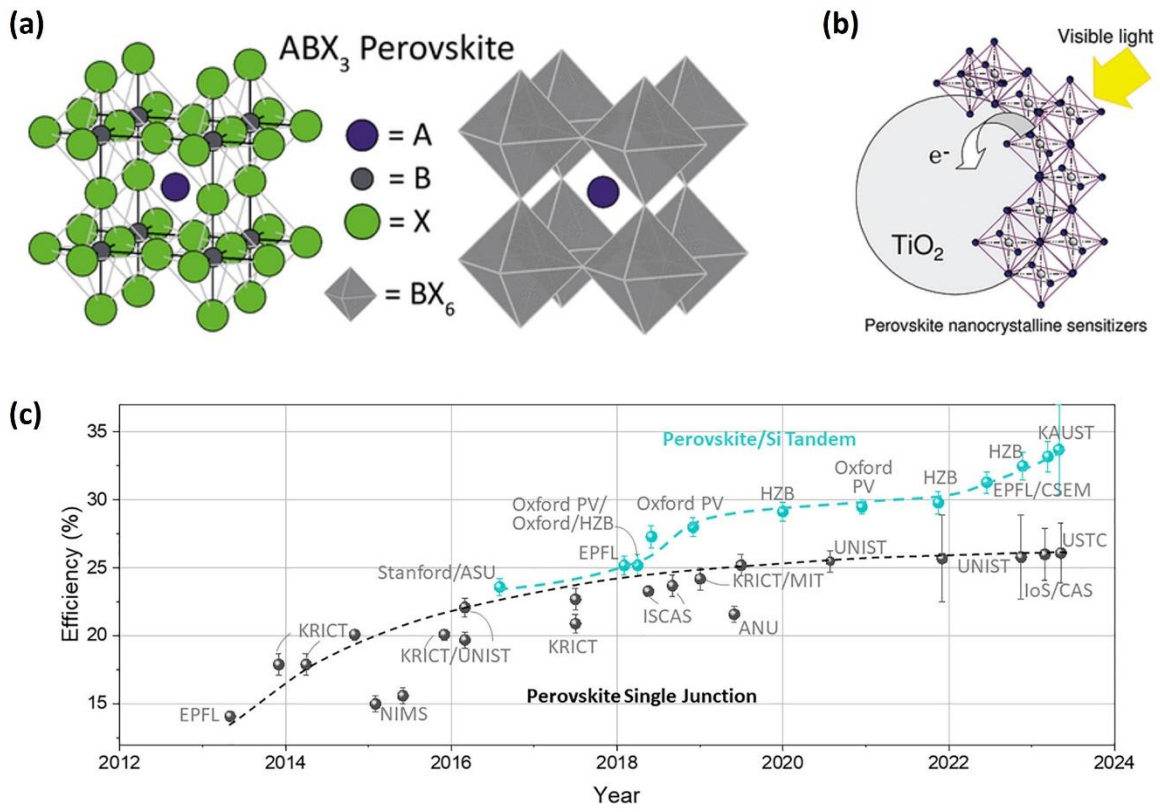

Figure 1.1. (**a**) Standard representation of the prototypical cubic perovskite lattices. Left displays all the atoms; right highlights the BX_6 inorganic octahedral framework and the A-site cations[14]. (**b**) Schematic of organometal halide perovskites as visible-light sensitizers[15]. (**c**) Power conversion efficiency of the perovskite-based single-junction and perovskite-silicon tandem solar cells from 2013 to 2023[16].

MHPs have a long history of study. The first synthesis of MHPs dates back to 1892[17], while initial exploration into their optoelectronic properties came later in the 1950s[18], when vividly colored $CsPbX_3$ (X = Cl, Br) perovskite crystals were found to exhibit a unique frequency-dependent photoconductive response, highlight the novel optoelectronic characteristics of MHPs. In addition to conventional three-dimensional perovskites, Mitzi and colleagues investigated low-dimensional layered halide perovskites in the early 1990s[19]. When combined with alkylammonium cations, these materials naturally form quantum well structures (QWS), exhibiting pronounced excitonic properties and holding great promise for electroluminescent applications such as LEDs and transistors. Shortly thereafter in 1998, the light emission and

lasing were also observed in the layered perovskite $(C_6H_{13}NH_3)_2PbI_4$, representing a significant milestone[20].

Entering the 2010s, metal halide perovskites (MHPs) have continued to astonish researchers with their novel and unexpected optoelectronic properties, leading to a surge of interest often referred to as "perovskite fever.". Since the first study of the perovskite-sensitized solar cell in 2009 with a power conversion efficiency (PCE) of 3.8%[15] (**Figure 1.1b**), numerous studies on PSCs have emerged. Currently, the certified PCE of single-junction PSCs has surpassed 26%[3], overperforming the commercial thin-film cells such as cadmium telluride and comparable to the 26.7% efficiency of champion silicon-based photovoltaics (**Figure 1.1c**). Moreover, the PCE for all-perovskite tandem solar cells, and hybrid tandem PSCs have also climbed to 28%, and 31.3%, respectively[21]. This rapid progress has driven extensive research into the intrinsic optoelectronic characteristics of MHPs, revealing their tunable bandgap[22], long carrier diffusion length[23], high light absorption[24], outstanding mobility[25], and solution processability[26]. In addition to solar cells, metal halide perovskites (MHPs) have emerged as promising materials for optical applications. In 2014, Xing *et al.* demonstrated high optical gain and stable amplified spontaneous emission (ASE) with a threshold of around 10 ± 2 μJcm^{-2} for $MAPbX_3$ perovskites (where X=Cl, Br, I) at room temperature[27]. In 2015, $CsPbX_3$ perovskite nanocrystal was reported to have a lower pump threshold of approximately 5 ± 2 μJcm^{-2} for ASE and lasing[28]. During the same period, the room-temperature perovskite LEDs with an external quantum efficiency (EQE) of about 0.76%, were first prepared by Friend and colleagues[29]. After about 10 years of development, the current EQE of green-based perovskite LED has reached up to 28.9%[30] and those for red- and near-infrared (NIR)-based perovskite LEDs have exceeded 20%[31,32]. Furthermore, highly sensitive X-ray PDs based on printable $MAPbI_3$ films were developed in 2017 achieving a performance level of up to 11 μC mGyair^{-1}cm^{-2} [33], facilitating further applications in sensing and display.

1.2 Challenge of Hybrid Perovskites

Metal halide perovskites (MHPs) are an excellent alternative for solar cells and transport devices primarily owing to their combination of high carrier mobilities, long carrier lifetimes, and high radiative efficiency[34]. However, perovskite devices currently suffer from significant nonradiative recombination losses, which considerably reduce open-circuit voltage (V_{oc}), serving as the main obstacle preventing PSCs from reaching their full theoretical efficiency limits. So far, the origin of nonradiative recombination decay in perovskite devices remains a topic of debate. To unlock the potential of PSCs as well as other perovskite-based optoelectronic applications, it is crucial to gain a deeper understanding of the underlying mechanisms and effectively suppress nonradiative decay[35].

In addition to the efficiency, the phase transition in halide perovskites also represents a significant challenge to practical stability. Within the family of metal halide perovskites, $FAPbI_3$ (where FA^+ represents formamidinium) stands out as one of the most efficient and commonly used active layers, primarily due to its superior charge transport parameters and narrow bandgap[36]. However, a major issue arises from the thermodynamic instability of the black α-$FAPbI_3$ phase[36–43]. At room temperature, this phase tends to spontaneously convert into the undesirable photoinactive non-perovskite phase (δ-$FAPbI_3$), posing a substantial obstacle in the development of commercial PSCs with high performance and durable stability.

Moreover, the chemical structure of halide perovskites is highly sensitive to a variety of environmental stressors, including light, oxygen, moisture, and heat, leading to potential damage and degradation[44]. Specifically, exposure to light can induce the formation of iodide defects, enhancing ionic mobility and subsequently reducing the activation energy required for other degradation pathways[45]. Additionally, the presence of oxygen and moisture during light exposure can also irreversibly degrade the perovskite photovoltaic efficiency[46,47]. Heat

exposure further complicates the stability of perovskites, inducing both reversible and irreversible changes that can lead to the decomposition into metal halide byproducts[48]. Recent studies have indicated that ion migration plays an important role in such degradation mechanisms[49]. Furthermore, ion migration has been held responsible for various anomalous phenomena, such as giant capacitance and hysteresis as commonly observed in PSCs. Hence, comprehending and controlling the ion migration in MHPs, a significant challenge for device operational stability, is crucial for advancing the development of state-of-the-art perovskite devices.

1.2.1 Non-Radiative Recombination

The radiative limit theory suggests that within a solar cell, all carrier recombination processes are radiative with each emitted photon being able to escape the cell[35]. Within this framework, the nonradiative recombination effect is considered negligible, thus not impacting the device performance. This ideal scenario underpins the highest theoretical efficiency of a solar cell that can be achieved, known as the thermodynamic efficiency limit. However, in practice, nonradiative recombination losses are an inherent and inescapable characteristic of all solar cells, especially for perovskite-based devices, where they can influence their overall efficiency and performance. These energy losses are primarily due to mechanisms such as defect-assisted recombination, electron-phonon coupling, Auger recombination, and band-tail recombination[50] (**Figure 1.2a**). Among them, the nonradiative recombination plays a crucial role in causing deviations in key performance parameters of solar cells-such as short-circuit current density (J_{sc}), open-circuit voltage (V_{oc}), fill factor, and PCE, from the idealized radiative limit[51,52] (**Figure 1.2b**). For perovskite absorbers, the significant presence of nonradiative recombination centers poses a challenge to achieving the Shockley-Queisser (SQ) radiative limit and further improving solar cell efficiency.

In principle, under continuous sunlight exposure, electrons in the perovskite absorbers are excited from the valence band to the conduction band, resulting in the splitting of the quasi-Fermi levels for electrons (E_{Fn}) and holes (E_{Fp})[53]. This splitting determines the maximum open-circuit voltage (V_{oc}) for the related photovoltaics. However, any nonradiative electron-hole recombination loss weakens this splitting, thereby reducing the attainable V_{oc}. The V_{oc} deficit, typically expressed as $E_g/q - V_{oc}$ (where E_g represents the bandgap of the perovskite and q is the elementary charge), is commonly employed to quantify the reduction in the photo-generated voltage. To date, significant efforts have been channelled into minimizing the V_{oc} deficit and enhancing the PCEs of solar cells, such as meticulous crystallization control[54], defect passivation[55], meticulous interface engineering[56], and the formation of graded junctions[39]. However, the recorded V_{oc} deficit in the best-performing perovskite solar cells (PSCs) remains between 0.3–0.4 V, which still exceeds the losses predicted by the Shockley-Queisser (SQ) theory (approximately 0.27 V)[57].

In perovskite solar cells, it is crucial for photogenerated carriers to possess sufficiently long lifetimes, enabling their collection by the respective charge transport materials (CTL) prior to being lost (recombination) to nonradiative recombination. Nonradiative recombination processes are exacerbated by various scatterers, including defects[54], phonons[58], impurities[59], and mobile species[60]. Particularly for the defects/impurities with one or more deep transition energy levels within the bandgap (typically refer to deep-level defects, with a thermal activation energy higher than k_BT, where k_B is the Boltzmann constant), based on the Shockley-Queisser (SQ) theory, they serve as the predominant nonradiative recombination centers in the material[51]. In contrast, shallow-level defects have a high probability of releasing trapped charges back into the conduction band minimum (CBM) or valence band maximum (VBM), making them “electrically benign”. As a result, they generally do not contribute to nonradiative decay processes or affect the resulting V_{oc}.

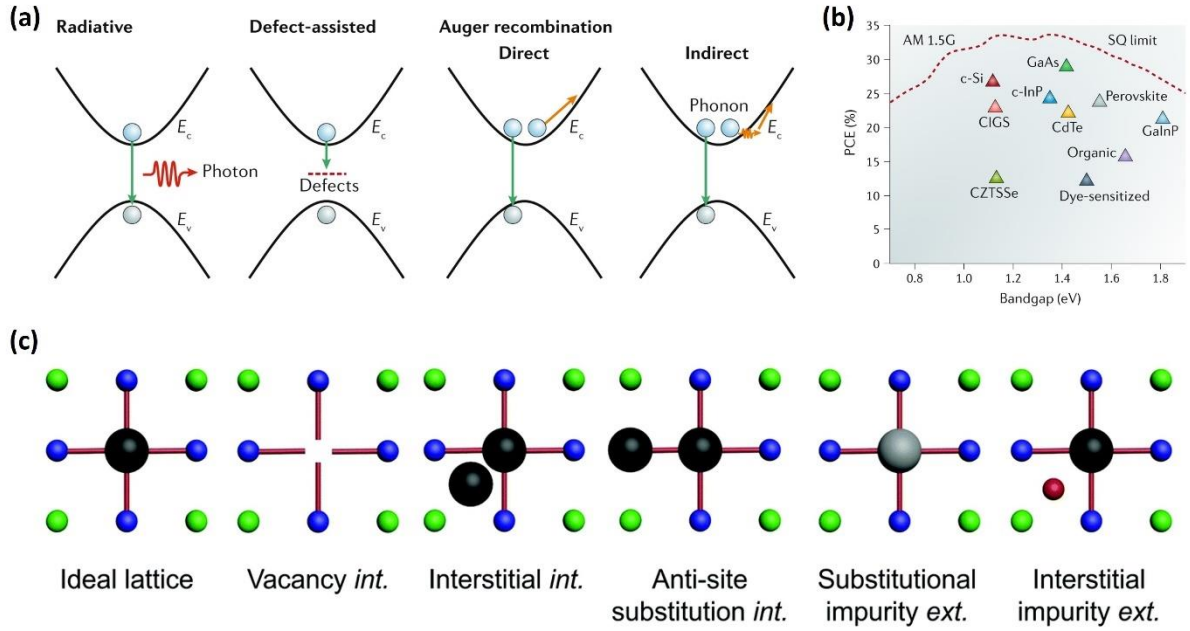

Figure 1.2. (**a**) Various recombination mechanisms of photo-generated carriers in halide perovskites, encompassing radiative recombination, defect-assisted recombination, as well as direct and indirect Auger recombination[35]. (**b**) The power-conversion efficiency limit for single-junction solar cells as a function of bandgap (dashed line), is calculated according to the Shockley–Queisser (SQ) theory. The record PCEs of various solar cell materials[35]. (**c**) Schematic representation of intrinsic (int.) and extrinsic (ext.) defect types in lead halide perovskites (LHPs) compared to an ideal lattice[61].

Intrinsic defects have been widely believed to be the primary source of nonradiative recombination centers in MHPs[62]. In these materials, the point defects typically occur as quasi-positive or quasi-negative charged entities, due to localized holes or electrons in their immediate vicinity (**Figure 1.2c**). Previous first-principles calculations suggest that most of the intrinsic defects with low formation energies are likely to form shallow states within the bandgap[63]. Conversely, deep-level defects tend to have higher formation energies at room temperature. However, experimental evidence has indicated the existence of deep-level defects in perovskite films, with halide vacancies (V_I) and interstitials (I_i) widely believed to be the primary contributors[50]. The discrepancy between theoretical predictions and experimental findings may be attributed to oversimplified defect calculations and varying experimental

conditions. That is, the diversity of perovskite chemical compositions and synthesis techniques results in complex defect-formation mechanisms. Most recently, by using high-level HSE-SOC calculations, Zhang *et al.* reported that native iodine interstitials and hydrogen vacancies are effective nonradiative recombination centers, while iodine vacancies do not contribute to nonradiative recombination in MHPs[64,65]. Therefore, precisely identifying the contribution of each type of defect to nonradiative recombination losses in MHPs, especially for those unintentionally incorporated external impurities, would be the next key step in advancing the study. This is pivotal in devising strategies to further mitigate the related energy losses and unlock the full potential of solar cell technologies and achieve higher power conversion efficiencies.

1.2.2 Phase transition

For the typical metal halide perovskites with a chemical formula of ABX_3, B is centrally located within an octahedron, whereas A is positioned at the eight vertices of the face-centered cubic lattice. Given that the ions in perovskites are densely packed, any alteration in the size of these ions can lead to structural distortion[66]. As a result, Goldschmidt's tolerance factor (t) and the octahedral factor (μ) have been widely used to evaluate the structural stability of halide perovskites (**Figure 1.3a**), providing a predictive measure for the likelihood of structural distortions and their impact on the material properties[67]:

$$t = \frac{R_A + R_X}{\sqrt{2}(R_B + R_X)} \tag{1.1}$$

$$\mu = \frac{R_B}{R_X} \tag{1.2}$$

Here, R_A, R_B, and R_X represent the ionic radii of A, B, and X, respectively. To ascertain the stability of a perovskite structure, it generally requires the tolerance factor (t) ranging between 0.8 and 1 and an octahedral factor (μ) between 0.442 and 0.895[68].

Specifically, perovskites with a tolerance factor (*t*) between 0.9 and 1.0 exhibit an ideally symmetric cubic lattice[69]. As the *t* factor decreases to between 0.8 and 0.9, the structure transitions into orthorhombic and tetragonal phases with reduced symmetry[69]. When the *t* factor exceeds 1 or falls below 0.8, a non-perovskite structure tends to be formed[69]. The phase transition in $FAPbI_3$ is intrinsically attributed to the large size of the FA cation (~0.252 nm)[70], which leads to a *t* factor of ~1.02. Note that this value, being slightly above 1, is over the upper limit of the perovskite stability range. Additionally, the rotation and stacking of the PbI_6 octahedron, resulting from large anisotropic lattice strain and FA-cation rotational disorder, further kinetically aggravate phase instability of $FAPbI_3$ perovskite[71].

It is well established that there are four crystal phases for $FAPbI_3$ perovskite[72]: α-$FAPbI_3$ (black phase), γ-$FAPbI_3$ (black phase), β-$FAPbI_3$ (black phase), and δ-$FAPbI_3$ (yellow phase), as depicted in **Figure 1.3b**. α-$FAPbI_3$ features an ideal cubic perovskite structure with corner-sharing octahedra. As the temperature decreases, reduced energy associated with lattice dynamics leads to a symmetry break in the cubic lattice due to PbI_6 octahedral tilting[73]. That is, α-$FAPbI_3$ tends to undergo a transition to β-$FAPbI_3$ at around -122 °C. Further cooling to -182 °C induces a transformation from β-phase to γ-phase. For both β-$FAPbI_3$ and γ-$FAPbI_3$ phases, which only exist at low temperatures, the tilting of PbI_6 octahedra reduces the disorder of FA cations and leads to preferential orientation[74].

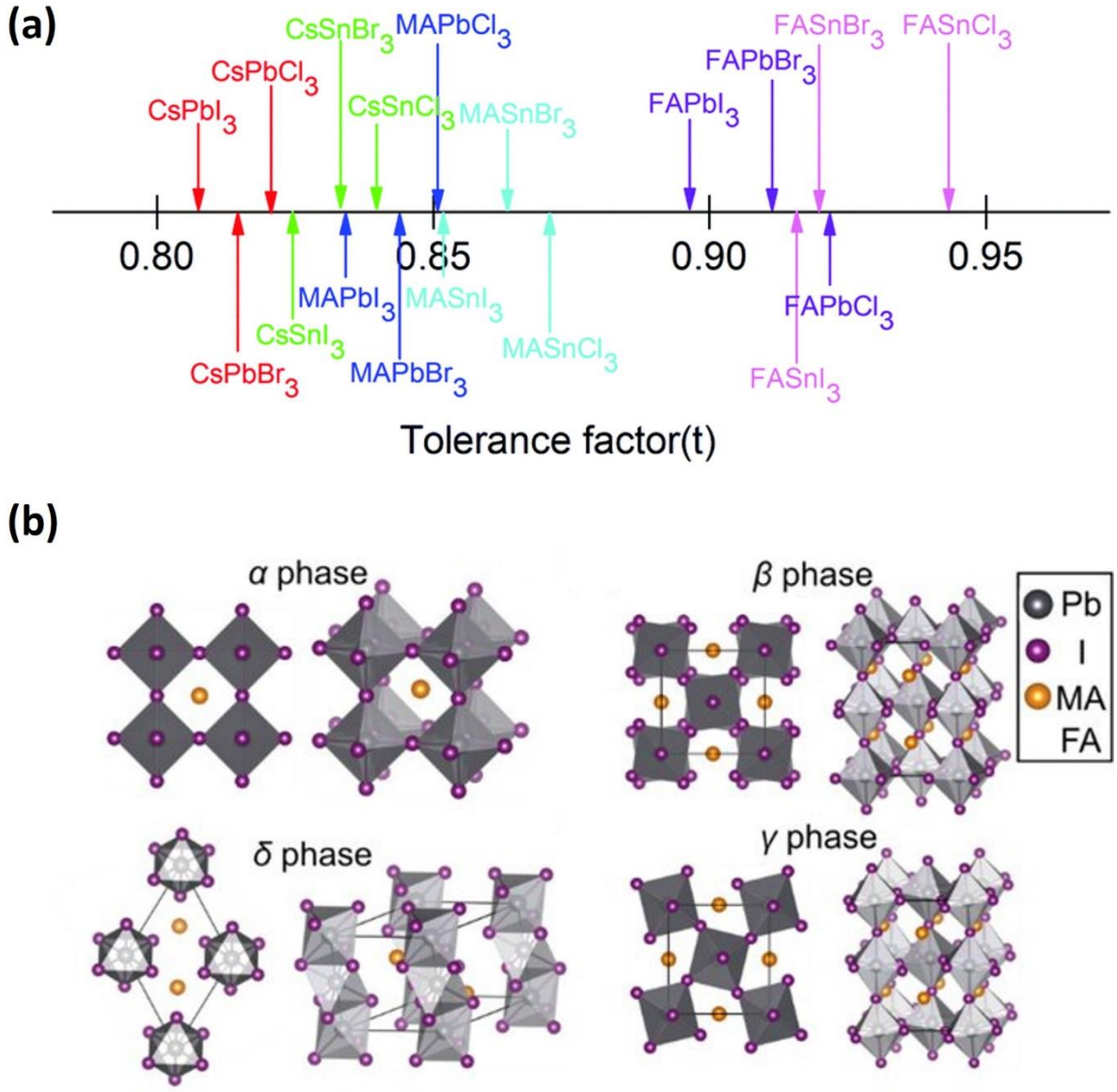

Figure 1.3. (**a**) Tolerance factors for various metal halide perovskites[75]. (**b**) Four different phases of $FAPbI_3$ perovskite: the cubic alpha (α)-phase, the tetragonal beta (β)-phase, the trigonal delta (δ)-phase, and the orthorhombic gamma (γ)-phase. where grey spheres represent lead atoms, purple spheres represent iodine atoms, and orange spheres represent formamidinium (FA) cation[76].

Significantly, the hexagonal-structural δ-$FAPbI_3$ is the most thermodynamically stable at room temperature, and consequently, the black α-$FAPbI_3$ phase is experimentally prone to a rapid phase transition to the yellow δ-$FAPbI_3$ phase especially when exposed to moisture[42]. δ-$FAPbI_3$ phase is undesirable for optoelectronic applications due to its large bandgap, low carrier mobility, weak light absorption, and insulating nature, stemming from its non-perovskite one-

dimensional PbI_6 octahedron lattice structure[77]. During the crystallization of $FAPbI_3$ perovskite, both α and δ phases emerge concurrently, with δ-$FAPbI_3$ capable of reversibly transitioning back to α-$FAPbI_3$ at temperatures above 150 °C[36]. However, such high temperatures also lead to the partial decomposition of $FAPbI_3$ into lead iodide (PbI_2), further compromising the phase stability[78]. To date, various fabrication methodologies have been employed to tackle this critical issue, including composition, dimensionality, strain engineering, and even crystalline process modulation. However, fabricating and stabilizing pure-phase, high-quality α-$FAPbI_3$ films remains a significant challenge for the current research community.

1.2.3 Ion Migration

Metal halide perovskites (MHPs) are highly susceptible to ion migration, contributing to various observed anomalous phenomena[79] such as *I-V* hysteresis and impacting the operational stability of perovskite-based optoelectronic devices. As one of the most intriguing and mysterious processes in perovskite-based devices, the ion migration phenomenon has been reported since the 1980s[80]. Note that some perovskite oxides, such as $LaMnO_3$[81] and $SrTiO_3$[82], are well-known for their ion-conducting properties. In the case of MHPs, they are widely reported as mixed conductors, where ionic conduction plays a significant role and significantly impacts the measured properties of the devices[83].

MHPs possess a soft crystal lattice nature that leads to relatively weak chemical bonds, resulting in low defect formation energy in the lattice. Ion migration in MHPs is often mediated through two types of stoichiometric defect pairs[49]: the Schottky-type and Frenkel-type defects. The Schottky defect involves a pair of vacancies with opposite charge states, while the Frenkel defect consists of a vacancy paired with its corresponding interstitial defect. In Schottky defect-assisted migration (**Figure 1.4a**), an ion moves from its initial lattice position to a neighboring vacancy. In Frenkel defect-assisted migration (**Figure 1.4b**) the ion diffuses through the

interstitial spaces within the lattice. Therefore, for both mechanisms, interstitials and vacancies act as pathways for ion migration[84]. In the prototypical perovskite $MAPbI_3$, the common Schottky defects are MA vacancies (V_{MA}) and I vacancies (V_I)[84]. while Frenkel defects predominantly occur as MA interstitials (MA_i) and I interstitials (I_i)[85]. In addition to the bulk defects, surfaces and grain boundaries (GBs) also act as critical channels for ion migration in MHPs. Surfaces and GBs inherently possess more defects and uncoordinated atoms due to weaker bonding energies compared with the bulk of the materials. The lack of constraints for charged defects at surfaces and GBs of MPHs pave freeways for ion migration, which occurs at lower activation energies than in the bulk material. Indeed, Shao *et al.* demonstrated that ion diffusion through GBs plays a significant role in polycrystalline perovskites, as evidenced by both nanoscopic- and macroscopic-level measurements[86].

In principle, the migration rate k of an ion is influenced by its activation energy E_a and temperature T, according to the relationship $k = Ce^{-\frac{E_a}{k_B T}}$. Here C stands for a constant and k_B the Boltzmann constant. As indicated, a lower E_a is expected for a fast diffusion process. By using first-principles calculations, various research groups have estimated the E_a for ion migration associated with Schottky defects, which have substantially low formation energy (around 0.14 eV per defect) in MHPs. Angelis *et al.* systematically investigated mobile species and mapped out the potential ion diffusion pathways for $MAPbI_3$ and $MAPbBr_3$[87]. They demonstrated that iodine vacancies and interstitials can easily transport across the perovskite lattice with E_a as low as ~0.1 eV. In contrast, the E_a for V_{MA} and V_{Pb} were found to were found to be higher, at 0.46 eV and 0.80 eV, respectively. Meanwhile, Eames's calculations indicated that iodine ion diffuses along an octahedron edge with a E_a of ~0.5 eV (**Figure 1.4d**), MA cation moves into a nearby A-site vacancy with a E_a of ~0.8 eV, and Pb ion migrates diagonally with an E_a of ~2.3 eV[88]. While different research groups report varying E_a values for different ions in MHPs due to various calculation schemes, there is a consensus that intrinsic iodine ions

are the most mobile species despite the relatively large ionic radius[89]. Generally, ions with smaller sizes tend to induce less significant lattice relaxation during migration and are thus more likely to migrate. The much faster motion of iodine ion in MHPs benefits from its shortest migration pathway (~4.46 Å), which likely contributes to a lower E_a during migration[90]. The migration and accumulation of ions not only induce local lattice deformation for MHPs, responsible for the decomposition of the materials, but also degrades electron transport layers (ETLs), hole transport layers (HTLs), and even electrodes[91]. On the other hand, ion migration has significance for the development of perovskite-based resistance-switching memory devices[92]. To date, the scientific community still lacks a comprehensive overview of this issue. Getting an in-depth understanding of the underlying mechanism and precise manipulation of ion migration behavior in MHP materials remain critical research focuses that could significantly advance cutting-edge perovskite applications.

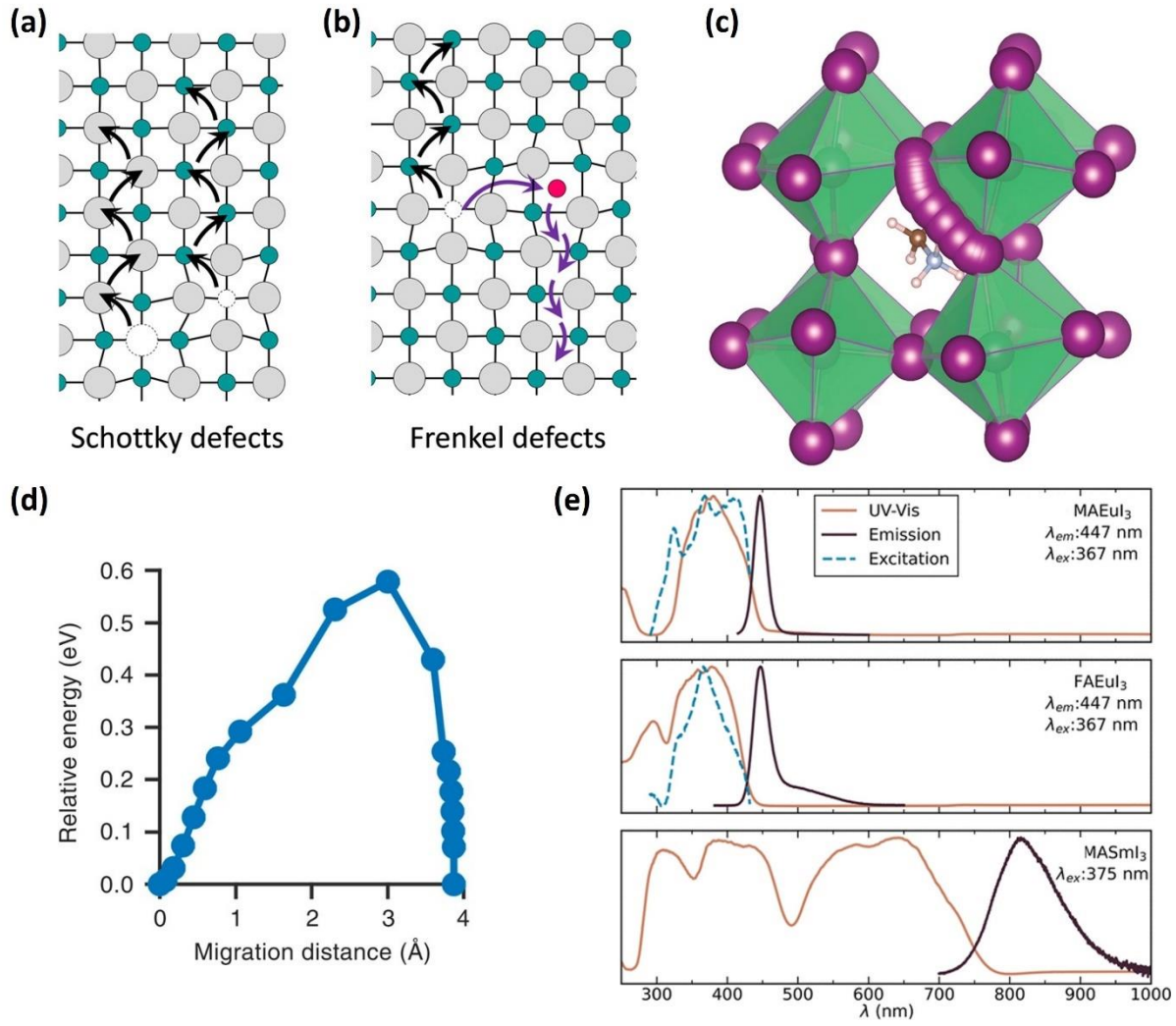

Figure 1.4. Depiction of ion migration pathways facilitated by (**a**) Schottky defects and (**b**) Frenkel defects[85]. (**c**) Computed migration path showing a slightly curved trajectory and local relaxation/tilting of the octahedra and (**d**) the associated energy profile[88]. (**e**) Optical absorption spectra (orange solid lines) along with photoluminescent excitation (blue dashed lines) and emission spectra (black solid lines) were measured for B-site doped $MAEuI_3$, $FAEuI_3$, and $MASmI_3$ room temperature.

1.3 Compositional Engineering Strategies for Efficient and Stable Halide Perovskite Photovoltaics

In the last decade, considerable research has focused on enhancing perovskite-based devices through various strategies, including surface/interface engineering, composition/crystalline structure optimization, and defect engineering[10,36,38,93,94]. While early PSC development has mainly centered on optimizing device architecture, recent efforts have increasingly targeted the

compositional tailoring of MHP active layers, which represents the potential breakthroughs for further technology improvement[95]. Compositional engineering is a proven strategy to effectively tune the fundamental physics of semiconductors for targeted applications by strategically modifying the composition and microstructure of materials. In MHPs, modifying the ABX_3 lattice through doping/alloying A-, B-, and X-sites with different ions often results in novel optoelectronic properties, and carrier transport and extraction characteristics. Notably, recent studies have demonstrated that efficiency-record-breaking solar cells have been predominantly based on multicomponent MHP active layers, which combine the advantages of different single-component perovskites, enabling improved stability and superior transport and extraction characteristics. This highlights the importance of further investigating the underlying design principles of composition-engineered compounds.

MHPs offer a wide range of ion selectivity for the A-, B-, and X-sites, when satisfying criteria for charge balance, ionic radius, and structural stability. Within such an ionic crystal structure, A-site cation does not form direct bonds with B-X ionic lattice, which is responsible for determining the electronic band edges of perovskites. Therefore, A-site cation has a negligible impact on the carrier excitation and transport characteristics[96]. On the other hand, A-site cation influences the lattice symmetry of MHPs through distorting the BX_6 octahedra. The position and size of the A cations play a critical role in affecting the crystal lattice parameters, defect density, and structural dimensions[97]. Some studies have shown that substitution with larger A-site cations such as azetidinium (Az) and guanidinium (GA) enhances the stability and better fill factors of perovskite devices[98], while the mechanism behind such improvement has not been fully understood.

In contrast, B-site engineering significantly influences the optoelectronic properties, as B-site cations directly contribute to the band edges of MHPs[99] (**Figure 1.4e**). Taking the prototypical hybrid perovskite $MAPbI_3$ as an example, partially substituting Pb with Sn leads to a bandgap

(E_g) range from 1.2 to 1.6 eV. Such continuous adjustment of the electronic structure through varying B-site composition affects the light-harvesting spectrum and impacts the carrier transport and extraction dynamics of the system, allowing for tailored optimization of material properties. Moreover, X-site engineering is also effective for tuning the E_g of MHPs within the visible spectrum by adjusting the ratio between the substitutional species and the host I. Specifically, the lower electronegativity of X-site anions (such as from Cl to Br to I) increases the covalent nature of B-X bonding, leading to a reduction in the bandgap[100]. However, X-site mixtures are prone to serious phase segregation[101], often resulting in the formation of I- or impurity-rich phases under continuous illumination or applied electric fields, posing challenges for practical applications. Promisingly, it has been reported[102] that A-site substitution can mitigate phase segregation in X-site mixed perovskites by enhancing crystalline properties, thereby forming stable multi-site alloyed perovskites. In addition, composition engineering in MHPs can alter the perovskite lattice structure from 3D network to lower dimensions (such as 2D, 1D, or 0D). Due to strong quantum and dielectric confinement effects, low-dimensional MPHs often exhibit exceptional photo- and electro-luminescence yields, highly promising for light-emission applications.

Doping and alloying are two important components of composition engineering, both involving the deliberate introduction of impurities into an intrinsic semiconductor. Doping entails adding small quantities of ions into the perovskite hosts, thereby modifying the electronic structure and optoelectronic characteristics of the pure perovskites[103]. In contrast, alloying often involves substituting host atoms with others of the same valence, leading to changes in the crystal structure and optoelectronic properties compared to the original perovskites, and often introducing new physical characteristics[104]. Despite the intriguing and distinct features of doped/alloyed MHPs, the variation in photo-physical properties is complicated owing to different influencing mechanisms. A comprehensive understanding of the underlying

mechanism of doping and alloying, along with their associated characteristics, is key to guiding the future design of highly stable and efficient MHPs and the related devices,

1.4 Conclusion

In this chapter, we provide an overview of the development of halide perovskite materials and highlight significant challenges in their current applications for devices. MHPs have garnered significant interest due to their exceptional optoelectronic properties, low processing costs, and substantial advancements in various optoelectronic applications. Notably, they have recently achieved impressive power conversion efficiencies in solar cell applications; however, MHPs are particularly vulnerable to nonradiative losses, ion migration, and phase transitions, because of their soft lattice and structural porosity, presenting significant challenges in realizing high-efficiency, long-term stable perovskite devices suitable for commercialization. Promisingly, compositional engineering stands out as a promising strategy to address the current challenge. In this thesis, we employ systematic first-principles calculations to thoroughly investigate the underlying mechanisms of nonradiative losses, ion migration, and phase transitions - critical issues in halide perovskites. We aim to offer technical guidelines for enhancing the crystal structure of halide perovskites and optimizing their optoelectronic properties, directly correlating to the ultimate performance of their devices in targeted applications. Moreover, the current research offers valuable insights for advancing well-established photovoltaic technologies.

Chapter 2 Theoretical Methodology

2.1 Introduction

First-principles theory, first introduced by the ancient Greek philosopher Aristotle, refers to fundamental, self-evident assumptions or propositions that cannot be derived from other assumptions. Before the 1900s, this concept was already well-known in fields like philosophy, chemistry, mathematics, and physics. In mathematics, first principles refer to fundamental postulates and axioms that do not require proof. In contrast, in physics, material sciences, and other science-related disciplines, the term refers to theories based purely on established science, without relying on empirical data or adjusting parameters. With the development of the Schrödinger equation in the early 20th century, quantum theory became the "first principle" for condensed matter physics, materials science, and chemistry. Solving this equation provides answers to many fundamental questions within these systems. However, the complexity of many-body problems makes solving the Schrödinger equation computationally intensive, significantly limiting its practical application in material sciences. There thus have been numerous efforts to simplify the equation. In response to the computational challenges, in the 1960s, the successive formulation of the Hohenberg-Kohn and Kohn-Sham theorems led to the creation of density functional theory (DFT), which effectively simplified the many-body problem of the Schrödinger equation into a single-body problem, offering a feasible pathway for exploring and understanding the quantum mechanical behavior of matter at an atomic level.

2.2 Density Functional Theory

As one of the most widely used, adaptable, and powerful quantum mechanics methods, Density Functional Theory (DFT) has been extensively applied across various fields related to science, including condensed matter physics, quantum chemistry, and materials science. Within the

DFT framework, the primary aim is to compute the total energy of a condensed matter system consisting of interacting electrons and nuclei, such as crystals, molecular ensembles, and various condensed phases, and to determine the spatial distribution of the ground-state electron density, providing accurate atomic-level insights into the structural and electronic properties of systems. The foundation of DFT was built on three key works: the Born-Oppenheimer Approximation, the Hohenberg-Kohn Theorem, and the Kohn-Sham Theorem. Specifically, the Born-Oppenheimer Approximation simplifies the problem by decoupling electronic motion from nuclear motion, enabling us to focus on the electronic structure with fixed nuclear positions. Further, the Hohenberg-Kohn Theorem put forward that the ground-state properties of a many-electron system are uniquely determined by its electron density, establishing one-to-one correspondence between the ground-state electron density and the external potential. This simplifies the complex many-body problem into a functional of the electron density. The Kohn-Sham Theorem makes DFT computationally achievable by introducing a theoretical non-interacting system.

2.2.1 Many-Body Issue and Born-Oppenheimer Approximation

Fundamentally, the many-body problem in quantum mechanics focuses on determining a wavefunction (state function), ψ, and its associated energy, E, which satisfies the non-relativistic, time-independent Schrödinger equation:

$$H\psi(\mathrm{R}_1, \mathrm{R}_2, \ldots . \mathrm{R}_n;\ \mathrm{r}_1, \mathrm{r}_2, \ldots . \mathrm{r}_n) = E\psi(\mathrm{R}_1, \mathrm{R}_2, \ldots . \mathrm{R}_n;\ \mathrm{r}_1, \mathrm{r}_2, \ldots . \mathrm{r}_n) \quad (2.1)$$

where H denotes the many-body quantum mechanical Hamiltonian operator for the system consisting of r_n electrons and R_n nuclei; E is the total energy of the system. The wavefunction $\psi(\mathrm{R}_1, \mathrm{R}_2, \ldots . \mathrm{R}_n;\ \mathrm{r}_1, \mathrm{r}_2, \ldots . \mathrm{r}_n)$ depends on the coordinates of both the electrons and the nuclei, encapsulating the quantum state of the entire system and the complex interactions among the particles.

The Hamiltonian operator, *H*, consists of five parts: the two kinetic energy operators for the nuclei $T_N(R_i)$ and electrons $T_e(r_i)$, as well as the three electrostatic Coulomb interaction operators, namely the nuclear-nuclear interaction $V_{NN}(R_i, R_j)$, the nuclear-electron interaction $V_{Ne}(R_i, r_i)$, and the electron-electron interaction $V_{ee}(r_i, r_j)$. Each component plays a critical role in determining the dynamics and interactions of the system, contributing to the overall energy as described by the Schrödinger equation:

$$H = T_N + T_e + V_{NN} + V_{Ne} + V_{ee} \quad (2.2)$$

For a many-body system that contains a number of nuclei and electrons, the Schrödinger equation (2.1) becomes a partial differential equation with many variables (3n+3N), making direct solutions impractical. This challenge is known as the "many-body problem".

To address the intricate interplay and complexity in many-body system, Born-Oppenheimer approximation[105] simplifies the Hamiltonian equation in 2.2 through de-coupling the nuclear and electronic motion. Generally, the nuclei are almost stationary relative to the rapid-motion electrons due to the significantly greater mass of nuclei compared to electrons. As a result, the nuclear motion is much slower, allowing them to be treated as "frozen" in a fixed position during the time scale of electronic movements. This approximation allows the kinetic energy operator for the nuclei $T_N(R_i)$ to be considered zero, as their motion contributes negligibly to the total molecular energy. Similarly, the electrostatic Coulomb interaction operator between nuclei $V_{NN}(R_i, R_j)$ becomes a constant because the nuclei are assumed to be at fixed positions R_i and R_j. This operator typically describes the nuclear-nuclear repulsion. By decoupling the nuclear and electronic movements, the many-body Schrödinger equation is significantly simplified, where the nuclear positions still affect the equation but are not treated as independent variables:

$$H = T_e + V_{ext} + V_{ee} = -\frac{\hbar^2}{2m_e}\sum_{i=1}^{n}\nabla_i^2 - \sum_{i,j}^{n}\frac{Z_i}{|R_i - r_j|} + \frac{1}{2}\sum_{i\neq j}\frac{1}{|r_i - r_j|} \quad (2.3)$$

Here, Z_i denotes the charge of nucleus i located at position R_i; r_i and r_j represent the positions of electrons i and j, respectively. The V_{ext} refers to the external potential, determined by the locations of the nuclei as well as the external influences on the system. If there is no external effects, the external potential will be $V_{ext} = V_{Ne}$, which is the potential due to nucleus-electron interactions.

This equation primarily focuses on the electronic structure, treating nuclei as a static framework creating a potential field for electron movement. However, it is essential to note that the Born-Oppenheimer approximation is just an approximation. In some cases, particularly with light atoms or excited states, the effects of nuclear motion on electronic states cannot be ignored.

2.2.2 Hartree-Fock Approximation

Born-Oppenheimer approximation simplifies the many-body Schrödinger equation by reducing the degrees of freedom, although the equation remains unsolvable for most systems. To address this, the Hartree-Fock (HF) approximation represents the many-body wavefunction as a single Slater determinant. This determinant is an anti-symmetrized product of single-particle wavefunctions of an orthogonal individual electron, $\psi_i(X_i)$, which treats each electron as if it moves independently within an average field created by all other electrons, thereby simplifying the complex electron-electron interactions into an average interaction:

$$\psi = \frac{1}{\sqrt{n!}}\begin{bmatrix} \psi_1(X_1) & \cdots & \psi_1(X_n) \\ \vdots & \ddots & \vdots \\ \psi_n(X_1) & \cdots & n(X_n) \end{bmatrix} \tag{2.4}$$

Here, each single-particle wavefunction consists of two fundamental parts: a spatial component $\emptyset(r)$, and a spin component $\eta(\sigma)$. Therefore, the wavefunction for an individual electron is formulated as the product of these components: $\psi_i(X_i) = \emptyset_i(r_i)\eta_i(\sigma_i)$. The term $\frac{1}{\sqrt{n!}}$ serves as a normalization factor for an N-electron system, ensuring that the total wavefunction has the correct magnitude. Within this framework, the complex many-body problem is further

simplified into a set of single-particle Schrödinger equations, where an electron at position X_1 experiences other electrons at position X_n as a continuous distribution of negative charge. In the Hartree-Fock method, the total ground state energy is calculated by summing the energies of all the individual one-electron Hartree-Fock orbitals:

$$E_0 = \sum_{i=1}^{n} h_i \sum_{i=1}^{n} \sum_{j=1}^{n} (J_{ij} - K_{ij}) \quad (2.5)$$

where the first term h_i represents the "one-electron" contribution to the total energy, including both the kinetic energy of the electron and its potential energy arising from the Coulomb interaction between the electron and the nucleus. The second and third terms J_{ij} and K_{ij} represent the Coulomb and exchange integrals, respectively, representing "two-electron" contributions that account for electron-electron interactions. The subscripts i and j indicate summation across all orbitals. The Coulomb integral in the Hartree-Fock equations introduces a self-interaction error, which is precisely offset by the exchange integrals when $J_{ij} = K_{ij}$. The exchange integral value is negative due to the antisymmetric nature of the wavefunction, which results in like-spin electrons repelling each other, thereby lowering the system total energy. It is important to note that the Hartree-Fock method approximates electron-electron interactions but fails to account for dynamic electron correlation, which involves subtle, instantaneous adjustments in electron positions.

2.2.3 Hohenberg-Kohn Theorem

Accurately solving the equation remains a highly challenging task even though the Born-Oppenheimer approximation significantly reduces the complexity of the many-body Schrödinger equation by decoupling electronic and nuclear motion. To address this, in 1964, Hohenberg and Kohn introduced two fundamental theorems, establishing the theoretical framework for DFT. These works further simplify the many-body problem into a single-

particle wavefunction with only three spatial coordinates, making the equations feasible for computation on modern computers.

In general, for a many-particle system, the external potential V_{ext} dictates Hamiltonian operator H and many-body wavefunction ψ, consequently on the electron density $\rho(r)$. The first Hohenberg-Kohn theorem demonstrates the inverse of such relationship: $V_{ext}(r)$ is a unique functional determined solely by the ground-state $\rho(r)$. In this way, the electron density serves as the primary input for the total-energy calculation. Based on the first Hohenberg-Kohn theorem, the system total energy can be expressed as a functional of electron density:

$$E(\rho) = \langle\psi|H|\psi\rangle = \min_{\psi\to\rho}\langle\psi|T_e + V_{ee}|\psi\rangle + \langle\psi|V_{ext}|\psi\rangle = F_{HK}(\rho) + \int V_{ext}(r)\rho(r)dr \qquad (2.6)$$

where the first term $F_{HK}(\rho) = \min_{\psi\to\rho}\langle\psi|T_e + V_{ee}|\psi\rangle$ represents the Hohenberg-Kohn functional and T_e is the electron kinetic energy and V_{ee} for the electron-electron interaction energy. Notably, this functional does not incorporate any specific information about the nuclei or their positions, making it applicable to a wide variety of systems. Such inherent universality renders $F_{HK}(\rho)$ so-called "universal functional". The second term $\int V_{ext}(r)\rho(r)dr$ represents the energy contribution from the external potential, as a functional of the electron density.

According to the second Hohenberg-Kohn theorem, the electron density that minimizes the total energy functional is the true ground-state density of the system. That is, by finding the electron density that minimizes the energy, one can determine the ground-state properties of the system. For instance, if ρ_0 is the density of the ground-state system and ρ' is the density for any other non-ground state situation, there will be $E(\rho_0) \leq E(\rho')$. In other words, if the $F_{HK}(\rho)$ is known and the ρ_0 is determined, one can deduce the ground state properties of the system. It is evident that this scheme transforms the task of solving the Schrödinger equation into the problem of minimizing the energy functional $E(\rho)$ with respect to the three-dimensional electron density, lowering the computational process to an acceptable level for high-performance computers.

2.2.4 Kohn-Sham Theorem

The Hohenberg-Kohn theorems present the term of $F_{HK}(\rho)$; however, the explicit form for $F_{HK}(\rho)$ remains unknown, impeding the direction determination of the ground-state electron density. To address this, Kohn and Sham[106] developed a theoretical framework that simplifies the complex many-body Schrödinger equation into a more manageable set of single-particle equations. This simplification is achieved by introducing a system of non-interacting electrons that has the same ground-state electron density as the real interacting system. These non-interacting electrons are described by a set of single-electron Schrödinger equation (known as the Kohn-Sham equation):

$$\left[\frac{-\hbar^2}{2m_e}\nabla^2 + V_{eff}(r)\right]\psi_i(r) = \varepsilon_i\psi_i(r) \tag{2.7}$$

Here, $\frac{-\hbar^2}{2m_e}\nabla^2$ represents the kinetic energy of a non-interacting electron, and $V_{eff}(r)$ is the effective potential within the non-interacting system, including the Hartree potential (classical electrostatic interaction) $e^2\int\frac{\rho(r')}{|r-r'|}dr'$, the external potential $V_{ext}(r)$, and the exchange-correlation potential $\frac{\delta E_{XC}[\rho]}{\delta n(r)}$. The functions $\psi_i(r)$ are the Kohn-Sham orbitals, representing the single-electron wavefunctions in this fictitious non-interacting system.

To solve the Kohn-Sham equations, the electron density, $\rho(r)$, must be determined. This is done by summing the squares of the Kohn-Sham orbitals:

$$\left[\frac{-\hbar^2}{2m_e}\nabla^2 + V_{ext}(r) + e^2\int\frac{\rho(r')}{|r-r'|}dr' + \frac{\delta E_{XC}[\rho]}{\delta n(r)}\right]\psi_i(r) = \varepsilon_i\psi_i(r) \tag{2.8}$$

In other words, the equations are solved self-consistently. Initially, a guess is made for the electron density $\rho(r)$, which is used to solve the Kohn-Sham equations and obtain a set of orbitals $\psi_i(r)$:

$$\rho(r) = \sum_{i=1}^{n}|\psi_i(r)|^2 \tag{2.9}$$

These orbitals are then used to calculate a new electron density. This new density is used as the input for the next iteration. The Kohn-Sham equations are solved again until convergence is achieved, where the total energy and electron density of the system settle at the ground state values.

2.2.5 Exchange and Correction Functionals

To determine the ground state properties of many-body systems, it is necessary to solve the Kohn-Sham equations. One major challenge is that the exact form of the exchange-correlation functional, E_{XC}, is unknown. This functional is vital for accurately describing electron interactions within the system. To solve the equation, various approximation strategies have been employed, each with its own set of assumptions and complexities.

Local Density Approximation. The Local Density Approximation (LDA) was introduced by Kohn and Sham in the same year they presented the Hohenberg-Kohn equations[106]. As one of the simplest and earliest approximations, LDA has been widely used and has proven effective in many applications. It breaks down the many-electron system into tiny regions, treating each as if it has a constant electron density, like a homogeneous electron gas. That is, it assumes that the exchange-correlation energy at each point in space is assumed to depend only on the local electron density at that point. Within the LDA framework, the exchange contribution to the energy can be calculated analytically. However, the correlation contribution is more complex and cannot be expressed analytically except under extreme conditions, such as infinitely weak or strong correlation. The LDA exchange-correlation functional, which relates to the electron density $\rho(r)$, is given by:

$$E_{xc}^{LDA}(\rho) = \int \rho(r) \in_{XC}^{hom} (\rho(r))dr \tag{2.10}$$

Here, $\in_{XC}^{hom}$ represents the exchange-correlation energy per electron in a homogeneous electron gas of density $\rho(r)$. Specifically, $\in_{XC}^{hom}$ can be further detailed as:

$$\in_{XC}^{hom}(\rho) = \frac{3}{10}(3\pi^2)^{\frac{2}{3}} \int \rho(r)^{\frac{5}{3}} dr \quad (2.11)$$

LDA is highly effective for systems with constant or slowly varying electron densities and provides a good approximation for the exchange-correlation energy. However, LDA limitations become apparent for the systems, where the electron density undergoes rapid spatial variations. In such cases, LDA tends to underestimate bandgaps and bond lengths while overestimating binding energies, particularly in semiconductors and insulators.

Generalized Gradient approximation. To overcome this limitation, the Generalized Gradient Approximation (GGA) improves upon the LDA by incorporating the gradients of the electron density $\nabla\rho$ into the exchange-correlation functional, providing a more accurate description of the electronic interactions in systems with rapid density variations. Specifically, the GGA exchange-correlation functional is formulated as follows:

$$E_{XC}^{GGA}(\rho) = \int \rho(r) f_{XC}(\rho, \nabla\rho) dr \quad (2.12)$$

Here, $f_{XC}(\rho, \nabla\rho)$ stands for an enhancement factor due to the inhomogeneities in the electron density. Note that GGA functional offers various forms for the exchange-correlation energies, such as Perdew-Wang functional (PW91)[107], Becke-Lee-Yang-Parr (BLYP)[108], Hamperecht-Tozer-Cohen-Handy (HTCH)[109] and Perdew-Burke-Ernzerhof (PBE)[110] *et al*. Indeed, each of these GGA functionals involves different levels of calculation complexity and computational cost. Among these, the Perdew-Burke-Ernzerhof (PBE) form has gained widespread popularity and is frequently used in the current material science research due to the balance between accuracy and computational efficiency. Specifically, it can be given by:

$$f_{XC}^{PBE}(\rho, \nabla\rho) = 1 + k\left(1 - \frac{1}{1 + \frac{\mu s(\rho, \nabla\rho)}{k}}\right) \quad (2.13)$$

In this expression, k is an empirical constant of 0.804, and the dimensionless density gradient $s(\rho, \nabla\rho) = \frac{|\nabla\rho|}{2k_F\rho}$ is the function of the local electron density ρ and the gradient $\nabla\rho$.

It is noted that GGA generally provides more reliable results than LDA because it accounts for electron kinetics and better handles variations in electron density. However, due to the self-interaction error, both LDA and GGA have limitations in accurately predicting the electronic structures of most semiconductors and insulators, particularly the notorious "bandgap error." The magnitude of this error varies depending on the specific system under consideration.

Hybrid Functionals. To address the limitations of the Generalized Gradient Approximation (GGA) in accurately predicting experimental bandgaps, a significant advancement was introduced by Becke in 1993: the hybrid functional method[111]. This method integrates a portion of the exact Hartree-Fock exchange functional into Density Functional Theory (DFT) calculations, including both LDA and GGA. The hybrid functional aims to combine the best features of DFT and Hartree-Fock approaches to provide more accurate predictions, particularly for band gaps in semiconductors and insulators. The hybrid functional expression is given by:

$$E_{XC} = \alpha E_X^{HF} + E_C^{DFT} + (1-\alpha)E_X^{DFT} \tag{2.14}$$

Here, E_X^{HF} is the Hartree-Fock exchange energy and α is the fraction of Hartree-Fock exchange. E_C^{DFT} and E_X^{DFT} represents the correlation and exchange energies from DFT, respectively. By combining Hartree-Fock exchange with DFT exchange-correlation, hybrid functionals aim to accurately capture the long-range behavior of the exchange interaction, which is often missing in conventional DFT. One particularly successful implementation of the hybrid functional is the screened hybrid proposed by Heyd, Scuseria, and Ernzerhof, known as the HSE exchange-correlation functional[112,113]. The HSE functional modifies the exchange interaction to include a portion of the Hartree-Fock exchange for short-range interactions while using the GGA functional of the PBE form for long-range interactions. The HSE functional is expressed as follows:

$$E_{XC}^{HSE} = \alpha E_X^{HF,SR}(\omega) + E_C^{PBE}(\omega) + (1-\alpha)E_X^{PBE,SR}(\omega) + E_X^{PBE,LR}(\omega) \tag{2.15}$$

where $E_X^{HF,SR}$ and $E_X^{PBE,SR}$ denote the short-range-interaction PBE and Hartree–Fock exact exchange functional, respectively. E_C^{PBE} stands for the PBE correlation functional. $E_X^{PBE,LR}$ is long-range component of PBE exchange functional. The coefficients α and ω are tunable parameters, enabling the optimization of the functional for different systems. Typically, values of 0.25 and 10 for α and ω are used in the standard implementation known as HSE06[113].

2.3 *Ab initio* Molecular Dynamics

Ab initio molecular dynamics (AIMD) is a crucial tool for designing new solid-state materials, offering insights into both equilibrium thermodynamic properties and the dynamic behavior of systems at finite temperatures. The accuracy of molecular dynamics simulations primarily depends on how the forces within the system are defined. Unlike classical molecular dynamics (MD), which relies on Newtonian equations of motion and predefined potential energy functions that often neglect electronic polarization and struggle to model chemical reactions, AIMD derives the forces directly from quantum mechanical calculations - the Kohn–Sham (KS) formulation of density functional theory as discussed above (specifically, these forces are obtained by minimizing the KS energy functional). This approach generates finite-temperature dynamical trajectories that more accurately represent complex systems, particularly in cases involving chemical bond formation and breaking, where conventional MD methods typically fall short. To date, AIMD has been successfully applied to a broad range of significant challenges in condensed matter physics, chemistry, and material science that empirical simulation methods cannot address, and it is now starting to make an impact in biology as well. For a many-particle system where the Born–Oppenheimer approximation applies, nuclear dynamics can be treated on the ground-state electronic surface and are governed by the following equation of motion, which integrates classical Newtonian mechanics with quantum mechanical principles:

$$m_i \frac{d^2 R_i(t)}{dt^2} = -\nabla_i \left[\varepsilon_0 \big(R(t)\big) + V_{NN}\big(R(t)\big) \right] \quad (2.16)$$

here, $\varepsilon_0\big(R(t)\big)$ represents the ground-state energy eigenvalue at the given nuclear configuration $R(t)$ at time t, and $V_{NN}\big(R(t)\big)$ stands for the electrostatic Coulomb interaction operator. As previously mentioned, the solution of the Kohn-Sham equation relies heavily on the approximation of the exchange-correlation functional, E_{XC}, which ultimately determines the quality of an AIMD simulation. Solving the equation of motion iteratively updates atomic positions and velocities over time, allowing the system to evolve and providing insights into its dynamic properties.

While the quantum-mechanical treatment of electrons in AIMD simulations is computationally demanding, the emergence of on-the-fly machine learning offers a promising solution to this challenge. In this thesis, Bayesian learning algorithm is employed to develop a machine-learned force field for predicting total energy and forces at each simulation (time) step. When the predicted (Bayesian) error exceeds a set threshold, *ab initio* calculation is triggered to treat the many-particle system quantum mechanically. The force field is then updated with the newly obtained data, allowing the simulation to proceed. This iterative process progressively refines the force field, minimizing the need for additional ab initio calculations as prediction accuracy increases. As a result, the machine-learned force field (MLFF) offers near-DFT accuracy with significantly lower computational costs compared to direct AIMD simulations.

Moreover, macroscopic properties such as particle number (N), volume (V), temperature (T), energy (E) pressure (P), and chemical potential (μ) can be controlled using statistical mechanics ensembles. Depending on the variables to be held constant, the canonical (NVT: constant volume and temperature), microcanonical (NVE: constant energy and volume), isothermal-isobaric (NPT: constant pressure and temperature), and grand canonical (μVT, known as the macrocanonical ensemble: constant volume and temperature and chemical potential)

ensembles can be chosen. Among these, the NVT and NPT ensembles are most commonly used.

2.4 Implementation

In this thesis, both DFT and AIMD studies are carried out as implemented in the Vienna Ab-initio Simulation Package (VASP) code[114], which is based on the plane-wave basis sets. The Projector-Augmented Wave (PAW) pseudopotential method is used to describe the interaction between atomic cores and valence electrons. In this approach, atomic cores are treated as frozen, primarily contributing to the screening of the nucleus Coulomb potential, while the valence electrons are represented by pseudo wavefunctions, which are divided into two regions with an augmentation sphere Ω_R to obtain an accurate description of electronic behavior in the proximity of the nucleus. Outside the Ω_R, the pseudo wavefunction is typically expanded with a plane-wave basis set, while inside the Ω_R, where electrons are close to the nucleus, a different basis set is employed to accurately account for complex interactions. Importantly, the wavefunction remains smoothly continuous at the boundary of the augmentation sphere, ensuring a seamless representation of electron behavior. Therefore, PAW can achieve accuracy comparable to the all-electron full-potential method but with significantly greater computational efficiency.

The widely used VASP code supports not only pure DFT calculations but also can incorporate advanced corrections such as hybrid functionals, dispersion corrections, DFT+U corrections, and spin-orbit coupling to enhance prediction accuracy. Particularly, the hybrid functional and spin-orbit coupling play an important role in studying optoelectronic characteristics in the MHPs materials, especially in investigating the transition energy levels, nonradiative carrier capture, and other key electrical properties for the charged defects and impurities. The input files for VASP consist of POSCAR (system geometry structure); POTCAR (the

pseudopotentials for ion-electron interactions); KPOINTS (the k-points for Brillouin zone sampling); and INCAR (calculation parameters). In each project, various files will be specifically customized for the respective systems to achieve optimal computational cost-effectiveness.

Chapter 3 Minimizing and Controlling Hydrogen for Highly Efficient Formamidinium Lead Triiodide Perovskite Solar Cells

3.1 Introduction

Metal halide perovskite semiconductors have emerged as front runners for next-generation photovoltaic cells with high power conversion efficiency (PCE) and low manufacturing cost. Compared to the prototypical $MAPbI_3$ (MA = Methylammonium, CH_3NH_3), $FAPbI_3$ (FA = Formamidinium, NH_2CHNH_2) films possess the improved thermal stability and the suitable bandgap (~1.48 eV) closer to the optimal value (1.34 eV) of the Shockley-Queisser (S-Q) limit, and thus have been the most attractive candidate in perovskite solar cells[3,37–40,115–118]. So far, the record PCE has catapulted to over 25.8% in $FAPbI_3$-based single-junction solar cells[3], comparable or even exceeding other single-junction solar cells[21].

It is well acknowledged that iodine management by optimizing the concentration of iodine during the growth and processing of the perovskite layers is crucial for achieving high PCE values in $FAPbI_3$-based solar cells[117,119–122]. In particular, synthesizing $FAPbI_3$ films with either scarce or excess iodide ions could result in inferior solar cell performance, which is closely associated with deep-level defects and their induced nonradiative recombination losses[117,119–122]. Specifically, the experimentally observed nonradiative recombination rates in $FAPbI_3$ active layers are typically $10^6 s^{-1}$ [116,120,123,124], serving as a major loss mechanism and restraining the PCE from approaching the theoretical maximum efficiency (~32%)[125]. The open-circuit voltage (V_{OC}), typically around 1.1 V for the state-of-the-art $FAPbI_3$-based solar cells[37,39,115], still lags behind the radiative limit (1.255 V from Ref.[37]). This is regarded as a direct consequence of the energy losses induced by the nonradiative recombination of photogenerated charge carriers[37,39,115]. On the other hand, it has been experimentally shown that tuning the iodine content can effectively shift the electrical conductivity of halide

perovskite materials, which could play an important role in the defect engineering in halide perovskites[103].

Notably, fewer first-principles defect investigations have been carried out on the $FAPbI_3$ perovskites[126] as compared with its predecessor $MAPbI_3$[64,65,84,127–133], whereas highly efficient perovskite solar cells are predominantly fabricated with $FAPbI_3$ active layers. This is significant because of the distinctively different defect-induced nonradiative recombination mechanisms between $FAPbI_3$ and $MAPbI_3$. Previous reports have shown that hydrogen vacancies (V_H)[65] and iodine interstitials (I_i)[64,132,133] are the dominant nonradiative recombination centers in $MAPbI_3$. In contrast, in $FAPbI_3$, iodine interstitials (I_i) are actually shallow defects[134], and hydrogen vacancies of FA cations could not cause significant nonradiative loss either[65]. The origin of defect-induced nonradiative losses in $FAPbI_3$ remains unknown. Identifying and then effectively suppressing such efficiency-killing defects would further improve the performance of $FAPbI_3$-based devices. This imperatively calls for an in-depth understanding of the underlying atomistic mechanism of the nonradiative recombination in $FAPbI_3$.

In this study, by performing first-principles calculations, we reveal that native point defects are not responsible for the nonradiative losses in $FAPbI_3$; instead, electrically active hydrogen interstitials, H_i, is the dominant nonradiative recombination center with a capture coefficient on the order of $10^{-8}\mathrm{cm}^3\mathrm{s}^{-1}$ at room temperature, consistent with the experimental measurements[135]. We propose that synthesizing the $FAPbI_3$ perovskite samples under the iodide-moderate and hydrogen-poor conditions can effectively suppress the nonradiative recombination loss, enabling the best device performance of the applications.

3.2 Simulation Method

3.2.1 Computational Method

First-principles calculations were performed based on density functional theory (DFT)[106] as implemented in Vienna Ab initio Simulation Package (VASP) code[114]. Projector augmented wave (PAW) pseudopotentials[136] were used with a plane-wave energy cutoff of 400 eV. The Tkatchenko-Scheffler (TS) scheme[137] was used for describing the dispersion interactions for the hybrid perovskite systems[138]. The more accurate Heyd–Scuseria–Ernzerhof hybrid functional[113] with the mixing parameter of 0.46 was employed and the spin-orbit coupling was included (HSE+SOC). All atoms were fully relaxed until the forces on atoms are less than 0.01 eV/Å. For defect calculations in perovskite $FAPbI_3$, a $3 \times 3 \times 2$ 216-atom supercell based on the cubic phase unit cell was employed with a Monkhorst–Pack sampling of $2 \times 2 \times 2$ k-point grid. A convergence test for a $3 \times 3 \times 3$ 324-atom supercell of $FAPbI_3$, for H_i^+, showed that the calculated formation energy difference between the 216-atom and 324-atom supercells is only 0.06 eV. Our HSE+SOC+TS calculations yield a bandgap of 1.46 eV, in good agreement with the experimental value of 1.47 eV[139]. Moreover, the optimized lattice parameter of 6.371 Å agrees well with the experimental values of 6.362 Å[139].

3.2.2 Defect Formation Energy

The defect formation energy is given by[140]:

$$\Delta H_f\left(H_i^q\right) = E\left(H_i^q\right) - E(host) - \sum n_i(\mu_i + \Delta\mu_i) + q(E_F + E(VBM) + \Delta V) \qquad (3.1.)$$

where $E\left(H_i^q\right)$ and $E(host)$ are total energies with and without defect, respectively. n_i indicates the number of defects added into the supercell. μ_i is the absolute value of the chemical potential of the defect atoms. $\Delta\mu_i$ stands for the relative value of the chemical potential, which is related to growth conditions. The chemical potentials of constitute elements (μ_I, μ_{Pb}, and μ_{FA}) refer to their corresponding most stable phases, namely, the elemental solids of Pb in the

cubic phase and I_2 in the orthorhombic phase. For μ_{FA}, the body-centered-cubic phase of FA was chosen. For the chemical potential of hydrogen (μ_H), under the H-rich conditions, it is well-defined and corresponds to half of the total energy of an isolated H_2 molecule ($\mu_H(H_2)$). We further calculated μ_H in other relevant H-containing compounds as possible intrinsic and extrinsic hydrogen sources, including gas H_2O, CH_4, liquid HI, DMF (C_3H_7NO), DMSO (C_2H_6OS), HBr, HCl, HF, and solid FAI ($CH(NH_2)_2I$), C_2N_3H, $C_6N_{11}H$, among which $\mu_H(FAI)$ was chosen as the μ_H under the H-poor conditions (FAI serves as an important intrinsic hydrogen source for the perovskite). The liquid-phase structures were obtained by melting the crystalline structure via *ab initio* molecular dynamics (AIMD) using the Nose-Hoover thermostat[141] with the temperatures chosen at above the melting points and below the boiling points of the respective liquids, specifically 230 K for HI, 190 K for HBr, 170 K for HCl, 200 K for HF, 300 K for DMF, and 300 K for DMSO. The chemical potential of hydrogen thus is given by $\mu_H = \frac{E(A_lB_nH_m)-l\mu_A-n\mu_B}{m}$, where $E(A_lB_nH_m)$ is the total energy of the H-containing compound; μ_A and μ_B stand for the chemical potentials of the constituent atoms with respect to the ground-state elemental sturtures. The Fermi energy, E_F, is referenced to the VBM of $FAPbI_3$, and $E(VBM)$ represents the energy of VBM. ΔV is added for correcting the effect of periodic images of charged defects[140].

3.2.3 Transition Energy Level

The transition level is defined as the Fermi-level position with respect to the bulk VBM for which the formation energies of different defect charge states are equal:

$$\mathcal{E}(q/q') = [E(a,q) - E(a,q') - (q-q')(E(VBM) + \Delta V)]/(q-q') \quad (3.2.)$$

3.2.4 Chemical Potential of $FAPbI_3$ Perovskite

When the cubic-phase $FAPbI_3$ is stable with respect to the secondary phases of FAI and PbI_2, the chemical potential of the host should satisfy the conditions:

$$\Delta\mu_{FA} + \Delta\mu_{Pb} + 3\Delta\mu_I = \Delta H_f(FAPbI_3)$$

$$\Delta\mu_{FA} + \Delta\mu_I < \Delta H_f(FAI)$$

$$\Delta\mu_{Pb} + 2\Delta\mu_I < \Delta H_f(PbI_2)$$

where $\Delta H_f(FAPbI_3)$, $\Delta H_f(FAI)$, and $\Delta H_f(PbI_2)$ are the formation enthalpies of $MAPbI_3$, MAI, and PbI_2, respectively. To avoid the formation of elemental phases, all the chemical potentials should be less than zero ($\Delta\mu_{FA} < 0$, $\Delta\mu_{Pb} < 0$, and $\Delta\mu_I < 0$).

3.2.5 Nonradiative Capture Coefficients

The nonradiative capture coefficients are calculated using the established multiphonon emission methodology[142,143] including the effect of lattice anharmonicity[64,65,144] by solving the one-dimensional Schrodinger equation for the anharmonic potential energy surfaces. The evaluation of the electron−phonon coupling matrix elements for electron and hole capture are evaluated using the PAW results by VASP processed with the NONRAD package[142,143].

The defect concentration at thermal equilibrium can be given by[140]: $N = N_0 e^{-\frac{\Delta H}{KT}}$, where N_0 stands for the number of the available sites for defect formation per volume (cm^{-3}), ΔH is the defect formation energy, K is the Boltzmann constant, and T is temperature, which was set to room temperature.

3.3 Results and Discussions

3.3.1 Phase Map for Thermal Equilibrium Growth Condition of $FAPbI_3$ Perovskite

Figure 3.1 shows the phase map for the equilibrium growth condition of $FAPbI_3$ as a function of the relative chemical potential of Pb ($\Delta\mu_{Pb}$) and I ($\Delta\mu_I$). The constraints are set by three elementary phases (FA, Pb, and I) and two competing secondary phases (PbI_2 and FAI). Within the chemical potential range that stabilizes $FAPbI_3$ determined, i.e., the red region in the figure, three representative points are labeled as points A, B, and C, corresponding to iodine-poor (I-poor), moderate, and iodine-rich (I-rich) growth conditions, respectively.

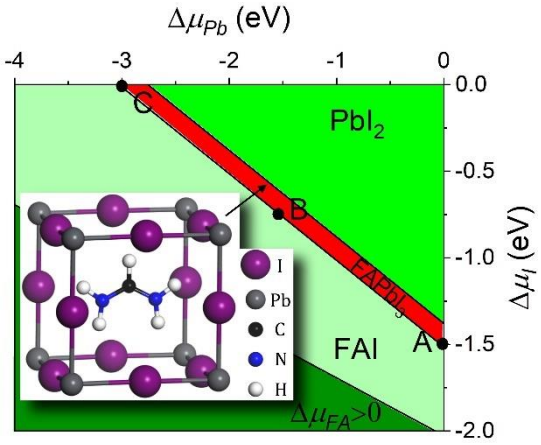

Figure 3.1. The phase map for thermal equilibrium growth condition of $FAPbI_3$ as a function of the relative chemical potentials $\Delta\mu_{Pb}$ and $\Delta\mu_I$. The red area shows the allowed chemical potential region where $FAPbI_3$ is thermodynamically stable. Three different growth conditions, i.e., point A, B, and C, corresponding to the I-poor, I-moderate, and I-rich conditions, respectively, were chosen for defect formation studies.

3.3.2 Intrinsic Defect Physics

We first systematically studied the stability of possible native point defects, including three vacancies (V_{FA}, V_{Pb}, and V_I), three interstitials (FA_i, Pb_i, and I_i), and six substitutions (FA_{Pb}, FA_I, Pb_{FA}, Pb_I, I_{FA}, and I_{Pb}), in $FAPbI_3$ with the high-level HSE+SOC+TS method. **Figure 3.2a-c** shows the calculated formation energies of seven lowest-energy native defects under the three representative iodine growth conditions. V_{FA} and V_{Pb} acceptors exhibit very low

formation energies in $FAPbI_3$, especially under I-rich conditions[145]. It can be seen that V_{FA} does not have a transition energy level and V_{Pb} produces a shallow acceptor level slightly (~0.06 eV) above the valence band maximum (VBM). Based on the Shockley-Read-Hall theory of recombination[146], the existence of a deep charge-state transition energy level in the bandgap is a prerequisite for a defect that acts as the nonradiative recombination center [140]. Hence, V_{FA} and V_{Pb} are not nonradiative recombination centers. Similarly, V_I and FA_i are also not nonradiative recombination centers with only +1 charge state stable in the Fermi level. The low formation energies of V_{Pb} and V_I are attributed to the strong Pb-*p* and I-*s* energetically unfavorable antibonding character of the valence band of $FAPbI_3$, resembling the *s*-*p* antibonding coupling in the prototypical $MAPbI_3$[131], which makes the Pb-I bonds easy to break and to form the defects. The low formation energy of V_{FA} can be attributed to the well-known weak van de Waals interaction between the PbI_6 inorganic framework and the organic cations of the hybrid perovskite structure[131]. While a previous pure-PBE study suggested that I_{FA} is a deep-level defect[126], our HSE+SOC+TS calculations show that I_{FA} is a shallow defect with a high formation energy, indicating that it can only play an insignificant role. For I_i (I interstitials), in contrast to the deep-level nature in $MAPbI_3$, it induces a shallow acceptor level $\varepsilon(0/-)$ near the VBM (~0.04 eV above the VBM) in $FAPbI_3$, consistent with experimental conclusion[134].

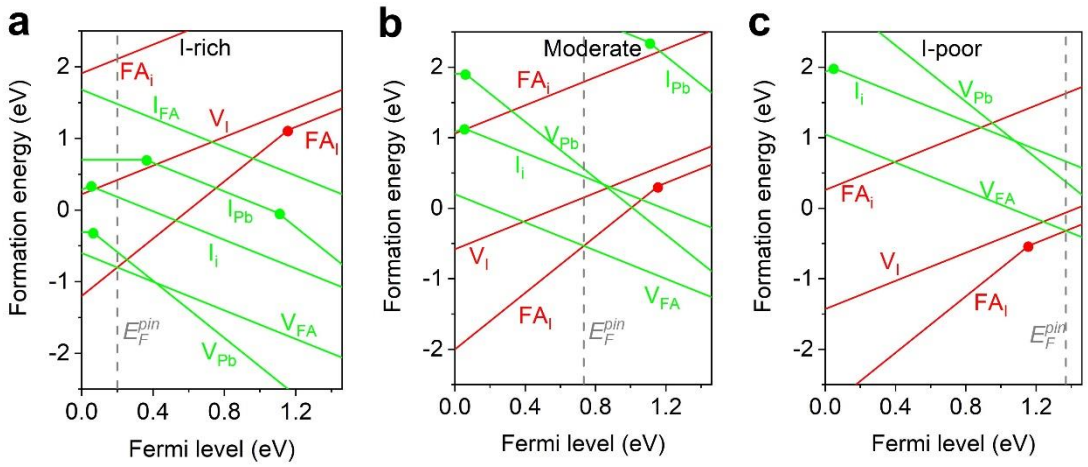

Figure 3.2. Formation energies of the seven low-energy intrinsic point defects in $FAPbI_3$ calculated using the chemical potentials corresponding to points C (a), B (b), and A (c) in **Figure 3.1**, namely, the I-rich, moderate, and I-poor growth conditions, respectively, as a function of the Fermi level. Red and green lines represent the donor and acceptor defects, respectively.

Significantly, both I_{Pb} and FA_I induce deep transition levels within the bandgap. The $\varepsilon(+2/+1)$ level of FA_I is located at 1.16 eV above the VBM. I_{Pb} has two transition levels within the bandgap; one is located at 0.36 eV and the other at 1.10 eV above the VBM. In principle, effective nonradiative recombination centers are often neutral and singly charged defects[125]. The nonradiative recombination process of higher charged defects involves the capture of charge carriers by the repulsive defect, namely, hole capture by a positively charged defect or electron capture by a negatively charged center, which results in much slower nonradiative recombination compared with that for neutral or attractive centers[146]. Similarly, a defect with multiple levels in the bandgap tends to be an inefficient nonradiative recombination center[144], because usually one of the levels involves a higher charged level that has a very low capture rate, e.g., $\varepsilon(-1/-2)$ of I_{Pb}, which limits the overall capture process[147]. Indeed, our explicit calculations confirm that FA_I and I_{Pb} are not efficient nonradiative recombination centers with the very low carrier capture coefficients of $2.3 \times 10^{-20} cm^3 s^{-1}$ and $6.6 \times 10^{-14} cm^3 s^{-1}$, respectively, at room temperature (see **Figure 3.3**). Notably the carrier capture

coefficient of I_{Pb} in $CsPbI_3$ is also on the order of $10^{-14}cm^3s^{-1}$ at room temperature[144], which could not cause significant nonradiative recombination.

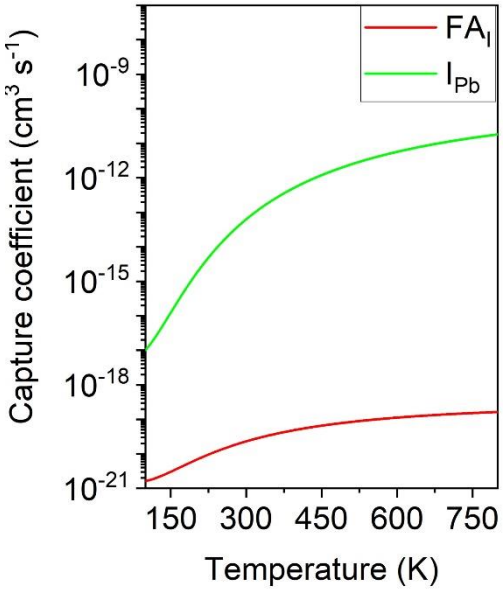

Figure 3.3. Calculated carrier capture coefficients of FA_I (red) and I_{Pb} (green) in $FAPbI_3$ as a function of temperature. These results are significantly lower, by the orders of 10^{13} for FA_I and 10^6 for I_{Pb}, than that of interstitial hydrogen at room temperature. Hence, they are not the efficient nonradiative recombination centers observed in experiments.

3.3.3 Hydrogen Interstitials as an Important Nonradiative Carrier Recombination Center in Hybrid Perovskites

Alternatively, unintentionally incorporated impurities may play an important role. It is well established that hydrogen is a common impurity in traditional semiconductors[148] and notably, our previous studies demonstrate that it can be abundant in the lattice of hybrid Methylammonium perovskites[149,150]. Motivated by this, we systematically studied the energetics and nonradiative recombination properties of interstitial hydrogen defects in $FAPbI_3$. **Figure 3.4a** shows the formation energies of atomic H_i and molecular H_2 in $FAPbI_3$. For each species, several structural configurations in different charged states were considered (**Figure 3.5**, **Table 3.1-3.4**). It can be seen that H_2 is electrically inactive with a thermodynamically stable neutral-charged state in $FAPbI_3$. For molecular H_2, the H-H bond length is 0.77 Å, close

to 0.75 Å for free hydrogen molecules. In contrast, atomic H_i behaves as an electric-active negative-U center in $FAPbI_3$. The neutral state H_i^0 is energetically unstable compared with the positively charged H_i^+ and negatively charged H_i^- over the whole range of the Fermi level. This leads to a deep $\varepsilon(+/-)$ transition energy level, i.e., the intersection of the formation energies of H_i^+ and H_i^-, at 0.73 eV above the VBM. In a *p*-type or *n*-type $FAPbI_3$, i.e., when the Fermi level is located at the proximity of the VBM or the conduction band minimum (CBM), respectively, H_2 is unstable and tends to dissociate into hydrogen ions. In an intrinsic (low-conductivity) $FAPbI_3$, H_2 is energetically more favourable.

Table 3.1. The total energy difference for the positively charged H_i^+ in the sites considered in the Figure S2, where $\Delta E = 0$ eV stands for the energetically most favorable defect site.

site	1	2	3	4	5	6
ΔE (eV)	0.46	0.46	0.44	0.44	0.67	0.67

site	7	8	9	10	11	12
ΔE (eV)	0.01	0	0	0.35	0.35	0.35

Table 3.2. The total energy difference for the neutral H_i^0 in the sites considered in the Figure S2, where $\Delta E = 0$ eV stands for the energetically most favorable defect site.

site	1	2	3	4	5	6
ΔE (eV)	0	0	0.01	0.01	0.22	0.23

site	7	8	9	10	11	12
ΔE (eV)	0.33	0.35	0.35	0.18	0.18	0.18

Table 3.3. The total energy difference for the negatively charged H_i^- in the sites considered in the Figure S2, where $\Delta E = 0$ eV stands for the energetically most favorable defect site.

site	1	2	3	4	5	6
ΔE (eV)	0.36	0.36	0.37	0.37	0	0.01
site	7	8	9	10	11	12
ΔE (eV)	0.73	0.70	0.71	0.49	0.47	0.47

Table 3.4. The total energy difference for H_2 in the sites considered in the Figure S2, where $\Delta E = 0$ eV stands for the energetically most favorable defect site.

site	1	2	3	4	5	6
ΔE (eV)	0.82	0.82	0.84	0.84	0.66	0.66
site	7	8	9	10	11	12
ΔE (eV)	0.58	0.58	0.58	0.01	0.02	0

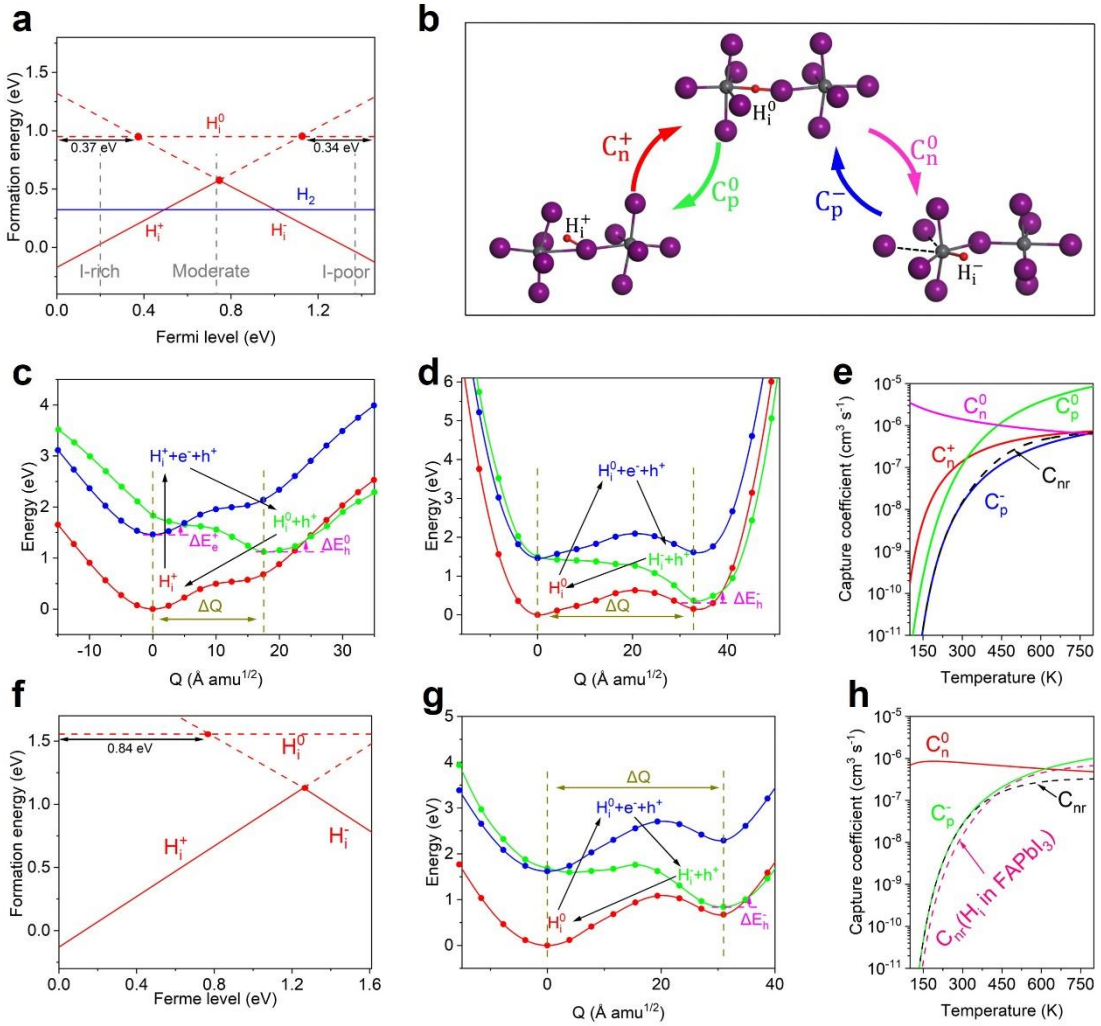

Figure 3.4. (a) The formation energies of hydrogen interstitials in $FAPbI_3$ as a function of the Fermi level under the H-rich conditions. The vertical dashed lines correspond to the pinned Fermi levels for the *p*-type, intrinsic, and *n*-type conductivities, respectively. (b) Local atomic configurations of H_i in the three charge states, where the notations of atoms are as those in **Figure 3.1** and the hydrogen interstitials are highlighted in red. The arrows and labels show the relevant carrier capture processes during the charge-state transitions. Configuration coordinate diagram for the transition of $H_i^+ \leftrightarrow H_i^0$ (c) and $H_i^0 \leftrightarrow H_i^-$ (d), respectively, as a function of a generalized configuration coordinate (Q). (e) Nonradiative capture coefficients of H_i as a function of temperature. (f) The formation energies of H_i in the predecessor $MAPbI_3$ as a function of the Fermi level under both the H-rich conditions. (g) Configuration coordinate diagram for the transition of $H_i^+ \leftrightarrow H_i^0$ in $MAPbI_3$, as a function of a generalized configuration coordinate (Q). (h) Nonradiative capture coefficients of H_i in $MAPbI_3$ as a function of temperature. The nonradiative recombination coefficient C_{nr} of H_i in $FAPbI_3$ was also included for comparison.

For such a negative-U defect, the $\varepsilon(+/-)$ transition level does not govern the nonradiative recombination even though it is deep in the bandgap, as found in the case of I_i in $MAPbI_3$[64,132],

because the defect cannot capture two charge carriers of the same type, e.g., two electrons or two holes, at once. Instead, the relevant transition levels are $\varepsilon(+/0)$ (0.34 eV below the CBM) and $\varepsilon(0/-)$ (0.37 eV above the VBM), and four capture processes (two electron captures and two hole captures) are involved during the nonradiative recombination via the center[64,132].

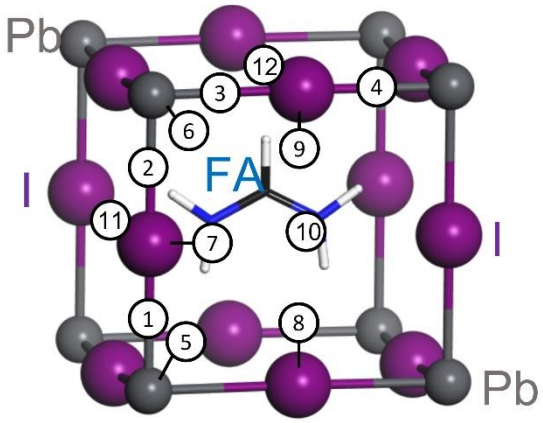

Figure 3.5. Schematic representation of the $FAPbI_3$ structure and the sites on which interstitial hydrogen can incorporate, namely, the bond-center sites (1, 2, 3, 4), the Pb antibonding sites (5,6), the I antibonding sites (7, 8, 9), and the lattice void sites (10, 11, 12).

As shown in **Figure 3.4b**, H_i exhibits distinctly different local atomic structures in three charge states (+, 0, and -) in $FAPbI_3$, which could be partially attributed to the ionic character of the perovskite. During the transition between different charged states of H_i, the carrier capture processes are abbreviated as C_a^b, as shown in the labels in **Figure 3.4b**, where the subscript *a* specifies the carrier type ("n" for electron, and "p" for hole), and superscript *b* indicates the charge state of the defect. In the case of H_i^+, atomic hydrogen tends to bind to an I anion with a chemical bond length of 1.71 Å, compared with 1.61 Å for HI molecule. With the capture of an electron (C_n^+), H_i^+ transform into neutral-charged H_i^0. H_i^0 adopts a bond-centered configuration, in which hydrogen atom resides between the connected Pb and I atoms, with the distances of 2.08 Å and 1.88 Å to Pb and I, respectively. By further capturing another electron (C_n^0), the hydrogen ion moves to the vicinity of the Pb cation, and the local atomic configuration

distorts significantly into a three-fold coordinated local PbI_6 octahedron, forming H_i^-. Conversely, the transition of $H_i^- \rightarrow H_i^0 \rightarrow H_i^+$ involves two hole-capture processes, i.e., C_p^- and C_p^0, respectively.

To quantitively determine the carrier capture coefficient of these processes, we first performed a carrier capture semiclassical analysis with the calculated configuration coordinate diagrams for the transition of $H_i^+ \leftrightarrow H_i^0$ and $H_i^0 \leftrightarrow H_i^-$. As shown in **Figure 3.4c**, the diagram depicts the potential energy surfaces (PES) of the charge state transition between H_i^+ and H_i^0 as a function of the generalized configuration coordinate (Q)[142,151]. The Q of each configuration is determined by its difference from a reference configuration, i.e., $Q = \sqrt{\sum_a m_a (R_a - R_{f,a})^2}$, where m_a and R_a are the mass and Cartesian coordinate of atom a; the subscript f stands for the final state of the charge transition[142]. For a H_i^+ with an electron (e^-) at the CBM and a hole (h^+) at the VBM (blue line in **Figure 3.4c**), it requires to overcome an energy barrier ΔE_e^+ (the intersection between potential energy surfaces of H_i^+ (blue line) and H_i^0 (green line)) to capture an electron and transition to H_i^0. Similarly, the hole capture process by H_i^0 overcomes a comparable energy barrier ΔE_h^0, as indicated by the intersection between the green line and red line in the figure, H_i^0 transitions back to H_i^+. Based on the quantum-mechanical vibronic overlap of the PES and the strength of electron-phonon coupling[142], the nonradiative electron (C_n^+) and hole (C_h^0) capture coefficients for the transition between H_i^+ and H_i^0 are $1.3 \times 10^{-7} cm^3 s^{-1}$ and $2.4 \times 10^{-8} cm^3 s^{-1}$, respectively, at room temperature, as shown in **Figure 3.4e**.

For the analysis of the charge state transition between H_i^0 and H_i^-, as shown in **Figure 3.4d**, an important feature is that the larger structural relaxation associated with the transition between H_i^0 and H_i^- results in a greater ΔQ (~ 33 Å $amu^{1/2}$). The strong electron-lattice coupling leads to a large anharmonicity for the PES, which further impacts the capture barriers. It can be seen

that the PES of H_i^0 exhibits a metastable minimum at the equilibrium configuration of H_i^-, which is similar to the case of I_i^0 in $MAPbI_3$[64,128]. The energy barrier of the charge-state transition determines the capture rate in principle. Notably, the transition of H_i^0 to H_i^- (C_n^0) is within the Marcus inverted region[65,152], where a very small electron-capture energy barrier (ΔE_n^0) occurs because the large anharmonicity enables that the PES of the final state (H_i^-, green line) is accidentally close to the minimum of the PES of the initial state (H_i^0, blue line) despite the large value of ΔQ. In contrast, the energy barrier (ΔE_h^-) for hole capture by H_i^- (C_p^-) is somewhat large ($\sim$0.24 eV) compared to other processes. Furthermore, there is an additional energy barrier of $\sim$0.56 eV as the structure recovers from $Q\sim33$ Å $amu^{1/2}$ to $Q\sim0$ Å $amu^{1/2}$ after overcoming ΔE_h^-. This further retards the hole capture by H_i^-. As expected, as shown in **Figure 3.4e**, the calculated nonradiative electron capture coefficient (C_n^0) for H_i^- is $1.4\times10^{-6}cm^3s^{-1}$, much higher than that of $1.4\times10^{-8}cm^3s^{-1}$ for the hole capture process (C_p^-), consistent with the semiclassical analysis of the capture barriers.

On the basis of balancing electron and hole capture under steady-state conditions[147], the nonradiative recombination coefficient per defect C_{nr} (C_{Tot} in Ref. 30) can be determined by $C_{nr}=\frac{C_n^0+C_p^0}{1+\frac{C_n^0}{C_p^-}+\frac{C_p^0}{C_n^+}}$, as indicated by the black dashed line in **Figure 3.4e**. At room temperature, the calculated C_{nr} of H_i is $1.50\times10^{-8}cm^3s^{-1}$, which is in good agreement with the experimental observation of $\sim10^{-8}cm^3s^{-1}$[135], strongly indicating that H_i is an important or even dominant recombination center in $FAPbI_3$. In addition to the nonradiative recombination coefficient C_{nr}, the overall nonradiative recombination rate constant A is also related to the defect density N in the material, namely, $A=NC_{nr}$, which describes the number of nonradiative recombination events unit time (the reciprocal of nonradiative lifetime τ_{nr}). Notably, the C_{nr} of H_i is comparable to that of hydrogen vacancies of FA cations $V_H(C)$ in $FAPbI_3$ ($3.2\times10^{-8}cm^3s^{-1}$)[65]. Our calculated formation energies of $V_H(C)$ and H_i are shown in **Figure 3.6**.

Even under the H-poor conditions, $V_H(C)$ exhibits much higher formation energies (~2.08 eV under the I-rich and moderate conditions, and ~1.93 eV under I-poor) than H_i (~0.71 eV under the I-rich, ~0.64 eV under the I-poor conditions, and ~1.08 eV under the I-moderate conditions). At room temperature, a difference in formation energy of 1 eV (under the moderate conditions) implies about sixteen orders of magnitude difference in the defect densities at thermal equilibrium. This clearly demonstrates that H_i can play a much more significant role than $V_H(C)$ in nonradiative recombination in $FAPbI_3$.

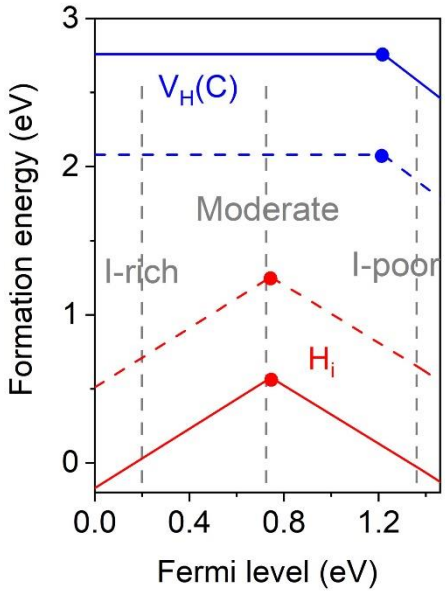

Figure 3.6. The formation energies of $V_H(C)$ (blue) and H_i (red) in $FAPbI_3$ as a function of the Fermi level under both H-rich and H-poor conditions, where the chemical potential of hydrogen are set to $\mu_H(H_2)$ and $\mu_H(FAI)$ under the H-rich (solid lines) and H-poor (dashed lines) conditions, respectively. The vertical dashed lines correspond to the pinned Fermi levels in $FAPbI_3$ under the I-rich, moderate, and I-poor conditions, respectively.

As we have recently reported[149,150], H_i is also a deep-level defect in $MAPbI_3$. To quantify its impact on nonradiative recombination in $MAPbI_3$ and explicitly compare it with $FAPbI_3$, we also calculated the C_{nr} of H_i in $MAPbI_3$ (see **Figures 3.4f-3.4h**). The relevant transition level is $\varepsilon(0/-)$, which is located at 0.84 eV above the VBM, as shown in **Figure 3.4f**. As similar in

$FAPbI_3$, H_i^- resides in the PbI_6 octahedron in $MAPbI_3$. The presence of H_i^- in $MAPbI_3$ results in a strong structural distortion of the nearby PbI_6 octahedron compared with the other charge states (namely H_i^+ and H_i^0)[149,150], and therefore, a large ΔQ (~ 31 Å $\mathrm{amu}^{1/2}$) is present in the calculated configuration coordinate diagram (see **Figure 3.4g**). The energy barrier for the electron capture process is very small (< 0.1 eV) and the energy barrier for the hole capture process is relatively higher (by ~ 0.22 eV). As expected, the calculated capture coefficients (see **Figure 3.4h**) suggest that at room temperature the electron capture process ($C_n^0 \sim 7.8 \times 10^{-7} \mathrm{cm}^3\mathrm{s}^{-1}$) is faster than the hole capture process ($C_p^- \sim 2.7 \times 10^{-8} \mathrm{cm}^3\mathrm{s}^{-1}$). The nonradiative recombination coefficient under steady-state conditions is derived as $C_{nr} = \frac{C_e C_h}{C_e + C_h}$. The calculated C_{nr} of H_i in $MAPbI_3$ is $2.6 \times 10^{-8} \mathrm{cm}^3\mathrm{s}^{-1}$, compared to $1.50 \times 10^{-8} \mathrm{cm}^3\mathrm{s}^{-1}$ in $FAPbI_3$, at room temperature.

The C_{nr} of H_i in $MAPbI_3$ is well comparable to that in $FAPbI_3$. This can be attributed to the similarity of the local chemical environments of PbI_6 octahedron and thus similar lattice coupling and anharmonicity of H_i^- during the charge-state transitions, as shown in the PES in **Figure 3.4d** and **3.4g**, resulting in similar energy barriers for hole capture by H_i^- (ΔE_h^-) in both systems. Notably, the hole-capture process is the rate-limiting step of the overall nonradiative recombination process for H_i in both $FAPbI_3$ and $MAPbI_3$. In p-type or intrinsic conductivities, H_i exhibits similar formation energies in both systems, indicative of similar induced recombination losses. In n-type conductivities, H_i in $FAPbI_3$ is more significant than in $MAPbI_3$ due to relatively lower formation energy and thus higher defect density. Experimentally, the perovskite solar cells are typically fabricated with the intrinsic-conductivity perovskite active layers[103]. Thus if we assume the position of the Fermi level at around 0.7 eV above the VBM, H_i has similar impacts on the device performance of $MAPbI_3$ and $FAPbI_3$. These results indicate that the engineering of the A-site substitution (ABX_3) between FA and MA cations will not effectively mitigate the nonradiative recombination losses

caused by H_i. That is, H_i is expected to be efficient nonradiative recombination centers in the FA-MA mixed lead halide perovskite solar cells[50].

It is important to note that I_i[64] and $V_H(N)$[65] of MA cations can also cause strong nonradiative recombination in $MAPbI_3$. I_i in $MAPbI_3$ has a similar nonradiative recombination coefficient ($C_{nr} \sim 0.7 \times 10^{-8} cm^3 s^{-1}$) and formation energy as H_i in $FAPbI_3$[64]. In particular, $V_H(N)$ is the most efficient nonradiative recombination center in $MAPbI_3$ reported so far with an exceptionally high C_{nr} of $0.8 \times 10^{-4} cm^3 s^{-1}$[65], around four orders of magnitude higher than that of H_i. These efficient nonradiative recombination centers are absent from $FAPbI_3$: I_i is a shallow defect in $FAPbI_3$ and hydrogen vacancy of FA cation has very high formation energy. Overall, $FAPbI_3$ exhibits a higher degree of defect tolerance in nonradiative carrier recombination than $MAPbI_3$. The results may explain the general experimental observations[123] that the nonradiative recombination rates in $FAPbI_3$ are typically lower than that in $MAPbI_3$, contributing to the better performance of the $FAPbI_3$-based devices. H_i serves as an important and even dominant origin of the experimentally observed nonradiative loss in the $FAPbI_3$-based devices[116,120,123,124].

3.3.4 Minimizing Hydrogen Interstitials to Enable Highly Efficient $FAPbI_3$ Perovskites

The defect density N is critical and therefore should be suppressed by carefully managing the growth conditions. Experiments have demonstrated that iodine management plays an important role in deep-level defect engineering in the $FAPbI_3$ active layers for high-performance solar cells[117,119–122]. An iodine-moderate growth condition is crucial for optimizing the optoelectronic performance of the perovskites, while the scarce or excess iodine conditions unavoidably lead to the formation of deep-level defects and therefore nonradiative recombination losses, resulting in inferior device performance. Here, our calculations suggest that the different iodine-content conditions can effectively affect the relative chemical

potentials and consequently the defect stabilities of the perovskites. Under the I-rich conditions (**Figure 3.2a**), the charge neutrality of $FAPbI_3$ is largely determined by the lowest-energy V_{FA} acceptor and FA_I donor, where the Fermi level is pinned approximately at the proximity of the VBM, which is a typical *p*-type conductivity. Similarly, under the I-poor conditions (**Figure 3.2c**), the Fermi level of $FAPbI_3$ is pinned at the proximity of the CBM, namely, an *n*-type conductivity. This is in line with experiments that the conductivity of $FAPbI_3$ can be flexibly tuned from *p*-type to *n*-type by increasing the PbI_2/FAI ratio in the precursor solution[103]. Significantly, the stabilities and densities of hydrogen interstitials are a function of the Fermi level. From **Figure 3.4a** and **Figure 3.7**, these two typical conditions indeed enhance the formation of H_i as efficient nonradiative recombination centers, which will strongly impact the carrier lifetime and power conversion. Notably, the I-rich conditions would also increase the density of shallow-level I_i that lowers the cubic-to-hexagonal transformation barrier of the $FAPbI_3$ active layer to accelerate its phase degradation, and hence, have significant repercussions on the long-term stability of perovskite solar cells[134]. Under the I-moderate conditions (**Figure 3.2b**), the Fermi level will be pinned around the middle of the bandgap, corresponding to an intrinsic (low) conductivity, where the formation energy of H_i increases and the electrical-inactive molecular hydrogen (H_2) serves as the dominant hydrogen interstitials under H-rich conditions (**Figure 3.4a** and **Figure 3.7**). On the other hand, the formation of H_i and their induced nonradiative energy loss will be suppressed in $FAPbI_3$ active layers.

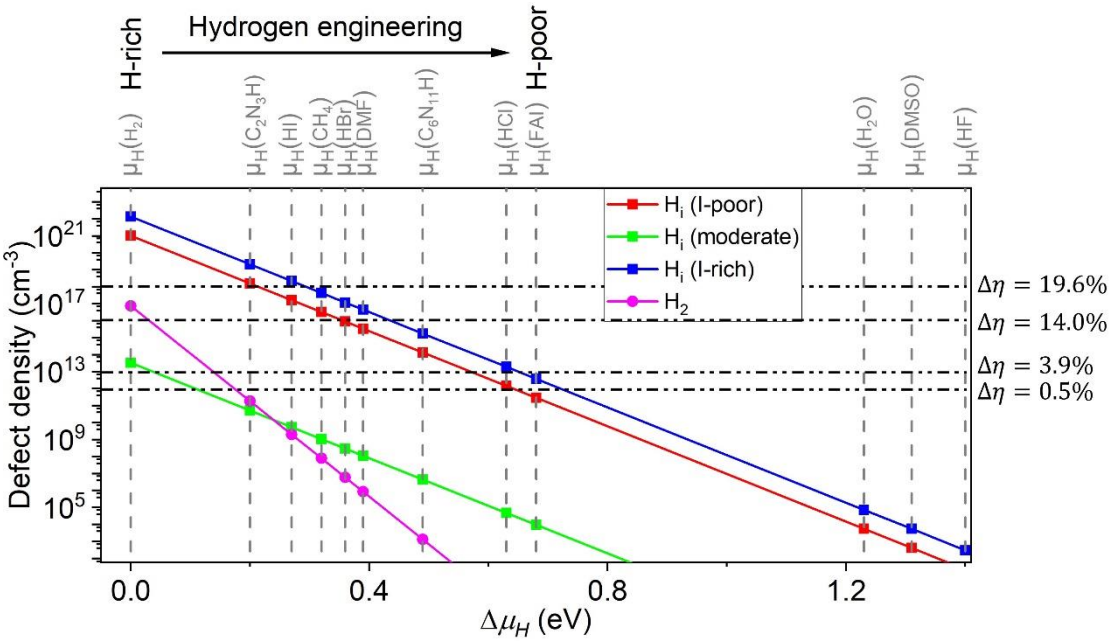

Figure 3.7. Calculated defect densities of H_i and H_2 at room temperature under the three representative iodine growth conditions in $FAPbI_3$, as a function of the relative chemical potential of hydrogen ($\Delta\mu_H$) in the relevant compounds (hydrogen sources). $\mu_H(H_2)$ and μ_H(FAI) correspond to the hydrogen (H)-rich and H-poor conditions, respectively. The resultant efficiency losses ($\Delta\eta$) by H_i in different defect densities are denoted.

Furthermore, we will show that, in addition to iodine management, careful control of the hydrogen environment for the preparation and operation is also important for suppressing $H_i$defects and further improving $FAPbI_3$-based solar cells. To reveal unintentional hydrogen incorporation under different possible hydrogen sources, we plot the defect densities of H_i and H_2 at room temperature as a function of the relative hydrogen chemical potential in **Figure 3.7**, under the three representative iodine growth conditions. Under the hydrogen (H)-rich conditions, it has been a common practice to set the μ_H as that in the isolated H_2 molecule. However, the H-poor condition can be simulated by considering the practical hydrogen sources. FAI, a precursor, serves as an important intrinsic hydrogen source for $FAPbI_3$, and therefore, the chemical potential of hydrogen can be around μ_H(FAI) under the H-poor conditions. As can be seen, the commonly used HI and HBr additives as well as some organic compounds, e.g., C_2N_3H and CH_4, and the DMF solvent, can be potential hydrogen sources leading to

unintentional hydrogen contamination, while the water vapor, DMSO solvent, and HF can play an insignificant role. Notably, under more H-poor conditions, the electrically inactive H_2 will be unstable with respect to dissociation into the detrimental H_i.

With the nonradiative recombination coefficient C_{nr} and defect density N, we can quantify the resultant PCE loss $\Delta\eta$ due to the nonradiative recombination by H_i. Under the detailed balance limit and ideal conditions, the light to electricity PCE is well known as the S-Q limit[125]. In the S-Q framework, the photocurrent of the solar cell is calculated as the difference between the photons absorbed and the photons flowing out the cell: $J(V) = J_P - J_{rad}(V)$, where $J_P \cong q\int_{E_g}^{\infty}\frac{2\pi}{h^3c^2}\frac{E^2}{e^{\left(\frac{E}{KT_{sun}}\right)}-1}dE$ stands for the photocurrent density, and $J_{rad}(V) \cong q\int_{E_g}^{\infty}\frac{2\pi}{h^3c^2}\frac{E^2}{e^{\left(\frac{E-qV}{KT_{cell}}\right)}-1}dE$ stands for the radiative recombination current density. q, h, K, and c are the elementary charge, Planck's constant, Boltzmann constant, and speed of light, respectively. V is the applied voltage and is equal to the splitting of the Fermi levels $qV = E_F^n - E_F^p$ under the steady condition. Therefore, the light to electricity PCE in the case of the radiative limit can be calculated by the formula $\eta = \frac{MAX(P_{out}(V))}{P_{in}} = \frac{MAX(J(V)\times V)}{P_{in}}$, where the input sun power density is given by $P_{in} = \frac{2\pi}{h^3c^2}\int_0^{\infty}\frac{E^3dE}{e^{\left(\frac{E}{KT_{sun}}\right)}-1}$. For $FAPbI_3$ with the calculated bandgap of 1.46 eV, under AM 1.5G spectrum, the ideal power conversion efficiency (S-Q limit) can be up to $\eta\sim32.13\%$ at room temperature, consistent with that reported in Ref.[153].

In the presence of the nonradiative recombination from H_i, the photocurrent of the solar cell will be given by: $J(V') = J_P - J_{rad}(V') - J_{nr}(V')$. The new term describes the current density loss due to the nonradiative recombination $J_{nr}(V') \cong qdAn_ie^{\left(\frac{qV'}{2KT_{cell}}\right)}$, where d, A, n_i are the thickness of the $FAPbI_3$ layer, nonradiative recombination rate constant, and intrinsic carrier concentration. We adopt the representative $d\sim300\ nm$ and $n_i\sim10^7 cm^{-3}$[154]. For the solar cell

application, the nonradiative recombination is usually dominated by the defect-induced process, and the Auger recombination can play an insignificant role[155]. Therefore, the nonradiative recombination rate constant is given by the aforementioned $A = NC_{nr}$. With $P_{out}(V') = J(V') \times V'$, the resultant efficiency loss by H_i can be obtained: $\Delta\eta = \eta - \eta' = \frac{MAX(P_{out}(V)) - MAX(P_{out}(V'))}{P_{in}}$.

The estimated $\Delta\eta$ values in different H_i densities are shown in **Figure 3.7**. Notice even under the preferred I-moderate growth conditions, H_i can impact the device performance with the induced efficiency loss $\Delta\eta$ being more than 4% under the H-rich conditions. This strongly suggests that H_i induced nonradiative loss can be an important loss mechanism in the $FAPbI_3$-based solar cells. To effectively suppress this detrimental effect on the device performance, the density of H_i should be controlled below the orders of $10^{12} cm^{-3}$, under which the induced $\Delta\eta$ would be less than 0.5 %. These results point to a target for hydrogen engineering to further improve the performance of the perovskite solar cells approaching their theoretical efficiency limit.

3.4 Conclusion

In summary, based on first-principles calculations, we demonstrate that native point defects are not responsible for the nonradiative losses in $FAPbI_3$. Instead, hydrogen ions can act as the dominant nonradiative recombination centers in $FAPbI_3$ with a high capture coefficient of $1.5 \times 10^{-8} cm^3 s^{-1}$ at room temperature, in good agreement with the experimentally measured values. Both iodine-poor and iodine-rich conditions would promote the formation of detrimental H_i in $FAPbI_3$ and reduce the PCEs of the related solar cells significantly ($\Delta\eta > 10\%$). In this sense, growing the $FAPbI_3$ active layers under the I-moderate conditions and carefully controlling the hydrogen environment can effectively suppress the formation of H_i

and the adverse effect on PCE. These findings are significant for possible further improvement of the $FAPbI_3$-based photovoltaic device performance.

Chapter 4 Trapped-Hydrogen-Induced Energy Loss in Tin-Based Hybrid Perovskite Solar Cells

4.1 Introduction

Owing to the unique photophysical properties, low-cost organic-inorganic hybrid perovskites have drawn intensive attention in the optoelectronic community[3,11,33,115]. In particular, rapid progress has been demonstrated in perovskite solar cells with a power conversion efficiency (PCE) exceeding 25.8%[3], which is already close to that of single-crystal silicon cells (26.6%)[156]. Nevertheless, the toxicity of lead (Pb) to the human body and environment poses a significant challenge for the further commercialization of the perovskite photovoltaic technology[118,157]. Isovalent tin (Sn) has been regarded as one of the most appropriate replacements for Pb in the perovskite layers among various nontoxic alternatives. Sn-based hybrid perovskites, such as methylammonium tin iodide ($MASnI_3$) and formamidinium tin iodide ($FASnI_3$), have the narrower optical bandgaps of 1.20-1.40 eV[158], closer to the Shockley-Queisser (S-Q) limit (1.34 eV)[125] than those of the Pb-based counterparts (1.5-1.7 eV), indicating the potential for higher efficiency limits. In addition, Sn-based perovskite materials exhibit high absorption coefficients[159] and small exciton binding energies[160]. Taking advantage of these merits, Sn-based perovskites hold great promise for lead-free perovskite photovoltaics and other device applications.

However, since the early demonstration of $MASnI_3$ perovskite solar cells yielding PCE of around 6% in 2014[161] and 9% in 2018[160], respectively, the highest PCE only reached 14% in $FASnI_3$-based solar cells[162], outperforming other Pb-free candidates but still lagging significantly behind the Pb-based counterparts. Defect-induced nonradiative charge recombination is generally considered an important loss mechanism for Sn-based perovskite solar cells[158,161,163–165]. As compared to the Pb-based halide perovskites, the much faster

crystallization process and easier oxidation of the Sn-based halide perovskites lead to the formation of a high density of defects, specifically deep-level nonradiative recombination centers[158,161,163–165]. Notably, Ng *et al.*[166,167] reported that the pristine $FASnI_3$ active layer displays a huge deep-level state density up to $\sim 10^{20}$ cm^{-3}, which is around five orders of magnitude higher than that in the Pb-based counterparts[128]. The measured nonradiative recombination rate often reaches up to $\sim 10^{9}$ s^{-1} [123,168,169], compared to $10^{6} - 10^{7}$ s^{-1} typically measured in the Pb-based perovskites[123]. The severe nonradiative recombination losses in Sn-based halide perovskites significantly hinder the photo-generated carrier transport and reduce the open-circuit voltage (V_{OC}), resulting in inferior solar cell efficiencies.

Accurately identifying the potential deep-level defects that act as detrimental nonradiative recombination centers is crucial for further optimizations of Sn-based perovskite (e.g., $FASnI_3$) devices. Experimental reports[166] have indicated that adding excess Sn halides, such as SnI_2 or SnF_2, namely a Sn-rich growth condition, can reduce the density of deep-trap states and the recombination rate to a certain extent, and thus improve the V_{OC} and PCE of $FASnI_3$-based solar cells, though such a strategy cannot completely remedy the problem. Due to this dependence, it has been proposed that the observed nonradiative recombination is closely associated with the emergence of high-density intrinsic Sn vacancies (V_{Sn})[170,171] as a result of the facile oxidation of Sn^{2+} into Sn^{4+}[172]. However, a first-principles investigation reveals that V_{Sn} acts as a shallow defect in $FASnI_3$[173]. Thus far the microscopic origin of the detrimental deep-level defects in $FASnI_3$ remains mysterious.

In addition to the intrinsic defects, hydrogen defects can be a candidate. As found in many traditional semiconductors[148,174], experimental[175–177] and theoretical[149,150,178–181] studies have reported the existence of interstitial hydrogen species in the lattice of the hybrid lead halide perovskites, especially under moisture conditions. In particular, Seok *et al.*[182] proposed that the

long-term instability of the perovskite-based devices can be partially attributed to the accumulation of hydrogen owing to its electrical activity and high mobility. Here, based on first-principles hybrid functional calculations, we found that, in $FASnI_3$, hydrogen prefers to exist in a "hidden" form: hydrogen interstitials tend to be trapped within the abundant native Sn vacancies and thus form $V_{Sn} - H_2$ complexes. Significantly, while neither V_{Sn} nor H_2 are deep-level defects in $FASnI_3$, the strong chemical interaction within the $V_{Sn} - H_2$ complex results in a deep transition level within the bandgap with a large capture coefficient of 2.1×10^{-9} cm^3 s^{-1}, which can cause sizable energy loss.

4.2 Simulation Method

4.2.1 Computational Method

First-principles calculations are performed based on density functional theory (DFT) as implemented in the Vienna Ab initio Simulation Package (VASP)[114]. Projector augmented wave (PAW) pseudopotentials[136] were employed. We studied $FASnI_3$ in a cubic (Pm3m) crystal structure[183]. A plane-wave energy cutoff of 400 eV and a Monkhors–Pack sampling of $2 \times 2 \times 2$ k-points were used for the $3 \times 2 \times 2$ supercells with 144 atoms. Tkatchenko-Scheffler (TS) scheme[137] was used to describe the dispersion interactions for the hybrid perovskite system[138]. All atoms are relaxed until the forces on atoms are below 0.01 eV/Å. Heyd–Scuseria–Ernzerhof hybrid functional ($\alpha = 0.43$) including the spin-orbit coupling (HSE+SOC) was used for the defect calculations, which can reproduce the bandgap value of 1.38 eV (see **Figure 4.1** for the band structures of $FASnI_3$ with HSE and HSE+SOC), compared with the experimental results of 1.40 eV[162].

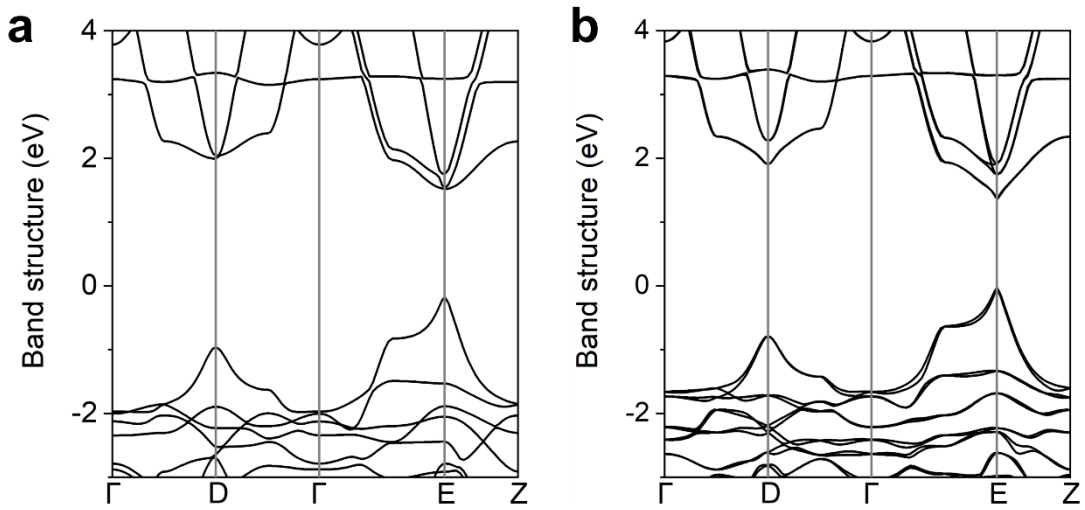

Figure 4.1. The calculated band structures of $FASnI_3$ with (a) HSE and (b) HSE+SOC, achieving a bandgap of 1.69 eV and 1.38 eV, respectively.

4.2.2 Defect Formation Energy

For a defect ionized the charge state *q*, its formation energy, $\Delta H_f(\mathrm{D_i^q})$, is calculated by[140]:

$$\Delta H_f(\mathrm{D_i^q}) = E(\mathrm{D_i^q}) - E(host) - \sum n_i(\mu_i + \Delta\mu_i) + q(E_f + E(VBM) + \Delta V) + \Delta_{corr}^{q} \quad (4.1)$$

Here, $E(\mathrm{D_i^q})$ and $E(host)$ are the total energies of the defect-containing and defect-free supercells, respectively; n_i and q are the differences in the number of atoms and charge states between the defect-containing and defect-free supercells, respectively. μ_i stands for the absolute value of the chemical potential of defect atoms. $\Delta\mu_i$ stands for the relative value of the chemical potential, which is related to growth conditions. Specifically, bounds can be placed on the range of relative chemical potentials by choosing values that ensure thermodynamic stability of $FASnI_3$ and prevent the formation of secondary common competing phases (FAI, SnI_2, SnI_4, and FA_2SnI_6):

$$\Delta\mu_{FA} + \Delta\mu_{Sn} + 3\Delta\mu_I = \Delta H_f(FASnI_3)$$

$$\Delta\mu_{FA} + \Delta\mu_I \leq \Delta H_f(FAI)$$

$$\Delta\mu_{Sn} + 2\Delta\mu_I \leq \Delta H_f(SnI_2)$$

$$\Delta\mu_{Sn} + 4\Delta\mu_I \leq \Delta H_f(SnI_4)$$

$$2\Delta\mu_{FA} + \Delta\mu_{Sn} + 6\Delta\mu_I \leq \Delta H_f(FA_2SnI_6)$$

E_f is the Fermi energy referenced to the valence band maximum (VBM), and $E(VBM)$ represents the energy of the VBM of the host material. ΔV is used for ensuring the alignment of the potential for the charged defect in supercells and Δ_{corr}^{q} stands for the finite-size correction term for the periodic images of the charged defects[184].

4.2.3 Transition Energy Level

The transition energy level is defined as the Fermi-level position for which the formation energies of different defect states are equal and can be given by:

$$\mathcal{E}(q/q') = \left[\Delta H_f\left(\mathrm{D_i^q}, E_f = 0\right) - \Delta H_f\left(\mathrm{D_i^{q'}}, E_f = 0\right)\right]/(q' - q) \quad (4.2)$$

4.2.4 Defect Concentration Calculation

The defect concentration at thermal equilibrium can be given by[140]: $N = N_0 e^{-\frac{\Delta H}{kT}}$, where N_0 stands for the number of available sites for defect formation in the $CsPbI_3$ lattice per volume, ΔH is the formation energy of defect, k is the Boltzmann constant, and T is temperature.

4.2.5 Nonradiative Capture Coefficient

The calculation of nonradiative capture coefficients is performed using the NONRAD package[142,143], which is based on the well-established multi-phonon emission methodology, and includes the effects of anharmonicity by directly solving the one-dimensional Schrödinger equation using the Fourier grid method[64,65]. The potential energy surfaces are obtained by interpolating the energies from first-principles calculations. The electron-phonon coupling matrix elements for electron and hole capture are evaluated within the linear-coupling approximation using the PAW as implemented in the VASP.

4.3 Results and Discussions

4.3.1 Phase Diagram and Intrinsic Defect Physics in Sn-based $FASnI_3$ Perovskite

Figure 4.2a shows the stability phase diagram of $FASnI_3$ and derivatives relative to the chemical potentials ($\Delta\mu_I$ and $\Delta\mu_{Sn}$). The thermodynamically stable $FASnI_3$ is represented as the red region with respect to its elemental phases (I, Sn, and FA) and the competing secondary phases (SnI_2, SnI_4, FAI, and FA_2SnI_6). Within the red region, three representative sets of chemical potentials, as marked as points A, B, and C, correspond to the Sn-rich/I-poor, moderate, and Sn-poor/I-rich growth conditions, respectively. Since there have been few reports on $FASnI_3$ grown under the Sn-poor growth conditions, we will focus on the moderate and Sn-rich growth conditions, which stand for the pristine $FASnI_3$ film and that with excess Sn treatment in experiment, respectively.

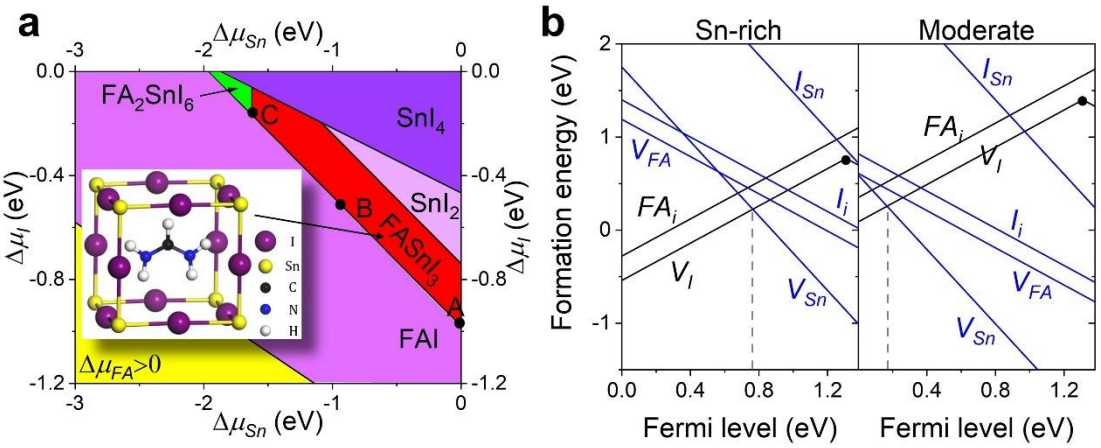

Figure 4.2. (**a**) Calculated stability phase diagram of $FASnI_3$ as a function of the chemical potentials of Sn (μ_{Sn}) and iodine (μ_I). The red region is the thermodynamically stable range for the equilibrium growth of $FASnI_3$. Points A, B, and C are three representative sets of chemical potentials. The inset shows the crystal structure of the $FASnI_3$ perovskite. (**b**) Formation energies of six dominant native defects (V_{Sn}, V_I, V_{FA}, FA_i, I_{Sn}, and I_i) in $FASnI_3$ as a function of the Fermi level under the Sn-rich and moderate conditions, corresponding to the chemical potentials of points A and B in (**a**), respectively. Black and blue lines represent the donor and acceptor defects, respectively. The vertical dashed lines represent the location at which the Fermi level is pinned, based on the condition of charge neutrality between the lowest-energy defects.

Figure 4.2b shows the formation energies of six dominant native defects[173] under the moderate and Sn-rich growth conditions by using the HSE+SOC+TS scheme, and those under the Sn-poor conditions are shown in **Figure 4.3**[185] for comparison. They are three types of vacancies (V_{Sn}, V_I, V_{FA}), two interstitials (FA_i, I_i), and one antisite defect (I_{Sn}, namely Sn substituted by I), respectively. Our results are qualitatively similar to prior semi-local generalized gradient approximation studies[173] except that the transition energy level of I_{Sn} is located at 0.06 eV above the valence band maximum (VBM) in the current study. Consistent with the experimental reports[160], V_{Sn} emerges as the major defect in $FASnI_3$ with extremely low formation energy and serves as a robust shallow acceptor. Particularly, under the moderate conditions, the formation energy of V_{Sn} is much lower than that of the lowest-energy donor V_I, with the Fermi level (E_F) being pinned at VBM+ 0.18 eV, accounting for the high background-hole concentration (i.e. the self-*p*-doping effect) observed for the pristine film[158,168]. Under the Sn-rich conditions, $FASnI_3$ will be an intrinsic (low-conductivity) semiconductor as V_I can compensate for V_{Sn}, and the E_F is thus pinned at the middle of the bandgap (VBM+0.78 eV). In contrast to the deep-level property in $MAPbI_3$[64], I_i behaves as a shallow defect in $FASnI_3$, as reported in $MASnI_3$[186] due to the higher band edge energies of hybrid Sn perovskite compared with the Pb-based counterparts[186,187]. Other low-energy intrinsic defects do not create a transition energy level in the bandgap either. These dominant native defects thus are not responsible for the observed nonradiative recombination of the $FASnI_3$-based devices.

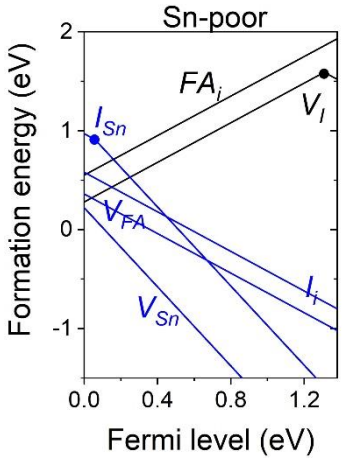

Figure 4.3. Formation energies of six dominant native defects (V_{Sn}, V_I, V_{FA}, FA_i, I_{Sn}, and I_i) in $FASnI_3$ as a function of the Fermi level under the Sn-poor conditions, corresponding to the chemical potentials of point C in **Figure 4.2a**.

4.3.2 Hydrogen and Related Impurities in $FASnI_3$

We then investigated an important, but hitherto overlooked type of defect, hydrogen. To analyze its stability in $FASnI_3$, we systematically studied various hydrogen-related defects and complexes, including isolated atomic and molecular H, and their interaction with different native defects. For hydrogen incorporated into the vacancies, they can form either substitutions or vacancy-hydrogen defect complexes, depending on the optimized atomic configurations (for example, $V_I - H$ complex of the off-center position in **Figure 4.4a**[185] and substitutional $(H_2)_I$ of the in-center position in **Figure 4.4b**[185]). The formation energies of various low-energy forms are presented in **Figure 4.5a**, and the other higher-energy complexes are shown in **Figure. 4.6**[185]. In $FASnI_3$, atomic hydrogen H_i tends to be ionized into the positively charged state, i.e., proton H_i^+, in the whole range of E_F. In contrast, the molecular form of hydrogen interstitial H_2 behaves as an electrically inactive defect, as reported in many traditional semiconductors[174]. Under the Sn-rich growth conditions, where the E_F is pinned at 0.78 eV above the VBM as mentioned above, the formation energy of H_2 are lower than that of H_i^+, and thus H_2 molecule is expected to be formed via the recombination of protons as reported in ZnO[188]. The calculated binding energy is: $H_i^+ + H_i^+ + 2e^- \xrightarrow{-0.96\ \text{eV}} H_2$, where e^- is the

electron with the energy of $E_F = 0.78$ eV. For comparison, under the Sn-moderate conditions, the material exhibits a strong *p*-type character with a high hole concentration, and H_i^+ has lower formation energy than H_2. That is, under such a hole-rich condition, H_2 tends to disassociate into H_i^+. The binding energy of the process is $H_2 - 2e^- \xrightarrow{-0.42\ \text{eV}} 2H_i^+$ with the energy of the electron e^- at $E_F = 0.18$ eV.

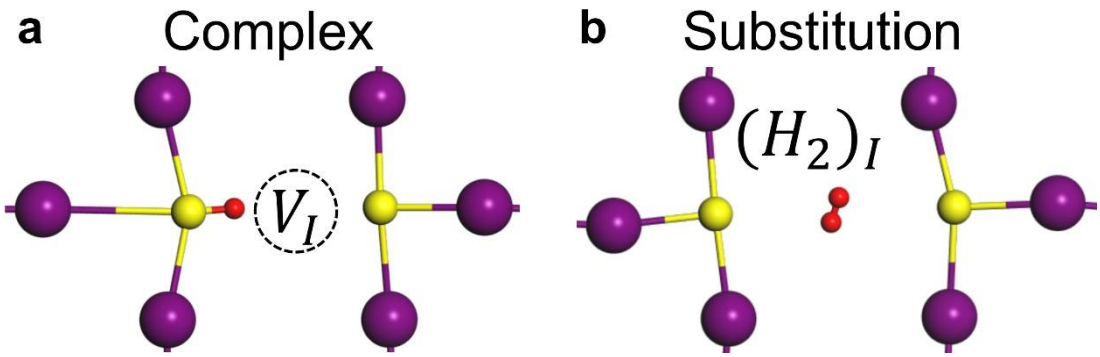

Figure 4.4. Local atomic structures of (a) the $(V_I - H)$ complex and (b) substitutional $(H_2)_I$, where H_i prefers to reside towards a nearby I atom of the V_I leading to a sizable deviation from the vacancy center, and $(H_2)_i$ is located at the center of V_I.

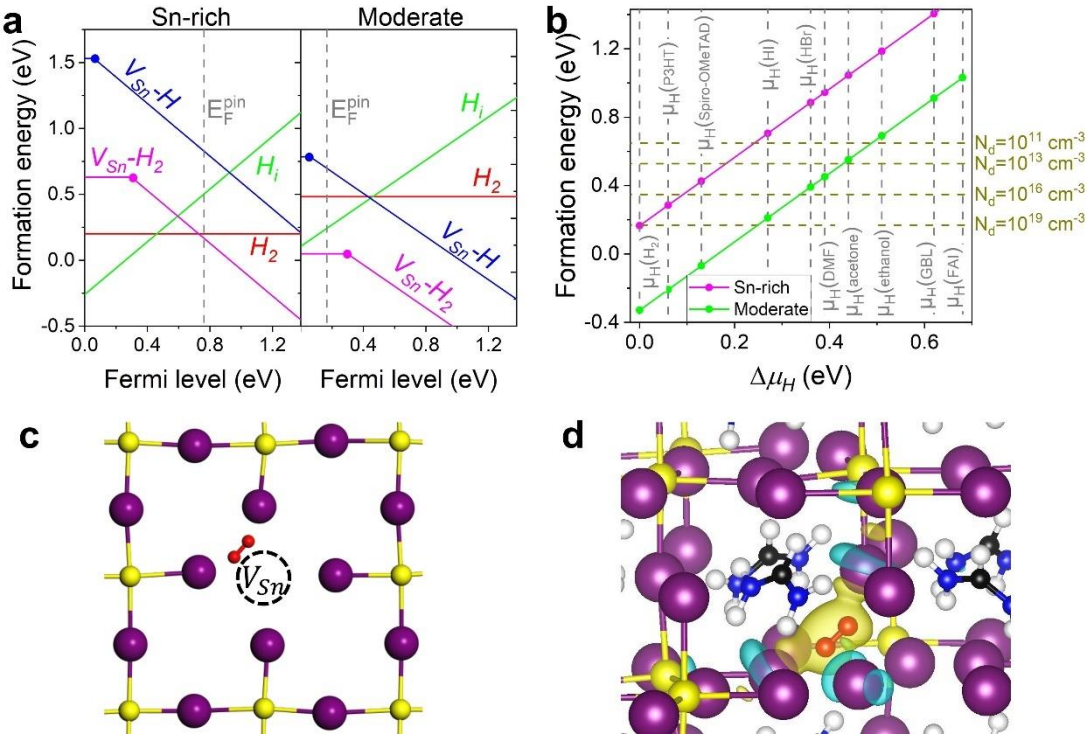

Figure 4.5. (**a**) Formation energies as a function of the Fermi level for hydrogen in the interstitial atomic hydrogen H_i, interstitial molecular hydrogen $(H_2)_i$, and Sn vacancy-hydrogen complexes $V_{Sn} - H$ and $V_{Sn} - H_2$, under the Sn-rich and Sn-moderate synthesis conditions in $FASnI_3$. The chemical potential of H is set at half of the total energy of an isolated H_2 molecule, namely the H-rich conditions, as a reference. The vertical dashed lines are the pinned Fermi levels by native low-energy defects as shown in **Figure 1b**. (**b**) Calculated formation energy of the deep-level $V_{Sn} - H_2$ complex as a function of the relative hydrogen chemical potential in various potential H sources, under the two representative Sn conditions. The corresponding defect densities (N_d) at room temperature are denoted. (**c**) Local atomic structures of the $(V_{Sn} - H_2)^0$ complexes in $FASnI_3$ perovskite lattice. (**d**) Calculated isosurfaces of the charge density differences for a $(V_{Sn} - H_2)^0$ complex, where electrons are relocated from the yellow to the blue regions. The isosurfaces are taken at 0.01 $|e|/Å^3$. The notations of atoms are as those in **Figure 1** and the hydrogen interstitials are highlighted in red.

Further, we found another dominant form of hydrogen: these isolated hydrogen interstitials can interact strongly with the abundant native Sn vacancies, resulting in defect complexes made of the hydrogen species trapped into V_{Sn}, namely, $V_{Sn} - H$ and $V_{Sn} - H_2$, as shown in **Figure 4.5a**. In the case of hydrogen interacting with other native vacancies, V_I and V_{FA}, the related substitutions and complexes exhibit considerably higher formation energies (> 1.5 eV) regardless of the growth conditions, as shown in **Figure 4.4**[185]. They are thus expected to play an insignificant role in $FASnI_3$.

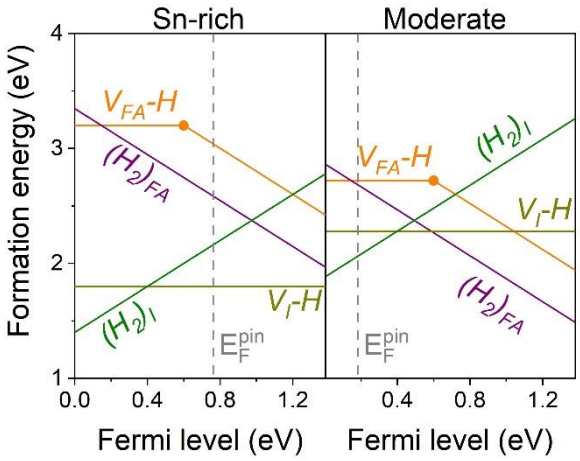

Figure 4.6. Formation energies of FA vacancy-hydrogen and I vacancy-hydrogen related defects under the Sn-rich and Sn-moderate growth conditions as a function of the Fermi level. The H-rich conditions are adopted as a reference.

The negatively charged state (-1) of $V_{Sn} - H$ complex is a shallow acceptor with a transition level $\varepsilon(0/-1)$ at VBM+0.06 eV. Significantly, regardless of the growth conditions, the $V_{Sn} - H_2$ complex is energetically more favorable compared with $V_{Sn} - H$ and gives rise to a deep charge-state transition level in the bandgap located at VBM+0.30 eV, which is similar to the experimentally measured energetic depth (~0.25 eV) of the trap states by the thermally stimulated current (TSC) studies[166]. In particular, under the moderate growth conditions, the formation energy of $V_{Sn} - H_2$ is ~ 0.76 eV lower than that of $V_{Sn} - H$, suggesting that $(V_{Sn} - H)^-$ tends to capture an additional H_i^+ to form $V_{Sn} - H_2$. Indeed, the calculated binding energy of $(V_{Sn} - H_2)^0$ with respect to $(V_{Sn} - H)^-$ and H_i^+, is 1.36 eV. $V_{Sn} - H$ serves as a metastable species. Under Sn-rich growth conditions, favoring H_2 as the dominant hydrogen interstitial, $V_{Sn} - H_2$ is expected to be formed via the direct trapping of H_2 into V_{Sn} and the related binding energy is $V_{Sn}^{2-} + H_2 - e^- \xrightarrow{-0.45\ \text{eV}} (V_{Sn} - H_2)^-$. Furthermore, we investigated the possibility of additional atomic or molecular hydrogen incorporation into a $V_{Sn} - H_2$ and confirmed their formation is energetically unfavored in $FASnI_3$ (see **Table 4.1**). Therefore, in

equilibrium, the $V_{Sn} - H_2$ complexes are the dominant forms of hydrogen in $FASnI_3$ in addition to the traditionally believed isolated hydrogen interstitials of H_i and H_2.

Table 4.1. Change of the total energy ΔE (eV) for trapping the additional hydrogen species (H_i and H_2) by the defect ($V_{Sn} - H_2$) complexes from the interstitial sites that are far from the complex center. $\Delta E = E_{multiple-hydrogen\ complex} - E_{[(V_{Sn}-H_2)+H_i/(H_2)]}$

Complex	ΔE (eV)	
	additional H_i	additional H_2
$(V_{Sn} - H_2)^0$	1.18	1.43
$(V_{Sn} - H_2)^{-1}$	0.87	1.41

To reveal the practical H environment during the growth and post-processing of the perovskites, we computed the formation energies of $V_{Sn} - H_2$, as a function of the relative H chemical potentials in various potential hydrogen sources, under the two representative Sn growth conditions, as shown in **Figure 4.5b**. The defect densities at different formation energies were calculated based on the thermal equilibrium equation. In addition to H_2 gas doping, the dehydrogenation of the organic hole-transporting materials (such as spiro-OMeTAD and P3HT), the widely used solvents (such as DMF, acetone, ethanol), and even the additives of HI and HBr, can serve as the potential source of unintentional H contamination. Note that, under the same H conditions, the density of deep-level $V_{Sn} - H_2$ under the Sn-rich growth conditions is lower than that under the moderate conditions, which is consistent with the general experimental observation of reduced deep-state density and nonradiative recombination rate in the $FASnI_3$ layers after excess Sn treatment[166,168]. Moreover, regardless of the Sn growth conditions, the density of $V_{Sn} - H_2$ can be up to $> 10^{19}\text{cm}^{-3}$ even under the H-rich conditions at room temperature.

4.3.3 Hydrogen-Vacancy Complex-Induced Nonradiative Energy Loss in Sn-based $FASnI_3$ Perovskite

Notably, neither native V_{Sn} nor H_2 are deep-level defects in $FASnI_3$, while their combined defect complexes exhibit deep-level characteristics. In V_{Sn}, the incorporated molecular H_2 resides between two I atoms with longer molecular bond lengths of 0.98 Å for $(V_{Sn} - H_2)^0$ and 0.91 Å for $(V_{Sn} - H_2)^-$, respectively, as compared to 0.77 Å for the interstitial sites and 0.75 Å for the free H_2, respectively, resulting in a structural distortion of the lattice (**Figure 4.5c**). This indicates the strong chemical interactions between each H and its nearby I atoms. We further studied the charge density difference during the formation of $V_{Sn} - H_2$ in $FASnI_3$. The charge originally located on the hydrogen species is redistributed to the nearest I atoms of the V_{Sn} (**Figure 4.5d**), confirming the strong chemical interactions between the trapped H_2 and V_{Sn} - giving rise to a deep transition level in the bandgap.

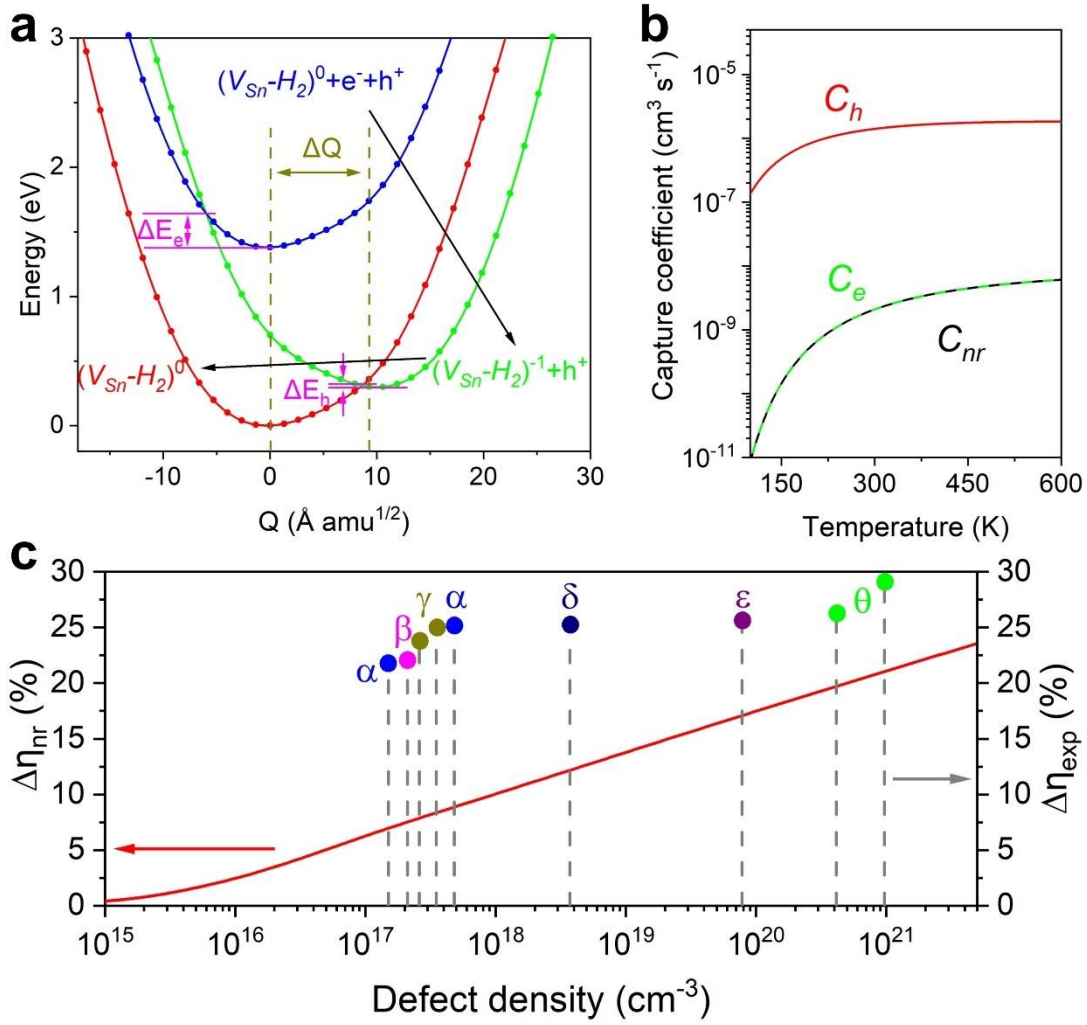

Figure 4.7. (**a**) Configuration coordinate diagrams for the $(0/-)$ charge-state transition of the $V_{Sn} - H_2$ complex. The generalized coordinate (Q) of each configuration is defined by its difference from the reference[142]: $Q = \sqrt{\sum_a m_a (R_a - R_{f,a})^2}$, where m_a and R_a are the mass and the Cartesian coordinate of atom a; subscript f stands for the final state of the charge transition. (**b**) Nonradiative capture coefficient of the $V_{Sn} - H_2$ complex as a function of temperature in $FASnI_3$. (**c**) The calculated and experimental PCE losses: the left-Y axis stands for the calculated nonradiative-induced PCE loss ($\Delta\eta_{nr}$) by the $V_{Sn} - H_2$ complexes as a function of the complex density at room temperature. The right-Y axis stands for the experimentally practical solar cell PCE losses relative to the S-Q efficiency limit of $FASnI_3$ (i.e., $\Delta\eta_{exp}$= 33.09% – the reported PCE values). The measured deep-level trap densities and PCE values of α are taken from Ref.[164], β from Ref.[189], γ from Ref.[190], δ from Ref.[167], ε from Ref.[191], and θ from Ref.[166].

To quantitatively and explicitly assess the effects of deep-level $V_{Sn} - H_2$ complexes on the nonradiative electron-hole recombination, we further calculated its carrier capture coefficient by following the established multi-phonon emission methodology[142,143]. We first performed the

semi-classical analysis and studied the configuration coordinate diagram (CCD) for the charged-state transition, which maps the potential energy surface (PES) of $(V_{Sn} - H_2)^0$ and $(V_{Sn} - H_2)^-$ as a function of a generalized coordinate (Q), as shown in **Figure 4.7a**. The CCD study not only provides a convenient illustration of a complete cycle of nonradiative capture but also derives important input parameters for further nonradiative coefficient calculations[143]. As shown in **Figure 4.7a**, starting from the neutral-state $(V_{Sn} - H_2)^0$ with a free electron (e^-) at the CBM and a hole (h^+) at the VBM (depicted by the blue curve), $(V_{Sn} - H_2)^0$ captures an electron and transits to negative-charged $(V_{Sn} - H_2)^-$ complex (depicted by the green curve). Subsequently, the negative-charged $(\mathrm{V_{Sn}} - \mathrm{H_2})^-$ captures a hole and relaxes back to neutral $(V_{Sn} - H_2)^0$ (depicted by the red curve). Semi-classically, these processes are required to overcome kinetic barriers, that is, the energy required to cross the intersection of the PES between the initial and final charge states in the configuration coordinate diagram, which thus determines the capture rates. Our calculations show that electron capture by $(V_{Sn} - H_2)^0$ is required to overcome an energy barrier (ΔE_e) of $\sim$0.26 eV. In comparison, the PES intersection of the hole capture process goes through the minimum of the PES of the initial state (the bottom of the green curve). Correspondingly, the hole capture barrier (ΔE_h) for $(V_{Sn} - H_2)^-$ is very small ($\sim$0.06 eV), indicative of a significantly faster hole capture process.

We then calculated the nonradiative capture coefficient according to the strength of the electron−phonon coupling and the vibronic overlap between potential energy surfaces[142]. **Figure 4.7b** shows the calculated electron capture coefficient ($\mathrm{C_e}$), hole capture coefficient ($\mathrm{C_h}$), and the nonradiative recombination coefficient ($\mathrm{C_{nr}}$) as the function of temperature. As expected, $(V_{Sn} - H_2)^0$ exhibits slower electron capture due to the relatively small capture coefficient, $C_e = 2.1 \times 10^{-9}$ cm^3 s^{-1} at room temperature; hole capture by $(V_{Sn} - H_2)^-$ is much faster with a coefficient ($\mathrm{C_h}$) of 1.4×10^{-6} cm^3 s^{-1} at room temperature. Based on the balance between electron and hole captures under steady-state conditions, the nonradiative

coefficient is $C_{nr} = \frac{C_e C_h}{C_e + C_h}$. At room temperature, the C_{nr} value of the deep-level $V_{Sn} - H_2$ complex is 2.1×10^{-9} cm^3 s^{-1}, compared with that of I_i in $MAPbI_3$ (7×10^{-9} cm^3 s^{-1})[64], which has been shown to be a dominant nonradiative recombination center to affect the $MAPbI_3$-based device performance. The nonradiative recombination rate constant A hence can be determined by both the defect density (N) and the capture coefficient per defect (C_{Tot}), yielding: $A = N \times C_{Tot}$, which stands for the number of nonradiative recombination events unit time, namely, the reciprocal of nonradiative lifetime τ_{nr}.

4.3.4 Implication for Device Performance

To further understand the impact of the nonradiative recombination on the device performance, we calculated the resultant PCE loss ($\Delta\eta_{nr}$) based on the detailed balance limit, which is commonly known as the S-Q limit[125]. For an ideal solar cell under steady-state conditions, the photocurrent can be expressed as $J(V) = J_P - J_{rad}(V)$, where $J_P \cong q\int_{E_g}^{\infty} \frac{2\pi}{h^3c^2} \frac{E^2}{e^{\left(\frac{E}{KT_{sun}}\right)} - 1} dE$ is the current density that is generated by the incident light, and $J_{rad}(V) \cong q\int_{E_g}^{\infty} \frac{2\pi}{h^3c^2} \frac{E^2}{e^{\left(\frac{E-qV}{KT_{cell}}\right)} - 1} dE$ is the radiative recombination current density. V stands for the applied voltage and is equal to the splitting of the Fermi levels $qV = E_F^n - E_F^p$. q, h, K, and c are the elementary charge, Planck's constant, Boltzmann constant, and speed of light, respectively. The electrical output power density of the solar cell is given by $P_{out}(V) = J(V) \times V$, and hence, the light to electricity PCE in the case of the radiative limit can be calculated by $\eta = \frac{MAX(P_{out}(V))}{P_{in}} = \frac{MAX(J(V) \times V)}{P_{in}}$, where the input sun power density can be given by $P_{in} \cong \frac{2\pi}{h^3c^2}\int_0^{\infty} \frac{E^3 dE}{e^{\left(\frac{E}{KT_{sun}}\right)} - 1}$. For $FASnI_3$ with a bandgap of $E_g = 1.38$ eV, under the standard air mass

1.5G spectrum, the PCE of the solar cell can reach a maximum value (S-Q efficiency limit) of $\eta \sim 33.09\%$ at room temperature, which agrees with that reported in Ref.[192].

In the presence of the nonradiative recombination from the $V_{Sn} - H_2$ complexes, the steady-state $J(V)$ characteristic of the solar cell will be described by: $J(V') = J_P - J_{rad}(V') - J_{nr}(V')$, where the new term of $J_{nr}(V') \cong qdAn_i e^{\left(\frac{qV'}{2KT_{cell}}\right)}$ describes the current density loss due to the nonradiative recombination. For the thickness (d) and intrinsic carrier density (n_i) of the perovskite active layer, we adopted the representative values of $d \sim 300$ nm and $n_i \sim 10^7 \text{cm}^{-3}$[168], respectively. Notably, the Auger recombination can have a negligible impact on the perovskite solar cells due to a relatively low carrier density[155], and thus the nonradiative loss is dominated by the defect-induced process with the nonradiative recombination rate constant being the aforementioned $A = NC_{Tot}$. Similarly, with the electrical output power density of the solar cell of $P_{out}(V') = J(V') \times V'$, the nonradiative-induced PCE loss by the $V_{Sn} - H_2$ complexes can be obtained with $\Delta\eta_{nr} = \eta - \eta' = \frac{MAX(P_{out}(V)) - MAX(P_{out}(V'))}{P_{in}}$.

Figure 4.7c shows the calculated $\Delta\eta_{nr}$ due to the $V_{Sn} - H_2$ complexes as a function of the defect density at room temperature. As expected, a higher $V_{Sn} - H_2$ density causes higher PCE loss $\Delta\eta_{nr}$, for a certain thickness of $FASnI_3$ (300 nm used in the current calculation). Our calculated nonradiative efficiency loss induced by $V_{Sn} - H_2$ complexes can be up to ~11% at room temperature at the representative defect density of $\sim 10^{18}$ cm^{-3}. Such a density is possible as mentioned above. A higher defect density can even result in a larger PCE loss especially for the pristine $FASnI_3$ layers mostly under the moderate growth conditions (with negative formation energies of $V_{Sn} - H_2$ occurring under the H-rich conditions as shown in **Figure 4.5b**). To reduce the PCE loss to a negligible level, we need to suppress the deep-level defects to $\sim 10^{15}$ cm^{-3}, under which the resultant $\Delta\eta_{nr}$ would be less than 1%.

To correlate our calculated results with experiments, we collected representative experimental PCE and trap density values from literature[166,167,189,189,191], and calculated PCE losses by comparing experimental PCE values with the S-Q limit ($\Delta\eta_{exp}$= 33.09% – the reported PCE values), and plotted them as dots in **Figure 4.7c**. The experimentally observed deep-level defect densities in the $FASnI_3$ active layers vary from 10^{17} cm^{-3} to 10^{21} cm^{-3}, and significantly, these devices have low PCE with $\Delta\eta_{exp} > 20\%$. The discrepancy between $\Delta\eta_{nr}$ and $\Delta\eta_{exp}$ originates from their different scopes: the former is the PCE loss solely induced by nonradiative recombination via $V_{Sn} - H_2$, while the latter is the PCE loss due to all the sources including the bulk, surface, and grain boundary recombination[140,193], and other types of energy losses (e.g., the device polarization due to ionic accumulation[140], and the energy level mismatch[194]). In particular, surface and grain boundaries are often significant as they provide the avenue for the segregation of some defects, which may behave differently compared to those in the bulk[140,193,195]. Although there could be other detrimental recombination centers in $FASnI_3$, $V_{Sn} - H_2$ with its induced energy loss offers an explanation for the experimental observation of Sn-conditions dependence of the recombination rate. Furthermore, it was noticeable that the trends of the PCE enhancement via defect passivation reported in Ref.[164] (denoted as α in the figure) and Ref.[166] (denoted as θ in the figure) are in agreement with the trend of the $\Delta\eta_{nr}$ reduction predicted in **Figure 4.7c**. These results indicate that $V_{Sn} - H_2$ complex stands out as a significant nonradiative recombination center in $FASnI_3$-based perovskite solar cells.

The above-analyzed findings offer valuable information for improving the performance of $FASnI_3$-based solar cells and other related optoelectronic devices. That is, it would be significant to mitigate the nonradiative recombination rate by reducing the density of $V_{Sn} - H_2$. The formation of such a defect is sensitive to the quantity of Sn and H during the growth and post-processing. This explains the experimental observation of different nonradiative

recombination rates (the range of $10^7 \sim 10^9$ s^{-1}) for the $FASnI_3$ active layers even that were synthesized with the same SnI_2/FAI ratio in the precursors[123,164,168,189]. Therefore, to effectively suppress the nonradiative recombination induced by $V_{Sn} - H_2$, in addition to the commonly used Sn-rich strategy, minimizing unintentional H contamination would be also a critical step, such as building an effective H-blocking layer between the organic transporting materials and the perovskite active layers as well as avoiding the H-rich solvents and additives.

4.4 Conclusion

In summary, our first-principles calculations unveil a significant nonradiative recombination center in $FASnI_3$ and the related solar cells. The general and abundant native Sn vacancies can effectively trap hydrogen and form $V_{Sn} - H_2$ complexes. The resultant $V_{Sn} - H_2$ complexes behave as effective nonradiative recombination centers in $FASnI_3$ and induce significant energy loss. Therefore, the combined Sn-rich and H-poor growth conditions are proposed to be critical for further enhancing the related-device performance. This work identifies an important microscopic origin of the nonradiative recombination losses in the Sn-based halide perovskite materials and provides valuable information for future developments of the nontoxic Sn-based perovskite solar cells and other broad device applications.

Chapter 5 Origin of Enhanced Nonradiative Carrier Recombination Induced by Oxygen in Hybrid Sn Perovskite

5.1 Introduction

Hybrid perovskites have recently attracted intense interest in optoelectronics due to their outstanding photophysical properties and low processing cost. The power conversion efficiencies (PCE) of perovskite solar cells have skyrocketed up to over 25% within a decade[1,3,115], surpassing that of the present photovoltaic market leader polycrystalline silicon. However, there are still challenges facing the successful commercialization of perovskite solar cells.

One critical negative aspect is the high vulnerability to the ambient air, particularly for Sn-based halide perovskites, which alleviate the health and environmental hazards raised by the Pb-based counterparts and deliver superior semiconductor properties such as the nearly-ideal bandgaps and higher absorption coefficients[158]. The performance of solar cells without encapsulation deteriorates rapidly in the air with the carrier lifetime being significantly reduced to that far below practical requirements[196]. Experimental reports indicate that atmospheric oxygen plays an important role in degrading the Sn-based perovskite active layers and substantially enhances the nonradiative charge recombination[197–200], which is the main cause of energy loss in perovskite photovoltaics[35,155]. Therefore, numerous efforts have been devoted to preventing oxygen diffusion into the Sn-based perovskite devices, such as via encapsulation[201], the introduction of the larger organic cations[202], and antioxidant additives[196]. However, these approaches fall short of fully addressing the issue due to uncontrollable oxygen leakage during fabrication and operation[199]. Indeed, Sn-based perovskite devices are typically required to be processed under extremely low oxygen concentration conditions (less than 0.1 ppm)[203], which significantly restricts scalable and industrial production. To date, the atomic-

scale mechanism underlying oxygen (air) exposure accelerating nonradiative carrier recombination in Sn-based perovskites remains poorly understood, and a full elucidation is key to developing accurate remedial strategies as well as the further design of efficient Sn-based perovskite solar cells and other broad device applications under ambient air operation.

In this study, by performing accurate first-principles hybrid density functional calculations, we report that in the prototypical Sn-based perovskite $MASnI_3$ ($MA=CH_3NH_3$), though oxygen can be readily incorporated into the lattice, it cannot cause nonradiative recombination by itself. Instead, oxygen atoms tend to be trapped into the native I vacancies (V_I) and form substitutional O_I as the dominant defect species. V_I acts as a dominant nonradiative recombination center, of which the capture of electrons is the rate-limiting step in $MASnI_3$. Our results show that the formation of O_I significantly accelerates the electron capture process and thus increases the overall nonradiative recombination rate further by two to three orders of magnitude. These results rationalize the observed sharp decline of carrier lifetime in perovskite active layers exposed to oxygen (air). In addition, contrary to the conventional notion that the carrier capture rate often declines exponentially with the transition energy, the results show that the formation of O_I actually leads to enhanced electron transition energy. Notably, the formation of O_I strengthens the lattice and reduces the structural relaxation upon electron capture, which plays an important role in decreasing the electron capture barrier, responsible for a substantially enhanced nonradiative recombination rate.

5.2 Simulation Method

5.2.1 Computational Method

The first-principles calculations in this work are performed based on density functional theory as implemented in the Vienna *ab initio* simulation package (VASP)[114]. The Heyd-Scuseria-Ernzerhof (HSE06) hybrid functional[113] including spin-orbit coupling (SOC) was employed

with a kinetic energy cutoff of 400 eV. The Tkatchenko-Scheffler (TS) scheme[137] was adopted to describe the Van der Waals interactions and all the structures were fully relaxed until the forces on atoms are less than 0.01 eV/Å. The HSE mixing parameter was set to 0.43, yielding a bandgap of 1.19 eV for α-$MASnI_3$, consistent with the experiment of 1.20 eV[204]. The cell parameter is fixed to the experimental value of 6.23 Å[204]. For the defect calculations, a Monkhorst–Pack sampling of $2 \times 2 \times 2$ k-points was employed for the $2 \times 2 \times 2$ supercells with 96 atoms. The convergence test was further performed using a larger $3 \times 3 \times 2$ 216-atom supercell of $MASnI_3$. For the relevant V_I^- and O_I^- defects, the calculated formation energy differences between the 96-atom and 216-atom supercells are less than 0.08 eV.

5.2.2 Oxygen Impurity Formation Energy

The formation energy of a defect (D) with charge state (q) is calculated by the equation below[140]:

$$\Delta H^f(D_i^q) = E(D_i^q) - E(host) - \sum n_i(\mu_i + \Delta\mu_i) + q(E_F + E(VBM) + \Delta V) + \Delta_{corr}^q \quad (5.1)$$

where $E(D_i^q)$ and $E(host)$ are ground-state total energies of the supercells with and without defects, respectively. n_i stands for the number of atoms added (removed) into the supercell to generate the defect. μ_i and $\Delta\mu_i$ are absolute and relative values of the chemical potential. The host chemical potentials were chosen according to the typical moderate growth condition, as shown in **Figure 5.1**. For the chemical potential of oxygen, we used half of the total energy of an isolated O_2, as a reference. We also considered that in other relevant oxygen compounds, namely SnO_2, SnO, ZnO, TiO_2, as well as CO, and CO_2. E_f is the Fermi energy measured from the valance band maximum of the pristine system $E(VBM)$. The correction term ΔV is used for ensuring the alignment of the potential for the charged defect in supercells and Δ_{corr}^q stands for the finite-size correction term for the periodic images of the charged defects[184].

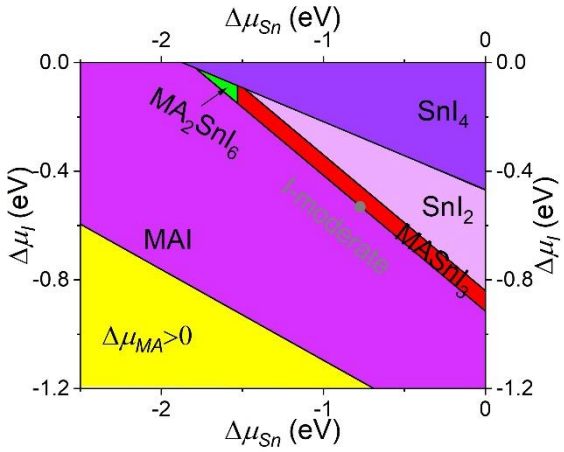

Figure 5.1. For the relative chemical potentials $\Delta\mu_i$ of host atoms (MA, Sn, I) in $MASnI_3$, they should be satisfied:

$$\Delta\mu_{MA} + \Delta\mu_{Sn} + 3\Delta\mu_I = \Delta H_f(MASnI_3)$$

To avoid the formation of the possible competing secondary compounds, including MAI, SnI_2, and SnI_4, and the pure elemental phases, there should be:

$$\Delta\mu_{MA} + \Delta\mu_I < \Delta H_f(MAI)$$
$$\Delta\mu_{Sn} + 2\Delta\mu_I < \Delta H_f(SnI_2)$$
$$\Delta\mu_{Sn} + 4\Delta\mu_I < \Delta H_f(SnI_4)$$
$$\Delta\mu_{FA} < 0;\ \Delta\mu_{Sn} < 0;\ \Delta\mu_{Br} < 0$$

where the $MASnI_3$ will be thermodynamically stable instead of its secondary phases or element phases of components. With all these conditions, the relative chemical potentials $\Delta\mu_i$ are restricted in red area. In this study, we chose the typical I-moderate growth conditions for further evaluating the native defect formation energies.

5.2.3 Impurity Density

With the formation energy of ΔH^f, the defect density at thermal equilibrium can be calculated by[140]: $N = N_0 e^{-\frac{\Delta H^f}{KT}}$, where N_0 stands for the number of available sites for defect formation per volume, and K the Boltzmann constant. Temperature (T) was set to room temperature.

With the defect density N, the nonradiative recombination rate constant A, namely the Shockley-Read-Hall (SRH) rate constant can thus be determined through $A = N \times C_{nr}$[147], where C_{nr} stands for the nonradiative capture coefficient of the related defects.

5.2.4 Transition Energy Level

The transition level is defined as the Fermi-level position for which the formation energies of different defect charge states are equal and thus is given by[140]:

$$\mathcal{E}(q/q') = \left[\Delta H^f\left(\mathrm{D_i^q}, E_F = 0\right) - \Delta H^f\left(\mathrm{D_i^{q'}}, E_F = 0\right)\right]/(q' - q) \quad (5.2)$$

5.2.5 Binding Energy

The binding energy of the oxygen interstitial with the three types of native vacancies (x=I, Sn, and MA) is calculated by: $\Delta \mathrm{E} = \mathrm{E_{tot}}(\mathrm{O_x}) - \mathrm{E_{tot}}(\mathrm{V_x} + \mathrm{O_i})$, where $\mathrm{E_{tot}}(\mathrm{O_x})$ and $\mathrm{E_{tot}}(\mathrm{V_x} + \mathrm{O_i})$ stands for the ground-state total energies of the systems with $\mathrm{O_i}$ residing in, and far away, from the native vacancies, respectively.

5.2.6 Diffusion Barrier Calculation

The defect diffusion barriers were calculated by the nudged elastic band method in conjunction with the climbing image method (CI-NEB)[205], as implemented using the VASP Transition State Tool (VTST) that enables the determination of the minimum energy path between two energetically stable endpoints. These calculations were performed by using the Perdew-Burke-Ernzerhof (PBE) functional[110] and a $3 \times 3 \times 3$ 324-atom supercell of $MASnI_3$.

5.2.7 Nonradiative Capture Coefficient

The nonradiative carrier capture coefficients were calculated using the established multiphonon emission methodology in conjunction with an extension to include the effect of lattice anharmonicity by solving the one-dimensional Schrodinger equation for the anharmonic potential energy surfaces[142,143]. The potential energy surfaces along the configuration coordinate are obtained by interpolating the energies from first-principles calculations. The electron−phonon coupling matrix elements for electron and hole capture are evaluated within the linear-coupling approximation based on the PAW results by VASP processed with the NONRAD package[142,143]. The current study is focused on the defect-induced recombination processes. We note that the nonperturbative carrier recombination dynamics (e.g., phonon-

assisted nonradiative recombination across the pristine CBM−VBM energy gap) may also play an important role in halide perovskites[206,207].

5.3 Results and Discussions

5.3.1 Atomic and Molecular Oxygen Interstitials in Sn-based Perovskite

To evaluate the impact of oxygen (O) on nonradiative recombination in Sn-based perovskites, we first analyzed the thermodynamic stability of O within the lattice of the prototypical hybrid Sn perovskite $MASnI_3$ (MA= CH_3NH_3). **Figure 5.2a** shows the calculated formation energies of atomic oxygen (O_i) and molecular oxygen (O_2) in the interstice of $MASnI_3$, as a function of the Fermi level within the bandgap. Both O_i and O_2 exhibit relatively low formation energies, especially for the negative values of the Fermi level in the proximity of the conduction band minimum (CBM). This indicates that oxygen impurities can be present in bulk $MASnI_3$ with a high density, once exposed to ambient air.

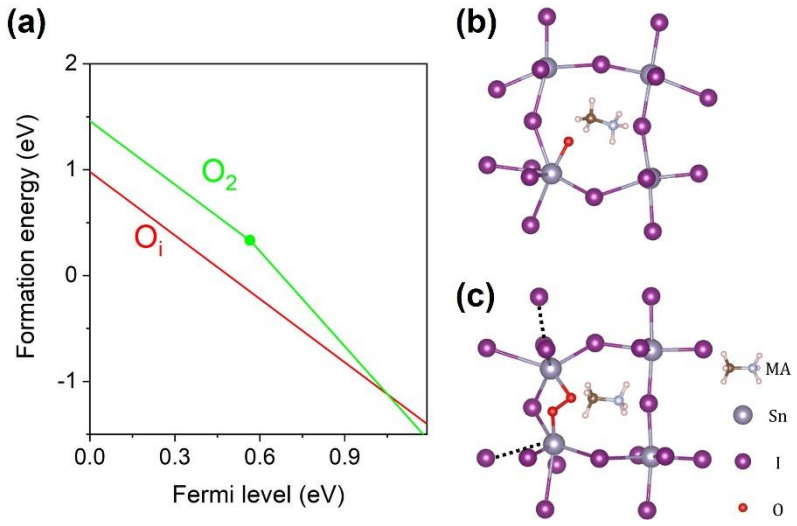

Figure 5.2. (a) Formation energies of interstitial atomic and molecular oxygen in $MASnI_3$ as a function of the Fermi level, in which the chemical potential of oxygen refers to half of the total energy of an isolated O_2. The local atomic structures of (b) O_i^{2-} and (c) O_2^{2-} in $MASnI_3$.

In $MASnI_3$, O_i tends to capture extra electrons as expected for a completely full *p* orbital leading to the formation of the negatively charged O_i^{2-} located next to the host Sn cation, as shown in **Figure 5.2b**. The O-bonded Sn is displaced toward the oxygen atom from the original position, and the nearby I atoms are repelled outward, resulting in local structural distortion, which can be attributed to the high ionic and soft lattice characteristics of halide perovskite materials. For O_2, as shown in **Figure 5.2c**, each oxygen atom of the molecule tends to bind with the neighboring Sn cations leading to the puckered Sn-I-Sn framework, which implies that both oxygen atoms in O_2 are slightly negatively charged. Indeed, O_2 in the bulk of $MASnI_3$ has a longer molecular bond length of 1.60 Å, compared with 1.21 Å for free O_2, making it more like an oxygen dimer. According to the Shockley−Read−Hall theory of recombination[208], the presence of a deep trap state (charge-state transition level) in the bandgap is a prerequisite for defects that serve as nonradiative recombination centers. Previous nonadiabatic molecular dynamics simulations show that O_2 can serve as a recombination center in $MAPbI_3$[206]. In $MASnI_3$, O_2 induces a deep transition level of $\varepsilon(-2/-3)$ ~0.57 eV above the valance band maximum (VBM), whereas its formation energy is higher than that of O_i over the wide range of the Fermi level within the bandgap. This, therefore, suggests that O_2 can be unstable within the lattice of $MASnI_3$ and tends to disassociate into the isolated O_i under equilibrium conditions (also see the positive binding energies of O_2 with respect to two isolated O_i in **Table 5.1**). On the other hand, O_i is stable in -2 charged state throughout the Fermi level with the transition level $\varepsilon(0/-2)$ being located at 0.21 eV below the VBM, namely a shallow acceptor, and thus cannot act as the charge carrier recombination center.

Table 5.1. Calculated binding energy of the oxygen interstitial O_i^{2-} with the three types of native vacancies.

Site	V_I^+	V_I^-	V_{Sn}^{2-}	V_{MA}^-

Binding energy (eV)	-1.06	0.72	0.95	0.24

5.3.2 Interaction of Oxygen and Intrinsic Defects in $MASnI_3$

It was experimentally reported that oxygen exposure leads to enhanced nonradiative charge carrier recombination in hybrid Sn perovskites[197–200], significantly reducing carrier lifetime and deteriorating the device performance. However, the present results indicate that oxygen interstitials are not responsible for the recombination center by themselves. To understand the role of oxygen incorporation in nonradiative recombination in Sn-based perovskites, we further considered the potential interactions of oxygen and native vacancies that usually exhibit low formation energies in halide perovskite materials[140] and could be the preferred lattice sites for incorporated oxygen. We thus calculated the binding energies of O_i^{2-} with three typical native vacancies, namely, V_I^+ (V_I^-), V_{Sn}^{2-}, and V_{MA}^-, respectively, as shown in **Table 5.2**. The results imply that, besides isolated O_i^{2-} ions, there exist other dominant forms of oxygen in $MASnI_3$: isolated oxygen interstitial O_i^{2-} can interact strongly with native V_I^+, resulting in the formation of a substitutional defect made of oxygen trapped into an I vacancy, namely, O_I^-. In addition, the NEB calculations show that the diffusion barriers of O_i^{2-} and V_I^+ in the lattice of $MASnI_3$ are 0.65 eV and 0.46 eV, respectively, indicating that these two types of charged defects are attractive to each other due to Coulombic interaction. Thus the combination of O_i^{2-} and V_I^+, i.e., the formation of O_I^-, are kinetically feasible. Moreover, placing a second O_i^{2-} into vacancy is energetically unfavorable with the calculated binding energy of 0.78 eV, which can be attributed to anionic Coulomb repulsion.

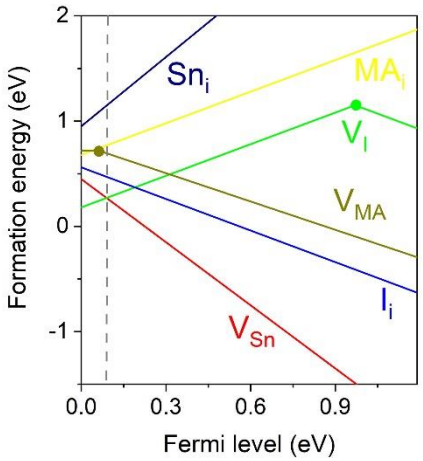

Figure 5.3. Calculated formation energies of six low-energy native defects in $MASnI_3$ under typical moderate growth conditions, as a function of the Fermi level. The vertical dashed line stands for the location at which the Fermi level is pinned, based on the condition of charge neutrality between the lowest-energy defects.

We have studied the formation energies of six common native defects in $MASnI_3$ (see **Figure 5.3**) and **Figure 5.4** shows the formation energies of the three energetically most favorable native defects as well as that of O_I as a function of the Fermi level in $MASnI_3$. These three lowest-energy native defects are the Sn vacancy (V_{Sn}), I vacancy (V_I) and I interstitial (I_i)[186,209]. V_{Sn} is the lowest-energy native defect in $MASnI_3$ and stands as a robust shallow acceptor. Previous static DFT calculations[64,127,132,149] and nonadiabatic molecular dynamics (NAMD) calculations[210,211] show that I_i is a highly efficient nonradiative recombination center in Pb-based perovskites even under thermal conditions; nevertheless, in the case of $MASnI_3$, I_i only exhibits the negatively charged state (-1), that is, a shallow acceptor. Notably for V_I, the neutral-state V_I^0 is energetically less favorable than either the positively charged V_I^+ and negatively charged V_I^- over the entire Fermi-level range, resulting in a deep transition energy level of $\varepsilon(+/-)$ being 0.22 eV below the CBM (the intersection of the formation energies of V_I^+ and V_I^-), which is characteristic of a so-called negative-U behavior. The results show that V_I and O_I are two deep-level defects in $MASnI_3$.

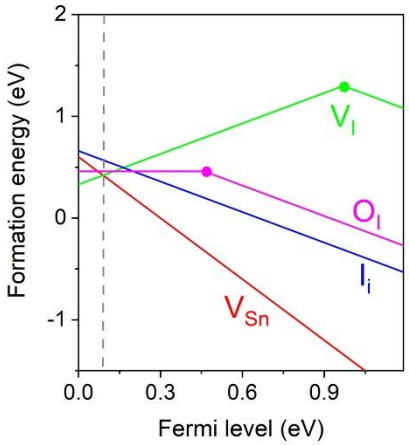

Figure 5.4. Calculated formation energies of three lowest-energy native defects (V_{Sn}, V_I, and I_i) and O_I of the dominant form of oxygen in $MASnI_3$ under typical moderate growth conditions. The chemical potential of oxygen in based on the half of the total energy of an isolated O_2. The vertical dashed line stands for the location at which the Fermi level is pinned, based on the condition of charge neutrality between the lowest-energy defects.

For the negative-U center V_I, $\varepsilon(+/-)$ is expected not to govern the nonradiative recombination process even though it is deep in the bandgap, since a defect does not capture simultaneously two electrons or holes. Effective carrier recombination typically involves single-charge-state transitions, namely, $\varepsilon(+/0)$ and $\varepsilon(0/-)$. As shown in **Figure 5.5a**, for V_I, $\varepsilon(+/0)$ is a shallow level located within the conduction band, and $\varepsilon(0/-)$ is a deep level being 0.71 eV above the VBM, hence is a relevant transition level for nonradiative recombination. Notably, after oxygen incorporation leading to the formation of O_I, it still possesses the deep-level characteristic and the $\varepsilon(0/-)$ level moves closer to the VBM (0.46 eV above the VBM). Furthermore, we calculated the formation energies of O_I using the oxygen chemical potential of other relevant oxygen compounds, as shown in **Figure 5.6**. These oxygen compounds are namely SnO, SnO_2, ZnO, and TiO_2, which are the commonly used electron transporting materials in perovskite solar cells[212], as well as CO and CO_2. The results indicate that in addition to oxygen gas, CO and CO_2 in the air can also be the potential oxygen sources leading to oxygen incorporation and the formation of the deep-level O_I in the $MASnI_3$ active layers.

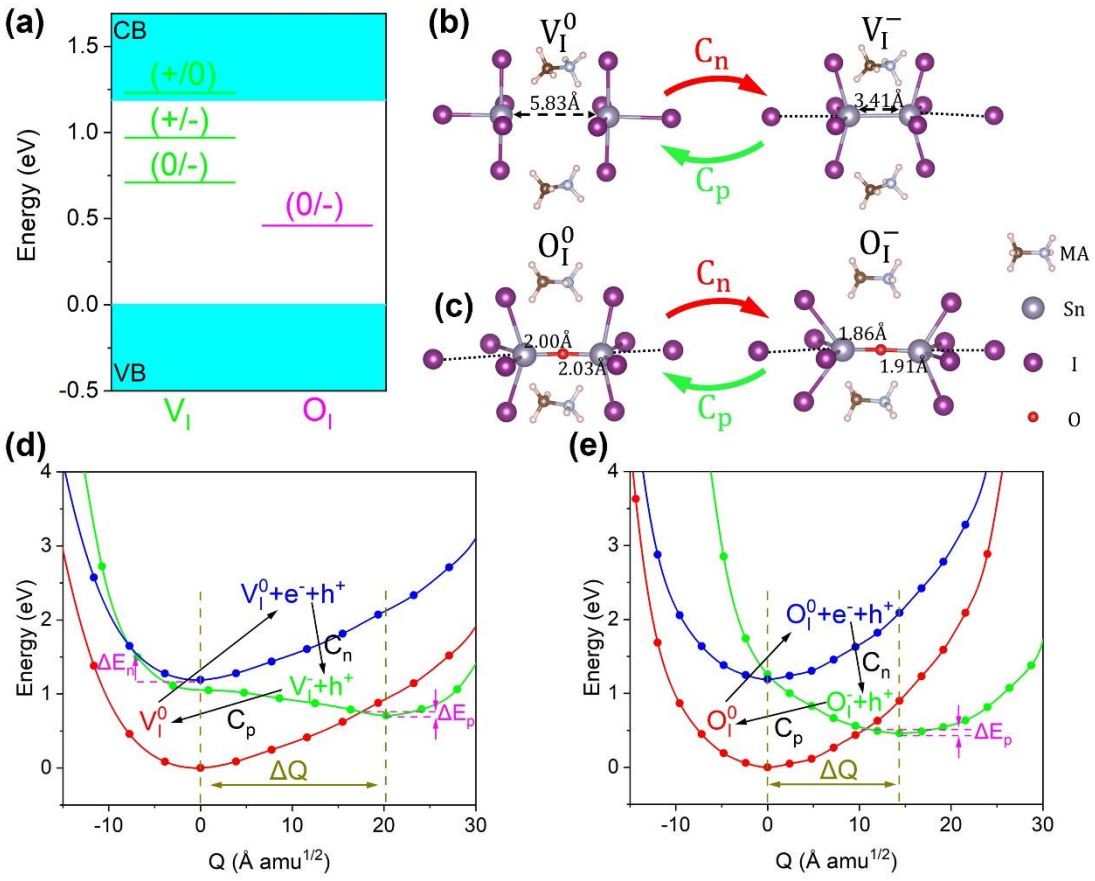

Figure 5.5. (a) Thermodynamic ionization levels of V_I and O_I in $MASnI_3$ calculated with the HSE-SOC-TS scheme. Local atomic structures of (b) V_I and (c) O_I in the two relevant charge states (0 and –), where the arrows and labels stand for the relevant carrier capture processes. Configuration coordinate diagrams for the charge-state transitions of (d) $V_I^0 \leftrightarrow V_I^-$ and (e) $O_I^0 \leftrightarrow O_I^-$ in $MASnI_3$ as a function of a generalized configuration coordinate (Q).

To explicitly assess the effect of deep-level V_I and O_I in nonradiative recombination, we studied the related carrier capture processes by following the established multiphonon emission methodology[142,143]. **Figures 5.5b and 5.5c** show the local atomic structures of V_I and O_I in the two related charged states, namely 0 and –, respectively. For the neutral V_I^0 (**Figure 5.5b**), the removal of the I atom results in a slight lattice contraction with the distance between two nearby Sn being 5.83 Å, compared with 6.22 Å for the perfect system. By capturing an electron (C_n), V_I^0 transforms into V_I^- with two nearby Sn moving closer to the vacancy site leading to the formation of an Sn dimer, which is known as a DX center, as reported in $MAPbI_3$[129,130]. Subsequently, the negatively charged V_I^- can capture a hole (C_p) and relax back to the neutral

V_I^0. Similarly, the transition of $O_I^0 \leftrightarrow O_I^-$ involves two carrier capture processes (electron capture C_n and hole capture C_p), as shown in **Figure 5.5c**. O occupies the center of I vacancy in both charge states and reduces the neighboring Sn-Sn distances, especially in the case of O_I^-.

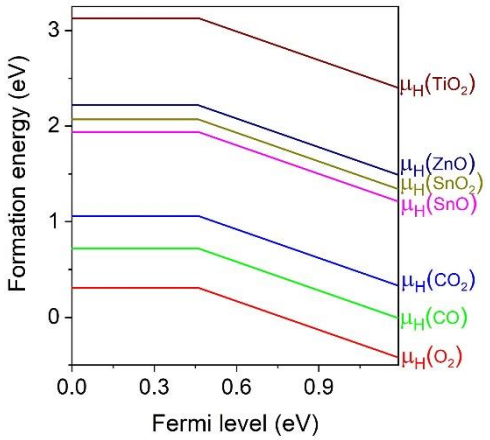

Figure 5.6. Formation energies of O_I using different chemical potentials of O in $MASnI_3$, as a function of the Fermi level.

5.3.3 Reduced Carrier Lifetime Induced by Oxygen Impurity and its Implication for Photovoltaic Applications

We further calculated the configuration coordinate diagrams (CCD) for the transitions of $V_I^0 \leftrightarrow V_I^-$ and $O_I^0 \leftrightarrow O_I^-$, as shown in **Figures 5.5d and 5.5e**, which not only provides an intuitive illustration of a complete cycle of nonradiative carrier capture, but also derives the important input parameters for further nonradiative coefficient calculations[143]. The CCD maps the potential energy surfaces (PESs) of the related charge-state transitions as a function of a generalized coordinate (Q), which reflects the geometric differences with respect to a reference configuration. Semiclassically, each carrier capture process requires overcoming kinetic barriers, which is the energy required to cross the intersection of the PESs between the initial and final charge states in the CCD and hence determines the capture rates.

As shown in **Figure 5.5d**, for a V_I^0 with an electron at the CBM and a hole at the VBM (blue line), the energy barrier for electron captured by V_I^0 (the intersection between the blue and green lines) is markedly larger ($\Delta E_n \sim 0.31$ eV) than that of the hole capture process by V_I^- (the intersection between the green line and red line, $\Delta E_h \sim 0.08$ eV), indicative of faster hole capture. On the other hand, the slower electron capture process can be the rate-limiting step in the overall nonradiative cycle. In the case of the carrier recombination process in O_I (**Figure 5.5e**), the hole capture process exhibits a similar kinetic barrier ($\Delta E_h \sim 0.05$ eV) as that for V_I, while the electron capture barrier is almost zero, since the PES of O_I^- (green line) almost goes through the minimum of the PES of O_I^0 (blue line).

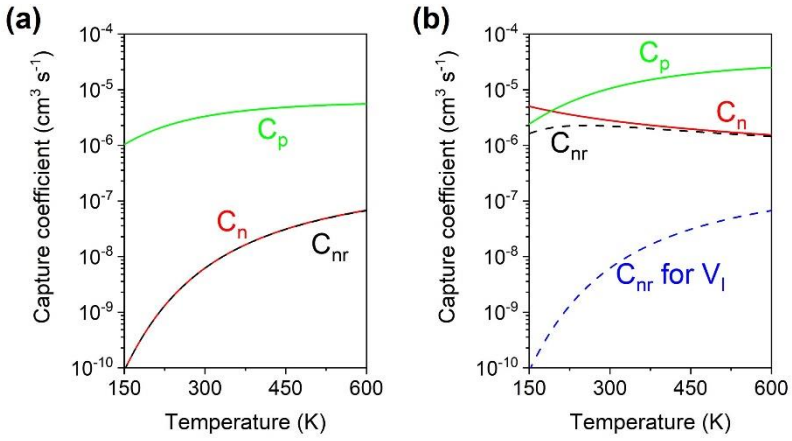

Figure 5.7. Nonradiative electron (red solid line) and hole (green solid line) capture, and recombination (black dashed line) coefficients of (a) V_I and (b) O_I in $MASnI_3$ as a function of temperature.

We then quantitively calculated the nonradiative carrier capture coefficients based on the strength of the electron-phonon coupling and the vibronic overlap between PESs. As shown in **Figure 5.7a**, consistent with the semiclassical CCD analysis, for V_I, the hole capture coefficient (C_p) is significantly higher than that for the electron (C_n) (around three orders of magnitude difference at room temperature). Additionally, the electron capture coefficient (C_n) exhibits a much faster enhancement trend with temperature (T) compared with C_p, which can be

attributed to the higher electron capture barrier. The carrier capture is a thermally activated process and therefore higher kinetic energy generally results in a stronger positive temperature dependence.

Based on the balance between electron and hole captures under steady-state conditions[147], the nonradiative carrier recombination coefficient C_{nr} can be given by $C_{nr} = \frac{C_n C_p}{C_n + C_p}$. At room temperature (i.e. 300 K), the nonradiative carrier recombination coefficient of V_I in $MASnI_3$ is 6.2×10^{-9} cm^3 s^{-1}, which is similar to that of I_i in $MAPbI_3$ ($C_{nr} \sim 7 \times 10^{-9}$ cm^3 s^{-1})[64] that has been demonstrated to be the dominant nonradiative recombination center impacting the $MAPbI_3$-based device performance. This indicates that V_I is likely the dominant native nonradiative recombination center in $MASnI_3$.

In the case of O_I, as shown in **Figure 5.7b**, the hole capture coefficient is comparable to that of V_I, consistent with the similar kinetic barriers predicted in the CCD. In contrast, the electron capture process exhibits a much higher capture coefficient with the C_n being up to 2.8×10^{-6} cm^3 s^{-1} at room temperature. Correspondingly, the nonradiative carrier recombination coefficient of O_I is up to $C_{nr} = 2.2 \times 10^{-6}$ cm^3 s^{-1} at room temperature.

The nonradiative recombination rate constant A, also known as the Shockley-Read-Hall (SRH) rate constant, hence can be obtained jointly by the defect density (N) and the nonradiative capture coefficient per defect (C_{nr}), yielding $A = N \times C_{nr}$[147], which represents the number of nonradiative recombination events per unit time, i.e., the reciprocal of nonradiative carrier lifetime τ_{nr}.

In $MASnI_3$, V_{Sn} serves as the lowest-energy acceptor and V_I as the lowest-energy donor even with O being incorporated into the material; thus, the Fermi level largely is pinned by V_{Sn} and V_I, at around 0.14 eV above the VBM, as depicted by the gray dashed line in **Figure 5.4**. This is consistent with the experimentally observed *p*-type conductivity behavior in the $MASnI_3$ samples[103]. Under this condition, V_I and O_I exhibit similar formation energies. According to

the thermal equilibrium equation, the densities (N) of V_I and O_I are estimated to be 1.5×10^{15} cm^{-3} and 0.8×10^{15} cm^{-3} at room temperature, respectively.

Without oxygen ingression, the SRH rate constant A induced by native V_I is 9.3×10^6 s^{-1}. Exposure to ambient air (oxygen) leads to the formation of O_I, whose $C_{nr} = 2.2 \times 10^{-6}$ cm^3 s^{-1}, and the SRH rate constant A increases to 1.8×10^9 s^{-1}. Such a significant enhancement of the nonradiative recombination rate constant implies an appreciable reduction of the carrier lifetime by around two to three orders of magnitude, which provides a rationale for the experimental fact that oxygen exposure results in a rapid decline of carrier lifetime and power conversion efficiency in $MASnI_3$-based devices[197,198]. Indeed, the SRH rate constant of O_I is close to the experimentally reported values, typically on the order of 10^9 s^{-1} for $MASnI_3$ samples[123,169,213].

5.3.4 Underlying Mechanism Behind Oxygen-Induced Fast Carrier Recombination

We noted that the capture of the electron serves as the rate-limiting process for the nonradiative carrier recombination for V_I and O_I. With O incorporation resulting in forming O_I, the electron capture process is significantly accelerated, which is thus responsible for a higher overall nonradiative recombination rate. However, the calculations show that the formation of O_I shifts the position of the $\varepsilon(0/-)$ level down with a larger electron transition energy, compared with the original V_I (**Figure 5.5a**). This is in contrast to the traditional notion that the carrier capture rate generally decreases exponentially with the depth of transition energy[214] (the energy difference between the transition level and the corresponding band edges; the CBM for electron and the VBM for hole). Such a counterintuitive behavior can be attributed to two other important effects associated with lattice strain.

First, the incorporated O in V_I can form a stronger ionic Sn-O-Sn bond even than the metallic Sn-Sn bond with V_I^- and thus reduces the softness of the lattice. The lattice strengthening

recovers the harmonicity (parabola) of the potential energy surface of O_I^- compared with the case of V_I^- (green lines in **Figures 5.5d 5.5e**), which thus pushes the system into the so-called Marcus inverted region[152] (the PESs intersect within $0 < Q < \Delta Q$). In this case, the enhancement of the electron transition energy actually results in a reduced capture kinetic barrier.

Second, the formation of O_I leads to a smaller lattice relaxation associated with the charge-state transition, as shown by a smaller ΔQ in the CCDs, compared with V_I, which reduces the kinetic barrier for the electron capture process further by moving the intersection of the PESs closer to the equilibrium configuration of O_I^0. Indeed, the PES of O_I^- almost goes through the minimum of the PES of the excited O_I^0, resulting in an extremely small electron capture barrier, rationalizing the counterintuitive enhancement of the electron capture process.

Furthermore, in the case of hole capture, both systems are within the Marcus inverted region. Compared with V_I , O_I reduces the hole transition energy and hence contributes to the enhancement of the capture barrier. On the other hand, the smaller lattice relaxation associated with the transition of $O_I^0 \leftrightarrow O_I^-$ contributes to the reduced hole capture barrier, which comparably alleviates the effect of the reduced transition energy. Consequently, V_I and O_I exhibit similar hole capture barriers and coefficients. However, they are not the rate-limiting steps for nonradiative recombination, and thus do not effectively impact the recombination rate. The results suggest that to effectively suppress the nonradiative recombination and increase carrier lifetime in the $MASnI_3$-based devices in air, in addition to developing encapsulation technology to prevent environmental oxygen contamination, defect engineering to minimize the density of native I vacancies would be a critical step. In principle, synthesizing the material under I-rich conditions can inhibit the formation of V_I in $MASnI_3$ active layers. However, such growth conditions can also increase the density of V_{Sn}[186,209], which would result in severe *p*-type conductivity and thus impacts photovoltaic performance. This implies that the commonly

used growth condition manipulation falls short of addressing the issue induced by intrinsic defects in $MASnI_3$, in stark contrast to that of Pb-based perovskites[140]. To further improve the performance of the related devices operating in the air, future research should focus on extrinsic anion engineering for suppressing the formation of V_I and alleviating *p*-type self-doping. Indeed, experiments show clues that appropriate extrinsic anion doping, such as Br^-, Cl^-, as well as the pseudo-halides of Ac^- (acetate) and $HCOO^-$ (formate), can efficiently decrease the density of deep traps and prolong the carrier lifetime in Sn-based perovskites[215–217]. V_I is filled by these anions, and the density of the detrimental O_I is effectively reduced, which is essential to enabling improved device performance. Our results provide a rationale for such enhancements.

5.4 Conclusion

In summary, based on first-principles hybrid DFT calculations, we have studied the mechanism of oxygen incorporation in accelerating carrier recombination in $MASnI_3$ and degrading the device performance. In $MASnI_3$, oxygen interstitials themselves are not responsible for nonradiative recombination. Rather, they tend to form the substitutional O_I by interacting strongly with the abundant native I vacancies (V_I) that are the dominant nonradiative recombination center in $MASnI_3$, and significantly enhance the original recombination rate from $9.3 \times 10^6\ s^{-1}$ to $1.8 \times 10^9\ s^{-1}$. Significantly, despite an enhancement in the electron transition energy (from 0.48 eV to 0.73 eV), the formation of O_I strengthens the lattice and reduces structural relaxation upon electron capture. These effects synergistically contribute to a higher electron capture coefficient, thus facilitating faster nonradiative carrier recombination in O_I. Our results thus point to a way to effectively suppress nonradiative recombination loss in $MASnI_3$: in addition to preventing O ingression, minimizing the density of native V_I would be a critical step. These insights advance our understanding of how oxygen impacts the carrier

dynamics and power conversion efficiency in $MASnI_3$-based devices, assisting in the future design and optimization of nontoxic Sn-based perovskite solar cells and other broad optoelectronics upon oxygen (ambient air) exposure.

Chapter 6 Toward Stabilization of Formamidinium Lead Iodide Perovskites by Defect Control and Composition Engineering

6.1 Introduction

Organic-inorganic halide perovskites have emerged as exceptional materials for next-generation photovoltaic applications, with solar power conversion efficiencies (PCE) exceeding 25.8%[3,115], rivalling that of the well-established silicon-based solar cells. Currently, the high-efficiency perovskite solar cells are predominantly fabricated with formamidinium lead iodide ($FAPbI_3$), which exhibits higher thermal stability against decomposition into the secondary compound of PbI_2, a broader absorption spectrum that extends further into the red, and an ideal bandgap (~1.4 eV) closer to the Shockley-Queisser optimum, as compared with the prototypical methylammonium lead iodide ($MAPbI_3$)[37,38,218]. The superior optoelectronic properties of $FAPbI_3$ originate from the high-symmetry cubic perovskite structure (black α-phase)[36]. Regrettably, this phase is vulnerable and prone to transition into a photovoltaically-inactive yellow non-perovskite δ-phase with hexagonal symmetry and a wide bandgap (~2.4 eV) below a temperature of 150 °C (ref. [36–43]), especially under humid environments or with excess photogenerated holes[219,220]. This instability is a major barrier to developing practical perovskite solar cells. An in-depth understanding of the key mechanisms underlying the phase instability of α-$FAPbI_3$ and the effective remedies are vital for achieving long-term stability in perovskite solar cells and other broadly ranged optoelectronic applications with high performance.

Traditionally, the studies of phase transitions of halide perovskites[221–223] have been mostly based on defect-free pristine models. The interaction between the phase transition and lattice defects has been typically overlooked, despite prevalent defects in metal halide perovskites especially synthesized through solution-based methods[140]. Indeed, it was reported that the

presence of defects can induce local symmetry breaking and significantly deteriorate the mechanical stability of perovskites, facilitating lattice distortion and octahedral tilting[149,224–226]. We are thus confronted with fundamental questions: what are the roles of intrinsic defects or unintentional impurities in impacting the α-δ phase transition in $FAPbI_3$, and more importantly, how can the perovskite phase instability of $FAPbI_3$ be effectively remedied?

Efforts to stabilize the photovoltaically-active $FAPbI_3$ lattice have led to various strategies, including composition engineering through doping engineering[36,37,39,43,77,227–232] and strain engineering[38,93,230]. The ternary composition of halide perovskites (ABX_3) provides a high degree of flexibility for doping engineering at its three available sites. Particularly, A-X doping for $FAPbI_3$ with MABr, MACl, CsBr, and/or CsCl has been one of the most popular strategies for suppressing the phase transition of $FAPbI_3$(ref. [36,43,77,227,228,230]), although the underlying mechanism and effectiveness trend remain elusive. B-site doping engineering, despite being less explored due to higher binding energy[233], holds great potential as a breakthrough for enhancing perovskite stability, given the wider variety of dopant species[103,234]. Rare-earth (RE) elements, like lanthanide (Ln) ions, have been effective in improving the phase stability of traditional semiconductors[235] and the ambient stability of halide perovskites against thermal, moisture, and light conditions[236,237] by strengthening lattice chemical bonds. This approach could potentially stabilize α-$FAPbI_3$, even though further validation is needed. To further design stable and efficient photovoltaic and optoelectronic devices, a thorough and systematic exploration on how the doping of foreign cations at three available sites, especially with lanthanide ions at the B sites, impacts the phase transition thermodynamics and kinetics in $FAPbI_3$ is crucial (ref. [238]).

In this study, by performing comprehensive first-principles calculations combined with machine learning, we reveal that intrinsic defects can indeed play an important role in aggravating the instability of α-$FAPbI_3$. In particular, the presence of iodine defects, i.e., iodine

vacancies and interstitials, can significantly lower the activation energy barrier of α-δ phase transition kinetics of $FAPbI_3$. We also identify the detrimental influence of atmospheric moisture and oxygen decomposition products on $FAPbI_3$ perovskite phase degradation. Our analysis shows that A-site cation engineering can effectively alter the thermodynamic driving force of the phase transition, while B-site doping plays a more significant role in affecting the phase transition kinetics, giving prominence to A-B mixed doping engineering as a highly efficient strategy for synergic improvements of stability and properties of $FAPbI_3$ perovskites. The analysis of the optimal the octahedral factor (μ) range for the stable FA-based perovskite phase offers a quantitative basis for future Ln doping research to optimize halide perovskite materials. Furthermore, we provide direct experimental evidence of significantly improved optoelectronic properties and phase stability in Cs-Eu mixed-doped $FAPbI_3$ as compared to its Cs-doped counterpart. Our study provides in-depth insights into the thermodynamics and kinetics of α-δ phase transition in $FAPbI_3$ and establishes a basis for advanced device designs with "on-demand" optoelectronic properties and stability through strategic defect and composition engineering.

6.2 Simulation Method

6.2.1 Computational Method

The first-principles calculations were performed based on the density functional theory (DFT) with the projector-augmented wave method as implemented in the Vienna *Ab initio* Simulation Package (VASP)[136]. The DFT-D3 scheme of Grimme was adopted for the van der Waals correction[239]. The kinetic energy cutoff of the plane-wave basis was set at 400 eV and a Monkhorst–Pack sampling of $2 \times 2 \times 2$ k-points was used for the $3 \times 3 \times 2$ supercells with 216 atoms. For the exchange-correlation functional, electronic structures, defect formation energies and transition energy levels were obtained using Heyd−Scuseria−Ernzerhof hybrid

functional (the mixing parameter of 0.46) with the spin−orbit coupling (HSE-SOC)[113], and the variable-cell nudged elastic band (VCNEB) calculation, *Ab initio* molecular dynamics (AIMD) and Machine Learning Molecular Dynamics simulations were performed based on the generalized gradient approximation of Perdew, Burke, and Ernzerhof (PBE)[110]. All the atomic positions were fully relaxed until the residual forces were less than 0.01 eV/Å.

6.2.2 Activation Energy Barrier

The activation energy barriers (E_b), defined as the energy difference between the α-phase $FAPbI_3$ and the configuration at the saddle point along the α-δ phase transition pathway, were calculated using the variable-cell nudged elastic band method (VCNEB)[240], which is an extension of elastic band method (NEB) technique, as implemented in the Universal Structure Predictor: Evolutionary Xtallography (USPEX) code in combination with the VASP. Compared with the traditional NEB algorithm, the VCNEB technique allows both the atomic positions and the supercell dimensions to relax for each configuration at constant pressure, thereby having been widely used for the analysis of the solid-solid phase transition pathways and activation energy barriers in both the hybrid perovskite systems[134,222] and other materials[241,242]. Note that the simulated lowest-energy transition path is similar to that reported in Ref.[222]. The effect of intrinsic defects, extrinsic doping, and unintentional impurities on the phase transition thermodynamics and kinetics was evaluated based on the $3 \times 3 \times 2$ supercells with 216 atoms (defect concentration of 5.56%).

6.2.3 *Ab initio* Molecular Dynamics

Ab initio molecular dynamics (AIMD) simulations lasted 30 ps with the time step of 1 fs in the canonical (NVT) ensemble. The temperature was controlled at 300K by using the Nose-Hoover thermostat[141].

6.2.4 Machine Learning Molecular Dynamics

Machine Learning Molecular Dynamics **(**MLMD)[243,244] was performed as implemented in VASP. All the datasets were trained based on the on-the-fly hybrid AIMD and MLMD calculations, in which first-principles *ab initio* calculations will be conducted when local molecular environments are significantly different from those already stored as the training data. In this study, Machine Learning Force Field (MLFF) was trained in an isobaric−isothermic (NpT) ensemble with a time step of 1 fs, using the $(3 \times 3 \times 2)$ 216-atom bulk supercells of α-$FAPbI_3$ and δ-$FAPbI_3$, 360-atom surface models of α-$FAPbI_3$ (111) and δ-$FAPbI_3$ (100) with a vacuum thickness of 15 Å, 312-atom (**Figure 6.7a**) and 1248-atom (**Figure 6.7b**) interface models between the α-$FAPbI_3$ (111) and δ-$FAPbI_3$ (100) phases, and those with a V_I^+. This interface model has been reported to exhibit the lowest total energy[245], and the lattice mismatch was less than 1%. The force field was generated with a cutoff radius of 7 Å for the angular descriptor and a width of 0.5 Å of Gaussian functions for broadening the atomic distributions of the radial descriptor. The MLFF training involves 10-ps NpT simulations at 200 K, 300 K, and 400 K for each configuration. Based on the obtained datasets of MLFF, 2 ns NpT-MLMD simulations with a time step of 1 fs were run for the 1248-atom interface models of pristine $FAPbI_3$ and that containing a V_I^+.

6.2.5 Defect formation energy

The defect formation energy was calculated by[140]:

$$\Delta H_f\left(X_i^q\right) = E\left(X_i^q\right) - E(host) - \sum n_i(\mu_i + \Delta\mu_i) + q(E_f + E(VBM) + \Delta V) + \Delta_{corr}^q \qquad (6.1)$$

where $E\left(X_i^q\right)$ and $E(host)$ are the total energies of the defective and defect-free supercells, respectively. n_i stands for the number of defects added into the supercell. μ_i is the absolute value of the chemical potential of the defect atoms, and $\Delta\mu_i$ the relative value of the chemical

potential, which is related to growth conditions. For the host chemical potentials, we chose that under the iodine-moderate conditions (see **Figure 6.1**), which are representative of the typical synthesis. The chemical potentials of lanthanide elements (Ln) correspond to those in lanthanide iodide salts LnI_3. $E(VBM)$ is the energy of the valance band maximum (VBM) of $CsPbI_3$ and E_f represents the Fermi energy measured from the VBM. ΔV is the correction term for ensuring the alignment of the potential for the charged defect in supercells, and the finite-size correction term, Δ_{corr}^{q}, was used for correcting the periodic images of the charged defects. Moreover, a convergence test was performed using a $3 \times 3 \times 3$ 324-atom supercell of $FAPbI_3$. The results show that, for V_I^+, the calculated formation energy difference between the 216-atom and 324-atom supercells is only 0.053 eV.

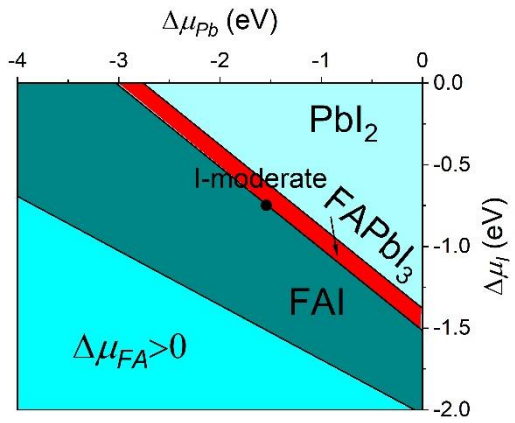

Figure 6.1. Phase map for thermal equilibrium growth condition of $FAPbI_3$. The relative chemical potentials $\Delta\mu_i$ of component atoms (FA, Pb, I) should satisfy:

$$\Delta\mu_{FA} + \Delta\mu_{Pb} + 3\Delta\mu_I = \Delta H_f(FAPbI_3)$$
$$\Delta\mu_{FA} + \Delta\mu_I < \Delta H_f(FAI)$$
$$\Delta\mu_{Pb} + 2\Delta\mu_I < \Delta H_f(PbI_2)$$
$$\Delta\mu_{FA} < 0;\ \Delta\mu_{Sn} < 0;\ \Delta\mu_{Br} < 0$$

where the $FAPbI_3$ will be thermodynamically stable instead of its secondary phases or element phases of components. With all these conditions, the relative chemical potentials $\Delta\mu_i$ are restricted in the red area. In this study, we chose the I-moderate growth conditions for further evaluating the defect formation energies.

6.2.6 Defect concentration

Based on the formation energy, the defect concentration at thermal equilibrium thus can be given by[140]: $N = N_0 e^{-\frac{\Delta H}{kT}}$, where N_0 stands for the number of available sites for defect formation in the $CsPbI_3$ lattice per volume, ΔH for the formation energy of defect, k for the Boltzmann constant, and T is temperature.

6.2.7 Transition Energy Level

The transition energy level $\mathcal{E}(q/q')$ was determined by the Fermi level position for which the formation energy of X_i^q is equal to that of $X_i^{q'}$, thus, can be determined by[140]:

$$\mathcal{E}(q/q') = [E(a,q) - E(a,q') - (q-q')(E(VBM) + \Delta V)]/(q-q') \quad (6.2)$$

6.2.8 Crystal growth

All the series of mixed-cation Pb-based perovskite single crystals were grown using the inverse temperature crystallization (ITC) method. Specifically, a stoichiometric molar ratio of CsFA precursor solution (1.0 M) was prepared by dissolving 1.55 g FAI (9.0 mmol), 0.26 g CsI (1.0 mmol), 0.55 g $PbBr_2$ (1.5 mmol), and 3.85 g PbI_2 (8.5 mmol) compounds in 10 ml γ-butyralactone (GBL). After stirring at room temperature for 12 h, the mixed solution was filtered through a 0.22 μm polytetrafluoroethylene filter and transferred into glass vials. Thereafter, the glass vials with the filtered solution were placed on the hot plate heated to 80 °C and kept this temperature for 3 h. Then, the temperature was gradually increased from 80 °C to 120 °C at a slow rate of 2 °C per hour. Small crystals would be formed in the crystallizing dish. For Cs/Eu-doped mixed-cation perovskite single crystal, a small amount of EuI_3 was dissolved into the solution of $Cs_{0.1}FA_{0.9}Pb(I_{0.9}Br_{0.1})_3$ at a specific concentration. The amounts of B-site dopants (Eu: 0.25%, 0.50% and 1.00%) in the perovskite solution are calculated according to the molar ratio with Pb.

6.2.9 Device fabrication

The hole-only device with vertical Au/Perovskite/Au structure was prepared for the SCLC method. An 80-nm gold (Au) anode was deposited on the top surface of the mixed-cation perovskite single crystal by thermal evaporation (AJA ATC-1800-E e-beam thermal evaporator). Then, a 105 nm Au cathode was deposited on the bottom surface of the single-crystal samples. The obtained devices will be used for the SCLC measurements.

6.2.10 Characterizations

The XRD patterns of the perovskite powder (by gridding the single crystals into powder) were measured using on PANalytical Pro Powder Diffractometer with a Cu Kα radiation source. The absorption spectrum measurement was taken in an Agilent Cary 5000 UV–vis–NIR spectrophotometer. Energy-dispersive X-ray spectroscopy (EDS) testing were carried out using Zeiss ULTRA plus under the operating voltage of 20 kV. The *I-V* characteristic curves of perovskite single crystals were measured using a two-terminal probe station (Everbeing Int'l Corp.) and 4200A-SCS Parameter Analyzer.

6.2.11 The Details for SCLC Analyses

We also performed current–voltage (*I–V*) measurements to assess the charge transport properties and trap behaviors of both Cs- and Cs-Eu mixed-cation-doped FA-based perovskite single crystals. The space-charge-limited-current (SCLC) analyses were carried out based on the obtained *I-V* data. As shown in **Figures 6.17f-i** in the main text, we can clearly find that three regions were identified in the *I–V* curves: Ohmic (n = 1), trap-filling (n > 3), and Child's (n = 2) regions.

At the low applied voltage, an Ohmic region is confirmed. Following the first region, it exhibits a rapid nonlinear rise in current starting at the point of trap-filled limit (TFL) voltage V_{TFL}, indicating the transition into the trap-filling region. In the second region, all the trap states are expected to be filled by the injected carriers. The trap density (N_t) can be evaluated by the following equation:

$$N_t = \frac{2V_{TFL}\varepsilon\varepsilon_0}{ed^2}$$

in which ε is the relative dielectric constant materials, ε_0 is the vacuum permittivity, e is the electronic charge, and d represents the thickness of the single crystals.

The carrier mobility (μ) could be extracted from the third region (Child's region) that shows trap-free characteristic at high bias, following the Mott–Gurney's SCLC theory expressed by the following equation:

$$\mu = \frac{8d^3}{9\varepsilon\varepsilon_0}\frac{\partial J}{\partial(V^2)}$$

where J is the current density and V is the corresponding applied voltage.

6.3 Results and Discussions

6.3.1 α-δ phase transition of FAPbI3

Pure α-$FAPbI_3$ (black phase) features a cubic perovskite structure (ABX_3) with the six-fold coordinated PbI_6 inorganic octahedra connected at the corner and the larger FA organic cations in 12-fold coordination (**Figures 6.2** and **Figure 6.3a)**. In contrast, δ- $FAPbI_3$ (yellow phase) exhibits a hexagonal structure with lower symmetry, where PbI_6 octahedra are face-sharing (**Figures 6.1** and **Figure 6.3b)**. Electronically, α-$FAPbI_3$ has a favorable direct bandgap of 1.42 eV with highly dispersive bands near the valance band maximum (VBM) and conduction band minimum (CBM) (see **Figures 6.3c-d**), while the non-perovskite δ-$FAPbI_3$ exhibits a larger indirect bandgap of 2.53 eV with relatively flatter band edges (see **Figures 6.3e-f**), due to the

disconnection of octahedra within the a-b plane that decreases the overlap of the Pb states and I states. Energetically, α-$FAPbI_3$ is higher in energy by 0.261 eV per formula unit than the δ-phase, which agrees with the experimental findings[37,40–42] of the metastable nature of the desired α-phase of $FAPbI_3$.

The undesired α-δ phase transition of $FAPbI_3$ active layers exhibits a large thermal hysteresis[42], indicative of a thermally activated process with a transition activation energy barrier. To quantitatively assess the underlying kinetics and gain a full understanding of phase transition mechanisms in $FAPbI_3$, we modelled the transition pathway of α-δ phase transition in $FAPbI_3$ using the well-established variable-cell nudged elastic band (VCNEB) method[240]. As shown in **Figure 6.2a**, the α-δ phase transition undergoes an elongation of the a and b lattice parameters accompanied by a lattice contraction along the c direction. A volume expansion occurs at the transition state, followed by a significant volume contraction to form the final state of δ-$FAPbI_3$ (**Figure 6.2b**). Similar behaviors were found in all-inorganic perovskite $CsPbI_3$ during its orthorhombic-to-hexagonal phase transition[221,246].

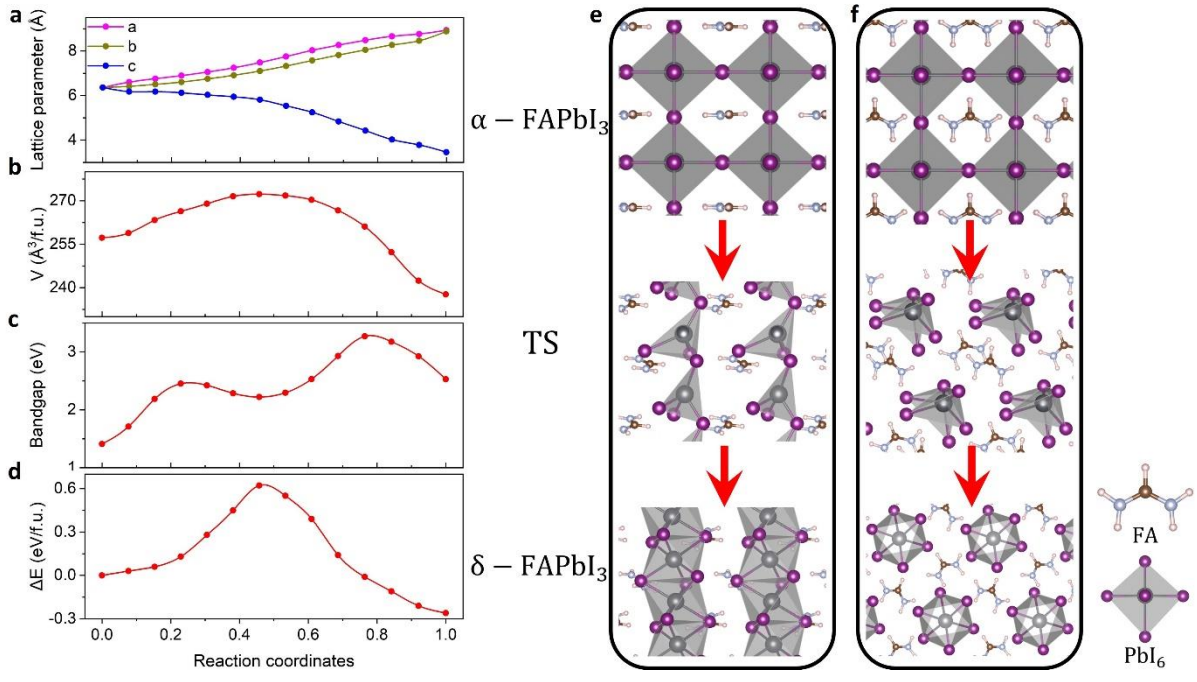

Figure 6.2. Evolution of (**a**) the lattice parameters, (**b**) volume, (**c**) bandgap, and (**d**) the potential energy as a function of reaction coordinate of the α-δ phase transition in $FAPbI_3$, where the starting point (x=0) of the reaction coordinate is defined as the configuration of the initial α-phase state, and the endpoint (x=1) stands for the final δ-phase state configuration. (**e**) Side and (**f**) top views of the atomic displacements along the α-δ phase transition in $FAPbI_3$, where TS stands for the transition state.

The phase transition involves complex atomic rearrangement especially on the inorganic octahedral skeleton, as shown in **Figures 6.2e-f**. It starts with rotations of the octahedra, followed by breaking of Pb-I bonds in the *a*-*b* plane and forming a one-dimensional PbI_4 tetrahedral chain at the transition state. This process leads to a volume expansion and a sharp increase in the lattice cavity. As a result, the FA cations are separated with the FA-FA distance being enhanced by a factor of 1.28 as compared to the initial state. As the transition proceeds, the Pb ions of the PbI_4 tetrahedral chain move much closer, forming the new Pb-I bonds (as reflected by the sharp decrease of the *c* lattice after the transition state in **Figure 6.2a**), and thus the face-shared PbI_6 octahedral chain, which further separates the chains within the *a*-*b* plane and enlarging the lattice cavity. This results in 1.09 times increase in FA-FA distance horizontally. Note that in this process, the vertical compression effect is greater than the expansion in the horizontal direction, hence responsible for the reduction in the material's volume. As discussed above, the inorganic Pb-I lattice plays an important role in tailoring the band edges of the perovskites. A large bandgap fluctuation of $FAPbI_3$ (**Figure 6.2c**) reflects the complex structural rearrangement of the inorganic skeleton during the phase transition. Moreover, the lattice variation during the transition implies that strain engineering could be a viable approach to remedy the phase instability of the $FAPbI_3$ active layers.

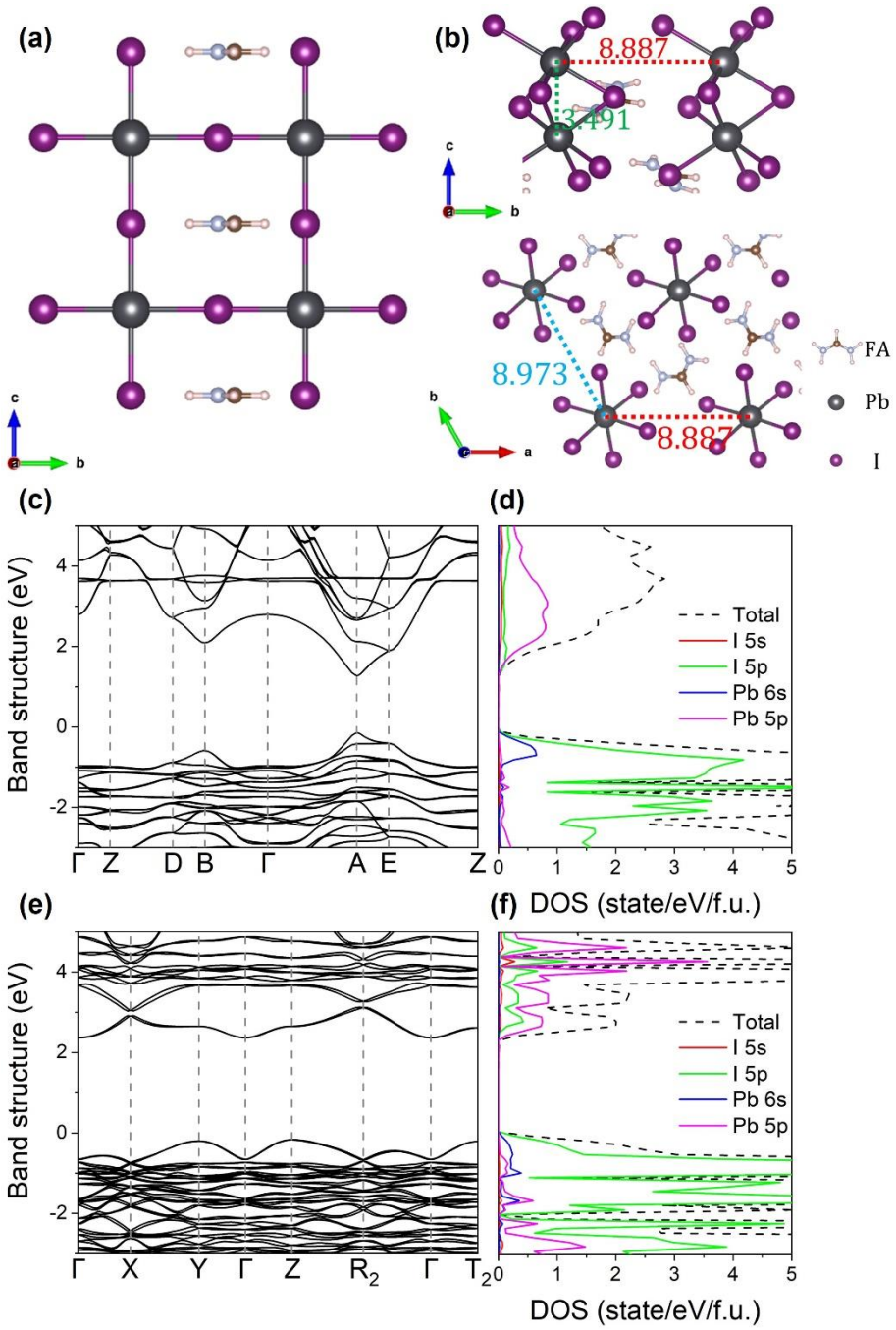

Figure 6.3. Optimized structures of the (**a**) α-phase and (**b**) δ-phase of $FAPbI_3$. (**c**) Calculated band structure and (**d**) the density of state (DOS) of α-$FAPbI_3$. (**e**) The band structure and (**f**) the DOS of δ-$FAPbI_3$. The calculations of the electronic properties were based on density functional theory with the hybrid Heyd–Scuseria–Ernzerhof functional and spin–orbit coupling (HSE06-SOC).

As shown in **Figure 6.2d**, the α-δ phase transition of $FAPbI_3$ requires overcoming an activation energy barrier (E_b) of 0.622 eV/f.u., which is close to the previous results of 0.6-0.7 eV/f.u. via various computational methods, including the nudged-elastic-band method, stochastic surface

walking (SSW) pathway sampling, and molecular dynamics simulations[41,42,134,222]. Given the orientationally disordered nature of FA cations in the realistic perovskites[139], we further extracted four low-energy perovskite structures with different FA-cationic orientations from *ab initio* molecular dynamic (AIMD) simulations at room temperature, as shown in **Figures 6.4a-d**, and studied their phase transition properties. From the extracted Str.1 to Str.4, the orientational disorder of the FA cations is increasingly significant relative to the pristine model (**Figure 6.4a**). As shown in **Figure 6.4e**, these cation-disordered systems almost preserve the pristine phase transition barrier (E_b~ 0.62 eV/f.u), whereas the energy difference between the α-phase and δ-phase ($\Delta E_{\delta-\alpha}$) of $FAPbI_3$ decreases. Notably, the reduction trend of $\Delta E_{\delta-\alpha}$ agrees with the degree of the FA-cationic disorder. This can be attributed to the fact that the rotation of A-site cations can thermodynamically stabilize the perovskite structure, which agrees with the previous experimental reports[42,138].

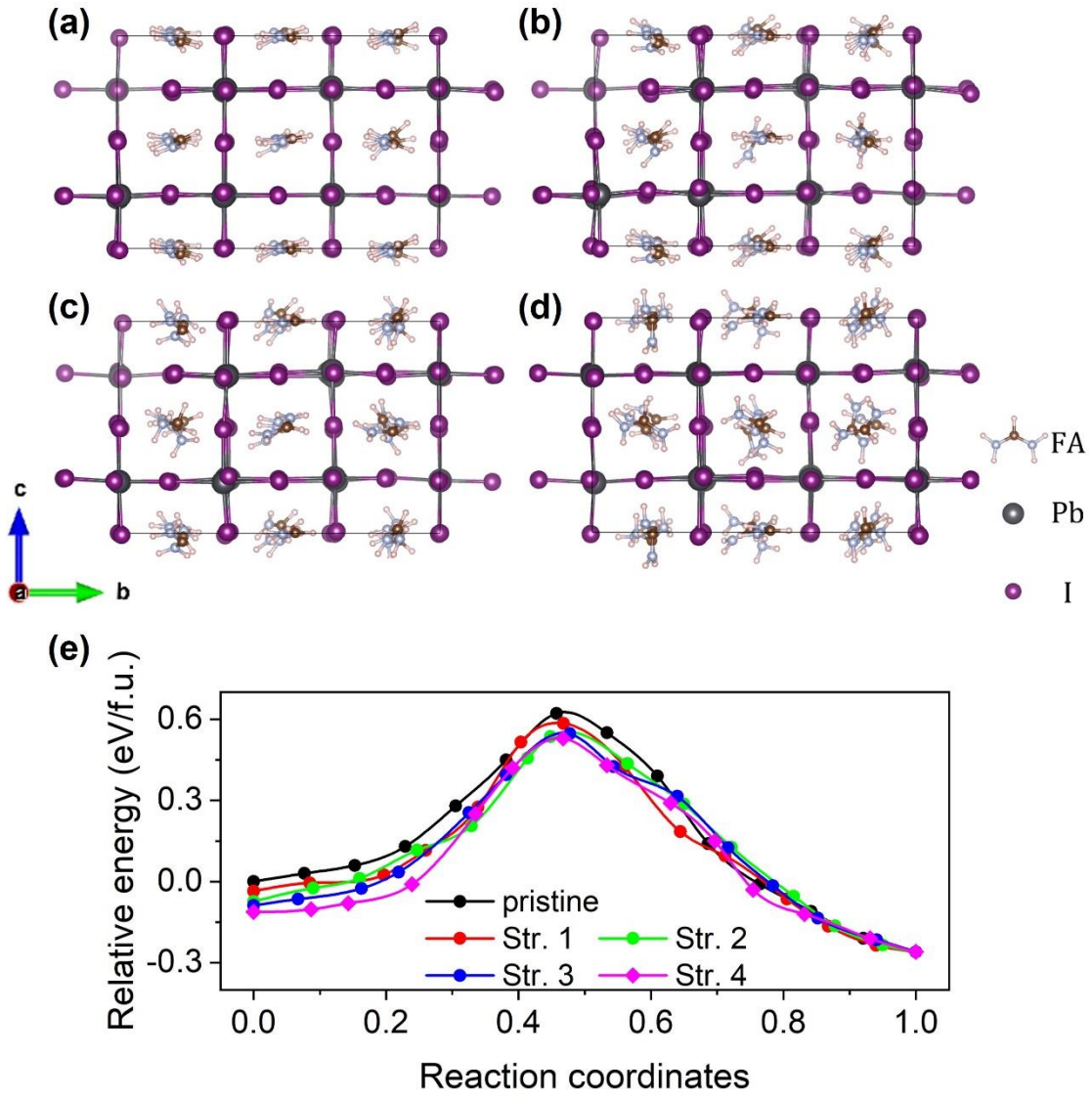

Figure 6.4. Atomic structures of $FAPbI_3$ perovskite with FA-cationic disorder in various degrees extracted from *ab initio* molecular dynamic (AIMD) simulations at room temperature, namely, (**a**) Str.1, (**b**) Str.2, (**c**) Str.1, and (**d**) Str.4. Note that from Str.1 to Str.4, the orientational disorder of the FA cations is increasingly more significant compared with the pristine structure in **Figure 6.2a**. (**e**) Evolution of and the potential energy as a function of reaction coordinate of α-δ phase transition of pristine $FAPbI_3$ and those with FA-cationic disorder (Str.1-Str.4).

In principle, a lower $\Delta E_{\delta-\alpha}$ contributes to the higher purity of FA-based perovskite crystallization, leading to a lower percentage of the undesired yellow δ-phase. Additionally, E_b dictates the phase transition rate during the device operation. These parameters, including $\Delta E_{\delta-\alpha}$ and E_b, are crucial indicators in describing the thermodynamics and kinetics of the phase transition in $FAPbI_3$ perovskites, relative to the initial performance and the stability of

the related devices, respectively. The results, as shown in **Figure 6.4**, highlight the importance of A-site cations in altering the structural transition thermodynamics of $FAPbI_3$.

In terms of kinetics, we noted that the magnitude of the E_b range (**Figures 6.2d** and **Figure 6.4e**, and Ref.[41,42,134,222]) is comparable to, and even slightly higher than, the diffusion barrier of the FA vacancy (~0.61 eV), which has been reported to be rather immobile in $FAPbI_3$ at room temperature[247]. This implies that even at temperatures slightly above room temperature, the α-δ reaction rate would be constrained by the intrinsic kinetic activation barrier. Consequently, there must be other factors responsible for the rapid phase transition of the $FAPbI_3$ perovskites typically observed in experiments.

6.3.2 Defect-induced phase instability of α-$FAPbI_3$

Lattice imperfections are prevalent in hybrid perovskites due to their propensity for defect formation, especially the ones fabricated using solution-based processes[140]. In other words, the actual phase transitions certainly happen in the presence of defects. It is thus necessary to evaluate how defects impact both the thermodynamics and kinetics of the phase transition. Among the various intrinsic point defects in $FAPbI_3$, we focus on those that are common and abundant in the lattice[126,179]. These typical defects are namely the I vacancy (V_I^+), I interstitial (I_i^-), Pb vacancy (V_{Pb}^{2-}), FA vacancy (V_{FA}^-), and the FA interstitial (FA_i^+), respectively[126,179].

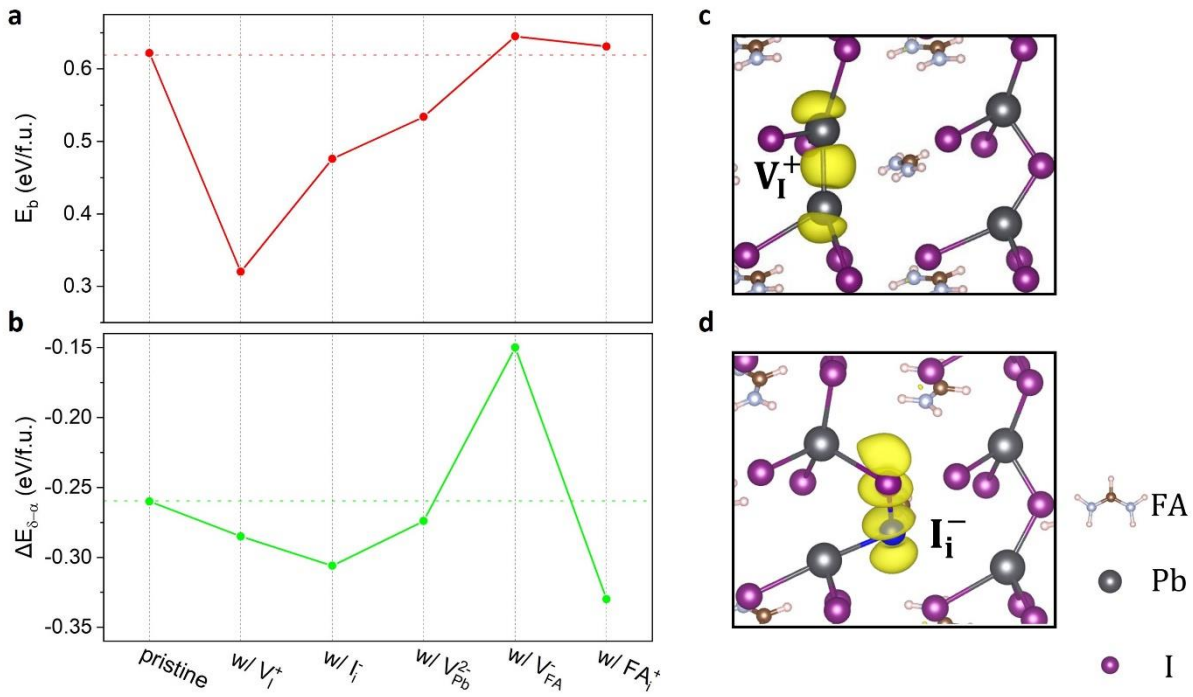

Figure 6.5. (**a**) The phase transition barriers (E_b) and (**b**) total energy differences between α- and δ-phase ($\Delta E_{\delta-\alpha}$) of pristine $FAPbI_3$ and systems with the presence of the low-energy intrinsic defects. The charge density plots for the transition states of α-δ phase transition of $FAPbI_3$ with (**c**) V_I^+ and (**d**) I_i^-, where the yellow iso-surfaces stand for the partial charge density for the states of the Pb dimer and I dimer. The iso-surfaces were taken at 0.01 $e/Å^3$.

Figures 6.5a-b show the calculated phase transition barriers (E_b) and thermodynamics ($\Delta E_{\delta-\alpha}$) of the pristine $FAPbI_3$ and those containing native low-energy defects. It is found that the presence of V_I^+, I_i^-, and V_{Pb}^{2-} reduces E_b, thereby accelerating the kinetics of the α-δ phase transition of $FAPbI_3$. However, these defects do not significantly impact $\Delta E_{\delta-\alpha}$. In contrast, FA-related defects, namely V_{FA}^- and FA_i^+, play an insignificant role in affecting the kinetics of the overall structural transition as the calculated E_b are close to that of the pristine case. Nevertheless, V_{FA}^- and FA_i^+ can impact the thermodynamics of the phase transition by reducing and increasing $\Delta E_{\delta-\alpha}$, respectively.

Notably, V_I^+, I_i^-, and V_{Pb}^{2-} defects share a common characteristic of being inherent to the inorganic Pb-I skeleton. In other words, the presence of these defects induces local symmetry breaking and introduces instability within the fundamental building block of the inorganic PbI_6

octahedra, which plays a dominant role in determining the phase transition barrier. In contrast, FA molecules undergo relatively simple migration and rotation and do not occur chemical bond stretching, breaking, and forming, which were found to overcome the rather low activation energy barrier during the structural transition[222,248,249].

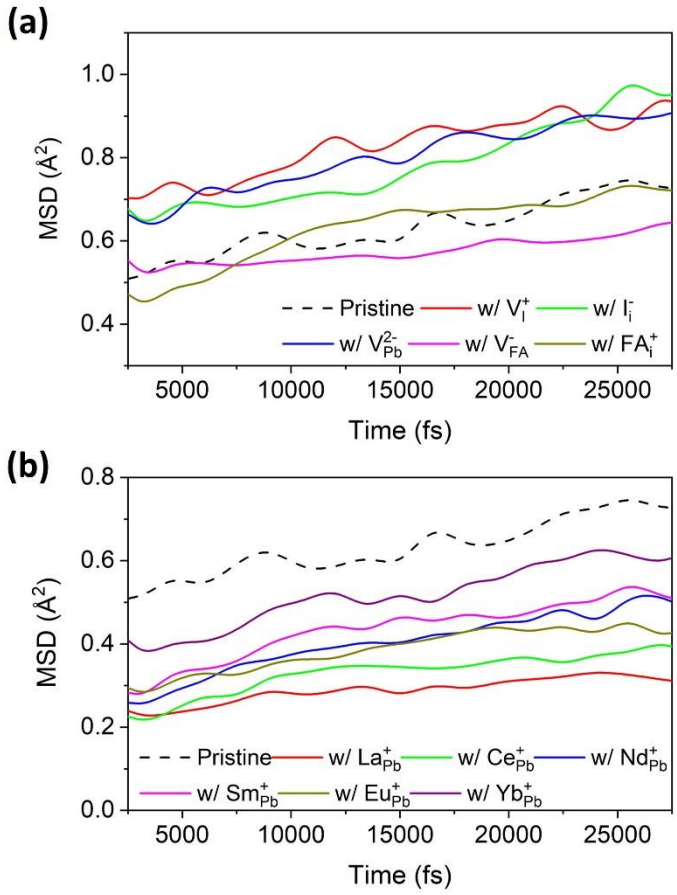

Figure 6.6. Mean square displacement (MSD) of the inorganic skeleton within 30 ps during AIMD simulations at 300 K: (**a**) for pristine and systems containing intrinsic defects, and (**b**) for pristine and Ln-doped systems.

To quantitively evaluate the effect of intrinsic defects on the lattice instability of $FAPbI_3$ under realistic conditions, we performed AIMD simulations on pristine α-$FAPbI_3$ and systems containing typical intrinsic defects at room temperature over a 30-ps period with a time step of 1 fs. While the simulations show no bond breaking and structure reconstruction for both defect-free and defective systems, the systems containing V_I^+, I_i^-, and V_{Pb}^{2-} display a noticeable

increase in the mean square displacements (MSD) of the inorganic Pb-I skeleton (**Figure 6.6a**). The enhanced MSD compared with the pristine system implies an enhanced vibrational motion of PbI_6 octahedron in the presence of V_I^+, I_i^-, and V_{Pb}^{2-}. As reported by Ghosh *et al.*[250], the unlocking of the PbI_6 octahedral vibration can hasten lattice breakage and tilting of the perovskites, thereby significantly reducing the structural dynamic stability.

Moreover, we noted that the systems containing V_I^+ and I_i^- exhibit much lower E_b (0.320 eV/f.u. for V_I^+ and 0.476 eV/f.u. for I_i^-) as compared to V_{Pb}^{2-} (0.534 eV/f.u.). This can be attributed to the strong covalency at the transition states induced by V_I^+ and I_i^- during the phase transition of $FAPbI_3$. In the case of V_I^+ (**Figure 6.5c**), the two uncoordinated Pb cations near the vacancy move closer to form a Pb dimer with a strong covalent bond at the transition state. Similarly, I_i^- induces a strong covalency between I anions that is characterized by the formation of an I dimer at the transition state (**Figure 6.5d**). Such a covalent interaction would contribute to the stabilization of the configuration, resulting in lower energy for the transition state and consequently a reduced E_b. The defect-induced covalency has also been reported for iodine defects in hybrid perovskites like $MAPbI_3$[130] and inorganic perovskites like $CsPbI_3$[251] due to the soft lattice nature of halide perovskites. In comparison, no covalent bond forming was observed during the phase transition in the case of V_{Pb}^{2-}. Therefore, the combined effects of reduced lattice dynamic stability and defect-induced covalent interaction at the transition state are responsible for the substantially lower E_b of $FAPbI_3$ perovskites with V_I^+ and I_i^-.

For V_{FA}^- and FA_i^+, the MSDs of the inorganic Pb-I lattice are similar to that of pristine $FAPbI_3$ (**Figure 6.6a**), confirming that the FA-related defects have a negligible impact on the structural dynamic stability of the perovskite. This agrees with the small changes in E_b obtained from the VCNEB calculations. On the other hand, as discussed above, the large size of FA cations is the key thermodynamic origin for the phase transition of FA-based perovskites, as also reflected by Goldschmidt's tolerance factor ($\tau = 1.02$) for $FAPbI_3$[182], which slightly exceeds the upper

limit of 1 required for forming a stable perovskite structure. The presence of V_{FA}^{-} increases the spatial cavity in α-$FAPbI_3$ and partially relieves the lattice strain induced by other large FA cations, thereby reducing the thermodynamic driving force for the conversion of the photo-active α-phase to the photo-inactive δ-phase. Conversely, FA_i^{+} aggravates the strained lattice, resulting in lower thermodynamic stability of the α-phase with respect to the δ-phase.

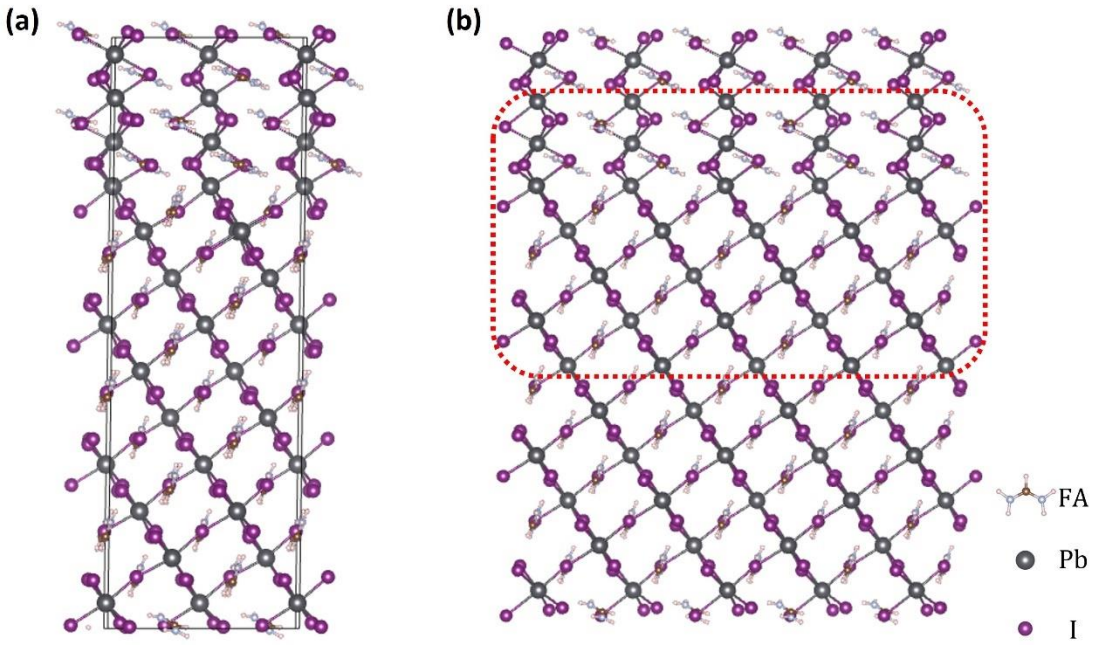

Figure 6.7. The 312-atom (**a**) and 1248-atom (**b**) interface models between α-$FAPbI_3$ (111) and δ-$FAPbI_3$ (100) phases.

Phase transition typically proceeds through the growth and propagation of the targeted phase nuclei. Given that V_I^{+} plays the most significant role in the local kinetic stability of $FAPbI_3$ with E_b suffering the sharpest decline by ~0.3 eV/f.u., we expected that the defects effectively facilitate the δ-phase propagation, responsible for a faster overall phase transition rate in $FAPbI_3$. To gain dynamic insights into the mechanism of phase transition aided by V_I^{+} and verify our DFT results, we proceeded to construct a configuration with planar interfaces between the α-$FAPbI_3$ (111) and δ-$FAPbI_3$ (100) phases (**Figure 6.7b**), and perform 2-ns NpT Machine Learning Molecular Dynamics (MLMD) simulation at 300 K based on the training

data set from on-the-fly hybrid AIMD. Energy calculations revealed that V_I^+ energetically prefers to reside at the interface than in the bulk of α-$FAPbI_3$ and δ-$FAPbI_3$ by 4.38 and 2.14 eV, respectively. Combing with the low diffusion barrier as previously reported[88], V_I^+ defects are expected to diffuse and aggregate around the interface between the two phases of $FAPbI_3$. As shown in **Figures 6.8a, b**, while no clear phase propagation was observed in the pristine system during the 2-ns MLFF simulation, a sign of notable transformation was evident in the V_I^+-defective system. Specifically, a PbI_6 octahedron at the interfacial plane around V_I^+ transformed to the face-sharing architecture of δ-$FAPbI_3$. This is further reflected by the analysis of MSD, as shown in **Figure 6.8c**. The Pb-I inorganic skeleton on the interfacial plane exhibited a significantly larger MSD compared to that of the pristine systems throughout the simulation time. For a typical diffusive transformation associated with the α-δ phase transition in $FAPbI_3$[252], a larger MSD of the Pb-I inorganic skeleton in the V_I^+ system indicates a more diffusive host ion property around the two-phase interface. The increased diffusivity significantly promotes the local atomic rearrangement and reconstruction of the interfacial plane, thereby promoting phase propagation.

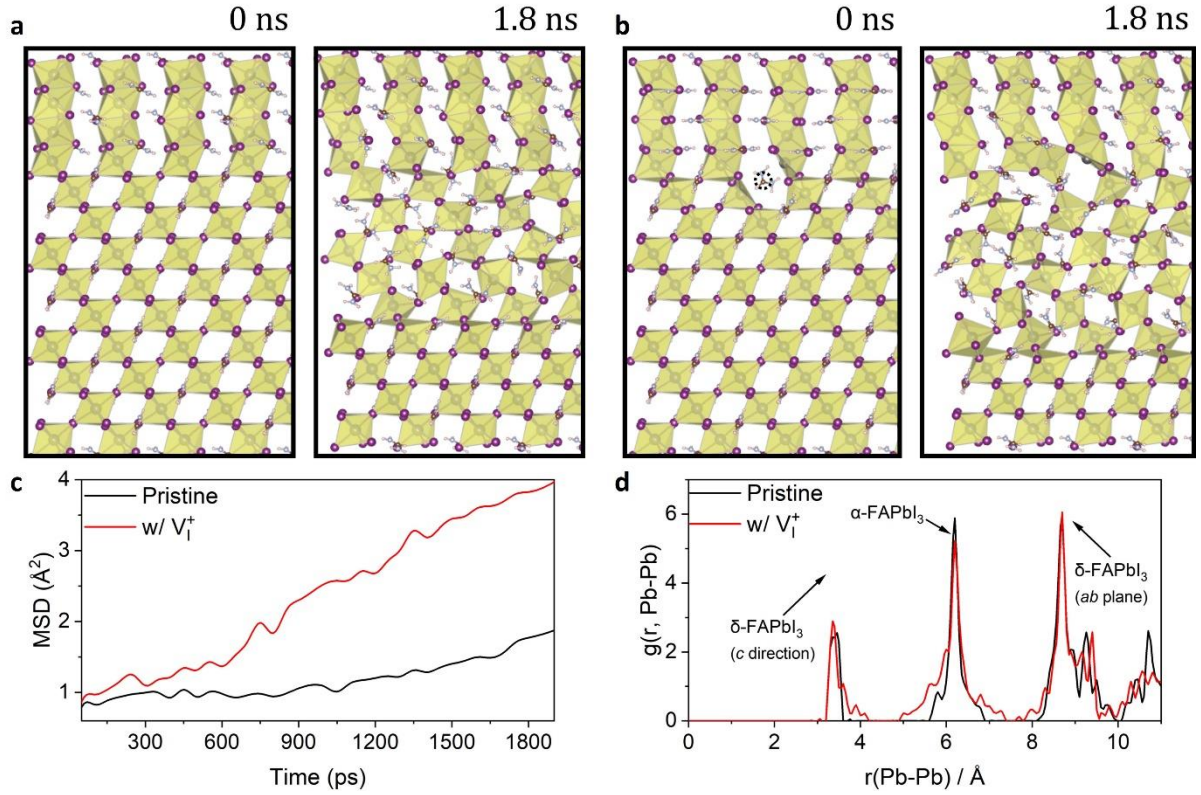

Figure 6.8. Snapshots captured at 0 and 1.8 ns from the Machine Learning Molecular Dynamics (MLMD) simulation of α-to-δ phase propagation in the (a) pristine and (b) V_I^+-defective planar interface models between α-$FAPbI_3$ (111) and δ-$FAPbI_3$ (100) at 300 K. (**c**) Mean square displacement (MSD) of the Pb-I inorganic skeleton of the interfacial plane (the region surrounded by the red dashed line in **Figure 6.6b**) and (**d**) the radial distribution function, $g(r, Pb-Pb)$, for Pb-Pb during the 2-ns MLMD simulations in the pristine and V_I^+-defective systems at 300 K.

Moreover, to quantify these visual observations, we compared the radial distribution function (RDF) for Pb-Pb interaction in both the pristine and V_I^+-defective systems (**Figure 6.8d**). For the ground-state atomic structures of α-$FAPbI_3$ and δ-$FAPbI_3$ (**Figure 6.3**), the second sharp peak corresponds to that in α-$FAPbI_3$, and the first and third sharp peaks stand for Pb-Pb along the *c*-direction and the *ab*-plane in δ-$FAPbI_3$, respectively. As can be seen, compared with the pristine system, the second peak in the V_I^+ system is broadened toward the first and third ones, accompanied by a slight reduction in coordination number. This implies a stronger tendency of the α-to-δ phase transition of $FAPbI_3$ in the V_I^+ system. Thus, a higher density of V_I^+ defects

can result in an increased propagation rate of the undesired α-to-δ phase transition in $FAPbI_3$. The MLMD simulation provides a dynamic understanding of the DFT results.

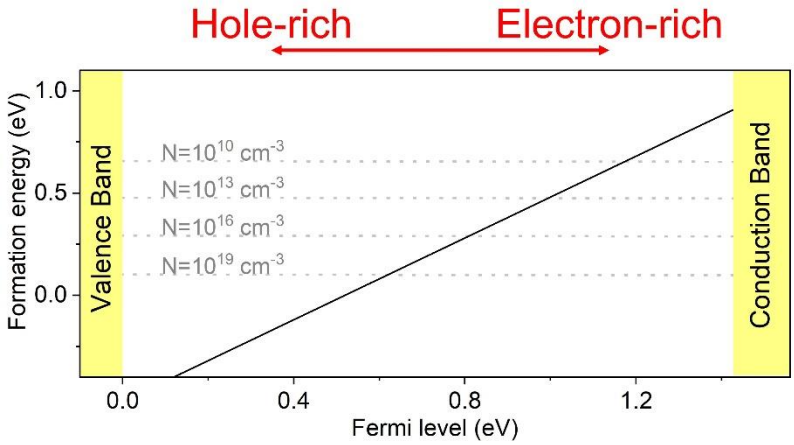

Figure 6.9. The formation energy of V_I in $FAPbI_3$ calculated under the I-moderate growth conditions, as a function of the Fermi level. The related defect densities at room temperature are denoted.

Experiments reported that an excess of hole carriers can accelerate the phase transition in $FAPbI_3$[219,220], although the microscopic origin remains unclear. Our formation energy calculations show that a hole-rich environment enhances the density of detrimental V_I^+ defects (**Figure 6.9**). This suggests that the observed hole-rich-induced faster phase transition may be attributed to the increased density of V_I^+ defects in $FAPbI_3$[219,220]. While iodine-rich growth conditions can inhibit the formation of the most detrimental V_I^+ in $FAPbI_3$, they may also enhance the density of I_i^-, which can lead to a substantially reduced kinetic barrier of the phase transition. Hence, I-moderate growth conditions are preferable to balance the formation of these two types of defects and to optimize the stability of $FAPbI_3$-based devices. Furthermore, the incorporation of certain additives, such as Lewis bases[253], to coordinate with the uncoordinated Pb of V_I^+ would also suppress the defect-accelerated phase propagation behavior. Moreover, the FA content should also be well controlled in the precursors, since the FA-rich

growth conditions would promote the formation of FA interstitials in the perovskite lattice, which thermodynamically destabilizes the α-phase of $FAPbI_3$.

6.3.3 Stabilization of α-$FAPbI_3$ by composition engineering

Doping engineering is a feasible strategy for improving the inherent phase stability of the $FAPbI_3$ active layers. To establish a rational and general design guideline for doping engineering in perovskites, we systematically explored the doping effects on stabilizing the phase of $FAPbI_3$ perovskites. We considered various isovalent substitution dopants on all the sites, namely A-site (MA^+, Cs^+, Fr^+, Rb^+, K^+, and NH_4^+), B-site (isovalent Sn^{2+}, Ge^{2+}, Ba^{2+}, Sr^{2+}, Ca^{2+}, Cd^{2+}, and Zn^{2+}, as well as lanthanide ions of La^{3+}, Ce^{3+}, Nd^{3+}, Sm^{3+}, Eu^{3+}, and Yb^{3+}) and X-site (Br^-, Cl^-, and pseudo-halides of SCN^- and CN^-). These substitution dopants have been widely used in halide perovskites to tailor the optoelectronic and mechanical properties of the perovskite materials[36,37,39,227–229,254–256]. Additionally, we also considered unintentionally incorporated impurity interstitials, such as H_2O, O_2, H_2, and their disassociated products OH^-, H^+, O^{2-}. They are often found in the interstitial spaces of perovskite lattices[175,179,257,258].

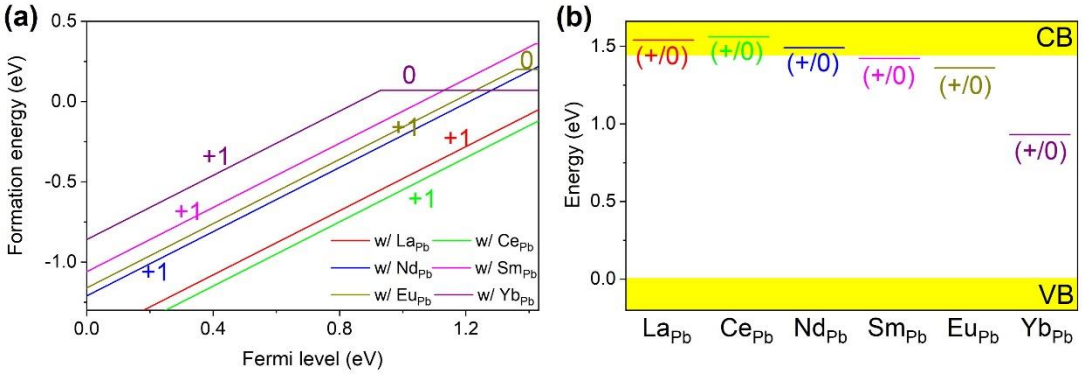

Figure 6.10. (**a**) Formation energies of Pb substituted by lanthanide ions (namely La_{Pb}, Ce_{Pb}, Nd_{Pb}, Sm_{Pb}, Eu_{Pb}, and Yb_{Pb}) in $FAPbI_3$, as a function of the Fermi level. (**b**) Transition energy levels of Pb substituted by Ln ions are plotted relative to the valence and conduction band edges of $FAPbI_3$.

Notably, unlike other isovalent candidates, lanthanide (Ln) ions are often stable in the (+3) oxidation state, which can lead to charged defect formation when substituting Pb^{2+}. The formation energy calculations suggest the positively charged state of these substitutions is stable in $FAPbI_3$, namely La_{Pb}^{+}, Ce_{Pb}^{+}, Nd_{Pb}^{+}, Sm_{Pb}^{+}, Eu_{Pb}^{+}, and Yb_{Pb}^{+} (**Figure 6.10a**). The substantially low formation energies, even in the negative region, over the whole range of the Fermi level within the bandgap, further verify the doping feasibility of Ln cations in the $FAPbI_3$ lattice. Such a high compatibility can be partially attributed to their similar ionic radius to Pb. Furthermore, the calculated transition energy levels (**Figure 6.10b**) indicate that the Ln dopants have shallow defect states except for Yb, and thus are electronically benign for $FAPbI_3$.

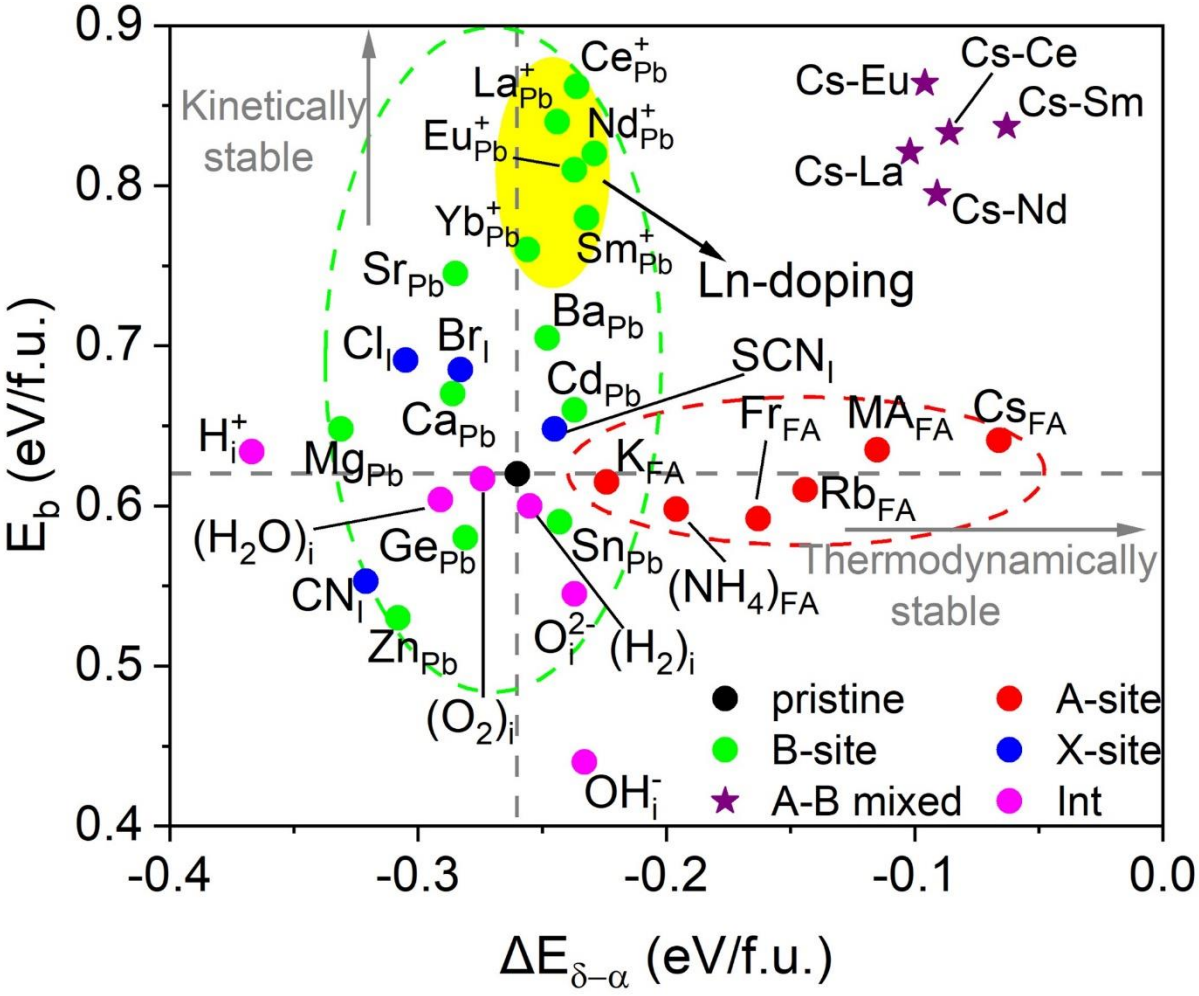

Figure 6.11. Kinetic α-δ phase transition barrier E_b and thermodynamic phase energy difference $\Delta E_{\delta-\alpha}$ of pristine $FAPbI_3$ and those with dopants and impurity interstitials. B-site cation engineering predominantly impacts the kinetics of the $FAPbI_3$ phase transition that dedicates the device longevity, as depicted by the green dashed circle (ellipse), whereas A-site doping more effectively alters the phase transition thermodynamics that can impact the perovskite crystallization, as depicted by the red dashed circle (ellipse). Moreover, the yellow region highlights various lanthanide doping and the purple stars stand for A-B mixed doping. The evolution of the bandgap and potential energy as a function of the reaction coordinate of the α-δ phase transition in the representative Cs-, Br-, Cl-, La-, and Ce-doped systems are shown in **Figure 6.12**.

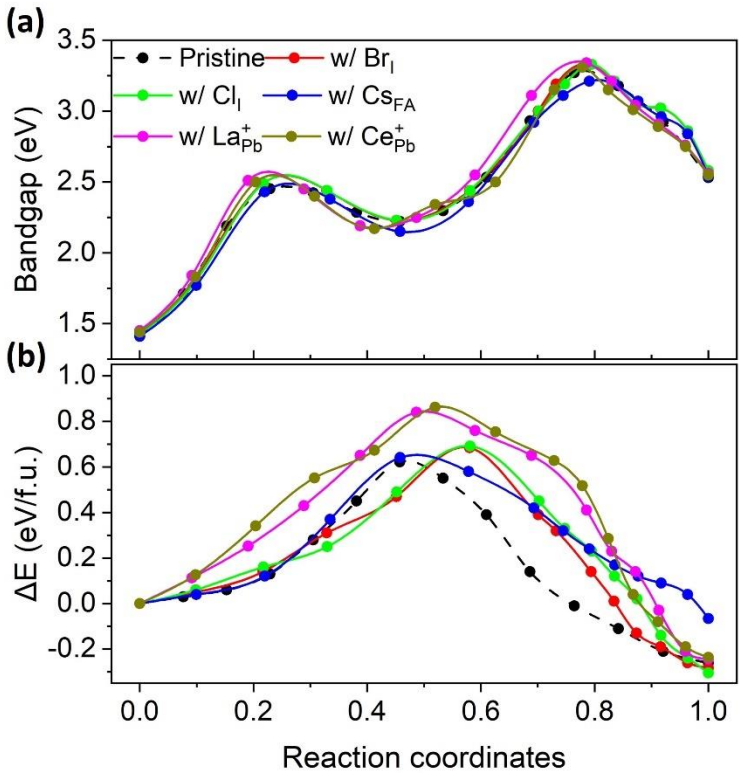

Figure 6.12. The evolution of the (**a**) bandgap and (**b**) potential energy as a function of the reaction coordinate of the α-δ phase transition in the representative Cs-, Br-, Cl-, La-, and Ce-doped $FAPbI_3$.

Figure 6.11 summarizes the phase transition barriers E_b and the phase transition thermodynamics $\Delta E_{\delta-\alpha}$ of pristine and doped (or defective) $FAPbI_3$. These intentional dopants and unintentional impurities exhibit varying effects on the phase transition of $FAPbI_3$. While atmospheric moisture-indued phase instability of $FAPbI_3$ has been experimentally reported, our results show that the water molecule itself has a negligible effect on the phase transition of $FAPbI_3$. Instead, the decomposition products of water, namely, OH^- and H^+, greatly hasten the kinetics and thermodynamics of the phase transition, respectively (**Figure 6.11**). The binding energy of H_2O with respect to isolated H^+ and OH^- ($H_2O \rightarrow H^+ + OH^-$) in $FAPbI_3$ was calculated to be -0.083 eV, implying that water disassociation in $FAPbI_3$ is energetically favorable. Light irradiation would facilitate this process and further aggravate the perovskite phase instability. Additionally, H_2 can be an effective hydrogen source for the incorporation of H^+ in $FAPbI_3$[179], though it plays an insignificant role by itself. Moreover, O^{2-}, which can be a

disassociation product of atmospheric O_2 and various oxide electron-transporting materials, would also accelerate the $FAPbI_3$ phase conversion kinetics by reducing E_b. Therefore, in addition to humidity control, minimizing the concentration of oxygen and hydrogen ions in the lattice is important to stabilize the photoactive α-$FAPbI_3$.

Interestingly, A-site doping with smaller-sized cations can dramatically suppress the thermodynamic driving force for the phase transition while almost preserving the pristine transition barrier. Indeed, previous experiments have reported a higher initial proportion of perovskite phase in the $FAPbI_3$ active layers when FA is doped with smaller-sized cations[259], due to the increased formation energy of δ-$FAPbI_3$. Such a mechanism is similar to the case of the FA vacancy as discussed earlier. Our results show that Cs, with a moderate ionic radius (1.74 Å), exhibits a higher effectiveness in increasing E_b, compared with that of MA (2.16 Å) and Fr (1.94 Å) of relatively larger ionic radius as well as the smaller NH_4 (1.43 Å), K (1.51 Å) and Rb (1.61 Å) ions. Hence, to crystallize a purer FA perovskite and thus obtain a higher initial performance of the devices, Cs would be a superior candidate for A-site cation engineering.

Among the X-site dopants, Br_I and Cl_I show a more significant improvement in the $FAPbI_3$ perovskite phase stability in kinetics, yet slightly increasing the thermodynamic energy difference between the two phases. This can be attributed to the improved stability of the sublattice as the result of the stronger Pb-Br and Pb-Cl bond than the Pb-I bond (because of the higher electronegativity of Cl and Br than I). In this case, more energy is required to convert the 3D octahedral structure to the 1D chain during the phase transition by stretching and breaking the stronger Pb-Br (Pb-Cl) bond. Experimentally, doping the $FAPbI_3$ active layers with MABr, CsBr, MACl, and CsCl additives has been a popular and efficient approach for stabilizing the α-phase $FAPbI_3$[36,43,77,227,228,230–232], though the underlying mechanisms and trends remain poorly understood[39,182]. Based on the findings discussed above, it is evident that

Br and Cl increase the activation energy for the phase transition of $FAPbI_3$, while MA and Cs improve its thermodynamic stability. Both effects synergistically stabilize α-phase $FAPbI_3$. Moreover, our results suggest that pseudo-halide SCN^- would be also a promising X-site dopant for enhancing the perovskite phase stability of $FAPbI_3$ in terms of both thermodynamics and kinetics.

For B-site cation engineering, the dopants have a positive impact on the thermodynamics of the $FAPbI_3$ phase transition with the exception of Mg, Ca, Ge, and Zn, due to their much smaller ionic radii (0.72-1 Å) than that of Pb (1.19 Å), resulting in a greater deviation of tolerance factor from the ideal range of the perovskite. As a result, their inclusion can disrupt the stability of the perovskite structure. In agreement with our predictions, experimental reports have indicated that Ca doping promotes the formation of a non-perovskite δ-$FAPbI_3$ during the initial crystallization at the dopant concentrations of 5%[256]. In contrast, most B-site dopants exhibit higher effectiveness on the kinetics of the phase transition, leading to a larger variation in E_b, as indicated by the green dashed circle in **Figure 6.11**.

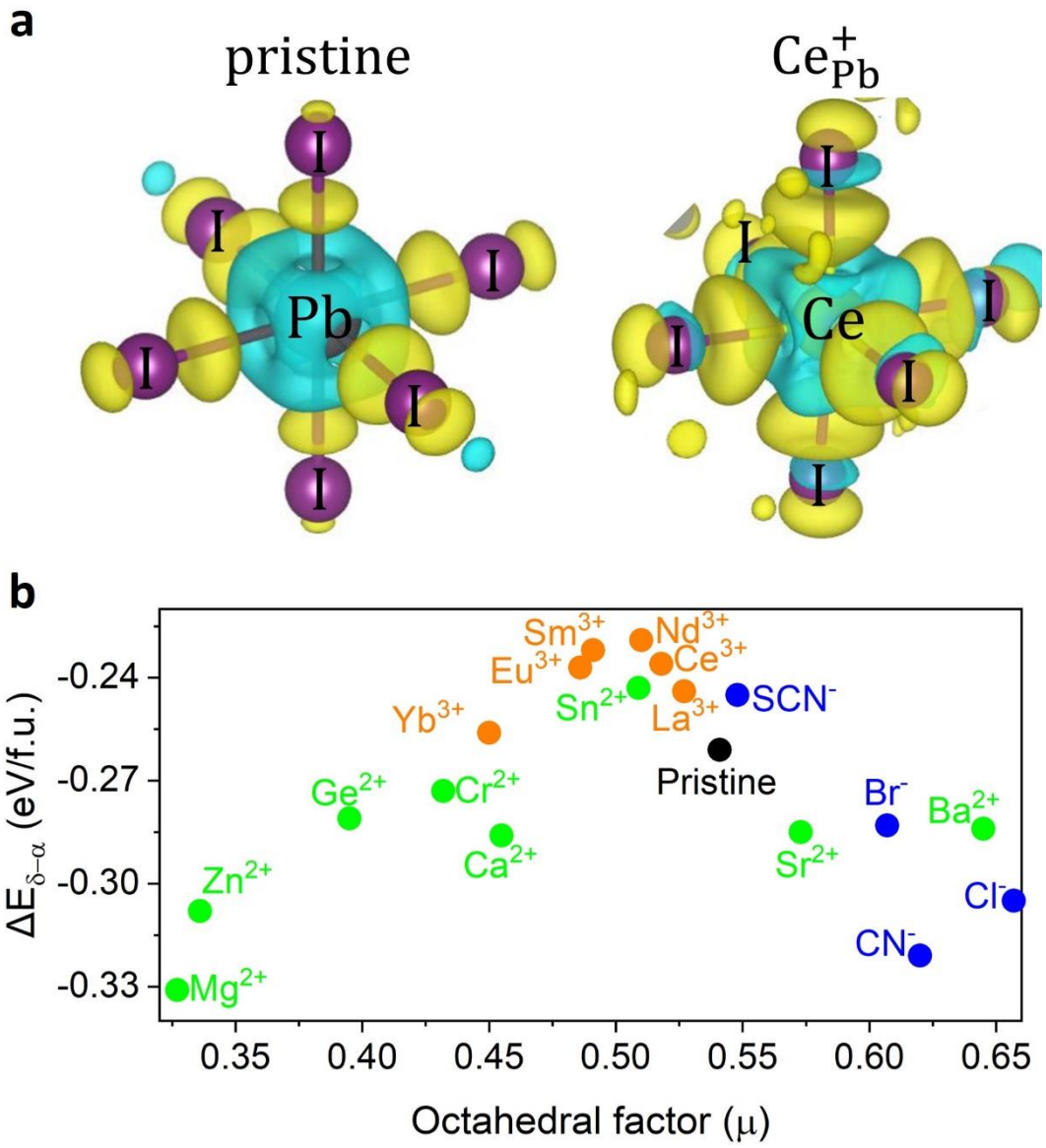

Figure 6.13. (**a**) Calculated isosurfaces of the charge density differences for PbI_6 and CeI_6 octahedra, where electrons are transferred from the yellow to the blue regions. The isosurfaces were taken at 0.01 $|e|/Å^3$. (**b**) The phase transition thermodynamics $\Delta E_{\delta-\alpha}$ of the B- and X-site doped $FAPbI_3$ as a function of the octahedral factor (μ), where the blue points stand for X-site isovalent dopants, green for B-site isovalent dopants, and orange highlights Ln dopants.

Significantly, the lanthanide (Ln) elements, which have been experimentally reported to be of benefit for the structural stability of halide perovskites[260], indeed represent ideal dopants of B-site doping for kinetically stabilizing α-$FAPbI_3$. As shown in the yellow region in **Figure 6.11**, the incorporation of Ln dopants leads to a noticeable increase in E_b with respect to the pristine $FAPbI_3$. The enhancement of E_b upon Ln doping is of the order of pristine→Yb→Sm→Eu→

Nd→La→Ce-doped systems. The enhanced transition barriers indicate improved lattice dynamic stability of α-$FAPbI_3$ upon Ln doping, which is also reflected by the reduced MSD of the inorganic skeleton in AIMD at 300K for the Ln_{Pb}-incorporated systems (**Figure 6.6b**). This is because of the stronger ionic interactions between Ln ions and the nearby I ions against large octahedral tilt and rotation during the phase transition compared with that of Pb, due to the much lower electronegativities of Ln (1.1-1.2) than that of Pb (2.3). Taking Ce as an example, a more pronounced charge redistribution occurs in CeI_6 octahedra than in PbI_6 (**Figure 6.13a**), confirming the stronger ionic bonding of Ce-I compared to the corresponding Pb-I in pristine $FAPbI_3$.

From a thermodynamic perspective, Ln-cation doping would also effectively reduce the driving force for the transition to the photoinactive δ-phase of $FAPbI_3$ as compared with other B- and X-site dopants, particularly for Nd and Sm-doped systems, even though the effectiveness is relatively smaller than that of the most A-site dopants. Regarding B- and X-site doping engineering, **Figure 6.13b** illustrates a correlation between the thermodynamic driving force variation and the octahedral factor (μ) of Pauling's rule, which is an important factor determining the coordination number of the cation and anion in stable crystal structures and is defined as the ratio of the radii of B cations and X anions in perovskites, namely $\mu = \frac{r_B}{r_X}$. In general, to stably construct the perovskite compounds of the six-fold coordinated octahedra, it requires $0.414 < \mu < 0.732$. Based on the present volcano-type relationship, we deduced that the optimal value μ (apex) for the stable $FAPbI_3$ perovskites phase would be around 0.5. Sn and Ln dopants, especially Nd, Eu, and Sm, are close to this optimal value of μ. Indeed, Sn halide perovskites typically exhibit higher phase stability in thermodynamics[158]. However, the facile oxidation of Sn^{2+} poses a serious impediment to the further development of Sn-based and Sn-doped perovskite optoelectronics operating in ambient air. B-site doping with Ln ion

represents a potential breakthrough for further stability improvement of $FAPbI_3$ perovskites and devices.

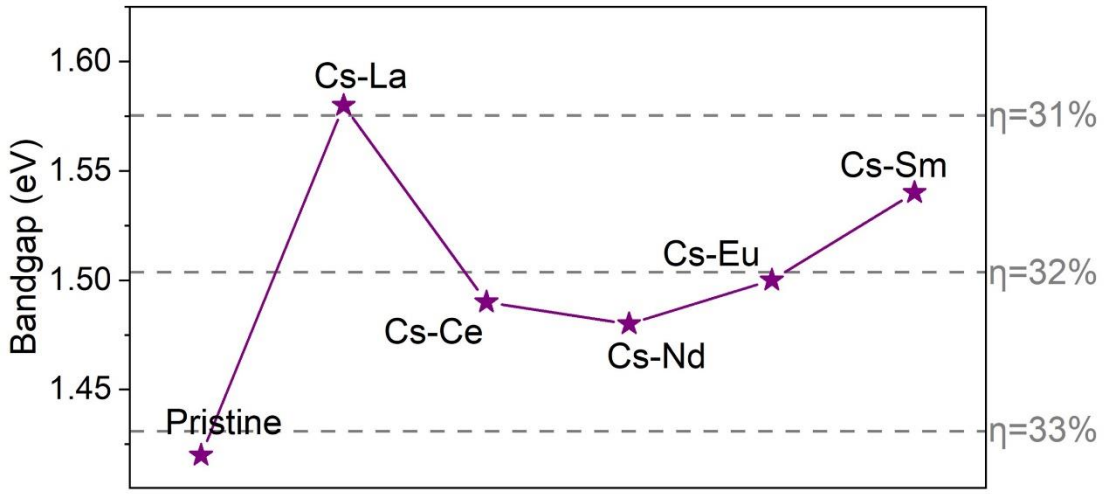

Figure 6.14. Calculated electronic bandgaps for pristine and A-B mixed-doped (namely, Cs-La, Cs-Ce, Cs-Nd, Cs-Eu, and Cs-Sm) $FAPbI_3$ based on HSE-SOC scheme. The corresponding photovoltaic efficiency limits were presented based on the detailed balance limit theory.

In addition to defect and impurity controls, the current results underline the effectiveness of proper doping engineering in stabilizing α-$FAPbI_3$. Particularly, B-site doping primarily impacts the kinetics of the $FAPbI_3$ phase transition, while A-site cation engineering is more effective in thermodynamics in controlling the phase stability of $FAPbI_3$. We thus suggest a highly stable $FAPbI_3$ perovskite active layer and the related devices by A-B mixed composition engineering from both thermodynamic and kinetic perspectives. This is confirmed by calculations demonstrating the synergic stabilizing effects of the exemplary Cs-La, Cs-Ce, Cs-Nd, Cs-Eu, and Cs-Sm doped systems (see the purple stars in **Figure 6.11**). Promisingly, based on Shockley−Queisser (SQ) limit[125], these doped perovskites still maintain the superior electronic bandgaps, which has direct implications for the observed efficiency in the conversion of solar light (**Figure 6.14**). Moreover, the findings also explain why state-of-the-art perovskite solar cells are normally based on mixed systems with the majority of $FAPbI_3$ perovskite[3,36–

[40,218], which synergistically stabilize $FAPbI_3$ perovskite and is essential for achieving long-term device operational stability.

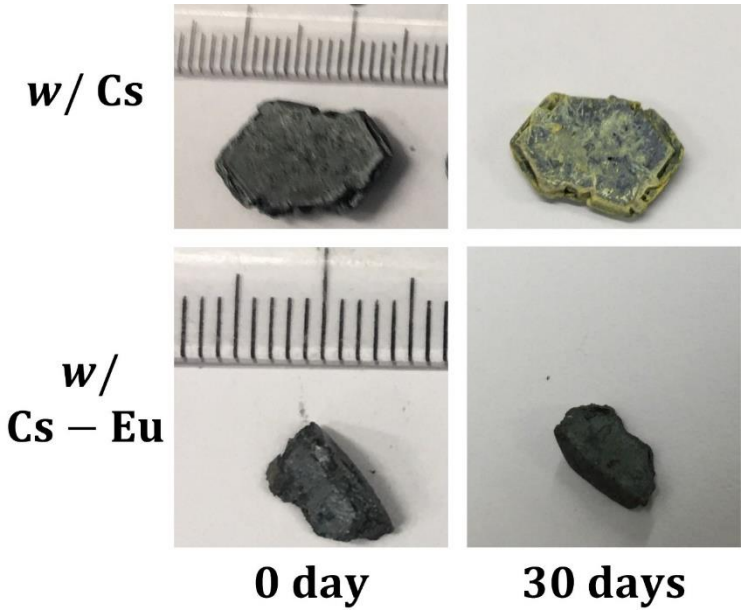

Figure 6.15. Photographs of the Cs-doped and Cs-Eu mixed-doped $FAPbI_3$ single-crystal samples, before and after a 30-day air exposure, respectively.

We noted that the majority of the proposed A-B mixed doped $FAPbI_3$ perovskites denoted by the purple stars in **Figure 6.11** have not yet been reported. To validate our theoretical findings, we pursued experimental studies on Cs-Eu mixed doping in $FAPbI_3$ as a representative example, which is predicted to significantly stabilize the α-$FAPbI_3$ - both kinetically and thermodynamically. To this end, we first grew single crystals of Cs-doped and Cs-Eu mixed-doped $FAPbI_3$ perovskites (**Figure 6.15**), and the related synthetic details are shown in the Experimental Method section. Energy-dispersive X-ray spectroscopy (EDS) measurement results on the Cs-Eu mixed-doped $FAPbI_3$ single crystal confirm the uniform distribution of the Eu element in the perovskite (**Figure 6.16**).

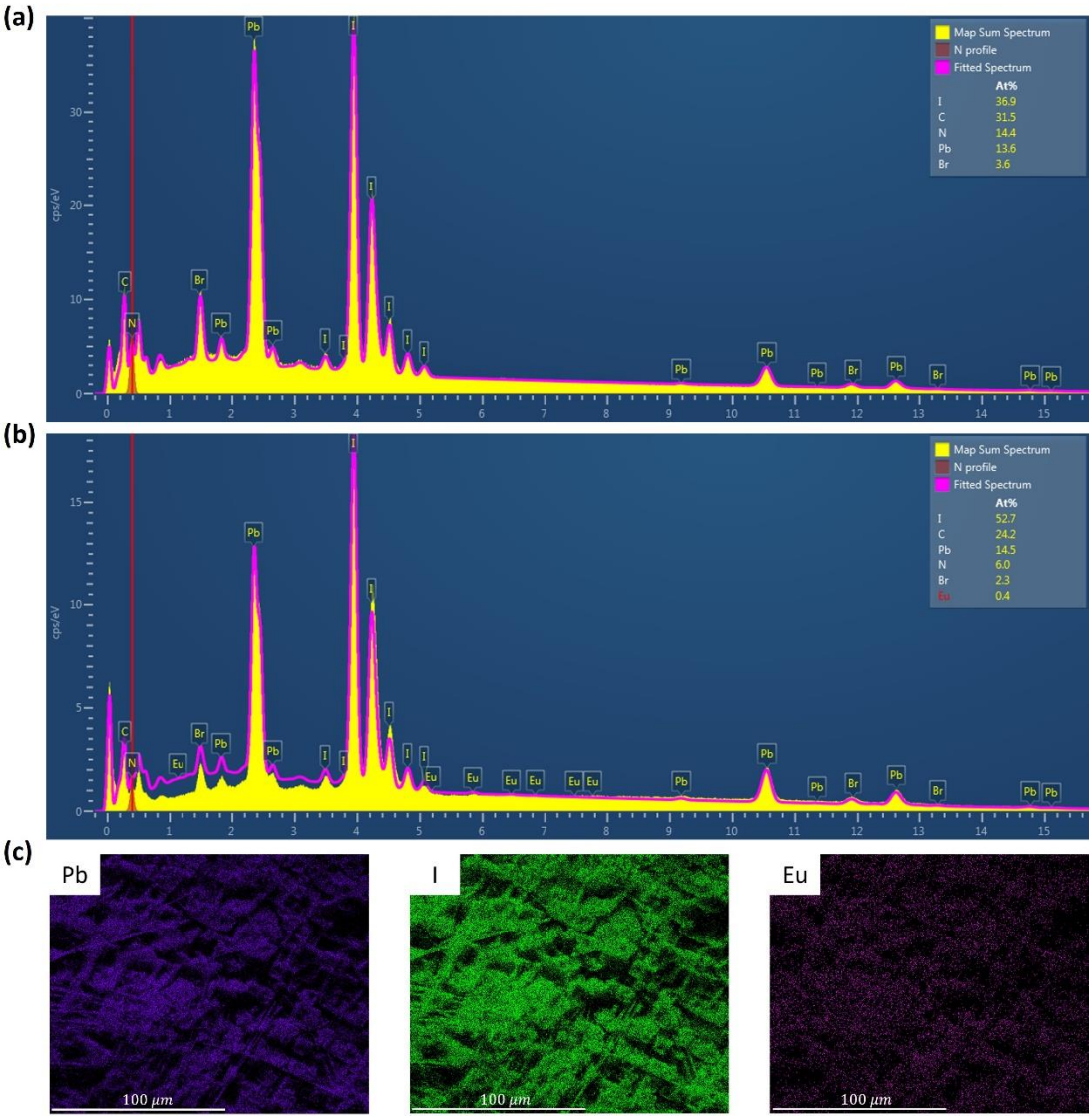

Figure 6.16. EDS of Cs and Cs-Eu doped $FAPbI_3$. EDS atomic composition of (**a**) Cs-doped and (**b**) Cs-Eu mixed-doped $FAPbI_3$ perovskite single crystals. (**c**) EDS mapping of Pb, I, Eu in the Cs-Eu mixed-doped $FAPbI_3$ perovskite single crystal.

6.3.4 Stability and optoelectronic properties of Cs-Eu mixed-doped perovskite

To assess the phase stability in the Cs-Eu mixed-doped perovskite single crystal, we then exposed the samples to air for 30 days. Initially, both as-grown samples (namely, Cs-doped and Cs-Eu mixed-doped $FAPbI_3$) exhibited black perovskite phases (α-phase) with high purity, as confirmed by the relevant X-ray diffraction (XRD) patterns (see **Figures 6.17a**,**b**). After the 30-day exposure, the Cs-doped sample visibly degraded to the yellow δ-$FAPbI_3$ phase (**Figure 6.16**). In contrast, the Cs-Eu mixed-cation-doped perovskite largely maintained the black α-

$FAPbI_3$ phase without significant changes in colour. This trend was also evident in the XRD spectra of the samples measured after 30-day and 45-day exposures. **Figures 6.17c-e** show the UV-Vis-NIR absorption spectra of the freshly prepared samples with different concentrations and those after the 30-day exposure. The optical bandgap derived from the Tauc plots exhibited a value of 1.50-1.52 eV for Cs-Eu mixed-doped $FAPbI_3$ (**Figure 6.17d**), in agreement with the value of 1.50 eV predicted by our HSE-SOC calculations. Indeed, compared with the Cs-doped $FAPbI_3$, we note that the bandgap and absorption profile of the Cs-Eu mixed-doped sample showed negligible change after 30-day exposure. Specifically, the average absorbances at 790 nm after 30-day exposure were dropped by 28.5% and 5.2% for Cs-doped and Cs-Eu mixed-doped (0.5% Eu doping) $FAPbI_3$ perovskite single crystals, respectively (see **Figure 6.17e**). Moreover, we investigated the phase stability improvement of the Cs-Eu mixed samples as a function of Eu dopant concentration. With increasing the concentration of Eu doping, the degradation of single-crystal perovskite optical properties was effectively suppressed (**Figure 6.17e**). The optimal concentration of Eu doping was tested to be 0.5%.

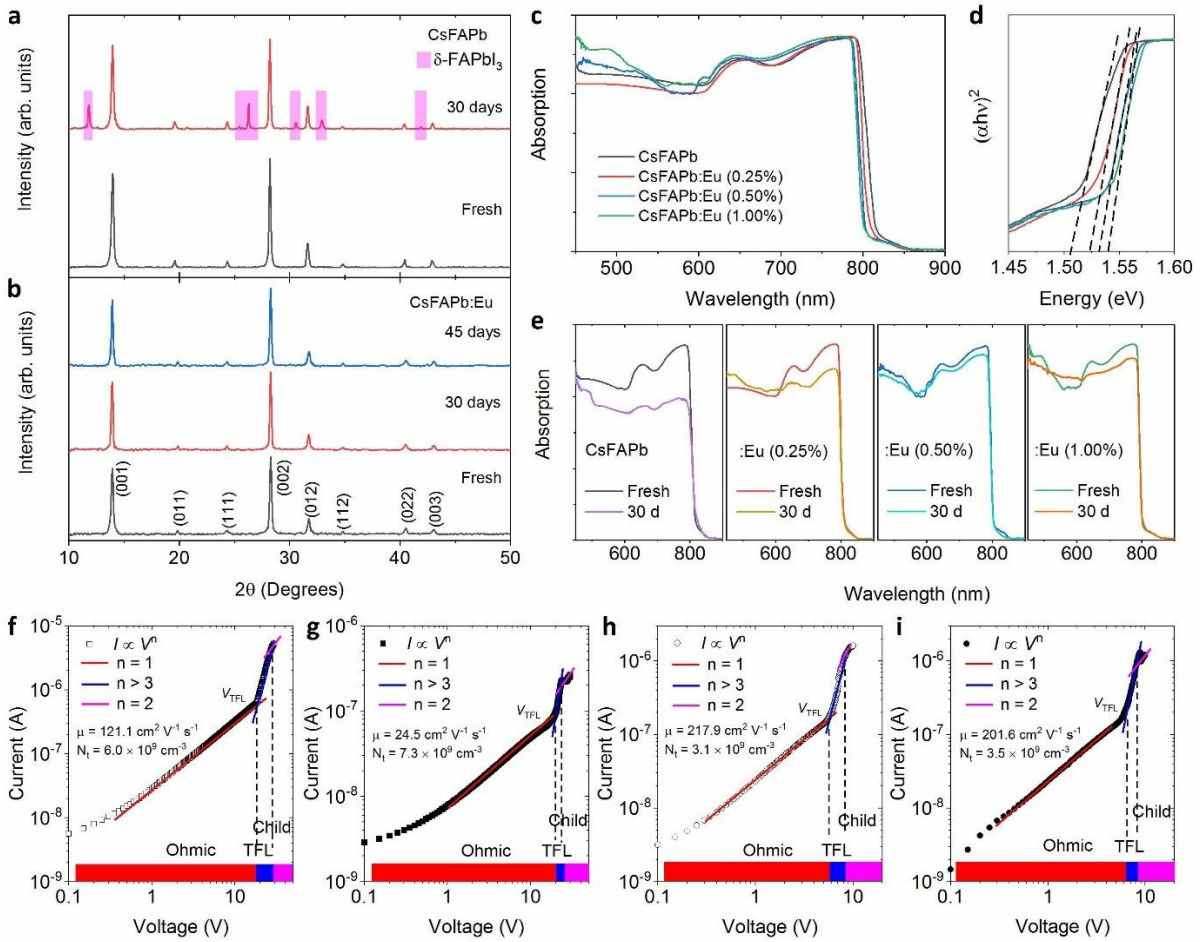

Figure 6.17. X-ray diffraction patterns of the (**a**) Cs-doped and (**b**) Cs-Eu mixed-cation-doped $FAPbI_3$ perovskite single crystals, before and after 30-day and 45-day air exposures. (**c**) UV–Vis-NIR absorption spectra of a series of freshly prepared perovskite single crystals. (**d**) The optical bandgap derived from the Tauc plots (based on the data in **c**). α is absorption coefficient, h is Planck constant, and ν is frequency of incident light. (**e**) UV–Vis-NIR absorption spectra of the Cs-doped and Cs-Eu mixed-cation-doped samples with the Eu doping concentrations of 0.25%, 0.50%, and 1.00% before and after 30-day exposure. Current−voltage (*I-V*) curves and relevant typical SCLC analyses of (**f**,**g**) Cs single-doped and (**h**,**i**) Cs-Eu mixed-doped $FAPbI_3$ perovskite single crystals, before and after a 30-day air exposure, respectively. The regions are marked for Ohmic (n =1), trap-filled limit (n > 3), and Child's regime (n = 2). V_{TFL} is the trap-filled limit voltage. We calculated the carrier mobility (μ) and trap densities (N_t) by fitting the *I-V* data.

We further investigated the carrier mobility and the trap density, which are the key semiconducting parameters for optoelectronic applications, by using the Space-Charge-Limited Current (SCLC) method[261] based on the hole-only device (see **Method Section**). Previous experimental studies[262] have shown that α-δ phase transition in $FAPbI_3$ leads to a significant degradation in carrier transport property. Indeed, our DFT calculations of the

effective masses of electrons and holes in the yellow δ-phase ($m_e^* = 0.945\, m_0; m_h^* = -1.137\, m_0$), are around 4.3 and 5.7 times higher than those in black α-phases of $FAPbI_3$ ($m_e^* = 0.218\, m_0; m_h^* = -0.199\, m_0$), respectively, also as explicitly evidenced by the substantially flatter band edges in δ-$FAPbI_3$ (**Figures 6.3c and 6.3e**). **Figures 6.17f-i** show the current-voltage (*I-V*) characteristics for the Cs single-doped and Cs-Eu mixed-doped $FAPbI_3$ single crystals in both fresh statues and after 30 days. The *I-V* curves can be divided into three regions: the first, second, and third regions stand for the ohmic (n = 1), trap-filling (n > 3), and child (n = 2) regions, respectively, where the trap density (N_t) and carrier mobility (μ) were calculated from the second and third regions (see the details in Supplementary Information). It is noted that, as compared with the Cs-doped sample ($n_t \sim 6.0 \times 10^9 cm^{-3}$; $\mu \sim 121.0\ cm^2V^{-1}s^{-1}$), a lower trap density ($n_t \sim 3.1 \times 10^9 cm^{-3}$) and a higher hole mobility ($\mu \sim 217.9\ cm^2V^{-1}s^{-1}$) were obtained for the freshly prepared Cs-Eu mixed-doped perovskite single crystal, confirming the promoting effect of Cs-Eu mixed doping on carrier dynamics of $FAPbI_3$ perovskites. After 30-day exposure, we observed a significant decline of hole mobility in Cs-doped sample ($\Delta\mu \sim 96.5\ cm^2V^{-1}s^{-1}$), as compared to that of Cs-Eu mixed-doped sample ($\Delta\mu \sim 16.3\ cm^2V^{-1}s^{-1}$), highlighting the effectiveness of A-B mixed composition engineering in stabilizing $FAPbI_3$ perovskite.

6.4 Conclusion

In summary, based on extensive first-principles atomistic calculations, we have elucidated the intricate mechanism underlying phase degradation from the photovoltaically active α phase to the inactive δ-phase in $FAPbI_3$. Our investigation not only sheds light on the critical role played by defects and impurities but also delves into potential mitigation strategies. Inherent iodine defects, namely iodine vacancies and interstitials, dramatically lower the activation barrier of the α-δ lattice transition in $FAPbI_3$, due to the compromised lattice dynamic stability and the

strong covalency induced by defects at transition states. The detrimental roles of the decomposition products of atmospheric moisture and oxygen in degrading the $FAPbI_3$ perovskite phase were also identified, rationalizing the faster phase transition of $FAPbI_3$ films under ambient air. Notably, we uncovered key compositional design principles: B-site cation engineering is a promising strategy to tailor the kinetics, whereas A-site doping predominantly impacts the thermodynamics of the phase transition of $FAPbI_3$, highlighting the synergetic perovskite phase stabilization role of A-B mixed-site doping. A significant correlation was discovered between the phase transition thermodynamics and the octahedral factor (μ) of Pauling's rule, underlining the optimal value of $\mu \sim 0.5$ for stable FA-based perovskites and suggesting co-lanthanide doping as a promising strategy for B-site cation engineering. Subsequent experimental findings support the prediction that Cs-Eu mixed-doped $FAPbI_3$, a theoretically identified superior doping candidate, exhibits superior absorption and carrier transport properties and greatly improved phase stability as compared to the Cs-doped counterpart. Overall, our study provides insights into defect control and synergetic composition engineering for developing $FAPbI_3$-based perovskite solar cells and other optoelectronic devices with superior initial device performance and highly improved long-term stability.

Chapter 7 Multiple B-site Doping Suppresses Ion Migration in Halide Perovskites

7.1 Introduction

Lead halide perovskites have recently emerged as highly promising semiconductor materials due to their remarkable optoelectronic properties and low-cost fabrication. Despite achieving a photovoltaic power conversion efficiency (PCE) exceeding 26%[263], their commercialization is largely hindered by inadequate long-term operational stability. One of the main drivers for this instability is ion migration, typically halide ions[87,88,118,247,264–267], which has been identified as a major cause of device performance degradation under operational conditions with electric field, light, and heat[85,118,150,180,236,256,266,267]. These mobile ions in the perovskite active layer are believed to be responsible for the widely observed anomalies, such as current-voltage hysteresis, slow conductivity response, and efficiency roll-off at high injection currents[85,118,266,267]. Recent experiments show that ion migration-induced internal field screening is the dominant factor in the initial efficiency loss in perovskite solar cells[268]. Suppression of ion migration is therefore crucial for achieving long-term operational stability in perovskite solar cells and other optoelectronic devices.

Various strategies, including strain[89,269–271] and compositional engineering[89,98,256,272–275], have been adopted to alleviate the migration of halide ions and improve device stability. Particularly, the ternary-stoichiometry ABX_3 perovskite structure offers a highly flexible platform for doping engineering at different atomic sites. While layer-perovskite engineering with large spacer cations effectively blocks ion migration, it disrupts the three-dimensional (3D) phases, leading to reduced charge carrier mobility and narrower absorption bands, thereby limiting the photovoltaic efficiency[49,89,118]. Many optimization approaches have been attempted with A-site or X-site substitutions to suppress the ion migration in halide perovskites without sacrificing the inherent superior optoelectronic properties[89,98,273,274], yet the issue remains inadequately

addressed. In contrast, B-site doping or alloying has been less explored due to its relatively higher formation energy, with a primary focus only on carbon group elements such as Ge, Sn, and Pb[49,275]. Notably, the wider variety of potential dopants, such as rare earth ions, alkaline earth metal ions, and transition metal ions, establishes B-site cation engineering as a promising avenue for effectively suppressing ion migration and improving the long-term stability of perovskites optoelectronics[276]. Furthermore, recent advances in B-site co-doping and multiple-element doping have demonstrated the creation of novel optoelectronic properties and a reduction in Pb toxicity for Pb-based perovskites[94,104,277,278]. This development significantly expands the scope of compositional engineering on the perovskite B-site, offering strong prospects for further improving the stability of halide perovskite materials and devices. However, a comprehensive model rationalizing how doping engineering impacts the ion migration in halide perovskites is still lacking, hindering the development of effective doping strategies to fundamentally address the prevalent ion migration in these materials.

Unlike conventional semiconductors such as GaAs and CdTe, hybrid perovskites are known for their physically 'soft' nature and highly dynamic characteristics[250]. In these materials, the inorganic octahedral lattice exhibits substantial atomic oscillations, which moderates the optoelectronic properties, particularly exciton binding energies and charge-carrier mobilities, thereby influencing the photovoltaic performance[250,279]. Previous studies on ion-conducting materials (e.g., Li-ion conductors) showed that low-frequency lattice excitations with significant atomic oscillation can facilitate ion hopping to adjacent sites[280]. Despite these observations, the impact of lattice dynamics upon the prevalent ion migration in halide perovskites remains poorly understood. Elucidating the underlying mechanism holds significance for developing design principles to effectively suppress the undesirable ion migration in halide perovskites and enhance the longevity of the corresponding devices.

In this work, through a systematic first-principles study combining density functional theory (DFT) and machine learning molecular dynamics (MLMD) simulations, we reveal the correlation between the perovskite lattice dynamics and ion migration, elucidating the underlying mechanism by which strain engineering mitigates ion migration in halide perovskites. We further demonstrate that B-site doping, especially for lanthanide (Ln) series elements and certain Group IIA alkaline earth elements, is more effective than A-site and X-site substitutions and interstitial doping in locking octahedral lattice rocking motion and mitigating undesired iodine ion migration in the prototypical $MAPbI_3$ ($MA=CH_3NH_3$) perovskite. Importantly, multiple-element B-site doping strategies, especially Eu-Yb-Ca and Sm-Yb-Ca doping, demonstrate superior effectiveness, guiding the experimental implementation of hysteresis-free perovskite single crystals with greatly improved ambient stability and optoelectronic properties.

7.2 Simulation Method

7.2.1 Computational Method

All the first-principles calculations in this work were carried out based on Density Functional Theory (DFT) in the Vienna Ab initio Simulation Package (VASP)[114] with the projector-augmented wave (PAW) method[136]. The kinetic energy cutoff of the plane-wave basis was set at 400 eV and a Monkhorst–Pack sampling of $2 \times 2 \times 2$ k-points was used for Brillouin zone integration. The DFT-D3 scheme of Grimme was adopted for the van der Waals correction[239]. For the exchange-correlation functional, the climbing-image nudged elastic band (CI-NEB) and *Ab initio* molecular dynamics (AIMD) simulations were performed based on the generalized gradient approximation of Perdew, Burke, and Ernzerhof (PBE)[110], and the reaction enthalpies and electronic bandgaps were obtained using Heyd−Scuseria−Ernzerhof hybrid functional (the mixing parameter of 0.46) with the spin−orbit coupling (HSE-SOC)[113].

To simulate the ion migration pathway, model doping lattice, and perform *Ab initio* molecular dynamics simulations, we used the 2 × 2 × 2 supercells of the tetragonal structure (384, 384, and 160 atoms for $MAPbI_3$, $FAPbI_3$, and $CsPbI_3$, respectively). All atoms were relaxed until the force on each atom was smaller than 0.01 eV/Å. The relaxed lattice parameters of the prototypical $MAPbI_3$ are 8.77 Å, 8.77 Å, and 12.77 Å, respectively, compared with the experimental values of 8.85 Å, 8.85 Å, and 12.44Å[281]. The configurations of the co- and multiple-element doped perovskites were obtained using the special-quasirandom-structures (SQS) method[282,283] implemented in the Alloy-Theoretic Automated Toolkit (ATAT) code[284]. The optimized atomic structures of the representative Eu-Ca and Eu-Yb-Ca doped $MAPbI_3$ are shown in **Figure 7.1**.

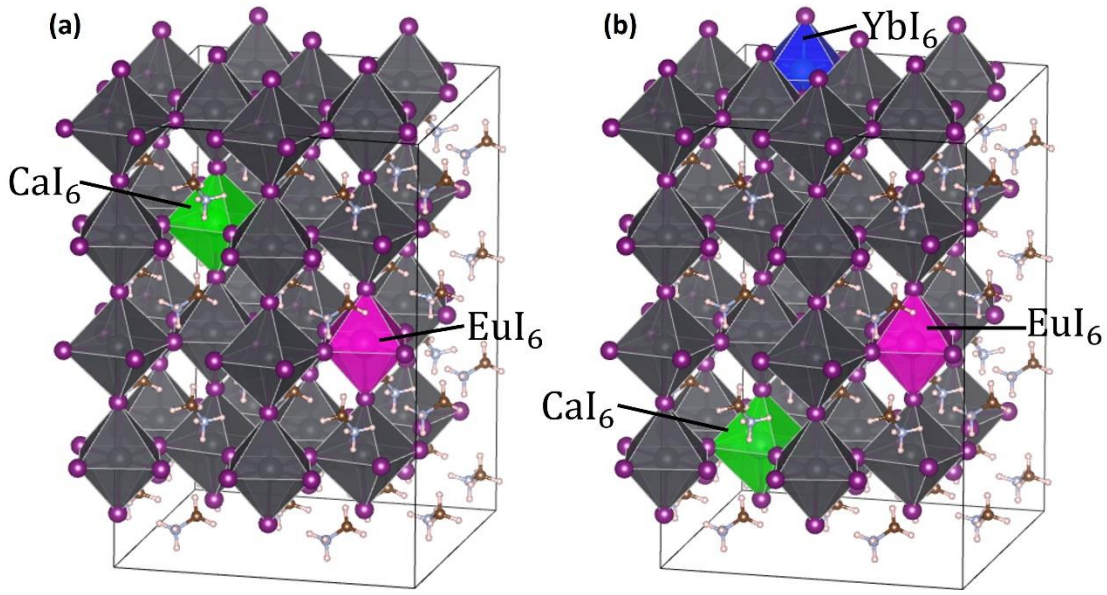

Figure 7.1. Optimized structures of the representative (**a**) Eu-Ca and (**b**) Eu-Yb-Ca doped $MAPbI_3$.

7.2.2 *Ab initio* Molecular Dynamics

Ab initio molecular dynamics (AIMD) simulations lasted 30 ps with the time step of 1 fs in the canonical (NVT) ensemble. The temperature was controlled at 300K by using the Nose-Hoover thermostat[141].

7.2.3 Diffusion Barrier Calculation

The ion migration pathway and its energy profile were calculated by the nudged elastic band (CI-NEB) method in conjunction with the climbing image method[205], as implemented using the VASP Transition State Tool. Given tetragonal perovskite lattices possess two inequivalent iodine sites, two potential migration pathways emerge, namely the equatorial-equatorial mechanism and the axial-equatorial mechanism[247,275]. We focused on the equatorial-equatorial one, which has been reported to exhibit a relatively lower migration barrier and thus serves as the dominant migration mechanism in halide perovskites[247,275]. For each pathway, eight intermediate images are linearly incorporated between the initial and final states of relaxed structures. The migration barriers were calculated by evaluating the energy difference between the diffusing species in their ground-state configuration and at the transition state during the migration. To investigate the iodine migration barrier in doped systems, we focused on that at the impurity center for reference. Additionally, to minimize the impact of MA-induced dipole polarization on the resulting migration barriers[285], we considered migration pathways that have a similar local MA arrangement (taking the interstitial Na_i-doped, and substitutional Eu- and Cl-doped systems as examples), as shown in **Figure 7.2**. Noted that a higher B-site dopant concentration was selected in the theoretical studies, compared to experimental conditions, to balance computational feasibility with trend observation. This approach, commonly used in computational studies, effectively demonstrates the influence of B-site doping on perovskite stability and provides qualitative insights into dopant behavior.

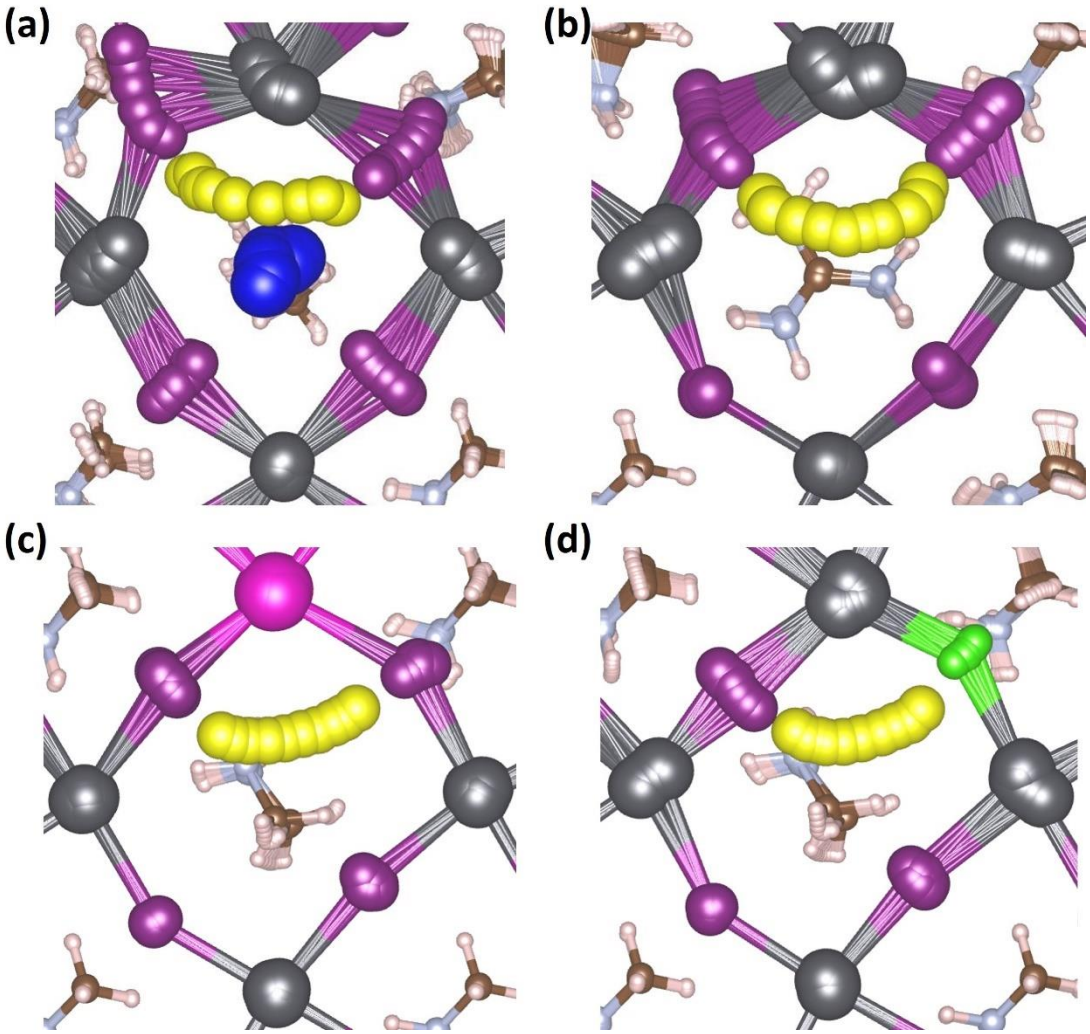

Figure 7.2. The migration of iodine ion in the representative (**a**) interstitial Na_i-doped, and (**b**) substitutional GA-, (**c**) Eu- and (**d**) Cl-doped $MAPbI_3$ lattices to the adjacent lattice site via interstitial mechanisms based on the NEB simulations. Here, grey, pink, purple, green, blue, brown, light cyan and white spheres represent lead, europium, iodine, chlorine, sodium, carbon, nitrogen and hydrogen atoms respectively. The yellow spheres highlight the diffusing iodine ions, and the red arrows point to the direction of iodide migration in the lattice.

7.2.4 Machine Learning Molecular Dynamics

Machine Learning Molecular Dynamics **(**MLMD)[243,244] was performed as implemented in VASP. All the datasets were trained based on the on-the-fly hybrid AIMD and MLMD calculations. In this scheme, first-principles *ab initio* calculations will be conducted when local molecular environments are significantly different from those already stored as the training data. The force field was generated with a cutoff radius of 7 Å for the angular descriptor and a width of 0.5 Å of Gaussian functions for broadening the atomic distributions of the radial

descriptor. In this study, Machine Learning Force Field (MLFF) was trained in a NVT ensemble with a time step of 1 fs. Specifically, the training involves 50-ps NVT simulations at 200 K, 300 K, 400 K and 500 K for the 2 × 2 × 2 (384-atom) supercells of the pristine and (Eu, Yb, Ca, Eu-Ca, and Eu-Yb-Ca) doped $MAPbI_3$, and those containing a I_i^-. Based on the obtained datasets of MLFF, 1.5 ns NVT-MLMD simulations with a time step of 1 fs were run for the 384-atom pristine and doped $MAPbI_3$ with I_i^-.

7.2.5 Sample Preparation

The $MAPbI_3$ perovskite single crystals were grown using the inverse temperature crystallization method. Specifically, a stoichiometric molar ratio of precursor solution (1.0 M) was prepared by dissolving MAI (10.0 mmol) and PbI_2 (10.0 mmol) compounds in 10 ml γ-butyralactone (one-step process). After stirring at 60 °C for 12 h, the mixed solution was filtered through a 0.22 μm polytetrafluoroethylene filter and transferred into glass vials. Thereafter, the glass vials with the filtered solution were placed on the hot plate heated to 95 - 110 °C and kept this temperature for 3 - 5 h. Then, the $MAPbI_3$ crystals would be formed in the crystallizing dish. For B-site-doped (Ca, Eu, and Ca/Eu) MA,Pb-based perovskite single crystals, a small amount of CaI_2, EuI_2, and their mixture was dissolved into the precursor solution of $MAPbI_3$ at a specific concentration to form MAPb(:B-site doping)I_3 perovskite single crystals. The concentration of B-site dopants in the perovskite solution is calculated at 0.5% according to the molar ratio with Pb.

7.2.6 Characterizations

XRD measurements on the halide perovskite powder (by gridding the single crystals into powders) were performed using PANalytical Pro Powder Diffractometer with Cu Kα (wavelength of 1.5418 Å) X-ray source. UV-Vis absorption spectra were recorded by using an

Agilent Cary 5000 UV–vis–NIR spectrophotometer. SEM and EDS testing were carried out using Zeiss ULTRA plus under the operating voltage of 20 kV. The hole-only devices with vertical Au/Perovskite/Au structure were fabricated for *I-V* measurements and SCLC analyses. In detail, an 80-nm gold (Au) anode was deposited on the top surface of the perovskite single crystals by thermal evaporation (AJA ATC-1800-E e-beam thermal evaporator). Then, a 105-nm Au cathode was deposited on the bottom surface of the single crystal samples. The devices with lateral Au/Perovskite/Au structure were fabricated for the voltage-sweep-rate-dependent *I-V* measurements, with the aim of the hysteresis analyses. Specifically, the 105-nm Au electrodes were deposited on the surface of the perovskite single crystal samples with the shadow marks. The *I-V* measurements of all the perovskite single crystals were carried out using a two-terminal probe station (Everbeing Int'l Corp.) and a 4200A-SCS Parameter Analyzer.

7.2.7 SCLC Analyses

We performed current–voltage (*I–V*) measurements to assess the charge transport properties and trap behaviors of all types of MA,Pb-based perovskite single crystals (including the pristine, Ca-, Eu-, and Cs-Eu co-doped samples). The space-charge-limited-current (SCLC) analyses were carried out based on the obtained *I-V* data. As shown in **Figures 5e,5f** in the main text and **Figure S13** as shown above, three regions can be clearly identified in the *I–V* curves, including Ohmic ($n = 1$), trap-filling ($n > 3$), and Child's ($n = 2$) regions.

At the low applied voltage, the *I–V* curves obey Ohm's law, that is, *I* values increase linearly with V values. Following the Ohmic region, the curves exhibit the rapid nonlinear rise in current values starting at the point of trap-filled limit (TFL) voltage V_{TFL}, indicating the transition into the trap-filling region. In the second region, all the trap states are expected to be filled by the injected carriers. The trap density (N_t) can be evaluated by the following equation:

$$N_t = \frac{2V_{\mathrm{TFL}}\varepsilon\varepsilon_0}{eL^2}$$

in which ε is the relative dielectric constant materials, ε_0 is the vacuum permittivity, e is the electronic charge, and L represents the thickness of the single crystals.

In the third region (Child's region), which shows trap-free characteristic at high bias, the I-V curves follow the Mott–Gurney's SCLC theory expressed by the following equation:

$$J = \frac{9\mu\varepsilon_0\varepsilon V^2}{8L^3}$$

where μ is the carrier mobility, J is current density, and V is the corresponding applied voltage. Thereby, the μ can then be obtained through the following equation:

$$\mu = \frac{8L^3}{9\varepsilon_0\varepsilon}\frac{\partial J}{\partial(V^2)}$$

7.3 Results and Discussions

7.3.1 Intricate Interplay Between Inherent Lattice Dynamics and Ionic Transport in Halide Perovskites

We first revisited and compared the interstitial-mediated iodine migration mechanism (I_i^-), which is believed as the most common ion migration process[87,88,247,264–266], in three common halide perovskite materials, namely, hybrid $FAPbI_3$ (FA=$HC(NH_2)_2$, formamidinium) and $MAPbI_3$ (MA=CH_3NH_3, methylammonium), and inorganic $CsPbI_3$. In tetragonal perovskite lattices, the two inequivalent iodine sites give rise to two potential migration pathways, namely the equatorial-equatorial mechanism and the axial-equatorial mechanism[247,275]. We focused on the equatorial-equatorial pathway, which has been reported to exhibit a relatively lower migration barrier and thus serves as the dominant migration mechanism in halide perovskites[247,275]. **Figure 7.3a** shows the minimum energy paths (MEP) for interstitial iodine migration, examined by using the climbing image nudged elastic band (CI-NEB) method. The

calculated migration barriers for these three perovskites are present in **Figure 7.3b**. As can be seen, iodine interstitials are highly mobile in the three perovskites, with the calculated migration barriers comparable to those of fast ion-conducting materials, e.g., Li-ion conductors[286]. Consistent with previous calculations[247] and experimental observations[287,288], the migration of I_i^- in $MAPbI_3$ is faster than in the other two perovskite systems. In comparison, $CsPbI_3$ exhibits the highest migration barrier for I_i^-, even though spatially $CsPbI_3$ with the smallest Cs cation possesses the largest interstitial void. The void cavity diameters[289] were estimated by calculating the average distance between the centers of the A-site cation to the nearby Pb (d_{A-Pb}), then subtracting their effective ionic radius (r_A and r_{Pb}), namely $d_{A-Pb} - r_A - r_{Pb}$. The calculated void sizes are 2.23 Å for $CsPbI_3$, 1.79 Å for $MAPbI_3$, and 1.86 Å for $FAPbI_3$. Additionally, $CsPbI_3$ has the shortest diffusion pathway (3.56 Å for $CsPbI_3$, 4.29 Å for $MAPbI_3$, and 4.57 Å for $FAPbI_3$ between two neighbouring equilibrium sites), which is conventionally expected to facilitate the fast interstitial ion motion due to due to reduced steric hindrance. The seemingly counterintuitive correlation between barrier energy and geometric factors indicates that other factors play a more important role in impacting ion migration in halide perovskites.

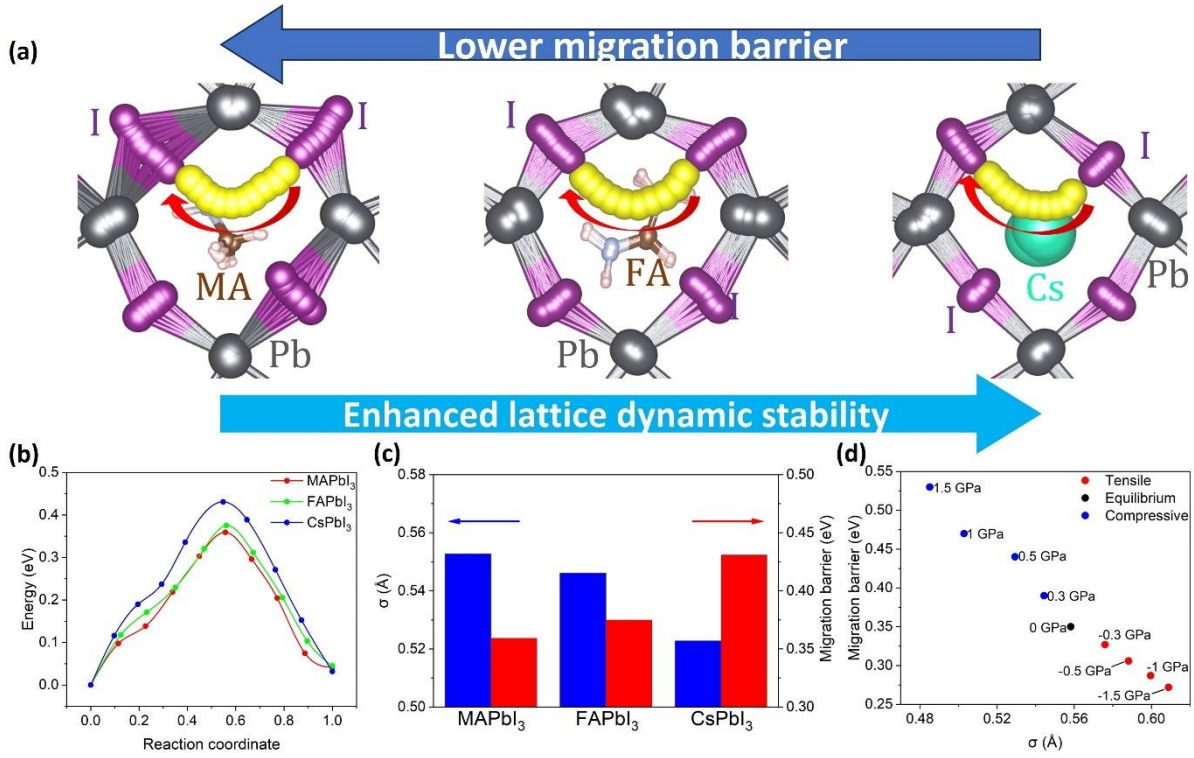

Figure 7.3. (**a**) The migration of interstitial iodine I_i^- ions in (left) $MAPbI_3$, (middle) $FAPbI_3$, and (right) $CsPbI_3$ lattice to the adjacent lattice site based on the NEB simulations. Here, grey, purple, cyan, brown, light blue and white spheres represent lead, iodine, caesium, carbon, nitrogen and hydrogen atoms, respectively. The yellow spheres highlight the diffusing iodine ions, and the red arrows point to the directions of iodide migration in the lattices. (**b**) Calculated ion migration energetic profiles for interstitial iodide in $MAPbI_3$, $FAPbI_3$ and $CsPbI_3$. (**c**) Average standard deviations (σ) of inorganic PbI_6 octahedral lattice from the equilibrium positions in $FAPbI_3$, $MAPbI_3$, and $CsPbI_3$ perovskites from AIMD simulation at 300K. (**d**) Migration barrier of I_i^- in the prototypical perovskite $MAPbI_3$ under the applied hydrostatic pressure as a function of the average standard deviations (σ) for the positions of inorganic PbI_6 octahedral lattice in AIMD trajectories at 300 K.

Previous studies on ion-conducting materials indicate a complex interplay between lattice dynamics and ion migration[280]. Indeed, the migration of I_i^- in perovskites involves significant structural relaxation of the host inorganic PbI_6 octahedral lattice (**Figure 7.3a**). This is intuitively related to the dynamic disorder within halide perovskites[267]. To quantitively characterize the lattice dynamics properties of the three perovskites, we performed AIMD simulations at room temperature and analysed the average standard deviations (σ) for the positions of the host inorganic PbI_6 octahedral lattice in the trajectories[279] through $\sigma =$

$\sqrt{\frac{\sum_{i=1}^{n}\sum_{j=1}^{m}(r_{i,j}-r_i)^2}{nm}}$. Here, r_i and $r_{i,j}$ stand for the position of host atom i (Pb/I) before and after j units of simulation time; n and m for the total number of Pb/I atoms and of steps of the AIMD simulation, respectively. A larger deviation implies stronger atomic vibration from the equilibrium position, suggesting enhanced dynamic disorder of the PbI_6 octahedral skeleton and reduced lattice stability.

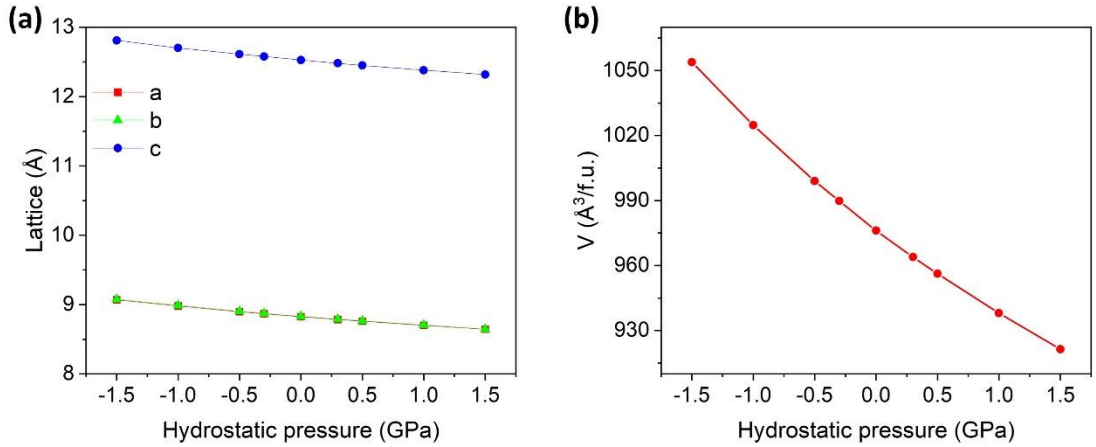

Figure 7.4. Changes in (**a**) lattice parameters (a, b, and c) and (**b**) volume of $MAPbI_3$ as a function of the applied hydrostatic pressure.

A-site cation indirectly impacts perovskite lattice stability. As shown in **Figure 7.4**, $MAPbI_3$ exhibits the lowest lattice dynamic stability, followed by $FAPbI_3$ and then $CsPbI_3$. A similar trend was observed in the previous studies[250,279]. Compared with organometal-based perovskites, the smaller Cs cations in all-inorganic $CsPbI_3$ lead to shorter Pb-I bonds and stronger ionic interactions within the inorganic lattice, thereby increasing the lattice dynamic stability. $FAPbI_3$ displays a slightly smaller amplitude of rocking motion of the Pb-I octahedron as compared to $MAPbI_3$, which can be attributed to weaker *s-p* antibonding coupling, resulting in a relatively stronger Pb-I ionic bond in FA-based perovskite[173]. Significantly, across these three perovskite systems, an increase in the lattice atomic dynamic deviation (σ) correlates

with higher ion migration barriers of I_i^-, as shown in **Figure 7.3c**, suggesting a link between octahedral lattice dynamic stability and ion migration in halide perovskites.

Halide perovskites, known for their lattice softness, are sensitive to pressure strain. To further explore the correlation between lattice and ion dynamics, we applied hydrostatic pressures ranging from −1.5 to 1.5 GPa on the prototypical $MAPbI_3$ and studied the migration behaviour of iodine interstitial. Negative pressure induces expansion, while positive pressure causes compression of the perovskite lattice, with the optimized lattice parameters and volumes shown in **Figure 7.4**. As shown in **Figure 7.3d**, the standard deviation σ of the inorganic PbI_6 octahedral lattice is indeed highly responsive to this modest stress range, comparable to and even surpassing the impact of the complete substitution of the A-site cation (**Figure 7.3c**). The calculated migration barriers for I_i^- show that the applied compressive strain leads to enhanced barriers, whereas the applied tensile strain reduces them. Generally speaking, compressive strain reduces the unit cell volume and lattice void space, thereby increasing the migration barrier. More importantly, the migration barriers visibly align with the average standard deviations (σ) of the host PbI_6 octahedral lattice in **Figure 7.3d**, reaffirming the critical role of lattice dynamics in the interstitial iodine migration. Specifically, compressive strain restricts the oscillation of the octahedra and diminishes local structural distortions, which in turn elevates the energy required to overcome the transition state for iodine migration. In contrast, tensile strain increases the diffusion space and lowers lattice dynamic stability, collectively promoting iodine migration through the perovskite lattice. Indeed, experiments have shown that the compressive strain mitigates the ion migration[269,270], and tensile strain increases the ion migration in the perovskite layers[271], though the detailed atomic-scale mechanism remains not fully understood. This relationship between octahedral dynamics and migration illustrates the intricate interplay between inherent lattice dynamics and ionic transport in halide perovskites.

7.3.2 Elemental Doping Strengthens the Perovskite Lattice

Alternatively, elemental doping offers a viable strategy to locally strengthen the lattice framework and mitigate ion migration in halide perovskites. As shown in **Figure 7.5**, 32 types of cations and anions were investigated, as substitutional and interstitial dopants at a concentration of 3.13%, to systematically assess the doping effect on the ion migration of I_i^- in the prototypical $MAPbI_3$. These substitutional dopants include A-site (FA^+, Cs^+, Rb^+, Fr^+, $GA^+ = \text{Guanidinium}$, and $DM^+ = \text{Dimethylammonium}$) in red, B-site ($Sn^{2+}$, Ge^{2+}, Ba^{2+}, Sr^{2+}, Ca^{2+}, Cd^{2+}, Zn^{2+}, Au^+, Ag^+, Bi^{3+}, Sb^{3+} La^{3+}, Ce^{3+}, Nd^{3+}, Sm^{2+}, Eu^{2+}, Tm^{2+}, Yb^{2+}) in green, and X-site (Br^-, Cl^-, F^-, and pseudo-halides of SCN^- and CN^-) in blue, and the interstitial dopants (Li_i, Na_i, K_i, and Rb_i) in magenta. Some of these dopants have been reported to be successfully incorporated into perovskite lattice and somewhat suppress ion migration behavior (such as FA^+, Cs^+, GA^+, Br^-, Cl^-, Sn^{2+}, Ca^{2+}, and Bi^{3+}, Rb_i and K_i)[89,98,256,272–275,290,291], while others have not yet been investigated and thus require further verification.

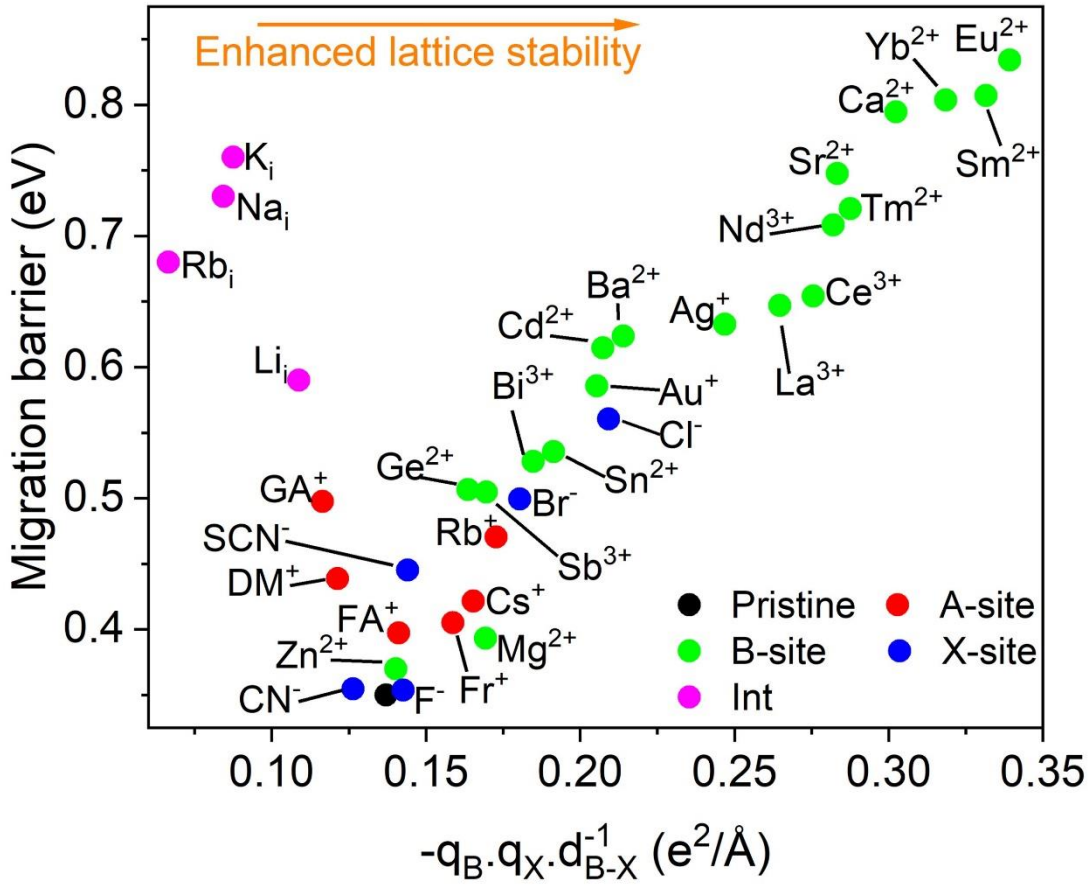

Figure 7.5. The interstitial iodine migration barriers in the doped and pristine $MAPbI_3$ as a function of the lattice ionic interaction term $-\frac{q_M q_X}{d_{B-X}}$. Red, green, blue, magenta and black dots denote substitutional doped at A-, B-, X-site, and interstitial doped and pristine perovskite, respectively. d_{B-X} represents the equilibrium average bond length of B- and X-site ions of the octahedron, and q_M and q_X are the valence states of the B- and X-site ions based on Bader charge analyses. To minimize the impact of MA-induced dipole polarization on the resulting migration barriers[285], we considered migration pathways that have a similar local MA arrangement (taking the interstitial Na_i-doped, and substitutional GA-, Eu-, and Cl-doped systems as examples), as shown in **Figure 7.2**.

The $-\frac{q_B q_X}{d_{B-X}}$-migration barrier map was constructed, outlining all the doped and pristine $MAPbI_3$ systems, as shown in **Figure 7.5**. Note that the term $-\frac{q_B q_X}{d_{B-X}}$ is closely related to the Madelung energy, namely, $U_{Mad} = -\alpha\frac{q_B q_X}{d_{B-X}}$, which is extensively utilized to describe the strength of Coulombic interactions in perovskite crystals (given that the ionic interaction is jointly influenced by both the bond length and the valence states of the ions involved). Here, α, $q_B(q_X)$, and d_{B-X} stand for the Madelung constant for the perovskite structure (ABX_3), and

the equilibrium average ionic charge states and bond length of B cation and X anion, respectively. To explicitly gain atomistic insights into how dopants strengthen the perovskite lattice, the ionic interaction term $-\frac{q_B q_X}{d_{B-X}}$ was calculated for the octahedron of the doping center, at which we determined the migration barrier for I_i^- (see **Figure 7.6**). A larger $-\frac{q_B q_X}{d_{B-X}}$ value indicates enhanced ionic attraction and thus lattice stability induced by the dopant. To determine q_B and q_X, we performed Bader charge analyses on both pristine and doped perovskites to ascertain the absolute valences of the doping element and bonded host ions.

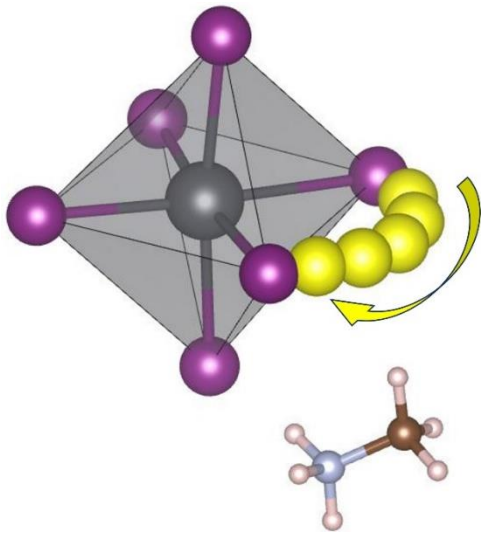

Figure 7.6. Schematics for the local BX_6 octahedron of the doping center for calculating the lattice ionic interaction term $-\frac{q_B q_X}{d_{B-X}}$. The yellow spheres highlight the simulated diffusing iodine ions, and the yellow arrows point to the direction of iodide migration in the lattice.

Interstitial dopants typically act as steric hindrance agents, narrowing the diffusion pathway of mobile ions (see **Figure 7.2a**). Hence, larger dopants would lead to higher migration barriers for I_i^-. On the other hand, we noted that the insertion of larger interstitial impurities causes lattice expansion and weakens the Pb-I bonds, resulting in lower lattice stability and increased octahedral dynamic disorder (see the magenta dots in **Figure 7.5** and **Figure 7.7**), which would facilitate iodine ion migration to some extent. The combination of these effects leads to that

moderate-sized Na and K are more effective alkali candidates for interstitial engineering to impede ion migration in perovskites. A similar effect was observed for the A-site substitution with larger-size cations (e.g., GA^+ and DM^+) (see a significant curved diffusion pathway that is bowed out of the Pb/I plane in **Figure 7.2b**), resulting in a higher migration barrier, though it somewhat weakens the ionic interaction within the octahedral lattice. The low lattice stability and pronounced octahedral dynamic disorder induced by these dopants (**Figure 7.7**) have critical implications on the optoelectronic performance of the perovskites. Specifically, the electronic bandgap, which directly impacts photovoltaic behavior, is associated with Pb-I bond hybridization[104]. This enhanced electronic disorder proves detrimental to charge carrier transport in the perovskite active layers[250].

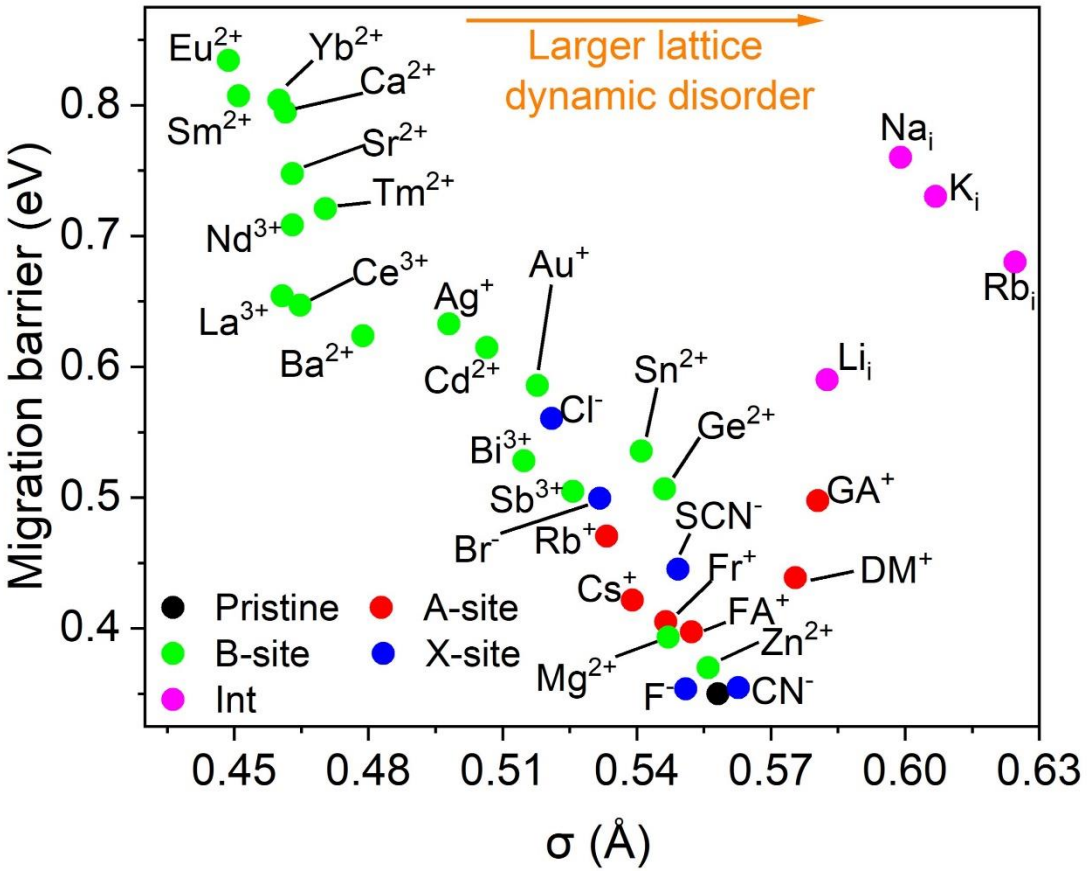

Figure 7.7. The iodine migration barriers via interstitial mechanisms in the doped and pristine $MAPbI_3$ as a function of the average squared derivations (σ) of inorganic octahedral lattice at 300 K in the pristine and various single-doped $MAPbI_3$ perovskites at the impurity concentration of 3.13%.

In contrast to interstitial doping, which impedes iodine motion by spatially blocking ion diffusion channels, substitutional doping (except with larger A-site dopants) may play a more important role in chemically strengthening perovskite lattice, thereby influencing ion migration. A roughly linear trend was observed for the substitutional dopants: the migration barrier increases as the $-\frac{q_B q_X}{d_{B-X}}$ for the local octahedron is enhanced, supporting the generalization of the proposed relationship between perovskite lattice stability and ion dynamics (also evidenced by the reduced lattice dynamic disorder in AIMD trajectories for the substitutionally doped system in **Figure 7.7**). Although A-site dopants do not directly bond with the Pb-I lattice, they indirectly influence the stability of the octahedral lattice by modulating the B-X bond length, with Rb and Cs dopants exhibiting superior effectiveness in mitigating iodine migration. Notably, B-site doping significantly enhances the rigidity of the inorganic PbI_6 octahedron network, leading to greater lattice stability and effectively reducing the mobility of iodine ions compared to alterations at either the A- or X-sites. In particular, low-electronegativity metals from the Ln-series and Group IIA (alkaline earth) increase the migration barrier by more than 90% compared to the pristine barrier.

7.3.3 Ion Migration Suppression through Multiple B-site Doping

The Goldschmidt tolerance factor (τ) and octahedral factor (μ), derived from Pauling's rule, are two important geometric quantities commonly used to assess the formability of cubic perovskite ABX_3 crystal structures. They are defined as $\tau = \frac{(r_A + r_X)}{\sqrt{2}(r_B + r_X)}$ and $\mu = \frac{r_B}{r_X}$, where r_A, r_B, and r_X are the ionic radius of A-site, B-site and X-site ions, respectively. A stable 3D perovskite structure generally requires $0.80 < \tau < 1.00$ and $0.41 < \mu < 0.75$. However, previous

studies have indicated that some materials within such stable ranges are unstable, while certain materials outside these ranges can indeed be stable[292], underscoring the limitations of accurately screening emerging stable perovskites using the simple empirical τ or μ factors alone. As shown in **Figure 7.8**, we identified a notable correlation between the migration barrier and $\mu\tau$ for promising B-site doping candidates. From a fundamental perspective, $\mu\tau$ improves the sensitivity of geometric descriptors by integrating the combined effects of perovskite geometry and octahedral coordination, surpassing the predictive power of single τ and μ factors in predicting perovskite crystallographic stability. The barrier-τ and barrier-μ relationships are also presented in **Figure 7.9** for reference. Importantly, the combined effect of ionic electronegativity and size leads to such a trend, pointing to key criteria for selecting doping candidates. Higher migration barriers were observed in systems doped at the B-site with cations of low electronegativity and moderate ionic radius (specifically within the range of $0.43 < \mu\tau < 0.46$, compared to the nominal wider stable range of $0.33 < \mu\tau < 0.75$), especially in cases involving Sm, Eu, Yb, Sr, and Ca doping. Conversely, cations with larger (e.g., Ba) or smaller (e.g., Mg) sizes, or higher electronegativity (e.g., Bi, Sn, and Tm) were found to be less effective, rendering them suboptimal choices for applications. The current results further underscore the significant effectiveness of B-site doping with certain Group IIA alkaline earth and Ln-series metals in stabilizing the perovskite lattice and reducing prevalent iodine migration in the perovskite active layer.

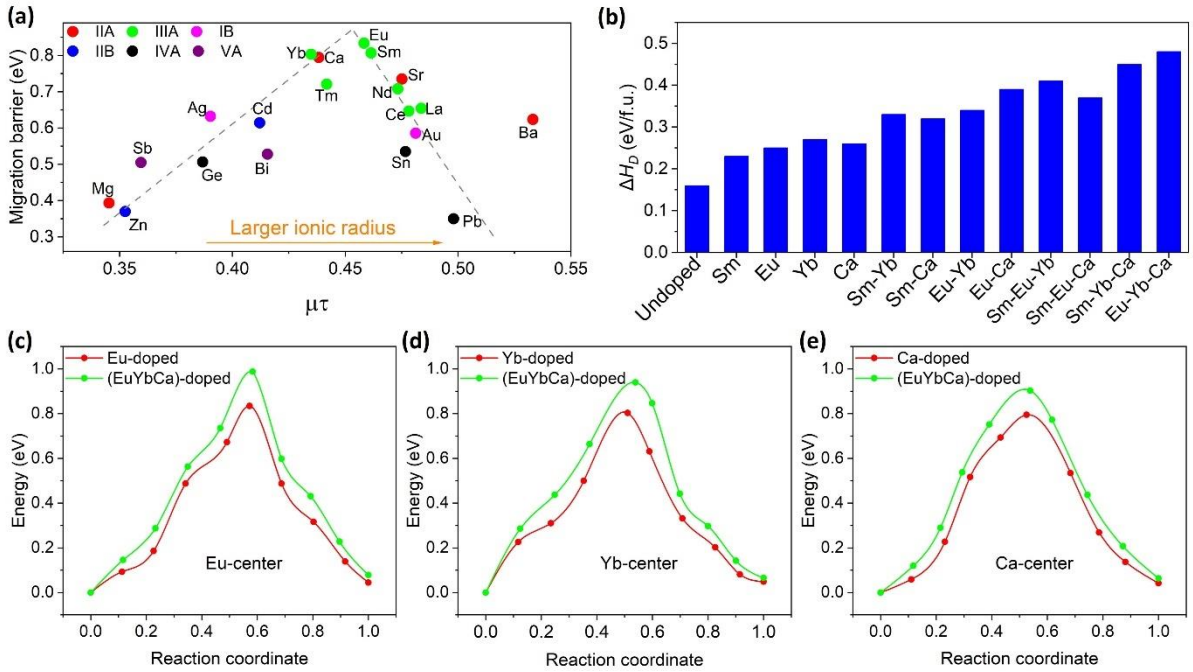

Figure 7.8. (**a**) Interstitial iodine migration barrier in various B-site doped $MAPbI_3$ as a function of $\mu\tau$, where τ and μ are tolerance factor and octahedral factor, respectively. (**b**) Histograms comparing the decomposition energies for pristine, single-doped (Sm, Eu, Yb, and Ca at an impurity concentration of 9.38%), co-doped (Sm-Yb, Sm-Ca, Eu-Yb, and Eu-Ca at an impurity concentration of 6.25%), and multiple-doped (Sm-Eu-Yb, Sn-Eu-Ca, Sm-Yb-Ca, and Eu-Yb-Ca at an impurity concentration of 9.38%) $MAPbI_3$. (**c**-**e**) Comparing the energy barrier for interstitial iodine migration at the corresponding impurity centers in the Eu-Yb-Ca multiple-doped $MAPbI_3$ and the Eu/Yb/Ca single-doped counterparts.

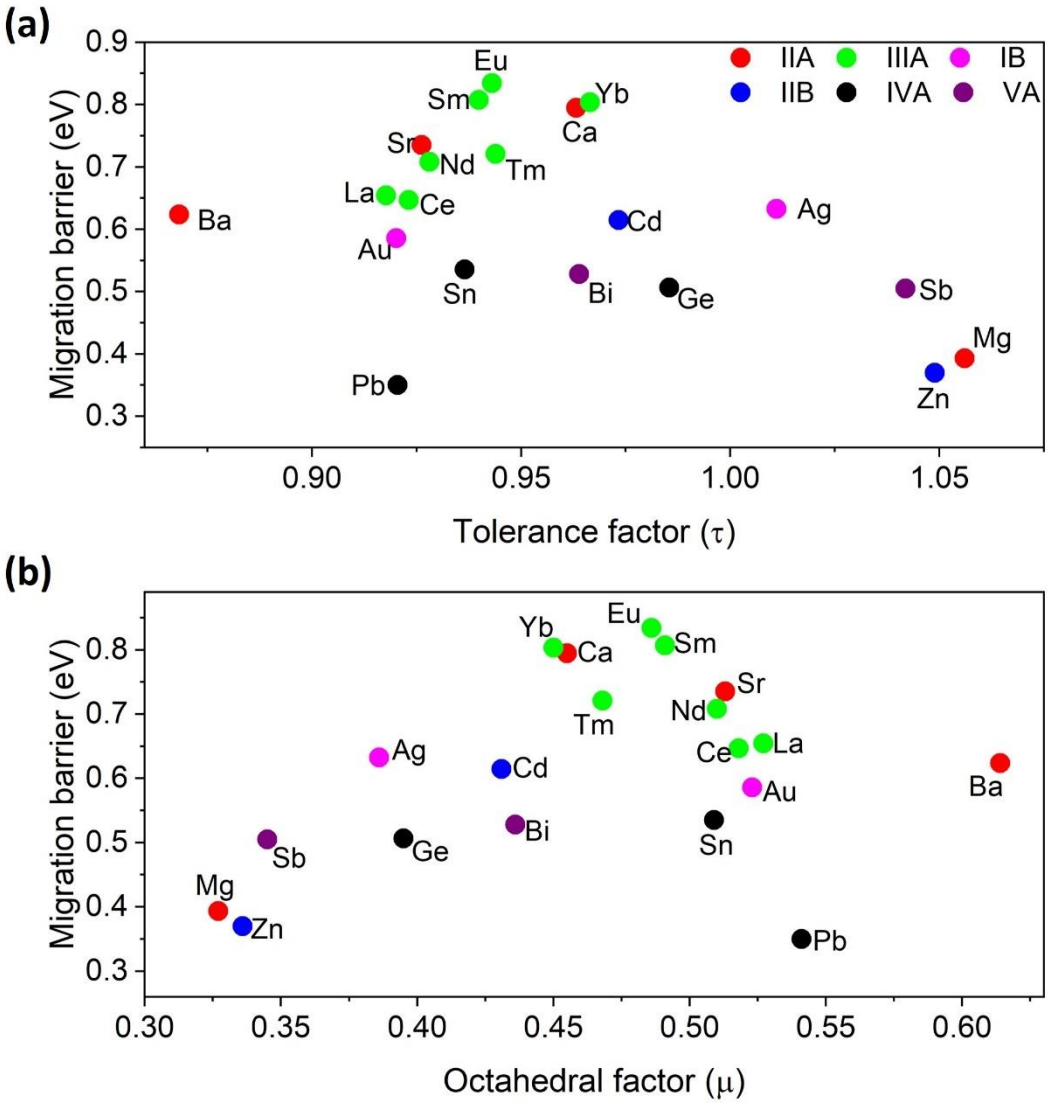

Figure 7.9. Interstitial iodine migration barrier in various B-site doped $MAPbI_3$ as a function of (**a**) tolerance factor (τ) and (**b**) the octahedral factor (μ), respectively.

Significantly, the inverted V-type trend for the migration barrier suggests a promising strategy for B-site cation engineering: co-doping or multiple-doping with relatively larger Eu (Sm) and smaller Ca (Yb) would further minimize size mismatch and induced microstrain, thereby effectively improving the perovskite lattice stability and alleviating the detrimental ion diffusion. Indeed, recent experiments have indicated that incorporating multiple specific doping elements in halide perovskites can stabilize sub-phases with significant lattice expansion and contraction[277]. For the co- and multiple-element doped systems, we generated the configurations using the special-quasirandom-structures (SQS) code[282] of the Alloy-

Theoretic Automated Toolkit (ATAT)[284], and the optimized atomic structure of the representative Eu-Ca and Eu-Yb-Ca doped $MAPbI_3$ are shown in **Figure 7.1**. Our calculations indeed reveal a more pronounced restriction of the octahedral dynamic disorder and higher lattice stability in the exemplary Eu-Ca, Eu-Yb, Sm-Ca, and Sm-Yb co-doped and Sm-Eu-Ca, Sm-Eu-Yb, Eu-Yb-Ca, and Sm-Yb-Ca multiple-doped system (see green and blue points in **Figure 7.10**), with the Eu-Yb-Ca multiple-doping showing the most significant effects. Static analysis indicates that multiple-doping $MAPbI_3$ with Eu-Yb-Ca substantially enhances ionic interaction at the corresponding impurity centers compared to the single-doped analogues at the same impurity concentration (see **Figure 7.11**). From a thermodynamic point of view, these co-doping and multiple-doping strategies significantly increase decomposition energy (with respect to their precursor phase iodide salts), demonstrating stronger stability than single-dopings, as shown in **Figure 7.8b**. Further, the HSE-SOC calculations (see **Figure 7.12**) indicate that these doped systems maintain favorable direct electronic bandgaps from the pristine perovskite, underscoring them as promising material candidates for the real-world photovoltaic and optoelectronic applications based on Shockley-Queisser (SQ) limit[125].

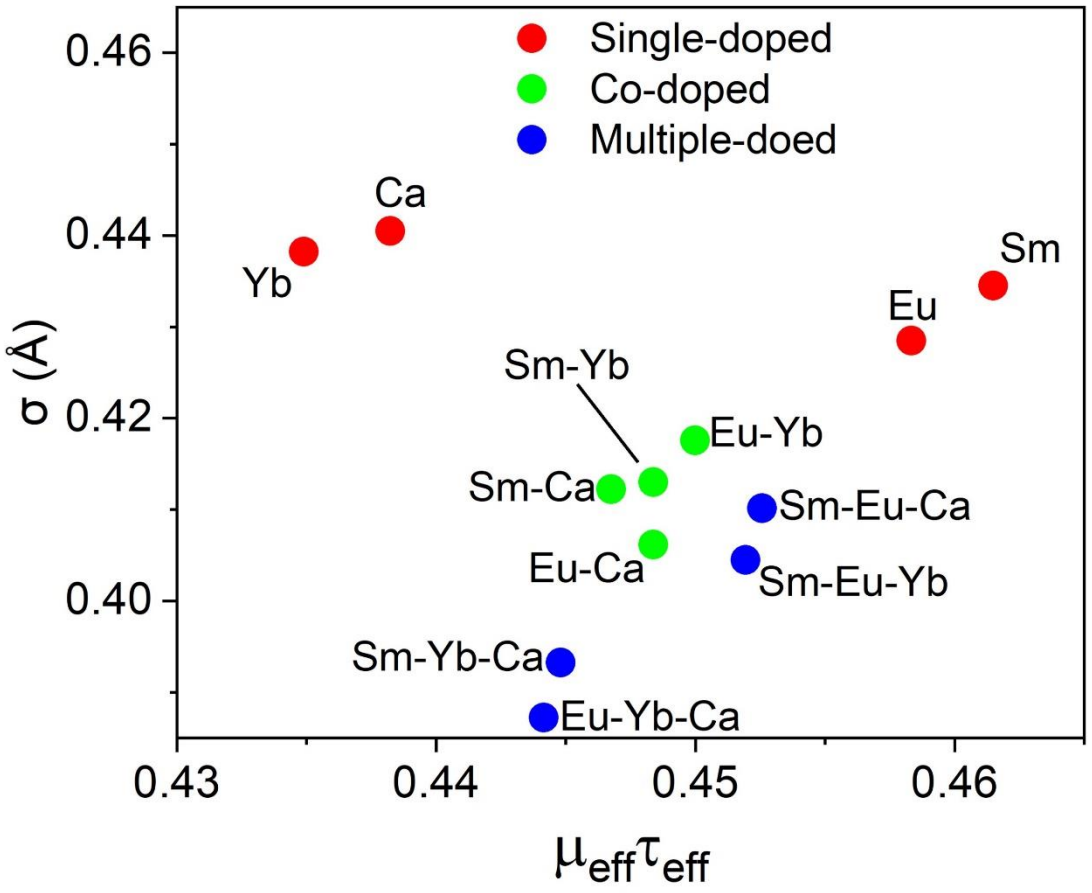

Figure 7.10. The average squared derivations (σ) of inorganic octahedral lattice at 300 K for pristine, single-doped (Sm, Eu, Yb, and Ca at an impurity concentration of 9.38%), co-doped (Sm-Yb, Sm-Ca, Eu-Yb, and Eu-Ca at an impurity concentration of 6.25%), and multiple-doped (Sm-Eu-Yb, Sm-Eu-Ca, Sm-Yb-Ca, and Eu-Yb-Ca at an impurity concentration of 9.38%) $MAPbI_3$, as a function of $\mu_{eff}\tau_{eff}$. For co- and multiple-element doping, the doping elements were considered as a single cation with r_B being determined by averaging the ionic radii of the impurities for reference, and accordingly, the effective tolerance factor τ_{eff} and octahedral factor μ_{eff} were defined, respectively.

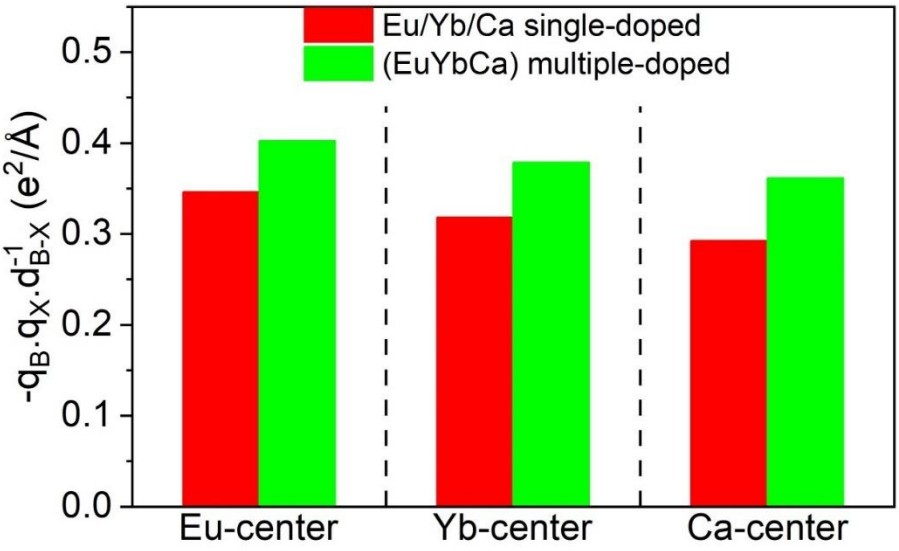

Figure 7.11. Calculated $-\frac{q_B q_X}{d_{B-X}}$ at impurity centers in Eu/Yb/Ca single-doped and comparing that in Eu-Yb-Ca multiple-doped $MAPbI_3$ perovskites.

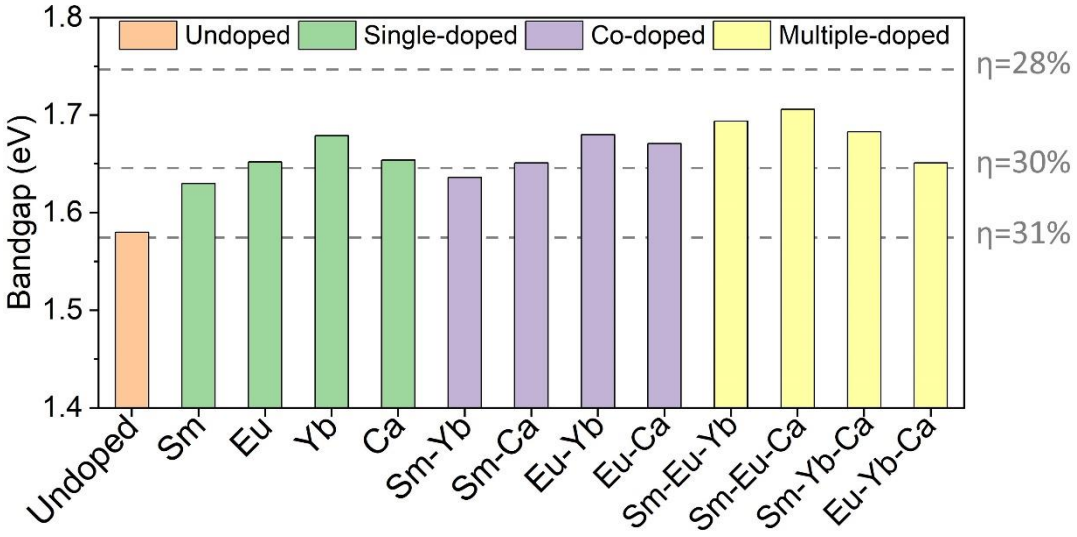

Figure 7.12. Electronic bandgaps for pristine, single-doped (Sm, Eu, Yb, and Ca at an impurity concentration of 9.38%), co-doped (Sm-Yb, Sm-Ca, Eu-Yb, and Eu-Ca at an impurity concentration of 6.25%), and multiple-doped (Sm-Eu-Yb, Sm-Eu-Ca, Sm-Yb-Ca, and Eu-Yb-Ca at an impurity concentration of 9.38%) $MAPbI_3$, based on the HSE-SOC calculation.

To explicitly evaluate the impact of B-site multiple-doping on the migration of iodide interstitials, we specifically focused on the exemplary Eu-Yb-Ca doped $MAPbI_3$ perovskite. Accordingly, we conducted static CI-NEB simulations and quantitively calculated the migration barrier for iodide ions at the doping centers in the Eu-Yb-Ca multiple-doped system

and compared it with those in the Eu, Yb, and Ca single-doped systems (at the same impurity concentration of 9.3%). The energy profiles, shown in **Figure 7.8c-e**, reveal that in the multiple-doped perovskite, migration barriers are enhanced by around 18%, 17% and 14% at the Eu, Yb and Ca centers, respectively, compared to the corresponding single-doped counterparts.

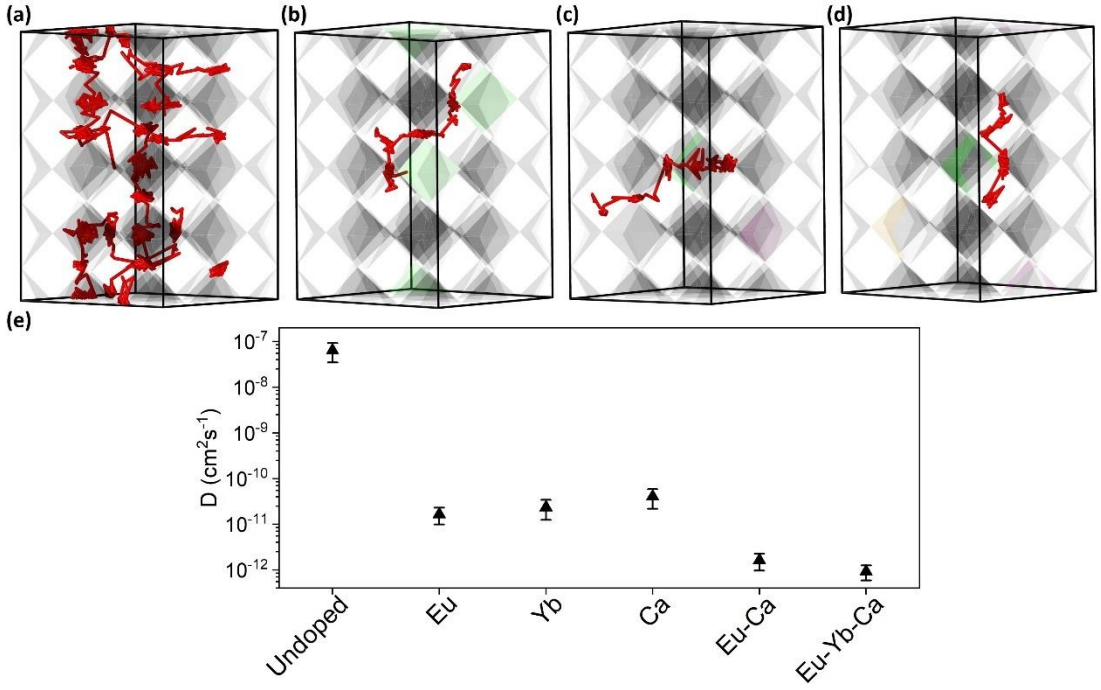

Figure 7.13. Diffusion trajectories for interstitial iodine ion in (**a**) pristine, (**b**) Eu single-doped, and (c) Eu-Ca, (**d**) Eu-Yb-Ca multiple-doped $MAPbI_3$ perovskites over the 1.5-ns MLDM simulation at 300 k, where the grey, green, orange, and purple octahedra stand for the inorganic PbI_6, EuI_6, YbI_6, and CaI_6 octahedra of the perovskite, respectively. (**e**) Diffusivity (D) of iodine interstitial in pristine, Eu-doped, Yb-doped, Ca-doped and Eu-Ca, Eu-Yb-Ca multiple-doped $MAPbI_3$ perovskites from MLMD simulation. The error bar of D is the statistical uncertainty from the linear fitting of mean square displacement over time.

To gain dynamic insight into the mechanism of ion migration remedied by multiple-element doping and to account for the thermodynamic effects under realistic device operational conditions, we further performed 1.5-ns NVT Machine Learning Molecular Dynamics (MLMD) simulation at 300 K based on the training data set from on-the-fly hybrid AIMD. As shown in **Figure 7.13a-d** and **Figure 7.14**, we extracted the random walking trajectories for interstitial

diffusion of iodine ion in pristine, single-doped, and multiple-doped systems over the MLDM simulation. As can be seen, the interstitial iodine trajectories in the three single-doped perovskites (**Figure 7.13b** and **7.14**) are significantly reduced compared to the pristine case (**Figure 7.13a**) during the 1.5-ns MLMD simulation. Notably, the Eu-Ca (**Figure 7.13c**) and Eu-Yb-Ca (**Figure 7.13d**) multiple-doping show more pronounced effects, indicating effective suppression of iodine migration in the perovskite lattice. To quantify these visual observations, we calculated the interstitial iodine diffusivity (D) based on the mean square displacement (MSD) measurement, as shown in **Figure 7.13d**. At room temperature, the interstitial iodine diffusivity in the pristine perovskite lattice is as high as $\sim 6.4 \times 10^{-8} cm^2/s$, aligning with the experimentally reported values of $10^{-8} - 10^{-11} cm^2/s$[49,293–295]. Increased stability is observed when ion migration is suppressed by single doping strategies with diffusivity values of $\sim 1.7 \times 10^{-11} cm^2/s$, $\sim 2.3 \times 10^{-11} cm^2/s$, and $\sim 4.0 \times 10^{-11} cm^2/s$ for Eu-, Yb-, and Ca-doped systems, respectively. Such a trend is consistent with the static CI-NEB predictions shown in **Figure 7.5**. Significantly, the iodine ion in Eu-Ca and Eu-Yb-Ca multiple-doped systems exhibits even lower diffusivity values of $\sim 1.6 \times 10^{-12} cm^2/s$ and $\sim 9.2 \times 10^{-13} cm^2/s$, respectively. These values are comparable to the range of $10^{-12} - 10^{-15} cm^2/s$ observed in lower-dimensional halide perovskites[49,89,118], which are known for their negligible ion migration.

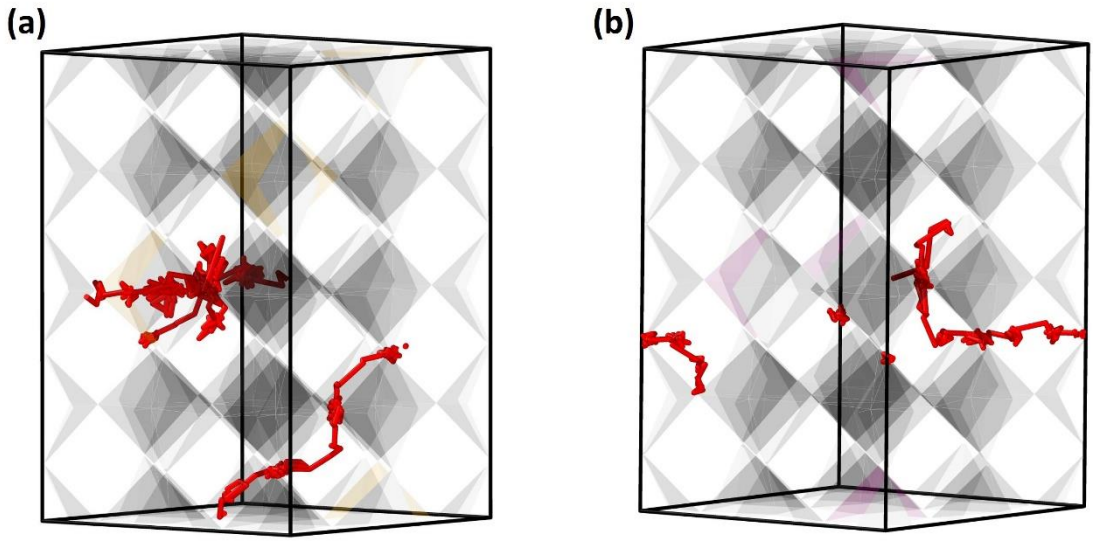

Figure 7.14. Diffusion trajectories for interstitial iodine ion in (**a**) Yb- and (**b**) Ca-doped, $MAPbI_3$ perovskites over the 1.5 ns MLDM simulation. The grey, orange, and purple octahedra stand for the inorganic PbI_6, YbI_6, and CaI_6 octahedra of the perovskite, respectively.

7.3.3 Experimental Implementation of Hysteresis-Free Perovskite Single Crystals with Greatly Improved Stability and Optoelectronic Properties

To experimentally validate the theoretical predictions for multiple B-site doping strategies, we pursued experimental studies focusing on single Eu doping of Ln-series, single Ca doping of alkaline earth, and Eu-Ca co-doping in the prototypical $MAPbI_3$ single crystals as representative examples, which are predicted to significantly suppress ion migration in the perovskite. We first grew single crystals of Eu-doped, Ca-doped, and Eu-Ca co-doped $MAPbI_3$ perovskites using the established inverse temperature crystallization (ITC) method, and the related synthetic details are shown in the Experimental Method section. X-ray diffraction (XRD) measurements (**Figures 7.15a and 7.15b**) reveal that both the pristine and the Eu-Ca doped $MAPbI_3$ single crystals have a tetragonal perovskite lattice with higher crystallinity. From the X-ray measurement results as shown in **Figure 7.15a**, the perovskite peaks for the pure single-crystal perovskite were largely reduced and a strong PbI_2 (12.7°) characteristic peak appeared in the spectrum after 7 days of air exposure. In contrast, for the Ca/Eu-co-doped perovskite single crystals, no clear PbI_2 peak was observed after even 30 days of air exposure. This clearly

demonstrates that co-doping of a small amount of Ln and alkaline earth metallic cations is highly beneficial for maintaining the stable perovskite structure of hybrid MA-based perovskites. Moreover, energy-dispersive X-ray spectroscopy (EDS) measurement (**Figure 7.16**) on these doped single crystal samples confirmed the even distribution of the doping elements within the perovskite structures. We also investigated the optical properties of a series of halide perovskite single crystals, including pure and a series of B-site-doped variants. The steady-state absorption spectra for all samples, as shown in **Figure 7.15c**, exhibited sharp band edges, demonstrating the high crystallinity of the as-grown perovskite single crystals. Band gaps extracted from Tauc plots show the values of 1.511 eV, 1.526 eV, 1.532 eV, and 1.557 eV for the pristine, Eu-doped, Ca-doped, and Eu-Ca co-doped $MAPbI_3$ single crystals, respectively (inset of **Figure 7.15c**). The red shift of the steady-state absorption spectrums of the perovskite single crystals after B-site doping, together with the relevant increased band gap values, are in good agreement with our simulation results predicted by our HSE-SOC calculations and the recent reports [296].

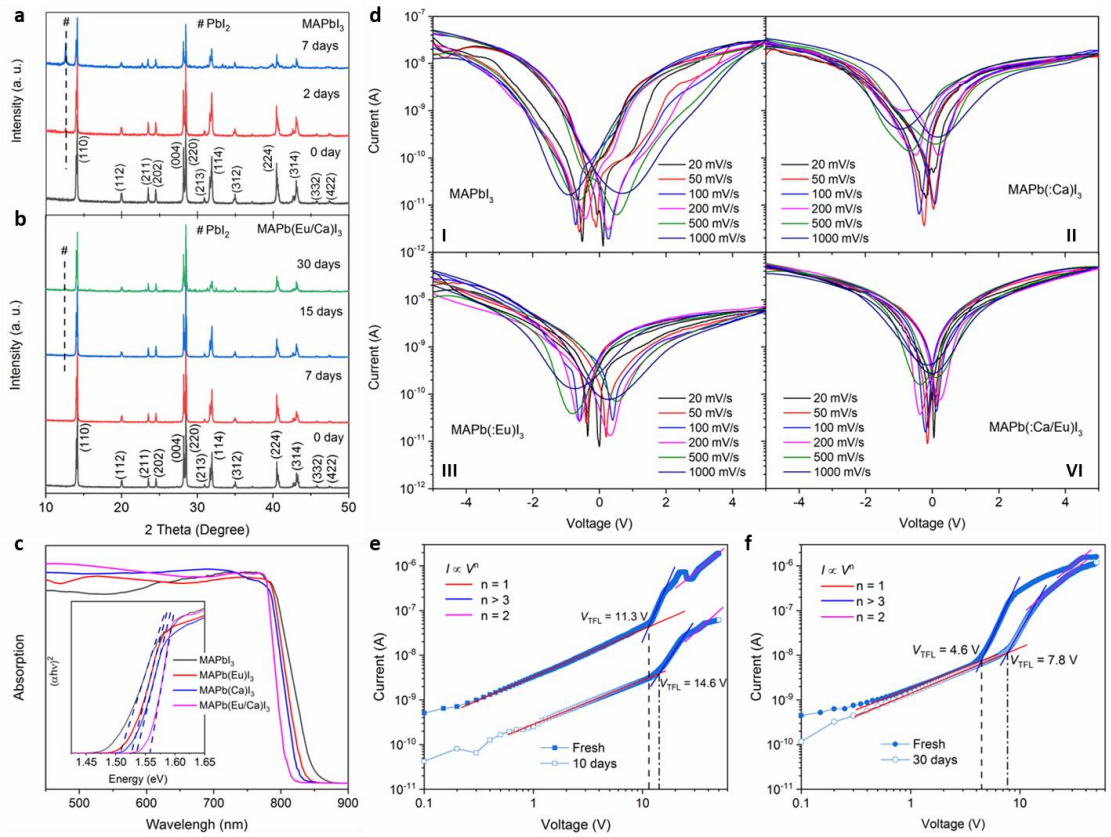

Figure 7.15. X-ray diffraction spectra comparing (**a**) the as-grown pristine $MAPbI_3$ perovskite single crystals to (**b**) the Eu-Ca co-doped $MAPbI_3$ perovskite single crystals, both initially and after 7 days and 30 days of air exposure. (**c**) Ultraviolet-visible absorption spectra of the pristine and various B-cite-doped $MAPbI_3$ perovskite single crystals. Inset: corresponding Tauc plots displaying the optical band gaps of the pure and a series of B-cite-doped perovskite single crystals. (**d**) Current-voltage characteristics of the (**I**) pristine, (**II**) Ca-doped, (**III**) Eu-doped, and (**VI**) Eu-Ca co-doped $MAPbI_3$ perovskite single crystals with different voltage sweep rates. SCLC measurements for the (**e**) pristine and (**f**) Eu-Ca co-doped $MAPbI_3$ perovskite single crystals (fresh and aged samples, respectively) showing three different dependence regions: the ohmic (n = 1), trap-filling (n > 3), and child (n = 2) regions, respectively.

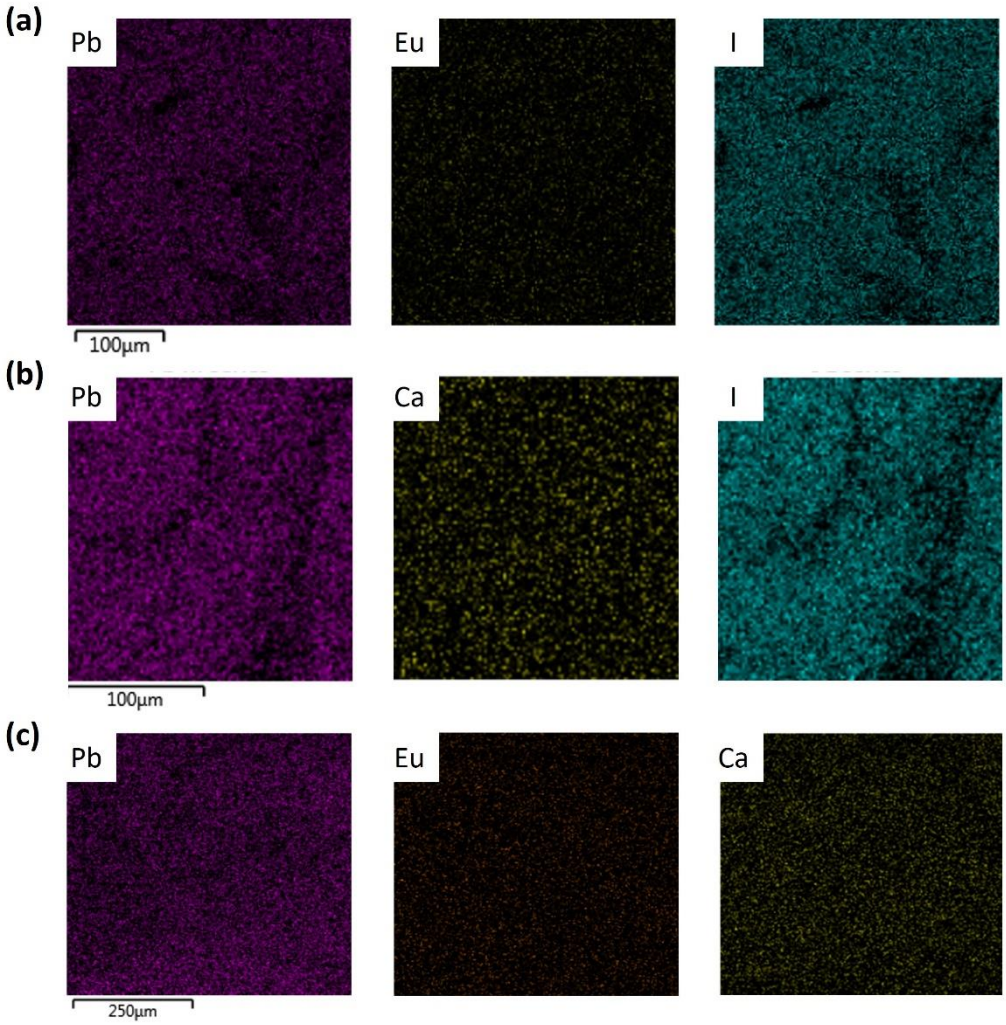

Figure 7.16. Energy-dispersive X-ray spectroscopy (EDS) mapping (**a**) of Pb, Eu, I in Eu-doped $MAPbI_3$ perovskite single crystals, (**b**) of Pb, Ca, I in Ca-doped $MAPbI_3$ perovskite single crystals, and (c) of Pb, Eu, Ca in Eu-Ca doped $MAPbI_3$ perovskite single crystals.

Iodine ion diffusion in the perovskite channel has important implications on current-voltage (*I-V*) hysteresis[266,267], which is strongly dependent on the sweep rates during the measurements of the related devices. To assess the impact of ion diffusion in pristine and the B-cite-doped $MAPbI_3$ perovskite single crystals, we performed scan-rate-dependent measurements of the *I-V* characteristics. In these measurements, the voltage was swept in sequence $-5 \rightarrow 0 \rightarrow +5 \rightarrow 0 \rightarrow -5\ V$ at the voltage sweeping rate ranging from 20 mV s^{-1} to 1000 mV s^{-1}. As shown in **Figure 7.15d (i)**, the pristine perovskite single-crystal sample exhibited significant current-

voltage hysteresis effects even at the relativity slow voltage sweeping rate of $20\ \mathrm{mV\ s^{-1}}$. Note that ion migration is more pronounced at slower sweeping rates due to the slower ion motion compared to electronic carriers (namely electrons and holes), resulting in severer hysteresis behaviors under faster voltage sweeping conditions. In contrast, the *I*-*V* hysteresis effect was somewhat weaker in the Eu-doped and Ca-doped perovskite single crystals, as shown in **Figures 7.15d (ii and iii)**, indicative of a notable suppression of ion migration in the B-site-doped halide perovskite crystals, which corroborates our theoretical prediction. Significantly, the Eu-Ca co-doped perovskite single-crystal sample exhibited almost hysteresis-free *I*-*V* curves across all the voltage sweeping rates, suggesting significant suppression of ion diffusion in the co-doped perovskite material (**Figure 7.15d (vi)**). Such negligible hysteresis effects are rare and have been challenging to achieve in many reported studies on conventional 3D perovskite or even 2D perovskite. This doping strategy is essential for achieving high operational stability in perovskite-based devices with high yield and reliability.

We further investigated the electrical properties of the perovskite single crystals, in particular their charge carrier mobility and trap density, which are key semiconducting quantities that directly affect the material's potential for realistic photovoltaic and optoelectronic applications. The carrier mobility and trap density values of the pristine and the doped perovskite single-crystal samples were determined using the space-charge-limited current (SCLC) method based on the *I*–*V* characteristics measured in hole-only devices (see details in the Experimental Method section). **Figures 7.15e**, **7.15f** and **Figure 7.17** show the current-voltage (*I*–*V*) characteristics for freshly prepared pristine, Eu-doped, Ca-doped, and Eu-Ca-co-doped $MAPbI_3$ single crystals. In principle, as for the SCLC analyses, the *I*–*V* curves ($I \propto V^n$) can be divided into three regions on the basis of the different Mott–Gurney's power law dependences (that is, different *n* values). In detail, the first, second, and third regions stand for the ohmic ($n = 1$), trap-filling ($n > 3$), and child ($n = 2$) regions, respectively (see details in Supplementary

Note. S1). The trap density (N_t) and charge carrier mobility (μ) values could be estimated from the trap-filled-limit (TFL) voltage (normally, the intersection of the Ohmic region and the trap-filling region) and by fitting the *I-V* curves in the third region following the Mott–Gurney equation (see details in Supplementary Note. S1). As shown in **Figure 7.15e**, the V_{TFL} value of the freshly prepared pristine $MAPbI_3$ single-crystal sample is about 11.3 V. Calculations reveal that the freshly prepared $MAPbI_3$ single crystal exhibits a hole mobility of approximately μ~64.7 $cm^2\ V^{-1}\ s^{-1}$ and a trap density of about $n_t \sim 9.07 \times 10^9\ cm^{-3}$ at room temperature. These values are comparable to, and even slightly better than, the previously reported values of $\mu \sim 20 - 60\ cm^2\ V^{-1}\ s^{-1}$ and $n_t \sim 10^9 - 10^{10}\ cm^{-3}$ [297]. Single doping with Eu and Ca enhances the hole mobilities of the Eu- and Ca-doped perovskite single crystals to μ~72.4 $cm^2\ V^{-1}\ s^{-1}$ and μ~73.8 $cm^2\ V^{-1}\ s^{-1}$, respectively, benefiting from their reduced trap densities ($n_t \sim 7.11 \times 10^9\ cm^{-3}$ and $n_t \sim 7.35 \times 10^9\ cm^{-3}$ for Eu- and Ca-doped samples, respectively) (see **Figure 7.17**). Importantly, the as-grown Eu-Ca co-doped perovskite single-crystal sample outperforms the single-doped cases with the lowest trap density of n_t~$7.03 \times 10^9 cm^{-3}$ and the highest mobility of $\mu \sim 81.2\ cm^2\ V^{-1}\ s^{-1}$ (see **Figure 7.15f**), which have profound implications for photovoltaic and optoelectronic device applications. Promisingly, the Eu-Ca-co-doped single-crystal perovskite showed negligible changes in trap density and carrier mobility after 30 days of air exposure compared to the pristine perovskite sample. Specifically, the hole mobility of the pristine perovskite single-crystal sample droped by more than 55% after only 10 days of air exposure, whereas, for the Eu-Ca-co-doped perovskite, the hole mobility reduced by only 5.3% after 30 days of air exposure. This trend is also evident in the XRD spectra of the samples (as shown in **Figure 7.15a**), demonstrating notably improved ambient stability of halide perovskite single crystal with Eu-Ca co-doping.

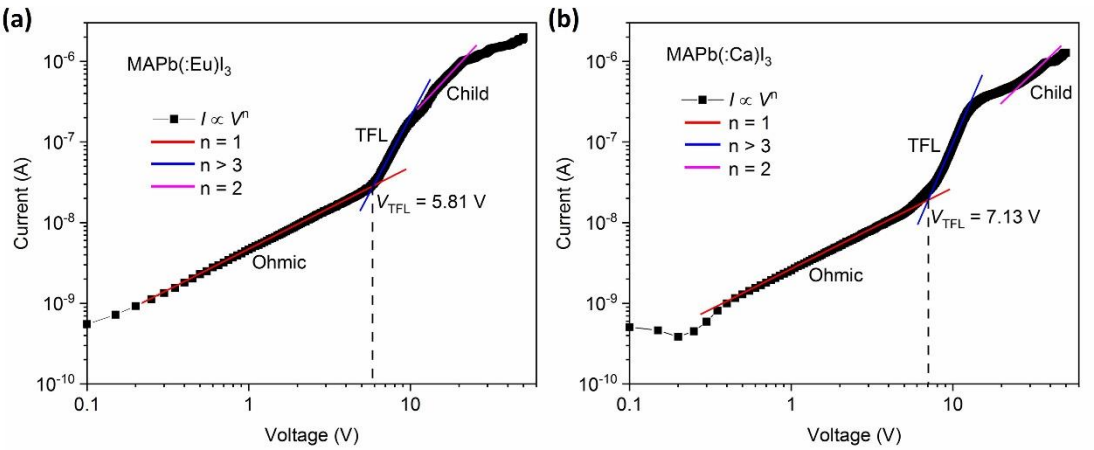

Figure 7.17. SCLC measurements for the single (**a**) Eu- and (**b**) Ca-doped $MAPbI_3$ perovskite single crystals showing three different dependence regions: the ohmic (n = 1), trap-filling (n > 3), and child (n = 2) regions, respectively.

To date, while A-site and X-site substitutions have been extensively, B-site doping holds great potential for further improvements in the device performance and stability. Our findings significantly extend the diversity of B-site compositional engineering beyond traditional single-element substitution. Co-doping and multiple-element doping emerge as a promising avenue, opening up prospects for designing lead-free or reduced-lead perovskite-based solar cells and a wide range of optoelectronic devices with improved device performance and operational stability. Although our current experimental results demonstrate the effectiveness of the Eu-Ca co-doped perovskite in inhibiting ion migration and enhancing ambient stability, theoretical predictions indicate that three-element doping strategies, especially Eu-Yb-Ca and Sm-Yb-Ca doped systems, would yield even more significant improvements. Thus far, the experimental implementation of uniformly incorporating multiple dopants (typically three or more elements) in the B-site in perovskites via pre- or post-processing remains challenging. Despite their theoretical thermodynamic stability, complexity arises from chemical difficulties in achieving well-mixed precursor solutions[94] and the tendency to form multiple phases[277]. This gap underscores the need for further experimental efforts to overcome these technical challenges. Successfully addressing them would allow for the full exploration of multiple-

element doping and even high-entropy alloying strategies, potentially broadening their capabilities across the halide perovskite family and unlocking new avenues for practical applications.

7.4 Conclusion

In summary, through a combination of density functional theory and machine learning molecular dynamics simulations, we identified a dynamic stability trend, where greater octahedral dynamic oscillation is intrinsically correlated with lower ion migration barriers in halide perovskites. Significantly, B-site composition engineering proves highly effective in stabilizing the perovskite lattice and suppressing interstitial iodine migration in $MAPbI_3$, surpassing the conventional substitutional modifications at the A- and X-sites and interstitial doping. The criteria governing the selection of the dopants are synergistically based on ionic electronegativity and size, underlining the superior effectiveness of B-site doping Group IIA alkaline earth metals and Ln-series metals. Moreover, we identified a notable correlation between the migration barrier and the product of structural tolerance factor and octahedral factor ($\mu\tau$), suggesting multiple-element doping as a superior strategy for B-site cation engineering, guiding the experimental achievement of exemplary hysteresis-free Eu-Ca co-doped halide perovskite single crystals with significantly improved ambient stability and optoelectronic characteristics. These insights significantly expand the flexibility of B-site compositional solutions within the halide perovskite family. More broadly, this study establishes a link between intrinsic lattice stability and ion migration behavior, offering a general and promising strategy for controlling ion migration through lattice engineering in a wide range of halide perovskites and other functional materials.

Chapter 8 Summary and Perspectives

Among the various sustainable renewable energy technologies available today, photovoltaic technology stands out as one of the most promising and rapidly advancing solutions to the future energy crisis. Solution-processable MHPs have rapidly achieved remarkable success across various applications, not only in solar cells, but also in light-emitting devices, photodetectors and other broad optoelectronic devices. Particularly in photovoltaics, the currently certified power conversion efficiency is comparable to and even exceeds those of crystalline silicon and GaAs, highlighting a commercially viable alternative to silicon photovoltaics could emerge within the next few years. Despite these advancements, unresolved issues in perovskite solar cells (PSCs)–including defect-induced nonradiative carrier recombination, low ambient stability, phase transition, and ion diffusion – pose significant challenges for real-world energy yields and the prospect of widespread commercialization.

Formamidinium lead triiodide ($FAPbI_3$) currently holds the record conversion efficiency in the single-junction perovskite solar cell. Proper iodine management is known to be essential to suppress defect-induced nonradiative losses in $FAPbI_3$ active layers. However, the origin of nonradiative losses and the underlying mechanism of suppressing such losses by iodine-concentration management remains unknown. In the first work of this thesis, we discovered that the conventionally believed intrinsic point defects are, in fact, not responsible for the nonradiative losses; instead, interstitial hydrogen ions (H_i), which can be abundant in the $FAPbI_3$ active layers under both iodine-rich and iodine-poor growth conditions, play a significant role in nonradiative charge recombination. By contrast, iodine-moderate growth conditions favour the formation of electrically inactive molecular hydrogen and reduce the detrimental hydrogen ions in the perovskites. This provides a rationale for the experimental observation. Moreover, we found that the commonly used HI and HBr additives, DMF solvent as well as some organics (e.g., C_2N_3H and NH_3) can be effective hydrogen sources for

unintentional hydrogen incorporation, while the water vapour, DMSO solvent, and HF can only play an insignificant role. These new findings have significant implications for potential further enhancement of $FAPbI_3$-based photovoltaic device performance.

The hitherto subdued power conversion efficiencies of Sn-based hybrid perovskite solar cells are generally attributed to severe nonradiative recombination; however, the responsible deep-level defects are still unclear. In contrast to the conventional Pb-based halide perovskite $FAPbI_3$, in the second work of this thesis, we demonstrated a different hydrogen-induced nonradiative loss mechanism in the prototypical Sn-based halide perovskite $FASnI_3$: molecular hydrogen (H_2) can be effectively captured by the native Sn vacancies (V_{Sn}), forming $V_{Sn} - H_2$ defect complexes. These $V_{Sn} - H_2$ complexes are energetically favorable hence a high defect density. Significantly, while both V_{Sn} and H_2 are not deep-level defects individually, the strong chemical interaction within the $V_{Sn} - H_2$ complex results in a deep transition level in the bandgap. Our work hence points to a new processing roadmap for improving the device performance. The roadmap emphasizes the importance of careful control of hydrogen content to suppress the formation of detrimental defects, thereby reducing the nonradiative-induced PCE losses in $FASnI_3$. This can be reasonably extended into a wide range of Sn-based halide perovskites and related devices.

Besides, the third study in this thesis uncovers the underlying mechanism behind the reduced carrier lifetime in Sn-based perovskites due to oxygen ingress. Our first-principles calculations reveal that oxygen alone is not responsible for nonradiative carrier recombination. Instead, it tends to interact strongly with the iodine vacancies and substantially enhances the native carrier recombination rate due to lattice strengthening and the suppressed structural relaxation associated with the transition of O_I. These insights provide rational guidance for the subsequent design and optimization of nontoxic Sn-based perovskite solar cells and other broad optoelectronics operating under ambient air conditions. It emphasizes that, in addition to the

commonly used control of oxygen content, native defect engineering would be a critical step to minimize the density of the iodine vacancies. Overall, hydrogen plays a primary role in efficiency loss of perovskite-based devices under moisture and acidic conditions, whereas oxygen more effectively promotes nonradiative carrier recombination upon exposure to ambient air conditions.

Phase instability poses another serious challenge to the commercialization of $FAPbI_3$-based solar cells and optoelectronic devices. In the fourth work of this thesis, we combine density functional theory and machine learning molecular dynamics simulations to investigate the atomistic mechanism underlying the undesired α-δ phase transition of $FAPbI_3$ and discovered that defects play a significant role in accelerating phase transition kinetics, aggravating the instability of the photoactive α-$FAPbI_3$. Furthermore, we methodically explore compositional engineering for α-$FAPbI_3$ stabilization, culminating in a new and rational strategy for crafting high-performance: A-site engineering predominantly influences the thermodynamics and B-site doping is more effective in manipulating the kinetics of the phase transition in $FAPbI_3$. Therefore, A-B mixed cation engineering emerges as a potent approach for synergistically stabilizing $FAPbI_3$ perovskite.

Halide ion migration is the primary cause of perovskite degradation under operational conditions involving electric fields, heat, light, and excess charge carriers, etc. This migration leads to internal field screening, significantly contributing to the initial efficiency loss of perovskite devices, surpassing the effects of the traditional defect-induced nonradiative carrier recombination. In the fifth work of this thesis, we investigated the atomistic mechanism underlying the undesired ion migration and uncovered the critical interplay between the dynamics of perovskite octahedral lattice and the diffusion energy barrier associated with ion migration. Moreover, we systematically examined doping engineering for perovskite lattice stabilization and ion migration suppression, leading to a new and rational substitutional strategy

for producing high-performance and durable perovskite solar cells and versatile optoelectronic devices.

To date, numerous efforts have been devoted to achieving high-efficiency and stable perovskite applications by investigating the bulk physics and chemistry of the materials. Note that the perovskite solar cells (PSCs) and even other related optoelectronic devices are often built by layering the perovskite thin film (the perovskite active layers) between electron transport layers (ETLs) and hole transport layers (HTLs). These layers are then connected with metallic contacts (metal electrodes) on both the top and bottom, assembled through a layer-by-layer method. In contrast to the bulk of the material, the surface of perovskite represents a discontinuity with numerous unterminated bonds and vacancies, which serve as primary sites for charge trapping and nonradiative recombination. Indeed, recent experimental reports[298] have indicated that the perovskite surfaces as well as the heterojunctions with the charge transport layers (CTLs) are the critical regions for energy dissipation, where the transport of photogenerated carriers is impacted, in turn restricting the maximum V_{OC} and consequently overall efficiency of the devices. Particularly, carrier recombination at the perovskite-fullerene interface, one of the most commonly used ETLs, has been demonstrated to exceed bulk carrier recombination by one to three orders of magnitude[298]. Such interfacial recombination could stem from the presence of charge transfer states or low-energy states caused by the broadening of the density of states[298]. A comprehensive understanding of such recombination loss mechanism, however, requires further investigation.

In contrast to conventional three-dimensional (3D) perovskites solar absorbers typically with an "ABX_3" stoichiometry, there exists a variety of "layered" or "low-dimensional" perovskites through composition engineering with larger A-site cations. These 2D perovskites often have larger bandgaps compared to their 3D counterparts but maintain similar lattice constants in the inorganic octahedral framework. Therefore, implementing layered perovskites on top of the 3D

perovskite, thus creating a 3D-2D perovskite heterojunction is a powerful passivation strategy to reduce interfacial recombination losses despite the underlying mechanism remaining elusive[299]. Moreover, precisely controlling the distribution of multiple quantum wells in layered perovskites can fine-tune the energy landscape, enabling high selectivity for photogenerated carriers at the interface. Further exploration of such strategies is still needed to realize ideal perovskite interfaces. Compared with traditional experimental characterization, first-principles atomistic simulations offer a powerful and efficient tool for probing and visualizing nanoscale crystallographic, chemical, and electrical information, and local carrier behaviour at the perovskite interface. The emerging and artificial intelligence, including machine learning, significantly accelerates the first-principles investigation by reducing computational costs and improving accuracy, enabling high-throughput materials discovery and optimization. Constructing a highly efficient theoretical-artificial intelligence-experimental scheme to uncover the remaining mysteries at the perovskite interfaces would advance the design of highly efficient halide perovskites, unlocking the full potential of perovskite photovoltaics and optoelectronics.

References

1. Kim, J. Y., Lee, J.-W., Jung, H. S., Shin, H. & Park, N.-G. High-Efficiency Perovskite Solar Cells. *Chem. Rev.* **120**, 7867–7918 (2020).
2. Stoumpos, C. C. & Kanatzidis, M. G. The Renaissance of Halide Perovskites and Their Evolution as Emerging Semiconductors. *Acc. Chem. Res.* **48**, 2791–2802 (2015).
3. Min, H. *et al.* Perovskite solar cells with atomically coherent interlayers on SnO2 electrodes. *Nature* **598**, 444–450 (2021).
4. Al-Ashouri, A. *et al.* Monolithic perovskite/silicon tandem solar cell with >29% efficiency by enhanced hole extraction. *Science* **370**, 1300–1309 (2020).
5. Correa-Baena, J.-P. *et al.* Promises and challenges of perovskite solar cells. *Science* **358**, 739–744 (2017).
6. Liu, A. *et al.* High-performance inorganic metal halide perovskite transistors. *Nat Electron* **5**, 78–83 (2022).
7. Kagan, C. R. Organic-Inorganic Hybrid Materials as Semiconducting Channels in Thin-Film Field-Effect Transistors. *Science* **286**, 945–947 (1999).
8. Wei, H. *et al.* Sensitive X-ray detectors made of methylammonium lead tribromide perovskite single crystals. *Nature Photon* **10**, 333–339 (2016).
9. Fang, Y., Dong, Q., Shao, Y., Yuan, Y. & Huang, J. Highly narrowband perovskite single-crystal photodetectors enabled by surface-charge recombination. *Nature Photon* **9**, 679–686 (2015).
10. Hassan, Y. *et al.* Ligand-engineered bandgap stability in mixed-halide perovskite LEDs. *Nature* **591**, 72–77 (2021).
11. Cao, Y. *et al.* Perovskite light-emitting diodes based on spontaneously formed submicrometre-scale structures. *Nature* **562**, 249–253 (2018).

12. Zhu, H. *et al.* Lead halide perovskite nanowire lasers with low lasing thresholds and high quality factors. *Nature Mater* **14**, 636–642 (2015).
13. Eaton, S. W. *et al.* Lasing in robust cesium lead halide perovskite nanowires. *Proceedings of the National Academy of Sciences* **113**, 1993–1998 (2016).
14. Akkerman, Q. A. & Manna, L. What Defines a Halide Perovskite? *ACS Energy Lett.* **5**, 604–610 (2020).
15. Kojima, A., Teshima, K., Shirai, Y. & Miyasaka, T. Organometal Halide Perovskites as Visible-Light Sensitizers for Photovoltaic Cells. *J. Am. Chem. Soc.* **131**, 6050–6051 (2009).
16. Szabó, G., Park, N.-G., De Angelis, F. & Kamat, P. V. Are Perovskite Solar Cells Reaching the Efficiency and Voltage Limits? *ACS Energy Lett.* **8**, 3829–3831 (2023).
17. Wells, H. L. Über die Cäsium- und Kalium-Bleihalogenide. *Z. Anorg. Chem.* **3**, 195–210 (1893).
18. Møller, C. K. Crystal Structure and Photoconductivity of Cæsium Plumbohalides. *Nature* **182**, 1436–1436 (1958).
19. Mitzi, D. B., Feild, C. A., Harrison, W. T. A. & Guloy, A. M. Conducting tin halides with a layered organic-based perovskite structure. *Nature* **369**, 467–469 (1994).
20. Kondo, T., Azuma, T., Yuasa, T. & Ito, R. Biexciton lasing in the layered perovskite-type material (C6H13NH3)2PbI4. *Solid State Communications* **105**, 253–255 (1998).
21. Best Research-Cell Efficiency Chart. *The efficiency chart published by the National Renewable Energy Laboratory.* https://www.nrel.gov/pv/assets/pdfs/best-research-cell-efficiencies-rev220630.pdf (2022).
22. Noh, J. H., Im, S. H., Heo, J. H., Mandal, T. N. & Seok, S. I. Chemical Management for Colorful, Efficient, and Stable Inorganic–Organic Hybrid Nanostructured Solar Cells. *Nano Lett.* **13**, 1764–1769 (2013).

23. Dong, Q. *et al.* Electron-hole diffusion lengths > 175 μm in solution-grown CH3NH3PbI3 single crystals. *Science* **347**, 967–970 (2015).

24. Law, C. *et al.* Performance and Stability of Lead Perovskite/TiO2, Polymer/PCBM, and Dye Sensitized Solar Cells at Light Intensities up to 70 Suns. *Advanced Materials* **26**, 6268–6273 (2014).

25. Xing, G. *et al.* Long-Range Balanced Electron- and Hole-Transport Lengths in Organic-Inorganic CH3NH3PbI3. *Science* **342**, 344–347 (2013).

26. Beaujuge, P. M. & Fréchet, J. M. J. Molecular Design and Ordering Effects in π-Functional Materials for Transistor and Solar Cell Applications. *J. Am. Chem. Soc.* **133**, 20009–20029 (2011).

27. Xing, G. *et al.* Low-temperature solution-processed wavelength-tunable perovskites for lasing. *Nat. Mater.* **13**, 476–480 (2014).

28. Yakunin, S. *et al.* Low-threshold amplified spontaneous emission and lasing from colloidal nanocrystals of caesium lead halide perovskites. *Nat Commun* **6**, 8056 (2015).

29. Tan, Z.-K. *et al.* Bright light-emitting diodes based on organometal halide perovskite. *Nature Nanotech* **9**, 687–692 (2014).

30. Zhang, L. *et al.* Ultra-bright and highly efficient inorganic based perovskite light-emitting diodes. *Nat Commun* **8**, 15640 (2017).

31. Chiba, T. *et al.* Anion-exchange red perovskite quantum dots with ammonium iodine salts for highly efficient light-emitting devices. *Nature Photon* **12**, 681–687 (2018).

32. Liu, Z. *et al.* Perovskite Light-Emitting Diodes with EQE Exceeding 28% through a Synergetic Dual-Additive Strategy for Defect Passivation and Nanostructure Regulation. *Advanced Materials* **33**, 2103268 (2021).

33. Kim, Y. C. *et al.* Printable organometallic perovskite enables large-area, low-dose X-ray imaging. *Nature* **550**, 87–91 (2017).

34. Stranks, S. D. Nonradiative Losses in Metal Halide Perovskites. *ACS Energy Lett.* **2**, 1515–1525 (2017).

35. Luo, D., Su, R., Zhang, W., Gong, Q. & Zhu, R. Minimizing non-radiative recombination losses in perovskite solar cells. *Nat. Rev. Mater.* **5**, 44–60 (2020).

36. Jeon, N. J. *et al.* Compositional engineering of perovskite materials for high-performance solar cells. *Nature* **517**, 476–480 (2015).

37. Lu, H. *et al.* Vapor-assisted deposition of highly efficient, stable black-phase FAPbI3 perovskite solar cells. *Science* **370**, (2020).

38. Kim, G. *et al.* Impact of strain relaxation on performance of α-formamidinium lead iodide perovskite solar cells. *Science* **370**, 108–112 (2020).

39. Min, H. *et al.* Efficient, stable solar cells by using inherent bandgap of α-phase formamidinium lead iodide. *Science* **366**, 749–753 (2019).

40. Hui, W. *et al.* Stabilizing black-phase formamidinium perovskite formation at room temperature and high humidity. *Science* **371**, 1359–1364 (2021).

41. Ahlawat, P. *et al.* A combined molecular dynamics and experimental study of two-step process enabling low-temperature formation of phase-pure α-FAPbI3. *Science Advances* **7**, eabe3326 (2021).

42. Chen, T. *et al.* Entropy-driven structural transition and kinetic trapping in formamidinium lead iodide perovskite. *Science Advances* **2**, e1601650 (2016).

43. Park, J. *et al.* Controlled growth of perovskite layers with volatile alkylammonium chlorides. *Nature* **616**, 724–730 (2023).

44. Zhu, H. *et al.* Long-term operating stability in perovskite photovoltaics. *Nat Rev Mater* **8**, 569–586 (2023).

45. Bitton, S. & Tessler, N. Perovskite ionics – elucidating degradation mechanisms in perovskite solar cells via device modelling and iodine chemistry. *Energy Environ. Sci.* **16**, 2621–2628 (2023).

46. Aristidou, N. *et al.* Fast oxygen diffusion and iodide defects mediate oxygen-induced degradation of perovskite solar cells. *Nat Commun* **8**, 15218 (2017).

47. Bryant, D. *et al.* Light and oxygen induced degradation limits the operational stability of methylammonium lead triiodide perovskite solar cells. *Energy Environ. Sci.* **9**, 1655–1660 (2016).

48. Divitini, G. *et al.* In situ observation of heat-induced degradation of perovskite solar cells. *Nat Energy* **1**, 1–6 (2016).

49. Bi, E., Song, Z., Li, C., Wu, Z. & Yan, Y. Mitigating ion migration in perovskite solar cells. *TRECHEM* **3**, 575–588 (2021).

50. Chen, J. & Park, N.-G. Causes and Solutions of Recombination in Perovskite Solar Cells. *Advanced Materials* **31**, 1803019 (2019).

51. Aydin, E., De Bastiani, M. & De Wolf, S. Defect and Contact Passivation for Perovskite Solar Cells. *Advanced Materials* **31**, 1900428 (2019).

52. Liu, Y. *et al.* Ultrahydrophobic 3D/2D fluoroarene bilayer-based water-resistant perovskite solar cells with efficiencies exceeding 22%. *Science Advances* **5**, eaaw2543 (2019).

53. Tvingstedt, K. *et al.* Radiative efficiency of lead iodide based perovskite solar cells. *Sci Rep* **4**, 6071 (2014).

54. Abdi-Jalebi, M. *et al.* Maximizing and stabilizing luminescence from halide perovskites with potassium passivation. *Nature* **555**, 497–501 (2018).

55. Yang, S. *et al.* Tailoring Passivation Molecular Structures for Extremely Small Open-Circuit Voltage Loss in Perovskite Solar Cells. *J. Am. Chem. Soc.* **141**, 5781–5787 (2019).

56. Shao, Y., Yuan, Y. & Huang, J. Correlation of energy disorder and open-circuit voltage in hybrid perovskite solar cells. *Nat Energy* **1**, 1–6 (2016).

57. Saliba, M. *et al.* Incorporation of rubidium cations into perovskite solar cells improves photovoltaic performance. *Science* **354**, 206–209 (2016).

58. Wright, A. D. *et al.* Electron–phonon coupling in hybrid lead halide perovskites. *Nat Commun* **7**, 11755 (2016).

59. Ran, C., Xu, J., Gao, W., Huang, C. & Dou, S. Defects in metal triiodide perovskite materials towards high-performance solar cells: origin, impact, characterization, and engineering. *Chem. Soc. Rev.* **47**, 4581–4610 (2018).

60. Wang, Z. *et al.* High irradiance performance of metal halide perovskites for concentrator photovoltaics. *Nat Energy* **3**, 855–861 (2018).

61. Jin, H. *et al.* It's a trap! On the nature of localised states and charge trapping in lead halide perovskites. *Mater. Horiz.* **7**, 397–410 (2020).

62. Jones, T. W. *et al.* Lattice strain causes non-radiative losses in halide perovskites. *Energy Environ. Sci.* **12**, 596–606 (2019).

63. Ball, J. M. & Petrozza, A. Defects in perovskite-halides and their effects in solar cells. *Nat Energy* **1**, 16149 (2016).

64. Zhang, X., Turiansky, M. E., Shen, J.-X. & Van de Walle, C. G. Iodine interstitials as a cause of nonradiative recombination in hybrid perovskites. *Phys. Rev. B* **101**, 140101 (2020).

65. Zhang, X., Shen, J.-X., Turiansky, M. E. & Van de Walle, C. G. Minimizing hydrogen vacancies to enable highly efficient hybrid perovskites. *Nat. Mater.* **20**, 971–976 (2021).

66. Amat, A. *et al.* Cation-Induced Band-Gap Tuning in Organohalide Perovskites: Interplay of Spin–Orbit Coupling and Octahedra Tilting. *Nano Lett.* **14**, 3608–3616 (2014).

67. Tai, Q. & Yan, F. Emerging Semitransparent Solar Cells: Materials and Device Design. *Advanced Materials* **29**, 1700192 (2017).

68. Leijtens, T. *et al.* Towards enabling stable lead halide perovskite solar cells; interplay between structural, environmental, and thermal stability. *J. Mater. Chem. A* **5**, 11483–11500 (2017).

69. Tai, Q., Tang, K.-C. & Yan, F. Recent progress of inorganic perovskite solar cells. *Energy Environ. Sci.* **12**, 2375–2405 (2019).

70. Deng, Y. *et al.* Surfactant-controlled ink drying enables high-speed deposition of perovskite films for efficient photovoltaic modules. *Nat Energy* **3**, 560–566 (2018).

71. Zhang, Y. *et al.* Ambient Fabrication of Organic–Inorganic Hybrid Perovskite Solar Cells. *Small Methods* **5**, 2000744 (2021).

72. Masi, S., Gualdrón-Reyes, A. F. & Mora-Seró, I. Stabilization of Black Perovskite Phase in FAPbI3 and CsPbI3. *ACS Energy Lett.* **5**, 1974–1985 (2020).

73. Bechtel, J. S. & Van der Ven, A. Octahedral tilting instabilities in inorganic halide perovskites. *Phys. Rev. Mater.* **2**, 025401 (2018).

74. Jiang, S. *et al.* Phase Transitions of Formamidinium Lead Iodide Perovskite under Pressure. *J. Am. Chem. Soc.* **140**, 13952–13957 (2018).

75. Zhu, Z. *et al.* Metal halide perovskites: stability and sensing-ability. *J. Mater. Chem. C* **6**, 10121–10137 (2018).

76. Kim, B., Kim, J. & Park, N. First-principles identification of the charge-shifting mechanism and ferroelectricity in hybrid halide perovskites. *Sci Rep* **10**, 19635 (2020).

77. Han, Q. *et al.* Single Crystal Formamidinium Lead Iodide (FAPbI3): Insight into the Structural, Optical, and Electrical Properties. *Advanced Materials* **28**, 2253–2258 (2016).

78. Nam, J. K. *et al.* Potassium Incorporation for Enhanced Performance and Stability of Fully Inorganic Cesium Lead Halide Perovskite Solar Cells. *Nano Lett.* **17**, 2028–2033 (2017).

79. Chen, B., Yang, M., Priya, S. & Zhu, K. Origin of J – V Hysteresis in Perovskite Solar Cells. *J. Phys. Chem. Lett.* **7**, 905–917 (2016).

80. Mizusaki, J., Arai, K. & Fueki, K. Ionic conduction of the perovskite-type halides. *Solid State Ionics* **11**, 203–211 (1983).

81. Ishihara, T., Matsuda, H. & Takita, Y. Doped LaGaO3 Perovskite Type Oxide as a New Oxide Ionic Conductor. *J. Am. Chem. Soc.* **116**, 3801–3803 (1994).

82. Inaguma, Y., Matsui, Y., Shan, Y.-J., Itoh, M. & Nakamura, T. Lithium ion conductivity in the perovskite-type LiTaO3-SrTiO3 solid solution. *Solid State Ionics* **79**, 91–97 (1995).

83. Yang, T.-Y., Gregori, G., Pellet, N., Grätzel, M. & Maier, J. The Significance of Ion Conduction in a Hybrid Organic–Inorganic Lead-Iodide-Based Perovskite Photosensitizer. *Angew. Chem.* **54**, 7905–7910 (2015).

84. Yin, W.-J., Shi, T. & Yan, Y. Unusual defect physics in $CH_3NH_3PbI_3$ perovskite solar cell absorber. *Appl. Phys. Lett.* **104**, 063903 (2014).

85. Yuan, Y. & Huang, J. Ion Migration in Organometal Trihalide Perovskite and Its Impact on Photovoltaic Efficiency and Stability. *Acc. Chem. Res.* **49**, 286–293 (2016).

86. Shao, Y. *et al.* Grain boundary dominated ion migration in polycrystalline organic–inorganic halide perovskite films. *Energy Environ. Sci.* **9**, 1752–1759 (2016).

87. Azpiroz, J. M., Mosconi, E., Bisquert, J. & De Angelis, F. Defect migration in methylammonium lead iodide and its role in perovskite solar cell operation. *Energy Environ. Sci.* **8**, 2118–2127 (2015).

88. Eames, C. *et al.* Ionic transport in hybrid lead iodide perovskite solar cells. *Nat Commun* **6**, 7497 (2015).

89. Zhong, Y. *et al.* Inhibition of Ion Migration for Highly Efficient and Stable Perovskite Solar Cells. *Advanced Materials* **35**, 2302552 (2023).

90. Almora, O. *et al.* Capacitive Dark Currents, Hysteresis, and Electrode Polarization in Lead Halide Perovskite Solar Cells. *J. Phys. Chem. Lett.* **6**, 1645–1652 (2015).

91. Berhe, T. A. *et al.* Organometal halide perovskite solar cells: degradation and stability. *Energy Environ. Sci.* **9**, 323–356 (2016).

92. Han, J. S. *et al.* Lead-Free All-Inorganic Cesium Tin Iodide Perovskite for Filamentary and Interface-Type Resistive Switching toward Environment-Friendly and Temperature-Tolerant Nonvolatile Memories. *ACS Appl. Mater. Interfaces* **11**, 8155–8163 (2019).

93. Chen, Y. *et al.* Strain engineering and epitaxial stabilization of halide perovskites. *Nature* **577**, 209–215 (2020).

94. Folgueras, M. C., Jiang, Y., Jin, J. & Yang, P. High-entropy halide perovskite single crystals stabilized by mild chemistry. *Nature* **621**, 282–288 (2023).

95. Zhou, Y. *et al.* Doping and alloying for improved perovskite solar cells. *J. Mater. Chem. A* **4**, 17623–17635 (2016).

96. Chen, J., Zhou, S., Jin, S., Li, H. & Zhai, T. Crystal organometal halide perovskites with promising optoelectronic applications. *J. Mater. Chem. C* **4**, 11–27 (2015).

97. Li, Z. *et al.* Stabilizing Perovskite Structures by Tuning Tolerance Factor: Formation of Formamidinium and Cesium Lead Iodide Solid-State Alloys. *Chem. Mater.* **28**, 284–292 (2016).

98. Ferdani, D. W. *et al.* Partial cation substitution reduces iodide ion transport in lead iodide perovskite solar cells. *Energy Environ. Sci.* **12**, 2264–2272 (2019).

99. Hao, F., Stoumpos, C. C., Chang, R. P. H. & Kanatzidis, M. G. Anomalous Band Gap Behavior in Mixed Sn and Pb Perovskites Enables Broadening of Absorption Spectrum in Solar Cells. *J. Am. Chem. Soc.* **136**, 8094–8099 (2014).

100. Guo, P. *et al.* Room-Temperature Red–Green–Blue Whispering-Gallery Mode Lasing and White-Light Emission from Cesium Lead Halide Perovskite (CsPbX3, X = Cl, Br, I) Microstructures. *Advanced Optical Materials* **6**, 1700993 (2018).

101. Knight, A. J. *et al.* Electronic Traps and Phase Segregation in Lead Mixed-Halide Perovskite. *ACS Energy Lett.* **4**, 75–84 (2019).

102. Knight, A. J. *et al.* Halide Segregation in Mixed-Halide Perovskites: Influence of A-Site Cations. *ACS Energy Lett.* **6**, 799–808 (2021).

103. Euvrard, J., Yan, Y. & Mitzi, D. B. Electrical doping in halide perovskites. *Nat Rev Mater* **6**, 531–549 (2021).

104. Du, K., Wang, X., Han, Q., Yan, Y. & Mitzi, D. B. Heterovalent B-Site Co-Alloying Approach for Halide Perovskite Bandgap Engineering. *ACS Energy Lett.* **2**, 2486–2490 (2017).

105. Born, M. & Oppenheimer, R. Zur Quantentheorie der Molekeln. *Ann. Phys.* **389**, 457–484 (1927).

106. Kohn, W. & Sham, L. J. Self-Consistent Equations Including Exchange and Correlation Effects. *Phys. Rev.* **140**, A1133–A1138 (1965).

107. Perdew, J. P. & Wang, Y. Pair-distribution function and its coupling-constant average for the spin-polarized electron gas. *Phys. Rev. B* **46**, 12947–12954 (1992).

108. Lee, C., Yang, W. & Parr, R. G. Development of the Colle-Salvetti correlation-energy formula into a functional of the electron density. *Phys. Rev. B* **37**, 785–789 (1988).

109. Hamprecht, F. A., Cohen, A. J., Tozer, D. J. & Handy, N. C. Development and assessment of new exchange-correlation functionals. *The Journal of Chemical Physics* **109**, 6264–6271 (1998).

110. Perdew, J. P., Burke, K. & Ernzerhof, M. Generalized Gradient Approximation Made Simple. *Phys. Rev. Lett.* **77**, 3865–3868 (1996).

111. Becke, A. D. A new mixing of Hartree–Fock and local density-functional theories. *The Journal of Chemical Physics* **98**, 1372–1377 (1993).

112. Heyd, J., Scuseria, G. E. & Ernzerhof, M. Hybrid functionals based on a screened Coulomb potential. *The Journal of Chemical Physics* **118**, 8207–8215 (2003).

113. Heyd, J., Scuseria, G. E. & Ernzerhof, M. Erratum: "Hybrid functionals based on a screened Coulomb potential" [J. Chem. Phys. 118, 8207 (2003)]. *The Journal of Chemical Physics* **124**, 219906 (2006).

114. Kresse, G. & Furthmüller, J. Efficiency of ab-initio total energy calculations for metals and semiconductors using a plane-wave basis set. *Comput. Mater. Sci.* **6**, 15–50 (1996).

115. Jeong, J. *et al.* Pseudo-halide anion engineering for α-FAPbI 3 perovskite solar cells. *Nature* **592**, 381–385 (2021).

116. Jeong, M. *et al.* Stable perovskite solar cells with efficiency exceeding 24.8% and 0.3-V voltage loss. *Science* **369**, 1615–1620 (2020).

117. Yang, W. S. *et al.* Iodide management in formamidinium-lead-halide–based perovskite layers for efficient solar cells. *Science* **356**, 1376–1379 (2017).

118. Liang, Y., Li, F. & Zheng, R. Low-Dimensional Hybrid Perovskites for Field-Effect Transistors with Improved Stability: Progress and Challenges. *Adv. Electron. Mater.* **6**, 2000137 (2020).

119. Kim, Y. C. *et al.* Beneficial Effects of PbI2 Incorporated in Organo-Lead Halide Perovskite Solar Cells. *Adv. Energy Mater.* **6**, 1502104 (2016).

120. Bi, D. *et al.* Efficient luminescent solar cells based on tailored mixed-cation perovskites. *Sci. Adv.* **2**, e1501170 (2016).

121. Park, B. *et al.* Understanding how excess lead iodide precursor improves halide perovskite solar cell performance. *Nat. Commun.* **9**, 3301 (2018).

122. Deng, Y. *et al.* Defect compensation in formamidinium–caesium perovskites for highly efficient solar mini-modules with improved photostability. *Nat. Energy* **6**, 633–641 (2021).

123. Johnston, M. B. & Herz, L. M. Hybrid Perovskites for Photovoltaics: Charge-Carrier Recombination, Diffusion, and Radiative Efficiencies. *Acc. Chem. Res.* **49**, 146–154 (2016).

124. Rehman, W. *et al.* Charge-Carrier Dynamics and Mobilities in Formamidinium Lead Mixed-Halide Perovskites. *Adv. Mater.* **27**, 7938–7944 (2015).

125. Shockley, W. & Queisser, H. J. Detailed Balance Limit of Efficiency of p-n Junction Solar Cells. *J. Appl. Phys.* **32**, 510–519 (1961).

126. Liu, N. & Yam, C. First-principles study of intrinsic defects in formamidinium lead triiodide perovskite solar cell absorbers. *Phys. Chem. Chem. Phys.* **20**, 6800–6804 (2018).

127. Meggiolaro, D. & De Angelis, F. First-Principles Modeling of Defects in Lead Halide Perovskites: Best Practices and Open Issues. *ACS Energy Lett.* **3**, 2206–2222 (2018).

128. Meggiolaro, D. *et al.* Iodine chemistry determines the defect tolerance of lead-halide perovskites. *Energy Environ. Sci.* **11**, 702–713 (2018).

129. Wang, J., Li, W. & Yin, W. Passivating Detrimental DX Centers in $CH_3NH_3PbI_3$ for Reducing Nonradiative Recombination and Elongating Carrier Lifetime. *Adv. Mater.* **32**, 1906115 (2020).

130. Agiorgousis, M. L., Sun, Y.-Y., Zeng, H. & Zhang, S. Strong Covalency-Induced Recombination Centers in Perovskite Solar Cell Material $CH_3NH_3PbI_3$. *J. Am. Chem. Soc.* **136**, 14570–14575 (2014).

131. Yin, W.-J., Yang, J.-H., Kang, J., Yan, Y. & Wei, S.-H. Halide perovskite materials for solar cells: a theoretical review. *J. Mater. Chem. A* **3**, 8926–8942 (2015).

132. Whalley, L. D. *et al.* Giant Huang–Rhys Factor for Electron Capture by the Iodine Intersitial in Perovskite Solar Cells. *J. Am. Chem. Soc.* **143**, 9123–9128 (2021).

133. Meggiolaro, D. & De Angelis, F. First-Principles Modeling of Defects in Lead Halide Perovskites: Best Practices and Open Issues. *ACS Energy Lett.* **3**, 2206–2222 (2018).

134. Tan, S. *et al.* Shallow Iodine Defects Accelerate the Degradation of α-Phase Formamidinium Perovskite. *Joule* **4**, 2426–2442 (2020).

135. Dagnall, K. A. *et al.* Relationship between the Nature of Monovalent Cations and Charge Recombination in Metal Halide Perovskites. *ACS Appl. Energy Mater.* **3**, 1298–1304 (2020).

136. Kresse, G. & Joubert, D. From ultrasoft pseudopotentials to the projector augmented-wave method. *Phys. Rev. B* **59**, 1758–1775 (1999).

137. Tkatchenko, A. & Scheffler, M. Accurate Molecular Van Der Waals Interactions from Ground-State Electron Density and Free-Atom Reference Data. *Phys. Rev. Lett.* **102**, 073005 (2009).

138. Motta, C. *et al.* Revealing the role of organic cations in hybrid halide perovskite CH3NH3PbI3. *Nat. Commun.* **6**, 7026 (2015).

139. Weller, M. T., Weber, O. J., Frost, J. M. & Walsh, A. Cubic Perovskite Structure of Black Formamidinium Lead Iodide, α-[HC(NH2)2]PbI3, at 298 K. *J. Phys. Chem. Lett.* **6**, 3209–3212 (2015).

140. Kang, J., Li, J. & Wei, S.-H. Atomic-scale understanding on the physics and control of intrinsic point defects in lead halide perovskites. *Applied Physics Reviews* **8**, 031302 (2021).

141. Nosé, S. A unified formulation of the constant temperature molecular dynamics methods. *J. Chem. Phys.* **81**, 511–519 (1984).

142. Alkauskas, A., Yan, Q. & Van de Walle, C. G. First-principles theory of nonradiative carrier capture via multiphonon emission. *Phys. Rev. B* **90**, 075202 (2014).

143. Turiansky, M. E. *et al.* Nonrad: Computing nonradiative capture coefficients from first principles. *Comput. Phys. Commun.* **267**, 108056 (2021).

144. Zhang, X., Turiansky, M. E. & Van de Walle, C. G. Correctly Assessing Defect Tolerance in Halide Perovskites. *J. Phys. Chem. C* **124**, 6022–6027 (2020).

145. Note: We noted that the negative defect formation energies have been widely reported, especially for the halide perovski.

146. Würfel, P. Physics of Solar Cells: From Principles to New Concepts. in *Physics of Solar Cells: From Principles to New Concepts* 7 (Wiley-VCH Verlag: Weinheim, 2008).

147. Alkauskas, A., Dreyer, C. E., Lyons, J. L. & Van de Walle, C. G. Role of excited states in Shockley-Read-Hall recombination in wide-band-gap semiconductors. *Phys. Rev. B* **93**, 201304 (2016).

148. Van de Walle, C. G. & Neugebauer, J. Universal alignment of hydrogen levels in semiconductors, insulators and solutions. *Nature* **423**, 626–628 (2003).

149. Liang, Y. *et al.* Hydrogen-Anion-Induced Carrier Recombination in MAPbI3 Perovskite Solar Cells. *J. Phys. Chem. Lett.* **12**, 10677–10683 (2021).

150. Liang, Y. *et al.* Atomic and Molecular Hydrogen Impurities in Hybrid Perovskite Solar Cells. *J. Phys. Chem. C* **126**, 1721–1728 (2022).

151. Alkauskas, A., McCluskey, M. D. & Van de Walle, C. G. Tutorial: Defects in semiconductors—Combining experiment and theory. *J. Appl. Phys.* **119**, 181101 (2016).

152. Suppan, P. The marcus inverted region. in *Photoinduced Electron Transfer IV* (ed. Mattay, J.) 95–130 (Springer, Berlin, Heidelberg, 1992). doi:10.1007/3-540-55117-4_5.

153. Lu, H., Krishna, A., Zakeeruddin, S. M., Grätzel, M. & Hagfeldt, A. Compositional and Interface Engineering of Organic-Inorganic Lead Halide Perovskite Solar Cells. *iScience* **23**, (2020).

154. Momblona, C. *et al.* Efficient methylammonium lead iodide perovskite solar cells with active layers from 300 to 900 nm. *APL Materials* **2**, 081504 (2014).

155. Zhang, X., Shen, J.-X. & Van de Walle, C. G. First-Principles Simulation of Carrier Recombination Mechanisms in Halide Perovskites. *Advanced Energy Materials* **10**, 1902830 (2020).

156. Meng, L., You, J. & Yang, Y. Addressing the stability issue of perovskite solar cells for commercial applications. *Nat. Commun.* **9**, 5265 (2018).

157. Ke, W., Stoumpos, C. C. & Kanatzidis, M. G. "Unleaded" Perovskites: Status Quo and Future Prospects of Tin-Based Perovskite Solar Cells. *Adv. Mater.* **31**, 1803230 (2019).

158. Cao, J. & Yan, F. Recent progress in tin-based perovskite solar cells. *Energy Environ. Sci.* **14**, 1286–1325 (2021).

159. Chung, I., Lee, B., He, J., Chang, R. P. H. & Kanatzidis, M. G. All-solid-state dye-sensitized solar cells with high efficiency. *Nature* **485**, 486–489 (2012).

160. Shao, S. *et al.* Highly Reproducible Sn-Based Hybrid Perovskite Solar Cells with 9% Efficiency. *Adv. Energy Mater.* **8**, 1702019 (2018).

161. Noel, N. K. *et al.* Lead-free organic–inorganic tin halide perovskites for photovoltaic applications. *Energy Environ. Sci.* **7**, 3061–3068 (2014).

162. Zhu, Z. *et al.* Smooth and Compact FASnI3 Films for Lead-Free Perovskite Solar Cells with over 14% Efficiency. *ACS Energy Lett.* **7**, 2079–2083 (2022).

163. Ma, L. *et al.* Carrier Diffusion Lengths of over 500 nm in Lead-Free Perovskite CH3NH3SnI3 Films. *J. Am. Chem. Soc.* **138**, 14750–14755 (2016).

164. Meng, X. *et al.* Crystallization Kinetics Modulation of FASnI3 Films with Pre-nucleation Clusters for Efficient Lead-Free Perovskite Solar Cells. *Angew. Chem. Int. Ed.* **60**, 3693–3698 (2021).

165. He, L. *et al.* Efficient Anti-solvent-free Spin-Coated and Printed Sn-Perovskite Solar Cells with Crystal-Based Precursor Solutions. *Matter* **2**, 167–180 (2020).

166. Ng, C. H. *et al.* Reducing trap density and carrier concentration by a Ge additive for an efficient quasi 2D/3D perovskite solar cell. *J. Mater. Chem. A* **8**, 2962–2968 (2020).

167. Ng, C. H. *et al.* Role of GeI2 and SnF2 additives for SnGe perovskite solar cells. *Nano Energy* **58**, 130–137 (2019).

168. Milot, R. L. *et al.* The Effects of Doping Density and Temperature on the Optoelectronic Properties of Formamidinium Tin Triiodide Thin Films. *Adv. Mater.* **30**, 1804506 (2018).

169. Tai, Q., Cao, J., Wang, T. & Yan, F. Recent advances toward efficient and stable tin-based perovskite solar cells. *EcoMat* **1**, e12004 (2019).

170. Yang, W.-F., Igbari, F., Lou, Y.-H., Wang, Z.-K. & Liao, L.-S. Tin Halide Perovskites: Progress and Challenges. *Advanced Energy Materials* **10**, 1902584 (2020).

171. Zhang, Q. *et al.* Stable Lead-Free Tin Halide Perovskite with Operational Stability >1200 h by Suppressing Tin(II) Oxidation. *Angewandte Chemie International Edition* **61**, e202205463 (2022).

172. Kumar, M. H. *et al.* Lead-Free Halide Perovskite Solar Cells with High Photocurrents Realized Through Vacancy Modulation. *Adv. Mater.* **26**, 7122–7127 (2014).

173. Shi, T. *et al.* Effects of organic cations on the defect physics of tin halide perovskites. *J. Mater. Chem. A* **5**, 15124–15129 (2017).

174. Van de Walle, C. G. & Neugebauer, J. Hydrogen in Semiconductors. *Annu. Rev. Mater. Res.* **36**, 179–198 (2006).

175. Ceratti, D. R. *et al.* Eppur si Muove: Proton Diffusion in Halide Perovskite Single Crystals. *Adv. Mater.* **32**, 2002467 (2020).

176. Sadhu, S., Buffeteau, T., Sandrez, S., Hirsch, L. & Bassani, D. M. Observing the Migration of Hydrogen Species in Hybrid Perovskite Materials through D/H Isotope Exchange. *J. Am. Chem. Soc.* **142**, 10431–10437 (2020).

177. Cardenas-Daw, C., Simon, T., Stolarczyk, J. K. & Feldmann, J. Migration of Constituent Protons in Hybrid Organic–Inorganic Perovskite Triggers Intrinsic Doping. *J. Am. Chem. Soc.* **139**, 16462–16465 (2017).

178. Egger, D. A., Kronik, L. & Rappe, A. M. Theory of Hydrogen Migration in Organic-Inorganic Halide Perovskites. *Angew. Chem. Int. Ed.* **54**, 12437–12441 (2015).

179. Liang, Y. *et al.* Minimizing and Controlling Hydrogen for Highly Efficient Formamidinium Lead Triiodide Solar Cells. *J. Am. Chem. Soc.* **144**, 6770–6778 (2022).

180. Liang, Y. *et al.* Hydrogen-Induced Nonradiative Recombination in All-Inorganic CsPbI3 Perovskite Solar Cells. *Solar RRL* **6**, 2200211 (2022).

181. Liang, Y. *et al.* Interstitial Hydrogen Anions: A Cause of p-Type Conductivity in CsSnI3. *J. Phys. Chem. C* (2022) doi:10.1021/acs.jpcc.2c04411.

182. Park, B. & Seok, S. I. Intrinsic Instability of Inorganic–Organic Hybrid Halide Perovskite Materials. *Adv. Mater.* **31**, 1805337 (2019).

183. Kahmann, S. *et al.* Negative Thermal Quenching in FASnI3 Perovskite Single Crystals and Thin Films. *ACS Energy Lett.* **5**, 2512–2519 (2020).

184. Freysoldt, C., Neugebauer, J. & Van de Walle, C. G. Fully Ab Initio Finite-Size Corrections for Charged-Defect Supercell Calculations. *Phys. Rev. Lett.* **102**, 016402 (2009).

185. See Supplemental Material at [URL will be inserted by publisher] for the intrinsic & H-related defects in FASnI3, local atomic structures of H substitution and complex, the calculated band structures of FASnI3, and change of the total energy for trapping the additional H species into the vacancy site.

186. Meggiolaro, D., Ricciarelli, D., Alasmari, A. A., Alasmary, F. A. S. & De Angelis, F. Tin versus Lead Redox Chemistry Modulates Charge Trapping and Self-Doping in Tin/Lead Iodide Perovskites. *J. Phys. Chem. Lett.* **11**, 3546–3556 (2020).

187. Tao, S. *et al.* Absolute energy level positions in tin- and lead-based halide perovskites. *Nat Commun* **10**, 2560 (2019).

188. Lavrov, E. V., Herklotz, F. & Weber, J. Identification of two hydrogen donors in ZnO. *Phys. Rev. B* **79**, 165210 (2009).

189. Meng, X. *et al.* Highly Reproducible and Efficient FASnI3 Perovskite Solar Cells Fabricated with Volatilizable Reducing Solvent. *J. Phys. Chem. Lett.* **11**, 2965–2971 (2020).

190. Meng, X. *et al.* Highly Stable and Efficient FASnI3-Based Perovskite Solar Cells by Introducing Hydrogen Bonding. *Advanced Materials* **31**, 1903721 (2019).

191. Subedi, B. *et al.* Effects of intrinsic and atmospherically induced defects in narrow bandgap (FASnI3)x(MAPbI3)1−x perovskite films and solar cells. *J. Chem. Phys.* **152**, 064705 (2020).

192. Nasti, G. & Abate, A. Tin Halide Perovskite (ASnX3) Solar Cells: A Comprehensive Guide toward the Highest Power Conversion Efficiency. *Advanced Energy Materials* **10**, 1902467 (2020).

193. Chen, Y. & Zhou, H. Defects chemistry in high-efficiency and stable perovskite solar cells. *Journal of Applied Physics* **128**, 060903 (2020).

194. Shao, Y., Yuan, Y. & Huang, J. Correlation of energy disorder and open-circuit voltage in hybrid perovskite solar cells. *Nat Energy* **1**, 1–6 (2016).

195. Ricciarelli, D., Meggiolaro, D., Ambrosio, F. & De Angelis, F. Instability of Tin Iodide Perovskites: Bulk p-Doping versus Surface Tin Oxidation. *ACS Energy Lett.* **5**, 2787–2795 (2020).

196. Tai, Q. *et al.* Antioxidant Grain Passivation for Air-Stable Tin-Based Perovskite Solar Cells. *Angewandte Chemie International Edition* **58**, 806–810 (2019).

197. Mundt, L. E. *et al.* Surface-Activated Corrosion in Tin–Lead Halide Perovskite Solar Cells. *ACS Energy Lett.* **5**, 3344–3351 (2020).

198. Lanzetta, L. *et al.* Degradation mechanism of hybrid tin-based perovskite solar cells and the critical role of tin (IV) iodide. *Nat Commun* **12**, 2853 (2021).

199. Zhang, Z. *et al.* Revealing superoxide-induced degradation in lead-free tin perovskite solar cells. *Energy Environ. Sci.* **15**, 5274–5283 (2022).

200. Li, H. *et al.* Surface Reconstruction for Tin-Based Perovskite Solar Cells. *ACS Energy Lett.* **7**, 3889–3899 (2022).

201. Liu, X. *et al.* Efficient and stable tin perovskite solar cells enabled by amorphous-polycrystalline structure. *Nat Commun* **11**, 2678 (2020).

202. Ke, W. *et al.* Enhanced photovoltaic performance and stability with a new type of hollow 3D perovskite {en}FASnI3. *Science Advances* **3**, e1701293 (2017).

203. Yao, H. *et al.* Strategies for Improving the Stability of Tin-Based Perovskite (ASnX3) Solar Cells. *Advanced Science* **7**, 1903540 (2020).

204. Stoumpos, C. C., Malliakas, C. D. & Kanatzidis, M. G. Semiconducting Tin and Lead Iodide Perovskites with Organic Cations: Phase Transitions, High Mobilities, and Near-Infrared Photoluminescent Properties. *Inorg. Chem.* **52**, 9019–9038 (2013).

205. Henkelman, G., Uberuaga, B. P. & Jónsson, H. A climbing image nudged elastic band method for finding saddle points and minimum energy paths. *The Journal of Chemical Physics* **113**, 9901–9904 (2000).

206. He, J., Fang, W.-H., Long, R. & Prezhdo, O. V. Why Oxygen Increases Carrier Lifetimes but Accelerates Degradation of CH3NH3PbI3 under Light Irradiation: Time-Domain Ab Initio Analysis. *J. Am. Chem. Soc.* **142**, 14664–14673 (2020).

207. Chu, W., Zheng, Q., Prezhdo, O. V., Zhao, J. & Saidi, W. A. Low-frequency lattice phonons in halide perovskites explain high defect tolerance toward electron-hole recombination. *Sci. Adv.* **6**, eaaw7453 (2020).

208. Shockley, W. & Read, W. T. Statistics of the Recombinations of Holes and Electrons. *Phys. Rev.* **87**, 835–842 (1952).

209. Shi, T. *et al.* Effects of organic cations on the defect physics of tin halide perovskites. *J. Mater. Chem. A* **5**, 15124–15129 (2017).

210. Qiao, L., Fang, W.-H., Long, R. & Prezhdo, O. V. Extending Carrier Lifetimes in Lead Halide Perovskites with Alkali Metals by Passivating and Eliminating Halide Interstitial Defects. *Angewandte Chemie* **132**, 4714–4720 (2020).

211. He, J., Fang, W.-H. & Long, R. Unravelling the effects of oxidation state of interstitial iodine and oxygen passivation on charge trapping and recombination in CH3NH3PbI3 perovskite: a time-domain ab initio study. *Chem. Sci.* **10**, 10079–10088 (2019).

212. Zhang, P. *et al.* Perovskite Solar Cells with ZnO Electron-Transporting Materials. *Advanced Materials* **30**, 1703737 (2018).

213. Noel, N. K. *et al.* Lead-free organic–inorganic tin halide perovskites for photovoltaic applications. *Energy Environ. Sci.* **7**, 3061–3068 (2014).

214. Henry, C. H. & Lang, D. V. Nonradiative capture and recombination by multiphonon emission in GaAs and GaP. *Phys. Rev. B* **15**, 989–1016 (1977).

215. Zhu, H. *et al.* High-performance hysteresis-free perovskite transistors through anion engineering. *Nat Commun* **13**, 1741 (2022).

216. Qiu, J., Xia, Y., Chen, Y. & Huang, W. Management of Crystallization Kinetics for Efficient and Stable Low-Dimensional Ruddlesden–Popper (LDRP) Lead-Free Perovskite Solar Cells. *Advanced Science* **6**, 1800793 (2019).

217. Liang, C. *et al.* Two-dimensional Ruddlesden–Popper layered perovskite solar cells based on phase-pure thin films. *Nat Energy* **6**, 38–45 (2021).

218. McMeekin, D. P. *et al.* A mixed-cation lead mixed-halide perovskite absorber for tandem solar cells. *Science* **351**, 151–155 (2016).

219. DuBose, J. T. & Kamat, P. V. TiO2-Assisted Halide Ion Segregation in Mixed Halide Perovskite Films. *J. Am. Chem. Soc.* **142**, 5362–5370 (2020).

220. DuBose, J. T. & Kamat, P. V. Hole Trapping in Halide Perovskites Induces Phase Segregation. *Acc. Mater. Res.* **3**, 761–771 (2022).

221. Chen, G.-Y., Guo, Z.-D., Gong, X.-G. & Yin, W.-J. Kinetic pathway of γ-to-δ phase transition in CsPbI3. *Chem* **8**, 3120–3129 (2022).

222. Oranskaia, A. & Schwingenschlögl, U. Suppressing X-Migrations and Enhancing the Phase Stability of Cubic FAPbX3 (X = Br, I). *Advanced Energy Materials* **9**, 1901411 (2019).

223. Yang, D. *et al.* Phase transition pathway of hybrid halide perovskites under compression: Insights from first-principles calculations. *Phys. Rev. Materials* **5**, 054603 (2021).

224. Dobrovolsky, A., Merdasa, A., Unger, E. L., Yartsev, A. & Scheblykin, I. G. Defect-induced local variation of crystal phase transition temperature in metal-halide perovskites. *Nat Commun* **8**, 34 (2017).

225. Ni, Z. *et al.* Evolution of defects during the degradation of metal halide perovskite solar cells under reverse bias and illumination. *Nat Energy* **7**, 65–73 (2022).

226. Wu, J. *et al.* Quantifying the Interface Defect for the Stability Origin of Perovskite Solar Cells. *Advanced Energy Materials* **9**, 1901352 (2019).

227. Ye, F. *et al.* Roles of MACl in Sequentially Deposited Bromine-Free Perovskite Absorbers for Efficient Solar Cells. *Adv. Mater.* **33**, 2007126 (2021).

228. Qin, M. *et al.* Manipulating the Mixed-Perovskite Crystallization Pathway Unveiled by In Situ GIWAXS. *Advanced Materials* **31**, 1901284 (2019).

229. Saliba, M. *et al.* Incorporation of rubidium cations into perovskite solar cells improves photovoltaic performance. *Science* **354**, 206–209 (2016).

230. Zheng, X. *et al.* Improved Phase Stability of Formamidinium Lead Triiodide Perovskite by Strain Relaxation. *ACS Energy Lett.* **1**, 1014–1020 (2016).

231. Kim, M. *et al.* Methylammonium Chloride Induces Intermediate Phase Stabilization for Efficient Perovskite Solar Cells. *Joule* **3**, 2179–2192 (2019).

232. Park, B. *et al.* Stabilization of formamidinium lead triiodide α-phase with isopropylammonium chloride for perovskite solar cells. *Nat Energy* **6**, 419–428 (2021).

233. Yang, Y. & You, J. Make perovskite solar cells stable. *Nature* **544**, 155–156 (2017).

234. Jiang, J. *et al.* Synergistic strain engineering of perovskite single crystals for highly stable and sensitive X-ray detectors with low-bias imaging and monitoring. *Nat. Photon.* **16**, 575–581 (2022).

235. Wang, F. *et al.* Simultaneous phase and size control of upconversion nanocrystals through lanthanide doping. *Nature* **463**, 1061–1065 (2010).

236. Wang, L. *et al.* A Eu3+-Eu2+ ion redox shuttle imparts operational durability to Pb-I perovskite solar cells. *Science* **363**, 265–270 (2019).

237. Duan, J. *et al.* Lanthanide Ions Doped CsPbBr3 Halides for HTM-Free 10.14%-Efficiency Inorganic Perovskite Solar Cell with an Ultrahigh Open-Circuit Voltage of 1.594 V. *Advanced Energy Materials* **8**, 1802346 (2018).

238. Zhang, X. *et al.* Defect-characterized phase transition kinetics. *Applied Physics Reviews* **9**, 041311 (2022).

239. Grimme, S., Antony, J., Ehrlich, S. & Krieg, H. A consistent and accurate ab initio parametrization of density functional dispersion correction (DFT-D) for the 94 elements H-Pu. *J. Chem. Phys.* **132**, 154104 (2010).

240. Qian, G.-R. *et al.* Variable cell nudged elastic band method for studying solid–solid structural phase transitions. *Computer Physics Communications* **184**, 2111–2118 (2013).

241. Saleh, G. & Artyukhin, S. First-Principles Theory of Phase Transitions in IrTe2. *J. Phys. Chem. Lett.* **11**, 2127–2132 (2020).

242. Fu, Z. *et al.* Atomic reconfiguration among tri-state transition at ferroelectric/antiferroelectric phase boundaries in Pb(Zr,Ti)O3. *Nat Commun* **13**, 1390 (2022).

243. Jinnouchi, R., Karsai, F. & Kresse, G. On-the-fly machine learning force field generation: Application to melting points. *Phys. Rev. B* **100**, 014105 (2019).

244. Jinnouchi, R., Lahnsteiner, J., Karsai, F., Kresse, G. & Bokdam, M. Phase Transitions of Hybrid Perovskites Simulated by Machine-Learning Force Fields Trained on the Fly with Bayesian Inference. *Phys. Rev. Lett.* **122**, 225701 (2019).

245. Maeng, I. *et al.* Unusual terahertz-wave absorptions in δ/α-mixed-phase FAPbI3 single crystals: interfacial phonon vibration modes. *NPG Asia Mater* **13**, 1–8 (2021).

246. Kweon, K. E. *et al.* Influence of External Conditions on the Black-to-Yellow Phase Transition of CsPbI3 Based on First-Principles Calculations: Pressure and Moisture. *Chem. Mater.* **35**, 2321–2329 (2023).

247. Haruyama, J., Sodeyama, K., Han, L. & Tateyama, Y. First-Principles Study of Ion Diffusion in Perovskite Solar Cell Sensitizers. *J. Am. Chem. Soc.* **137**, 10048–10051 (2015).

248. Motta, C., El-Mellouhi, F. & Sanvito, S. Exploring the cation dynamics in lead-bromide hybrid perovskites. *Phys. Rev. B* **93**, 235412 (2016).

249. Kanno, S., Imamura, Y. & Hada, M. Theoretical Study on Rotational Controllability of Organic Cations in Organic–Inorganic Hybrid Perovskites: Hydrogen Bonds and Halogen Substitution. *J. Phys. Chem. C* **121**, 26188–26195 (2017).

250. Ghosh, D., Walsh Atkins, P., Islam, M. S., Walker, A. B. & Eames, C. Good Vibrations: Locking of Octahedral Tilting in Mixed-Cation Iodide Perovskites for Solar Cells. *ACS Energy Lett.* **2**, 2424–2429 (2017).

251. Chu, W., Saidi, W. A., Zhao, J. & Prezhdo, O. V. Soft Lattice and Defect Covalency Rationalize Tolerance of β-CsPbI3 Perovskite Solar Cells to Native Defects. *Angewandte Chemie International Edition* **59**, 6435–6441 (2020).

252. Lu, C., Wang, Y., Zhang, R. & Xu, S. Demystifying phase transformations in metal halide perovskites. *Matter* **4**, 2627–2629 (2021).

253. Lee, J.-W., Kim, H.-S. & Park, N.-G. Lewis Acid–Base Adduct Approach for High Efficiency Perovskite Solar Cells. *Acc. Chem. Res.* **49**, 311–319 (2016).

254. Phung, N. *et al.* The Doping Mechanism of Halide Perovskite Unveiled by Alkaline Earth Metals. *J. Am. Chem. Soc.* **142**, 2364–2374 (2020).

255. Zhang, X., Li, L., Sun, Z. & Luo, J. Rational chemical doping of metal halide perovskites. *Chemical Society Reviews* **48**, 517–539 (2019).

256. Zhao, Y. *et al.* Suppressing ion migration in metal halide perovskite via interstitial doping with a trace amount of multivalent cations. *Nat. Mater.* **21**, 1396–1402 (2022).

257. Liang, Y. *et al.* Origin of Enhanced Nonradiative Carrier Recombination Induced by Oxygen in Hybrid Sn Perovskite. *J. Phys. Chem. Lett.* **14**, 2950–2957 (2023).

258. Liang, Y. *et al.* Trapped-Hydrogen-Induced Energy Loss in Tin-Based Hybrid Perovskite Solar Cells. *Phys. Rev. Applied* **18**, 034084 (2022).

259. Yi, C. *et al.* Entropic stabilization of mixed A-cation ABX3 metal halide perovskites for high performance perovskite solar cells. *Energy Environ. Sci.* **9**, 656–662 (2016).

260. Pazoki, M. *et al.* Electronic structure of organic–inorganic lanthanide iodide perovskite solar cell materials. *J. Mater. Chem. A* **5**, 23131–23138 (2017).

261. Smith, R. W. & Rose, A. Space-Charge-Limited Currents in Single Crystals of Cadmium Sulfide. *Phys. Rev.* **97**, 1531–1537 (1955).

262. Yoo, J. J. *et al.* Efficient perovskite solar cells via improved carrier management. *Nature* **590**, 587–593 (2021).

263. Liang, Z. *et al.* Out-of-plane cations homogenise perovskite composition for solar cells. *Nature* 1–3 (2023) doi:10.1038/s41586-023-06784-0.

264. Yang, J.-H., Yin, W.-J., Park, J.-S. & Wei, S.-H. Fast self-diffusion of ions in CH3NH3PbI3: the interstiticaly mechanism versus vacancy-assisted mechanism. *J. Mater. Chem. A* **4**, 13105–13112 (2016).

265. Yang, D., Ming, W., Shi, H., Zhang, L. & Du, M.-H. Fast Diffusion of Native Defects and Impurities in Perovskite Solar Cell Material $CH_3NH_3PbI_3$. *Chem. Mater.* **28**, 4349–4357 (2016).

266. Walsh, A. & Stranks, S. D. Taking Control of Ion Transport in Halide Perovskite Solar Cells. *ACS Energy Lett.* **3**, 1983–1990 (2018).

267. Frost, J. M. & Walsh, A. What Is Moving in Hybrid Halide Perovskite Solar Cells? *Acc. Chem. Res.* **49**, 528–535 (2016).

268. Thiesbrummel, J. *et al.* Ion-induced field screening as a dominant factor in perovskite solar cell operational stability. *Nat Energy* 1–13 (2024) doi:10.1038/s41560-024-01487-w.

269. Muscarella, L. A. *et al.* Lattice Compression Increases the Activation Barrier for Phase Segregation in Mixed-Halide Perovskites. *ACS Energy Lett.* **5**, 3152–3158 (2020).

270. Xue, D.-J. *et al.* Regulating strain in perovskite thin films through charge-transport layers. *Nat Commun* **11**, 1514 (2020).

271. Zhao, J. *et al.* Strained hybrid perovskite thin films and their impact on the intrinsic stability of perovskite solar cells. *Sci. Adv.* **3**, eaao5616 (2017).

272. Senanayak, S. P. *et al.* Charge transport in mixed metal halide perovskite semiconductors. *Nat. Mater.* **22**, 216–224 (2023).

273. Tan, S. *et al.* Steric Impediment of Ion Migration Contributes to Improved Operational Stability of Perovskite Solar Cells. *Advanced Materials* **32**, 1906995 (2020).

274. Jodlowski, A. D. *et al.* Large guanidinium cation mixed with methylammonium in lead iodide perovskites for 19% efficient solar cells. *Nat Energy* **2**, 972–979 (2017).

275. Dey, K. *et al.* Substitution of Lead with Tin Suppresses Ionic Transport in Halide Perovskite Optoelectronics. *Energy Environ. Sci.* (2023) doi:10.1039/D3EE03772J.

276. Swarnkar, A., Mir, W. J. & Nag, A. Can B-Site Doping or Alloying Improve Thermal- and Phase-Stability of All-Inorganic CsPbX3 (X = Cl, Br, I) Perovskites? *ACS Energy Lett.* **3**, 286–289 (2018).

277. Solari, S. F. *et al.* Stabilization of Lead-Reduced Metal Halide Perovskite Nanocrystals by High-Entropy Alloying. *J. Am. Chem. Soc.* **144**, 5864–5870 (2022).

278. Zhang, W. *et al.* B-Site Co-Doping Coupled with Additive Passivation Pushes the Efficiency of Pb–Sn Mixed Inorganic Perovskite Solar Cells to Over 17%. *Advanced Materials* **n/a**, 2309193.

279. Guo, Z., Wang, J. & Yin, W.-J. Atomistic origin of lattice softness and its impact on structural and carrier dynamics in three dimensional perovskites. *Energy Environ. Sci.* **15**, 660–671 (2022).

280. Muy, S. *et al.* Tuning mobility and stability of lithium ion conductors based on lattice dynamics. *Energy Environ. Sci.* **11**, 850–859 (2018).

281. Baikie, T. *et al.* Synthesis and crystal chemistry of the hybrid perovskite (CH3NH3)PbI3 for solid-state sensitised solar cell applications. *J. Mater. Chem. A* **1**, 5628–5641 (2013).

282. van de Walle, A. *et al.* Efficient stochastic generation of special quasirandom structures. *Calphad* **42**, 13–18 (2013).

283. Wang, J. & Yin, W.-J. Effect of alloying on the carrier dynamics in high-performance perovskite solar cells. *Journal of Energy Chemistry* **68**, 267–274 (2022).

284. van de Walle, A. Multicomponent multisublattice alloys, nonconfigurational entropy and other additions to the Alloy Theoretic Automated Toolkit. *Calphad* **33**, 266–278 (2009).

285. Tong, C.-J., Geng, W., Prezhdo, O. V. & Liu, L.-M. Role of Methylammonium Orientation in Ion Diffusion and Current–Voltage Hysteresis in the CH3NH3PbI3 Perovskite. *ACS Energy Lett.* **2**, 1997–2004 (2017).

286. He, X., Zhu, Y. & Mo, Y. Origin of fast ion diffusion in super-ionic conductors. *Nat Commun* **8**, 15893 (2017).

287. Bag, M. *et al.* Kinetics of Ion Transport in Perovskite Active Layers and Its Implications for Active Layer Stability. *J. Am. Chem. Soc.* **137**, 13130–13137 (2015).

288. Moia, D. & Maier, J. Ion Transport, Defect Chemistry, and the Device Physics of Hybrid Perovskite Solar Cells. *ACS Energy Lett.* **6**, 1566–1576 (2021).

289. Jana, A., Ba, Q., Nissimagoudar, A. S. & Kim, K. S. Formation of a photoactive quasi-2D formamidinium lead iodide perovskite in water. *J. Mater. Chem. A* **7**, 25785–25790 (2019).

290. Aranda, C. A. *et al.* Overcoming ionic migration in perovskite solar cells through alkali metals. *Joule* **8**, 241–254 (2024).

291. Cao, J., Tao, S. X., Bobbert, P. A., Wong, C.-P. & Zhao, N. Interstitial Occupancy by Extrinsic Alkali Cations in Perovskites and Its Impact on Ion Migration. *Advanced Materials* **30**, 1707350 (2018).

292. Sun, Q. & Yin, W.-J. Thermodynamic Stability Trend of Cubic Perovskites. *J. Am. Chem. Soc.* **139**, 14905–14908 (2017).

293. Futscher, M. H. *et al.* Quantification of ion migration in $CH_3NH_3PbI_3$ perovskite solar cells by transient capacitance measurements. *Mater. Horiz.* **6**, 1497–1503 (2019).

294. Peng, W. *et al.* Quantification of Ionic Diffusion in Lead Halide Perovskite Single Crystals. *ACS Energy Lett.* **3**, 1477–1481 (2018).

295. Sakhatskyi, K. *et al.* Assessing the Drawbacks and Benefits of Ion Migration in Lead Halide Perovskites. *ACS Energy Lett.* **7**, 3401–3414 (2022).

296. Liang, Y. *et al.* Toward stabilization of formamidinium lead iodide perovskites by defect control and composition engineering. *Nat Commun* **15**, 1707 (2024).

297. Liu, Y., Yang, Z. & Liu, S. (Frank). Recent Progress in Single-Crystalline Perovskite Research Including Crystal Preparation, Property Evaluation, and Applications. *Advanced Science* **5**, 1700471 (2018).

298. Xiao, Y., Yang, X., Zhu, R. & Snaith, H. J. Unlocking interfaces in photovoltaics. *Science* **384**, 846–848 (2024).

299. McGott, D. L. *et al.* 3D/2D passivation as a secret to success for polycrystalline thin-film solar cells. *Joule* **5**, 1057–1073 (2021).